Yasuaki Einaga *Editor*

Diamond Electrodes

Fundamentals and Applications

Springer

Diamond Electrodes

https://www.twirpx.org & http://chemistry-chemists.com

Yasuaki Einaga
Editor

Diamond Electrodes

Fundamentals and Applications

Springer

https://www.twirpx.org & http://chemistry-chemists.com

Editor
Yasuaki Einaga
Department of Chemistry
Keio University
Yokohama, Kanagawa, Japan

ISBN 978-981-16-7833-2 ISBN 978-981-16-7834-9 (eBook)
https://doi.org/10.1007/978-981-16-7834-9

© Springer Nature Singapore Pte Ltd. 2022
This work is subject to copyright. All rights are reserved by the Publisher, whether the whole or part of the material is concerned, specifically the rights of translation, reprinting, reuse of illustrations, recitation, broadcasting, reproduction on microfilms or in any other physical way, and transmission or information storage and retrieval, electronic adaptation, computer software, or by similar or dissimilar methodology now known or hereafter developed.
The use of general descriptive names, registered names, trademarks, service marks, etc. in this publication does not imply, even in the absence of a specific statement, that such names are exempt from the relevant protective laws and regulations and therefore free for general use.
The publisher, the authors and the editors are safe to assume that the advice and information in this book are believed to be true and accurate at the date of publication. Neither the publisher nor the authors or the editors give a warranty, expressed or implied, with respect to the material contained herein or for any errors or omissions that may have been made. The publisher remains neutral with regard to jurisdictional claims in published maps and institutional affiliations.

This Springer imprint is published by the registered company Springer Nature Singapore Pte Ltd.
The registered company address is: 152 Beach Road, #21-01/04 Gateway East, Singapore 189721, Singapore

https://www.twirpx.org & http://chemistry-chemists.com

Preface

The application development of "utilizing diamond as a chemical electrode" has made rapid progress in both fundamental physical properties and application development in the last 10–20 years. In particular, this "diamond electrode" was mainly used for waste water treatment and purification in the early years for environmental improvement, but in these days, this is utilized for electrochemical analysis and sensors such as environmental monitoring and biomedical measurement. Then, it has been found that the application range is extremely diverse, including as an electrode for ozone generation, an electrode for synthesizing organic compounds that lead to drug discovery, and an electrode for synthesizing useful chemicals by CO_2 reduction, etc. In that sense, it is becoming more attractive than before. On the other hand, the "diamond electrode" that contributes to such applications exhibits superior electrochemical properties that are unique compared to conventional electrode materials, so the fundamental studies on physical properties of the electrode interface and the correlation between physical properties and electrochemical properties are attracting increasing attention.

In particular, since 2011, national projects for Strategic Basic research Programs on diamond electrodes (CREST (2011–2015) and ACCEL (2014–2020)), whose director is Prof. Yasuaki Einaga, have been adopted by Japan Science and Technology Agency (JST). Then, we could accelerate the "diamond electrodes" research with relevant active researchers. In the meantime, although research activity on diamond electrodes has been increasing year by year worldwide, this book especially focuses on the attractive development of diamond electrodes on fundamentals and applications in Japan related to these national projects.

In "Introduction" part, current status of diamond electrochemistry and the future prospects are described. In this book, fundamentals are described in the first half and developments on electrochemical applications are described in the second half. In chapter "Electrochemical Properties of BDD Electrodes by Surface Control", Einaga et al. discuss the importance of surfaces on Boron-Doped Diamond (BDD) electrodes. In chapter "Localized Surface Characterization of Boron-Doped Diamond Film Electrodes", Catalan et al. examined localized surface of BDD electrodes. In chapter "Electrochemical Imaging of BDD", Takahashi et al. focused on the imaging

https://www.twirpx.org & http://chemistry-chemists.com

of BDD surface. In chapter "Computational Aspects of Surface and Interface of BDD Electrode", Tateyama et al. applied the theoretical calculation to understand the superior electrochemical properties of BDD electrodes. In chapter "Porous Diamond Electrodes and Application to Electrochemical Capacitors", Kondo prepared porous diamond electrodes and reported the application to electrochemical capacitors. In chapter "Boron-Doped Diamond Powder", Kondo introduced the advances of boron-doped diamond powder for electrochemical sensor application. In chapter "Electrogenerated Chemiluminescence at Diamond Electrode", Irkham et al. developed an application for electrochemiluminescence using BDD electrodes. In chapter "Photoelectrocatalytic and Photocatalytic Reduction Using Diamond", Nakata et al. focused on photoelectrocatalytic and photocatalytic reduction using BDD electrodes. In chapter "Electrochemical CO_2 Reduction", Tomisaki et al. summarized the recent development of CO_2 reduction by BDD electrodes to produce useful compounds. In chapter "Electro-Organic Synthesis", Yamamoto et al. focused on electrochemical organic synthesis application. In chapter "Industrial Application of Electrochemical Chlorine Sensor", Einaga et al. introduced a recent development of practical electrochemical sensor application for free chlorine detection. In chapter "Modified Boron–Doped Diamond Electrodes for Sensors and Electroanalysis", Jiwanti et al. focused on modified BDD electrodes for sensors and electroanalysis application. In chapter "In Vivo Real-Time Measurement of Drugs", Ogata et al. discussed in vivo real-time measurement of drugs for biomedical application. Finally, in chapter "Influenza Virus", Matsubara et al. discussed the application of influenza virus detection.

Lastly, I would very much like to acknowledge Prof. Akira Fujishima (Distinguished Professor, Tokyo University of Science), who is my supervisor and led me to this research area of diamond electrochemistry. Furthermore, I would like to thank Prof. Kohei Tamao (Research supervisor of JST-CREST) and Prof. Yoichiro Matsumoto (Chair, R&D Management Committee of JST-ACCEL and President of Tokyo University of Science) for giving us a chance to accelerate the researches on diamond electrochemistry. Finally, I would like to thank all the authors for their efforts and great contributions.

Yokohama, Japan Yasuaki Einaga

https://www.twirpx.org & http://chemistry-chemists.com

Contents

Introduction 1
Yasuaki Einaga

Electrochemical Properties of BDD Electrodes by Surface Control 9
Yasuaki Einaga, Seiji Kasahara, and Keisuke Natsui

Localized Surface Characterization of Boron-Doped Diamond Film Electrodes 23
Francesca Celine I. Catalan and Yousoo Kim

Electrochemical Image of BDD 43
Yasufumi Takahashi, Makarova Marina, Tomohiro Ando, and Takeshi Fukuma

Computational Aspects of Surface and Interface of BDD Electrode 57
Yoshitaka Tateyama, Zdenek Futera, Yusuke Ootani, Shota Iizuka, and Le The Anh

Porous Diamond Electrodes and Application to Electrochemical Capacitors 73
Takeshi Kondo

Boron-Doped Diamond Powder 97
Takeshi Kondo

Electrogenerated Chemiluminescence at Diamond Electrode 119
Irkham, Andrea Fiorani, and Yasuaki Einaga

Photoelectrocatalytic and Photocatalytic Reduction Using Diamond 139
Kazuya Nakata and Chiaki Terashima

Electrochemical CO_2 Reduction 161
Mai Tomisaki and Yasuaki Einaga

Electro-Organic Synthesis 177
Takashi Yamamoto and Tsuyoshi Saitoh

https://www.twirpx.org & http://chemistry-chemists.com

Industrial Application of Electrochemical Chlorine Sensor 197
Yasuaki Einaga

Modified Boron-Doped Diamond Electrodes for Sensors and Electroanalysis 207
Prastika K. Jiwanti, Shafrizal R. Atriardi, Yulia M. T. A. Putri, Tribidasari A. Ivandini, and Yasuaki Einaga

In Vivo Real-Time Measurement of Drugs 227
Genki Ogata, Seishiro Sawamura, Kai Asai, Hiroyuki Kusuhara, Yasuaki Einaga, and Hiroshi Hibino

Influenza Virus 237
Teruhiko Matsubara and Toshinori Sato

https://www.twirpx.org & http://chemistry-chemists.com

Introduction

Yasuaki Einaga

1 History of Research on Diamond Electrodes

A first example of electrochemical measurement using diamond as an electrode is a study by Iwaki et al. (RIKEN) in 1983. They are investigating the electrochemical properties as a semiconducting electrode. However, the conductivity was due to the damaged surface by ion implantation into insulating diamond [1]. Although this is the first example of using diamond as a working electrode, it is a little different from "diamond electrode" (basically consisting of sp^3 carbon) in this book, which is doped with impurities to make it conductive. In fact, research into this direction has not been pursued since then.

On the other hand, diamond materials have been actively studied and developed as wide bandgap semiconductor. From the viewpoint, photoelectrochemical properties as a semiconducting diamond are discussed after 1987. At first, Pleskov et al. observed the photocurrent by photoexciting semiconducting diamond [2], and then, Fujishima et al. carefully investigated the behavior of photoelectrochemistry [3]. On the other hand, Swain et al. showed the possibility of applying boron-doped polycrystalline diamond to electrodes for electrochemical analysis (1993) [4], and Ramesham et al. used this electrode for wastewater treatment [5]. Most of the diamond used at the periods, which was called "Diamond electrode," was mainly p-type semiconducting diamond with a low boron doping level.

Then, several companies in Europe have begun commercializing water treatment systems using diamond electrodes. In terms of "industrialization" of diamond electrodes, this application to wastewater treatment and water purification is the first one [6]. Around the periods, the number of reports for fundamental researches and application of electrochemical analysis has begun to increase along with application to the waste water treatment.

Y. Einaga (✉)
Department of Chemistry, Keio University, 3-14-1 Hiyoshi, Yokohama 223-8522, Japan
e-mail: eianga@chem.keio.ac.jp

© Springer Nature Singapore Pte Ltd. 2022

Y. Einaga (ed.), *Diamond Electrodes*,
https://doi.org/10.1007/978-981-16-7834-9_1

https://www.twirpx.org & http://chemistry-chemists.com

Since then, also, the number of research papers has continued to increase since 2000, and most of them are related to electrochemical analysis such as sensor applications [7, 8], wastewater treatment and purification [9, 10]. Especially around this time, Fujishima and Einaga have mainly focused on highly boron-doped diamond, which exhibits metal-like conductivity, and has been developing them for electrochemical applications. Especially in these days, for many applications, the "highly boron-doped diamond" with metal-like conductivity can be developed as "boron-doped diamond (BDD) electrodes."

The first industrialization of electrochemical sensor application was done by HORIBA, Ltd. and Einaga's collaboration as a production of prototype for heavy metal sensing in 2010, and it has been expanding significantly since then.

On the other hand, along with these developments on applications, studies on the fundamental electrochemical properties of BDD electrodes have attracted much attention. For example, because surface chemical terminations (hydrogen, oxygen) have a great influence on the electrochemical properties of BDD, the study on the physicochemical properties of electrode surface is becoming more and more important [11, 12].

Furthermore, after 2012, we report a possibility of "useful chemicals can be synthesized by electrochemical organic electrolysis" [13] and "useful compounds can be synthesized by electrochemical reduction of carbon dioxide (CO_2)" [14] by using BDD electrodes. It can be spreading as a new application development, and it is expected that BDD electrodes can contribute to many fields as next-generation electrode materials.

The increasing activity of research on "diamond electrodes" can be well understood by the number of related publications. The number of publications has increased sharply since the turn of the century, and a number of review articles and publications have been published [15–21]. (In 2005, we have published a first Japanese book on "Diamond Electrochemistry" [22]). As shown in Fig. 1, the activity of academic research in this field has increased rapidly in recent years.

On the other hand, in recent years, "element strategy" is attracting attention as one of the most important strategy for realizing a sustainable society. The "element strategy" aimed at expanding the science of elements to solve our resource problems. For this direction, environmental problems, resource, and energy should be solved also from the viewpoint of materials science, i.e., to create innovative functions of intelligent materials that are quite different from conventional functions [23]. Under such situations, the interest in "diamond electrodes" can be very important in terms of the "elemental strategy," because boron-doped diamond (BDD) electrodes consist of light elements such as "rare metal-free" carbon and boron, and also can surpass the properties of metals.

https://www.twirpx.org & http://chemistry-chemists.com

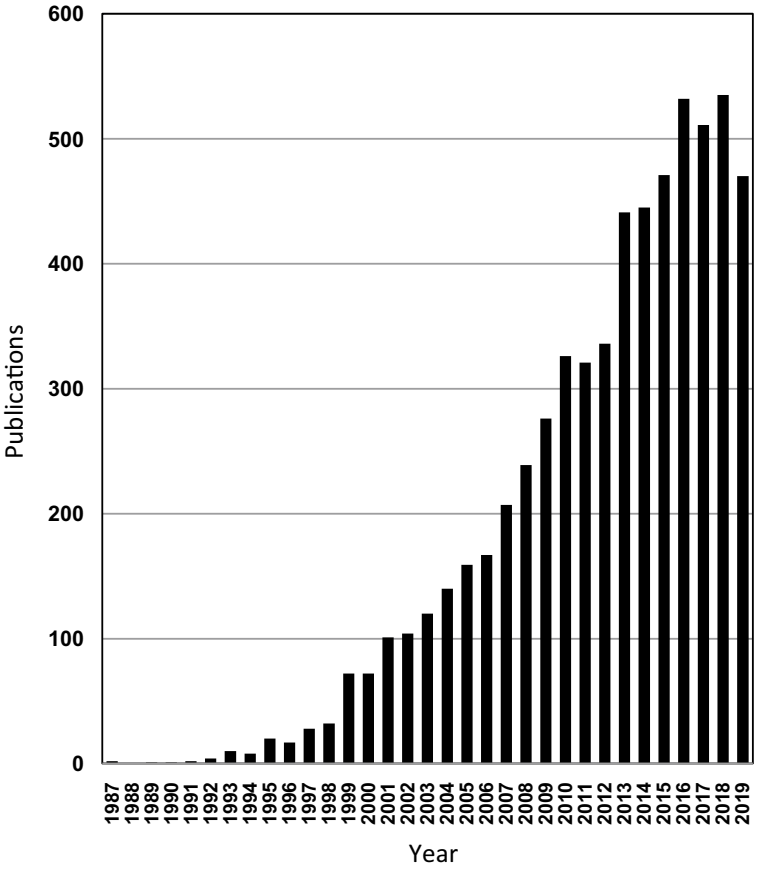

Fig. 1 Publications on diamond electrochemistry

2 Accelerating Research Development Through Research Projects Related to "Diamond Electrodes" (JST-CREST and JST-ACCEL)

JST-CREST (April 2011-March 2015).

After getting a Ph.D degree in 1999, the author (Einaga) started a research on diamond electrodes as a research associate in Professor Akira Fujishima's group at the University of Tokyo. Then, in 2001, when I became independent and had my own research group at Keio University, I have promoted the research on diamond electrodes in real earnest. At that time, the main direction of application was an "electrochemical sensor," which was a fundamental research on high-sensitive analysis of various environmental biological important species.

https://www.twirpx.org & http://chemistry-chemists.com

Then, as a strategic creation research promotion project (CREST) of the Japan Science and Technology Agency (JST), a new research area "From the perspective of material science/physical science with elemental strategy as a common concept for resource/energy/environmental problems" has started in 2011. The title was "Creation of Innovative Functions of Intelligent Materials on the Basis of Element Strategy" (Research Supervisor, Professor Kohei Tamao). Fortunately, Einaga was awarded as a research director of a project "Development of Innovative Technologies Using Diamond Electrodes for Improving Environment" since 2011. Because the main theme of this project is "elemental strategy," the development of "diamond" as a material is exactly the appropriate for the elemental strategy. Therefore, we could promote research toward new functional developments of diamond electrodes.

In addition to the development of new functions of diamond electrodes, we were able to obtain a lot of fundamental knowledges such as the correlation between the physical properties and electrochemical properties. In particular, the main functions newly discovered by this project are (1) "electrochemical CO_2 reduction" and (2) "electrochemical organic synthesis. "From these results, it became clear that the "diamond electrodes" can apply to a wide range from environmental improvement to biomedical applications. However, each application does not necessarily require the same properties of the electrodes. Consequently, the electrode design appropriate for each application is necessary in order to realize the full potential of diamond electrodes. Then, the factors that determine the properties of the electrode have gradually been clear [24]. It was very important for the development of this field that the knowledge about the relationship between fundamental physical properties and electrochemical properties as materials increased along with the development of applications.

JST-ACCEL (for industrialization) (December 2014–March 2020)

Initially, the JST-CREST project was supposed to be carried out for 5 years from April 2011 to March 2016. However, in December 2014, fortunately, industrialization was expected based on the above-mentioned new functions and developments, and then, a new project (JST-ACCEL) started. It means that we were given the opportunity to more strongly promote the application development of "diamond electrodes" (CREST project was finished early by March 2015.).

In Web site of JST, [25] "What is ACCLE?" is as follows. "ACCEL aims to set a path to the next phase, such as company R&D, venture start-up, and other public funding, based on the outputs of the Strategic Basic Research Programs (CREST, etc.) that have the potential to be world-leading but cannot be continued by companies and other organizations due to their perceived risks. The Program Manager (PM) leads research and development with the innovation requirements and goals, demonstrating Proof of Concept (POC) and promoting the appropriate rights arrangements." For this project, Mr. Tsukahara, who is good at intellectual property management, was assigned as a PM, and he and Einaga (Principal Investigator = PI) proceeded it together. At that time, just as the number of inquiries and requests for diamond electrodes provided by companies has increased and PI could see the limit to responding to them, it was the good timing for PI to promote the project together with PM. Thanks to PM-led communication with companies and management of intellectual

https://www.twirpx.org & http://chemistry-chemists.com

property, collaboration works with companies were accelerating. For example, an "ozone water generator" for medical hand washing using a diamond electrode has been in commercially available (in 2017).

Another important development is that several Japanese companies have begun to focus on "manufacturing optimal diamond electrodes for their applications". It is also a major achievement of the ACCEL project for the social implementation of diamond electrodes.

Contents of ACCEL project

The topics in ACCEL project was as follows: (1) application to electrochemical sensors, (2) electrochemical synthesis of useful compounds (including CO_2 reduction), other (3) ozone water generation, and (4) wastewater treatment. Some of them include collaboration research with companies. However, "fundamental knowledge" is also indispensable for advancing application development.

We are also making efforts to evaluate the physical properties of boron-doped diamond as a material.

Expansion to medical application and healthcare

Apart from the above-mentioned application examples, expectations are also rising for "contribution to medical sciences" of diamond electrodes as a direction for major expansion in the near future. In particular, recently, we are focusing on "In vivo real-time measurement." In 2007, we first reported in vivo detection of dopamine in mouse brain, where the boron-doped diamond microelectrode was inserted into the corpus striatum of the mouse brain. [26] A clear signal current response could be monitored with high sensitivity in vivo. However, although, at that time, the manufacturing (fabrication) yield of BDD microelectrode was not so good, we have concentrated on developing the fabrication of the diamond microelectrodes to increase the fabrication yield. Then, after our improvement of the BDD microelectrode fabrication, the manufacturing yield was stable. Thanks to the improvements, we could frequently apply to biomedical measurements such as in vivo measurements. In 2017, we could develop a system "in vivo" that can study pharmacokinetics in real time and directly understand the correlation with biological functions such as hearing ability by collaboration with Prof. Hiroshi Hibino (School of Medicine, Niigata University).[27] Such real-time measurement of pharmacokinetics and pharmacodynamics of drugs in vivo can contribute to various animals and various organs. Also, it is greatly expected to contribute to the research of clarifying the function of living organs.

3 Future Outlook

At present, the stage of practical application depends on the application. For example, an application that has already been put into practical use, an application that will soon be put into practical use, and an application that will be greatly expanded in a few years. In any case, it can be said that the "diamond electrode" is a capable functional

https://www.twirpx.org & http://chemistry-chemists.com

electrode material that has sufficient potential to play an active role in next-generation environmental improvement and medical applications in various situations.

That is, it enables highly sensitive "environmental pollutant sensing" on the spot and enables "high-efficiency waste water treatment".

It is not a dream that every household is equipped with a small water purifier with a diamond electrode, which is useful at the time of a disaster. Also, for example, each home is equipped with a simple health check device such as disposable one, and medical institutions including hospital use a "high-sensitive health check system" not only for blood and urine tests but also for monitoring important species during surgery.

As another direction to resource, environment, and energy issues, especially, the electrochemical CO_2 reduction and the development of electrochemical organic synthesis are highly expected (Fig. 2).

Although for electrochemical sensor application, a small diamond electrode can be used, for applications such as water treatment and electrochemical organic synthesis including CO_2 reduction, diamond electrodes with large area is necessary. The problem of electrode manufacturing cost can be a bottleneck for industrialization. To that end, attempts are being made to manufacture and reduce the cost of large-area "diamond electrodes" that ensure the quality of the electrodes. Also, developments are being made toward large-scale equipment.

In addition, while research and development related to applications have been active, interest in understanding the physical and physicochemical properties of the "diamond electrode" and the importance of fundamental studies are also rapidly

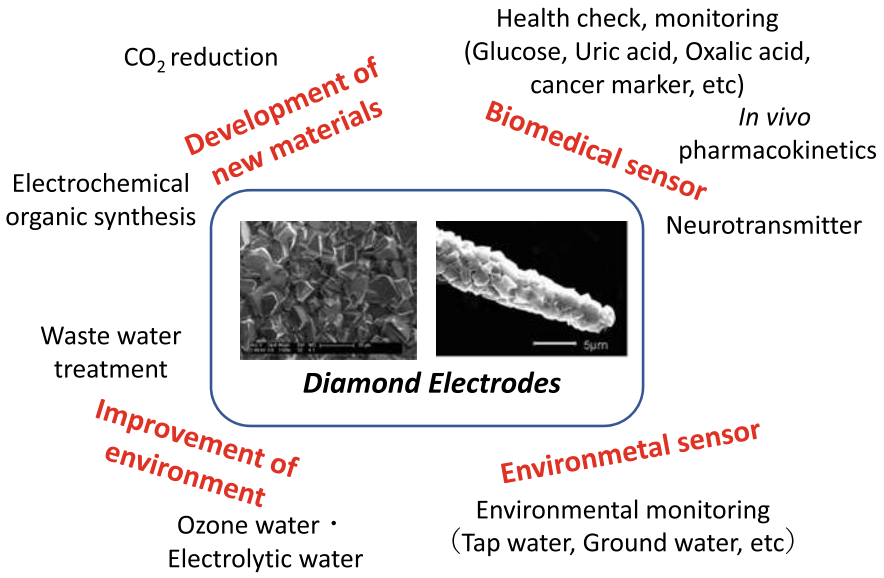

Fig. 2 Outlook of applications on diamond electrodes

https://www.twirpx.org & http://chemistry-chemists.com

increasing. In fact, in the process of developing the application, it is always necessary to return to the fundamental studies of the "diamond electrode". "Polycrystalline boron-doped diamond," which is currently mainly used for applications, is actually a very complicated material. Although, at first glance, the constituent elements of diamond electrode are only "carbon and boron" and seem to be a relatively simple material, and the electrochemical properties are very complicated because "boron doping level," "trace amount of sp^2 carbon," "grain boundary," and "surface termination," and so on are intricately related to determine the electrode characteristics.

However, based on the fundamental studies including theoretical calculations, the applications will be in industrialization in the future. I believe that diamond electrodes are "old and new materials" with great hope.

References

1. Iwaki M, Sato S, Takahashi K, Sakairi H (1983) Nucl Instrum Methods Phys Res 209:1129
2. Pleskov YV, Sakharova AY, Krotova M, Bouilov LL, Spitsyn BV (1987) J Electroanal Chem 228:19
3. Boonma L, Yano T, Tryk DA, Hashimoto K, Fujishima A (1997) J Electrochem Soc 144:L142
4. Swain GM, Ramesham R (1993) Anal Chem 65:345
5. Ramesham R, Askew RF, Rose MF, Loo BH (1993) J Electrochem Soc 140:3018
6. For example, CONDIAS. https://www.condias.de/, NeoCoat http://www.neocoat.ch/en
7. Rao TN, Yagi I, Miwa T, Tryk DA, Fujishima A (1999) Anal Chem 71:2506
8. Koppang MD, Witek M, Blau J, Swain GM (1999) Anal Chem 71:1188
9. Panizza M, Michaud PA, Cerisola G, Comninellis Ch (2001) J Electroanal Chem 507:206
10. Rodrigo PA, Michaud I, Duo M, Panizza G, Cerisola Ch, Comninellis J (2001) Electrochem Soc 148:D60
11. Szunerits S, Nebel CE, Hamers RJ (2014) MRS Bull 39:517
12. Kasahara S, Natsui K, Watanabe T, Yokota Y, Kim Y, Iizuka S, Tateyama Y, Einaga Y (2017) Anal Chem 89:11341
13. Sumi T, Saitoh T, Natsui K, Yamamoto T, Atobe M, Einaga Y, Nishiyama S (2012) Angew Chem Int Ed 51:5443
14. Nakata K, Ozaki T, Terashima C, Fujishima A, Einaga Y (2014) Angew Chem Int Ed 53:871
15. Kraft A (2007) Int J Electrochem Sci 2:355
16. Macpherson JV (2015) Phys Chem Chem Phys 17:2935
17. Fujishima A, Einaga Y, Rao TN, Tryk DA (eds) (2005) Diamond electrochemistry. BKC and Elsevier
18. Brillas E, Maltinez-Huitle CA (eds) (2011) Synthetic diamond films: preparation, electrochemistry, characterization and applications. Wiley
19. Einaga Y, Foord JS, Swain GM (2014) MRS Bull 39:525
20. Yang N, Foord JS, Jiang X (2016) Carbon 99:90–110
21. Yang N, Yu S, Macpherson JV, Einaga Y, Zhao H, Zhao G, Swain GM, Jiang X (2018) Chem Soc Rev 48:157–204
22. Einaga Y (2015) Diamond Denkyoku (Diamond Electrodes) (Japanese). Kyoritsu Shuppan Co., Ltd
23. Element Strategy Initiative: To Form Core Research Centers. https://elements-strategy.jp/en/
24. Watanabe T, Honda Y, Kanda K, Einaga Y (2014) Physica status solidi a:211:2709
25. JST (Japan Science and Technology Agency). https://www.jst.go.jp/kisoken/accel/en/about/index.html

https://www.twirpx.org & http://chemistry-chemists.com

26. Suzuki A, Ivandini TA, Yoshimi K, Fujishima A, Oyama G, Nakazato T, Hattori N, Kitazawa S, Einaga Y (2007) Anal Chem 79:8608
27. Ogata G, Ishii Y, Asai K, Sano Y, Nin F, Yoshida T, Higuchi T, Sawamura S, Ota T, Hori K, Maeda K, Komune S, Doi K, Takai M, Findlay I, Kusuhara H, Einaga Y, Hibino H (2017) Nature. Biomed Eng 1:654

https://www.twirpx.org & http://chemistry-chemists.com

Electrochemical Properties of BDD Electrodes by Surface Control

Yasuaki Einaga, Seiji Kasahara, and Keisuke Natsui

Abstract Boron-doped diamond (BDD) has attracted much attention as a promising electrode material, because it has excellent electrochemical properties such as a wide potential window and low background current. It is known that the electrochemical properties of BDD electrodes are very sensitive to the surface termination such as to whether it is hydrogen- or oxygen-terminated. Especially for electrochemical sensor application, pretreating BDD electrodes by cathodic reduction (CR) to hydrogenate the surface has been widely used to achieve high sensitivity. However, little is known about the effects of the CR treatment conditions on surface hydrogenation. In this chapter, at first, a systematic study of CR treatments in order that we can achieve effective surface hydrogenation is discussed. Also, direct observation of surface hydroxylation by anodic oxidation was reported. We have developed in situ spectroscopic measurement systems on BDD electrodes, i.e., in situ attenuated total reflection infrared spectroscopy (ATR-IR) and electrochemical X-ray photoelectron spectroscopy (EC-XPS). Furthermore, surface modification by functional molecules to introduce specific functions is also discussed. As examples, photochemical modification method via UV irradiation and electrochemical modification method are introduced. These surface control and modification should be important not only for better understanding of BDD's fundamentals but also for a variety of applications.

Keywords Boron-doped diamond · Electrochemistry · Cathodic reduction treatment · Surface termination · In situ spectroscopy · ATR-IR · EC-XPS · Surface hydroxylation

Y. Einaga (✉) · S. Kasahara · K. Natsui
Department of Chemistry, Keio University, 3-14-1 Hiyoshi, Yokohama 223-8522, Japan
e-mail: einaga@chem.keio.ac.jp

© Springer Nature Singapore Pte Ltd. 2022

Y. Einaga (ed.), *Diamond Electrodes*,
https://doi.org/10.1007/978-981-16-7834-9_2

https://www.twirpx.org & http://chemistry-chemists.com

1 Introduction

1.1 Surface Control of BDD Electrodes

Boron-doped diamond (BDD) electrodes exhibit unique electrochemical properties, so it can be used as a next generation electrode material in various fields such as waste water treatment, electrochemical sensor, carbon dioxide reduction, and electrochemical organic synthesis [1–7].

For example, based on the properties of wide potential window in an aqueous solution and low background current, research on electrochemical sensor application is being actively developed [2, 6, 8–12].

"Wide potential window" means that a wide range of measurable species can be detected, and "low background current" indicates that highly sensitive detection is possible.

For example, the BDD electrode has succeeded in highly sensitive detection of free chlorine, which shows an electrochemical oxidation reaction at a high potential of 1.3 V versus Ag/AgCl, which causes oxygen evolution at conventional electrodes [11].

On the other hand, it is known that the electrochemical properties of BDD electrodes are affected by their boron doping level, surface termination, crystal orientation, and sp^2 carbon impurities [13]. In particular, the surface termination is an important factor that determines the electrochemical properties of the BDD electrode. Typical surface terminations of diamond include hydrogen termination and oxygen termination. BDD electrodes with these two surface terminations exhibit different electrochemical properties [14]. For example, although oxalic acid can be detected using hydrogen-terminated BDD, no signal can be observed at oxygen-terminated BDD [15]. Also, dopamine and ascorbic acid show an oxidation reaction at almost the same potential at the hydrogen-terminated BDD, but the oxidation potential of ascorbic acid shifts significantly at the oxygen-terminated BDD [12]. Therefore, dopamine detection can be possible by separation of ascorbic acid in real samples, for example, in vivo. Furthermore, there have been reports of high sensitive detection achieved by modification of organic molecules that interact with the analytes [10, 16–18].

As above, the electrochemical properties of the BDD electrode depend on the surface termination, so surface termination control technology is indispensable. In this chapter, we systematically studied the surface termination conversion of BDD electrodes.

https://www.twirpx.org & http://chemistry-chemists.com

1.2 *Hydrogen-Termination and Oxygen-Termination of BDD Electrodes*

Many conversion methods have been reported for hydrogen termination and oxygen termination, which are typical surface terminations of diamond described above (Fig. 1). Generally, as-grown BDD is hydrogen-terminated because it is synthesized by chemical vapor deposition (CVD) in a hydrogen ambient.

Conversion from hydrogen- to oxygen-termination can be performed by treating the BDD. Oxygen plasma treatment, [19] annealing treatment in an oxygen atmosphere or in the air, [20] and ozone treatment by irradiation with UV light in the air [21] are used as the gas phase treatment. In addition, heat treatment in strong acid [22] and electrochemical anodic oxidation [23] are used as liquid phase treatments.

On the other hand, for hydrogen termination, hydrogen plasma treatment [24] and annealing treatment in a hydrogen atmosphere [25] are used as gas phase treatment, and electrochemical cathodic reduction treatment [26] is used as liquid phase treatment. Although terminal conversion is possible with any processing method, the conversion rate depends on the processing conditions. Also, diamond etching and graphitization might occur by some methods. Therefore, it is necessary to apply appropriate conditions depending on the application.

In order to realize "identical" BDD electrode surface for electrochemical sensor, hydrogen termination or oxygen termination are often selected as surfaces that can be controlled. Also, generally, since hydrogen termination has higher electrochemical activity than oxygen termination, hydrogen termination is selected to increase the detection sensitivity except in specific cases where separation detection is possible by oxygen termination. However, the hydrogen termination gradually changes to the oxygen termination by exposure in air for a long time such as several days [27] and by electrochemical measurements repeatedly many times. Therefore, in order to ensure the reproducibility of the measurement, the hydrogen termination should be realized as a pre-treatment of the BDD electrodes. For the reasons, to activate BDD electrodes, cathodic reduction (CR) treatment, which can be easily performed, has been widely used.

However, the CR conditions given in previous reports are diverse. Furthermore, there is little knowledge about which factors of the CR treatment are important for effective surface activation.

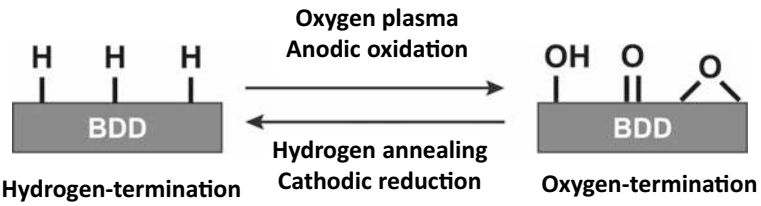

Fig. 1 Hydrogen-termination and oxygen-termination

https://www.twirpx.org & http://chemistry-chemists.com

Here, we systematically examined the conditions for the CR treatment for BDD electrodes [28].

2 Hydrogenation of BDD Surface by Cathodic Reduction

2.1 PH Dependence

First, the pH dependence of the solution used for the treatment was examined. Solutions with pH = 0.9, 3.2, 7.5, 10.8, and 13.0 were prepared by mixing aqueous solution of 0.1 M H_2SO_4 and 0.1 M Na_2SO_4 (pH < 7) and by mixing aqueous solution of 0.1 M NaOH and 0.05 M Na_2SO_4 (pH > 7), respectively.

The cathodic reduction potential was fixed at -3.0 V versus Ag/AgCl, and the total amount of charge was fixed at 9.25 C/cm^2. Prior to the cathodic reduction treatment, surface hydroxylation was performed by anodic oxidation treatment with +3.0 V versus Ag/AgCl for 5 min. Cathodic reduction treatment was applied to the solutions at each pH, and the electrochemical properties were studied by cyclic voltammetry (CV) measurement of 1 M KCl aqueous solution containing 1 mM $K_3[Fe(CN)_6]$ (Fig. 2, Table 1).

As shown in Table 1, after the reduction treatment, the redox peak-to-peak potential separation (ΔE_p) decreased compared to the oxygen termination regardless of the solution pH. ΔE_p is related to the electron transfer rate between the electrode and the redox species in the solution. When it is smaller, the electrochemical reactivity of the BDD electrode is higher. In other words, the reactivity of the electrode is improved by the cathodic reduction treatment. As mentioned above, the electrochemical reactivity of hydrogen-terminated BDD is higher than that of oxygen-terminated BDD, suggesting that hydrogenation is proceeding by cathodic reduction treatment.

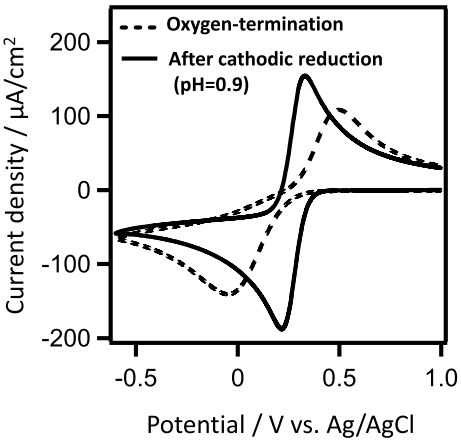

Fig. 2 Cyclic voltammograms in aqueous solutions of 1 mM $K_3[Fe(CN)_6]$ containing 1 M KCl before and after cathodic reduction with pH = 0.9

https://www.twirpx.org & http://chemistry-chemists.com

Table 1 Electrochemical behavior of BDD electrodes before and after cathodic reduction in solutions with various pH: ΔE_p denotes the peak-to-peak potential separation in $K_3[Fe(CN)_6]$ solution

	ΔE_p/ V
Oxygen-termination	0.545
Cathodic reduction (pH = 13.0)	0.376
Cathodic reduction (pH = 10.8)	0.381
Cathodic reduction (pH = 7.5)	0.330
Cathodic reduction (pH = 3.2)	0.210
Cathodic reduction (pH = 0.9)	0.114

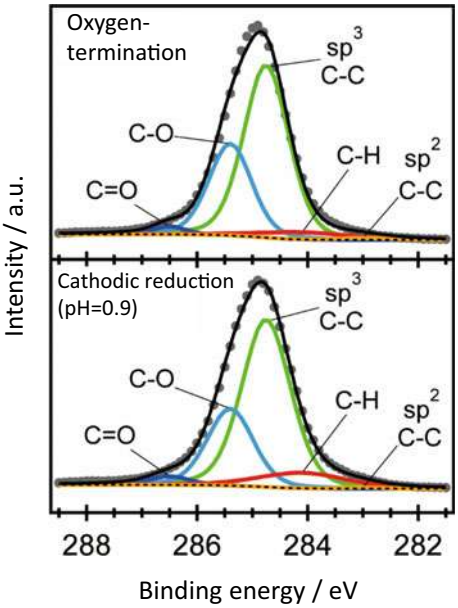

Fig. 3 Deconvoluted C 1 s spectra for a BDD electrode before (top) and after cathodic reduction in a solution with pH 0.9 (bottom)

Furthermore, ΔE_p decreased when the cathodic reduction was performed in solutions with lower pH. It is suggested that hydrogenation is promoted by cathodic reduction treatment in acidic solution. In fact, when the surface of the BDD electrode was evaluated by XPS, the peak area attributed to C–H bond increased and the peak area attributed to C–O bond decreased as the treatment with a solution with a lower pH was performed (Fig. 3, Table 2).

2.2 Potential Dependence

Next, the potential dependence used for processing was examined. Cathodic reduction treatment was performed at five different potentials (-1.5, -2.0, -2.5, -3.0, and -5.0 V vs. Ag/AgCl) in 0.1 M H_2SO_4 aqueous solution (pH 0.9). The total amount of

https://www.twirpx.org & http://chemistry-chemists.com

Table 2 The relative abundance of the components obtained from deconvolution of the C 1 s spectra for BDD electrodes before and after cathodic reduction in solutions with pH 0.9, 7.5 and 13.0

	Peak area/%				
	Sp^2 C–C	C-H	Sp^3 C–C	C-O	C = O
Oxygen-termination	0.8	5.1	61.2	30.9	2.0
Cathodic reduction (pH = 13.0)	0.1	0.1	64.8	32.3	2.8
Cathodic reduction (pH = 7.5)	0.0	8.0	61.1	27.6	3.2
Cathodic reduction (pH = 0.9)	0.3	10.0	60.9	26.3	2.5

charge was fixed at 9.25 C/cm^2. Similar to the pH dependence study, surface hydroxylation was performed by anodic oxidation treatment with +3.0 V versus Ag/AgCl for 5 min. The electrochemical characteristics after the cathode reduction treatment at each potential were evaluated by measuring the CV of a 1 M KCl aqueous solution containing 1 mM $K_3[Fe(CN)_6]$ (Fig. 4, Table 3). As shown in Table 3, ΔE_p decreased as the potential increased, and when treated at a potential of −2.5 V versus Ag/AgCl or higher, the value was equivalent to that of as-grown BDD. In addition, from the XPS measurement, as the higher potential was applied, the peak area attributed to the C–H

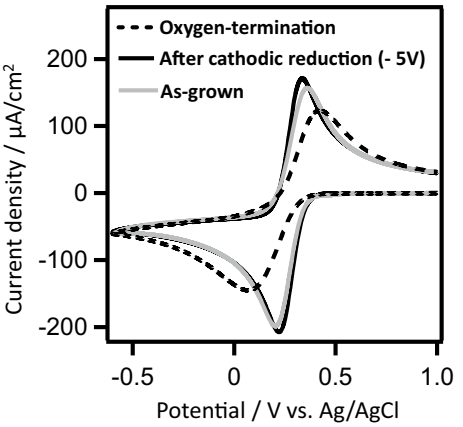

Fig. 4 Cyclic voltammograms in aqueous solutions of 1 mM $K_3[Fe(CN)_6]$ containing 1 M KCl before and after cathodic reduction at—5.0 V versus Ag/AgCl. For comparison, that on as-grown BDD electrode is also shown

Table 3 Electrochemical behavior of BDD electrodes before and after cathodic reduction at various potentials: ΔE_p denotes the peak-to-peak potential separation in $K_3[Fe(CN)_6]$ solution

	ΔE_p/V
Oxygen-termination	0.353
Cathodic reduction (-1.5 V)	0.298
Cathodic reduction (-2.0 V)	0.246
Cathodic reduction (-2.5 V)	0.157
Cathodic reduction (-3.0 V)	0.123
Cathodic reduction (-5.0 V)	0.115
As-grown	0.160

https://www.twirpx.org & http://chemistry-chemists.com

bond increased and the peak area attributed to the C–O bond decreased (Fig. 5, Table 4). From the above results, it was suggested that the higher the potential, the more hydrogenation of the BDD electrode is promoted and the electrochemical reactivity is improved. It should be noted here that the results of XPS measurement indicate

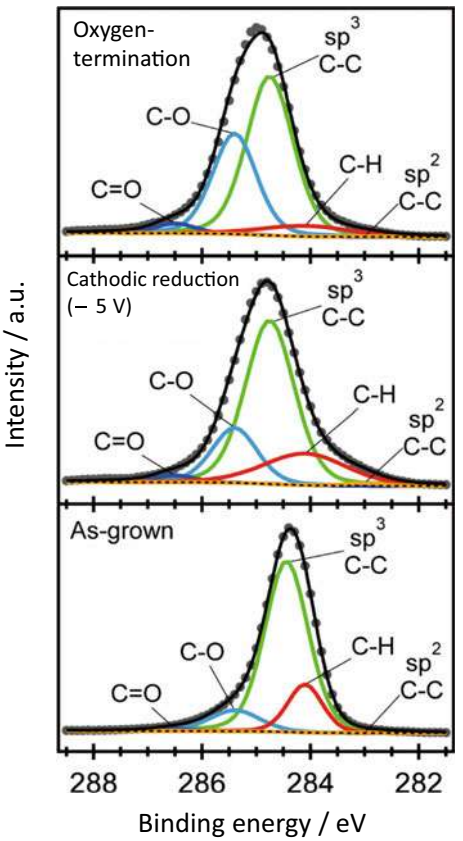

Fig. 5 Deconvoluted C 1 s spectra for BDD electrodes before (top) and after cathodic reduction at—5 V versus Ag/AgCl (middle). For comparison, that on as-grown BDD electrode is also shown

Table 4 The relative abundance of the components obtained from deconvolution of the C 1 s spectra for BDD electrodes before and after cathodic reduction at potential of −1.5 V, −3 V and −5 V versus Ag/AgCl

	Peak area/%				
	Sp^2 C–C	c-H	Sp^3 C–C	C-O	C = O
Oxygen-termination	0.2	7.0	56.4	33.5	2.0
Cathodic reduction (-1.5 V)	0.2	7.0	61.1	29.6	2.8
Cathodic reduction (-3.0 V)	0.3	10.0	60.9	26.3	3.2
Cathodic reduction (-5.0 V)	0.7	19.5	59.4	18.4	2.5
As-grown	0.0	16.3	72.5	10.4	0.8

https://www.twirpx.org & http://chemistry-chemists.com

that the surface of the BDD electrode is not completely hydrogen-terminated BDD in the present conditions of cathodic reduction treatment. In other words, although it is a partial hydrogen-terminated BDD, the electrochemical reactivity is considered to be improved to the same level as the hydrogen-terminated BDD.

2.3 Possible Mechanisms for Surface Hydrogenation

From the results above, it was confirmed that hydrogen-terminated BDD is realized by applying a higher potential using a solution with a lower pH. Here, we consider the reaction mechanism for hydrogenation from oxygen-terminated BDD.

It is suggested that protons (H^+) are involved in the reaction because hydrogenation is promoted in a solution with a low pH. Protons are theoretically thought to be reduced at a potential of −2.3 V versus Ag/AgCl to produce atomic hydrogen ($H^\bullet$). Thus, it is considered that the amount of atomic hydrogen increases by applying a higher potential (applying a larger current). From the above, the reaction mechanism was estimated as follows. First, atomic hydrogen generated by the reduction of protons abstracts OH on the surface of the BDD electrode, and a dangling bond is formed on the surface of the BDD. Then, another atomic hydrogen reacts with the generated dangling bond to form a C–H bond (Fig. 6).

Density functional theory (DFT) calculation supports the proposed mechanisms. Assuming that two atomic hydrogens are present near the surface of the BDD electrode, the following two reactions can occur. (1) Atomic hydrogen reacts with each other to generate hydrogen molecule. (2) A surface conversion reaction occurs, surface hydrogenated BDD and water are generated. DFT calculation of the energies of these two final states revealed that the state of (2) is thermodynamically more stable than the state of (1) by about 2.6 eV. In other words, it is suggested that the hydrogen termination reaction takes precedence over the hydrogen generation reaction if atomic hydrogen is abundantly present near the surface of the BDD electrode.

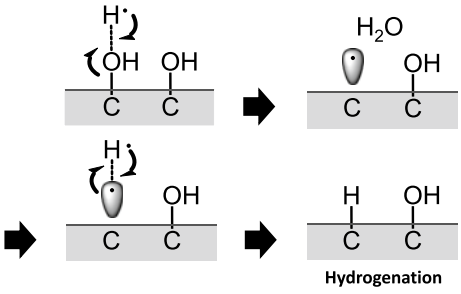

Fig. 6 Proposed mechanisms on hydrogenation by cathodic reduction

https://www.twirpx.org & http://chemistry-chemists.com

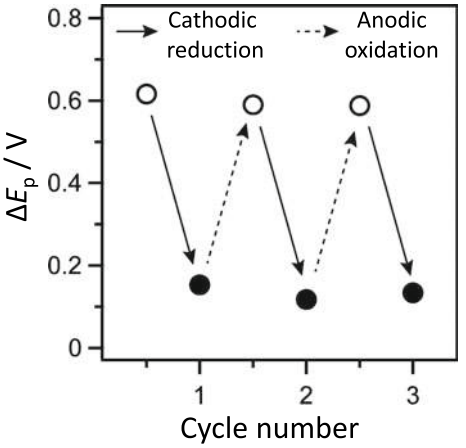

Fig. 7 Plots of ΔE_p in $K_3[Fe(CN)_6]$ solution with the number of the cycles of the electrochemical treatment

2.4 Reversible Control of the Surface Termination

For practical application, it was confirmed whether the electrochemical characteristics change with good reproducibility when hydrogen-terminated BDD and oxygen-terminated BDD are alternately repeated electrochemically.

For the cathodic reduction treatment, the conditions where hydrogenation was most advanced in this study (potential: -5.0 V versus Ag/AgCl, solution: 0.1 M H_2SO_4 aqueous solution (pH 0.9), total amount of charge: 9.25 C/cm^2) were applied. For surface hydroxylation was performed by anodic oxidation treatment with +3.0 V versus Ag/AgCl for 5 min.

The electrochemical properties after each treatment were evaluated by measuring the CV of a 1 M KCl aqueous solution containing 1 mM $K_3[Fe(CN)_6]$. From Fig. 7, it was repeatedly observed that ΔE_p decreased by the cathodic reduction treatment and increased by the anodic oxidation treatment. From this, it was clarified that the surface of the BDD electrode can be reproducibly converted to hydrogen termination with high electrochemical reactivity by using the appropriate conditions of the cathodic reduction treatment.

3 Hydroxylation of BDD Surface

In order to monitor the conversion of the surface by the anodic treatment, potential-controlled attenuated total reflection infrared spectroscopy (ATR-IR) spectra were measured. Figure 8 shows in-situ ATR-IR spectra collected under anodic oxidation (AO) in 0.1 M $HClO_4$ aqueous solution. The applied potential was varied from + 0.5 to +3.0 V versus Ag/AgCl in 0.5 V increments, and from +3.0 to +0.5 V versus Ag/AgCl in 0.5 V decrements. The growth of vibrations at 1100 cm^{-1}, assigned to

https://www.twirpx.org & http://chemistry-chemists.com

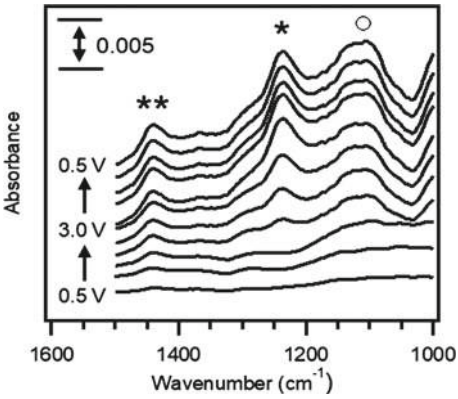

Fig. 8 In situ potential-dependent ATR-IR spectra in 0.1 M $HClO_4$ aqueous solution. The potential was changed from +0.5 to +3.0 V versus Ag/AgCl in 0.5 V increments, and from +3.0 to +0.5 V in 0.5 V decrements. Reference spectra were collected at 0.0 V. The arrows show the order in which the measurements were made. Peaks marked ○, *, and ** are positioned at 1100, 1240, and 1440 cm^{-1}, respectively. Reprinted from Ref (29), Copyright 2019, with permission from American Chemical Society

the presence of perchlorate anions, was observed with increasing applied potential. Furthermore, characteristic bands at 1240 cm^{-1}, assigned to C–O stretching, and at 1440 cm^{-1}, assigned to C–O–H bending, were observed at more positive potentials than 1.5 V versus Ag/AgCl. Thus, these bands are visible even after lowering the applied potential. From the results, both peaks (at 1240 cm^{-1} and at 1440 cm^{-1}) likely originate from irreversible surface hydroxylation of the BDD by anodic oxidation [29].

4 Surface Modification of Alkenes by Photochemical Reaction

Modification of BDD surfaces for analytical or catalytic purposes attracts much attention. Alkyl-terminated surfaces of BDD can be produced by UV irradiation of hydrogen-terminated BDD in solution containing alkene molecules (Fig. 9). It is suggested that the reaction can be possible by using photochemical reaction with hydrogen-terminated BDD surface. The proposed mechanisms are as follows: Dangling bond of carbon on BDD surface formed by UV irradiation react very rapidly with unsaturated carbon–carbon bond of alkene, and the C–C bond is formed. Facile step of the C–C bonding formation make the surface bound carbon-based radical on the β-carbon. Then, abstraction of a neighboring hydrogen induces the next dangling bond on BDD surface, and the next modification occurs sequentially.

Based on the methods, allyltriethylammonium bromide (ATAB) was covalently modified to the surface of BDD electrodes in order to fabricate positively charged

https://www.twirpx.org & http://chemistry-chemists.com

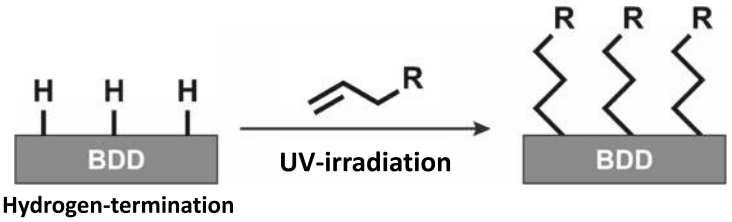

Fig. 9 Surface modification of alkenes by photochemical reaction

BDD surface by Kondo et al. [16]. The anodic current for oxalate oxidation was found to be up to two times larger than at an unmodified BDD electrode. This was due to the electrostatic interaction between the oxalate anion and the electrode surface. They also fabricated cobalt phthalocyanine-modified BDD electrode for highly sensitive detection of hydrogen peroxide [17].

5 Surface Modification of Aryl Diazonium Salt by Electrochemical Reaction

Modification of organic molecules by electrochemical methods also shows the possibility of grafting a many kinds of functional molecules. Electrochemical reduction of aryl diazonium salts can lead to a very solid covalent attachment of aryl groups onto the carbon surface. The method can apply to modify a large variety of functionalized aryl groups, hence allowing the modification of a broad spectrum of molecules. It is suggested that the covalent attachment of the aryl groups is due to the binding of the aryl radical produced by one-electron reduction of the diazonium salt to the carbon surface (Fig. 10) [30].

Based on the methods, influenza virus was electrochemical detected with high sensitivity by BDD electrodes modified by sialic acid-mimic peptide. At first, aryl diazonium salts with alkynes was modified on BDD surface. Then, the peptide with

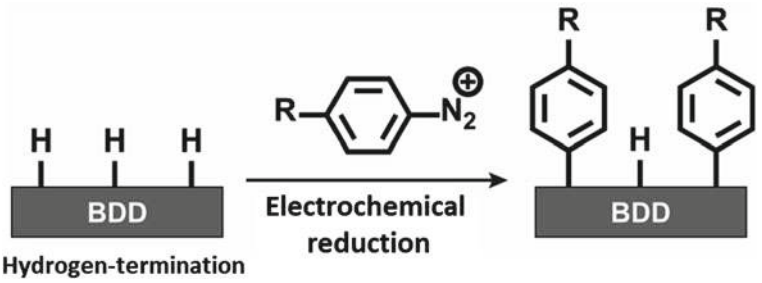

Fig. 10 Surface modification of aryl diazonium salt by electrochemical reaction

https://www.twirpx.org & http://chemistry-chemists.com

azido group, which was previously identified by phage-display technology, was attached by click chemistry with the modified BDD. Electrochemical impedance spectroscopy revealed that H1N1 and H3N2 influenza virus were detectable in the range of 20–500 pfu by using the peptide-terminated BDD electrode [10]. Also, J.-F. Zhi et al. report an application of amperometric biosensor by tyrosinase modified BDD electrodes. After 4-nitrobenzenediazonium tetrafluoroborate was modified on BDD surface by electrochemical reduction, the tyrosinase was covalently immobilized on the reduced aminophenyl-modified BDD surface via carbodiimide coupling [18].

6 Summary

In this chapter, we introduced an importance of the surface control and surface modification of BDD electrodes. First, a method for controlling surface termination of BDD electrodes, especially hydrogen termination by cathode reduction treatment and oxygen termination by anodic oxidation treatment, was shown. The surface termination of the BDD electrode has a great influence on its electrochemical properties, so it is important to control the surface to be suitable for each application. Furthermore, surface modification by functional molecules is also important not only for better understanding of BDD's fundamentals but also for a variety of applications.

References

1. Fujishima A, Einaga Y, Rao TN, Tryk DA (2005) Diamond Electrochemistry; Elsevier
2. Einaga Y (1807) Diamond electrodes for electrochemical analysis. J Appl Electrochem 2010:40
3. Einaga Y, Foord JS, Swain GM (2014) Diamond electrodes: diversity and maturity. MRS Bull 39:525
4. Macpherson JV (2015) A practical guide to using boron doped diamond in electrochemical research. Phys Chem Chem Phys 17:2935
5. Einaga Y (2018) Development of the electrochemical applications of boron-doped diamond electrodes. Bull Chem Soc Jpn 91:1752–1762
6. Yang N, Yu S, Macpherson JV, Einaga Y, Zhao H, Zhao G, Swain GM, Jiang X (2018) Conductive diamond: synthesis, properties, and electrochemical applications. Chem Soc Rev 48:157−204
7. Muzyka K, Sun J, Fereja TH, Lan Y, Zhang W, Xu G (2019) Boron-doped diamnd: current progress and challenges in view of electroanalytical applications. Anal Methods 11:397–414
8. Ogata G, Ishii Y, Asai K, Sano Y, Nin F, Yoshida T, Higuchi T, Sawamura S, Ota T, Hori K, Maeda K, Komune S, Doi K, Takai M, Findlay I, Kusuhara H, Einaga Y, Hibino H (2017) A microsensing system for the in vivo real-time detection of local drug kinetics. Nat Biomed Eng 1:654
9. Asai K, Ivandini TA, Einaga Y (2016) Continuous and selective measurement of oxytocin and vasopressin using boron-doped diamond electrodes. Sci Rep 6:32429
10. Matsubara T, Ujie M, Yamamoto T, Akahori M, Einaga Y, Sato T (2016) Highly sensitive detection of influenza virus by boron-doped diamond electrode terminated with sialic acid-mimic peptide. Proc Natl Acad Sci USA 113:8981

https://www.twirpx.org & http://chemistry-chemists.com

11. Murata M, Ivandini TA, Shibata M, Nomura S, Fujishima A, Einaga Y (2008) Electrochemical detection of free chlorine at highly boron-doped diamond electrodes. J Electro-anal Chem 612:29
12. Suzuki A, Ivandini TA, Yoshimi K, Fujishima A, Oyama G, Nakazato T, Hattori N, Kitazawa S, Einaga Y (2007) Fabrication, characterization, and application of boron-doped diamond microelectrodes for in vivo dopamine detection. Anal Chem 79:8608
13. Watanabe T, Honda Y, Kanda K, Einaga Y (2014) Tailored design of boron-doped diamond electrodes for various electrochemical applications with boron-doping level and sp2-bonded carbon impuritiesPhys. Status Solidi A 211:2709
14. Szunerits S, Boukherroub R (2008) Different strategies for functionalization of diamond surfaces. J Solid State Electrochem 12:1205–1218
15. Ivandini TA, Rao TN, Fujishima A, Einaga Y (2006) Electrochemical oxidation of oxalic acid at highly boron-doped diamond electrodes. Anal Chem 78:3467–3471
16. Kondo T, Niwano Y, Tamura A, Ivandini TA, Einaga Y, Tryk DA, Fujishima A, Kawai T (2008) Sensitive electrochemical detection of oxalate at a positively charged boron-doped diamond surface. Electroanalysis 20:1556–1564
17. Kondo T, Tamura A, Kawai T (2009) Cobalt phthalocyanine-modified boron-doped diamond electrode for highly sensitive detection of hydrogen peroxide. J Electrochem Soc 156:F145–F150
18. Zhou Y, Zhi JF (2006) Development of an amperometric biosensor based on covalent immobilization of tyrosinase on a boron-doped diamond electrode. Electrochem Commun 8:1811–1816
19. Yagi I, Notsu H, Kondo T, Tryk DA, Fujishima A (1999) Electrochemical selectivity for redox systems at oxygen-terminated diamond electrodes. J Electroanal Chem 473:173–178
20. Ferro S, Colle MD, Battisti AD (2005) Chemical surface characterization of electrochemically and thermally oxidized boron-doped diamond film electrodes. Carbon 43:1191–1203
21. Sakai T, Song KS, Kanazawa H, Nakamura Y, Umezawa H, Tachiki M, Kawarada H (2003) Ozone-treated channel diamond field-effect transistors. Diamond Relat Mater 12:1971–1975
22. Liu FB, Wang JD, Liu B, Li XM, Chen DR (2007) Effect of electronic structures on electrochemical behaviors of surface-terminated boron-doped diamond film electrodes. Diamond Relat Mater 16:454–460
23. Denisenko A, Pietzka C, Romanyuk A, El-Hajj H, Kohn E (2008) The electronic surface barrier of boron-doped diamond by anodic oxidation. J Appl Phys 103:014904
24. Hutton LA, Iacobini JG, Bitziou E, Channon RB, Newton ME, Macpherson JV (2013) Examination of the factors affecting the electrochemical performance of oxygen-terminated polycrystalline boron-doped diamond electrodes. Anal Chem 85:7230–7240
25. Ando T, Ishii M, Kamo M, Sato Y (1993) Thermal hydrogenation of diamond surfaces studied by diffuse reflectance Fourier-transform infrared, temperature-programmed desorption and laser Raman spectroscopy. J Chem Soc Faraday Trans 89:1783–1789
26. Hoffmann R, Kriele A, Obloh H, Hees J, Wolfer M, Smirnov W, Yang N, Nabel CE (2010) Electrochemical hydrogen termination of boron-doped diamond. Appl Phys Lett 97:052103
27. Salazar-Banda GR, Andrade LS, Nascente PAP, Pizani PS, Rocha-Filho RC, Avaca LA (2006) On the changing electrochemical behaviour of boron-doped diamond surfaces with time after cathodic pre-treatments. Electrochim Acta 51:4612–4619
28. Kasahara S, Natsui K, Watanabe T, Yokota Y, Kim Y, Iizuka S, Tateyama Y, Einaga Y (2017) Surface hydrogenation of boron-doped diamond electrodes by cathodic reduction. Anal Chem, 11341–11347

https://www.twirpx.org & http://chemistry-chemists.com

29. Kasahara S, Ogose T, Ikemiya N, Yamamoto T, Natsui K, Yokota Y, Wong R, Iizuka S, Hoshi N, Tateyama Y, Kim Y, Nakamura M, Einaga Y (2019) In-Situ spectroscopic study on the surface hydroxylation of diamond electrodes. Anal Chem 91:4980–4986
30. Leroux YR, Fei H, Noel J-M, Roux C, Hapiot P (2010) Efficient covalent modification of a carbon surface: use of a Silyl protecting group to form an active monolayer. J Am Chem Soc 132:14039–14041

https://www.twirpx.org & http://chemistry-chemists.com

Localized Surface Characterization of Boron-Doped Diamond Film Electrodes

Francesca Celine I. Catalan and Yousoo Kim

Abstract The expanding application of boron-doped diamond (BDD) to various fields as an efficient electrode and sensor has continuously encouraged fundamental investigations of its properties. To fully realize BDD's potential, a deep understanding of the relationship between its local morphology and electrochemical properties is essential. This chapter focuses on localized imaging and spectroscopy of CVD-grown BDD film electrodes—from micro- to atomic-scale—and how such measurements can clarify phenomena affecting BDD's performance as an electrode.

Keywords Boron-doped diamond · Raman spectroscopy · Scanning tunneling microscopy · Facet-dependent · Corrosion

1 Introduction

Diamond has enjoyed considerable attention in the past decades due to its unique and interesting characteristics, such as extreme hardness, chemical inertness, and exceptional carrier mobility. Remarkably, its electrical conductivity can be easily tailored with surface functionalization and doping [1–3]. In boron-doped diamond (BDD), the amount of boron in the diamond lattice, [B], determines the electrical conductivity of the material—turning an intrinsic insulator into a wide-bandgap semiconductor ([B] < 10^{19} cm^{-3}) and even to a semi-metal ([B] ~ 10^{19}–10^{22} cm^{-3})—rendering a promising electrode material for various electrochemical analysis [4, 5] and biochemical sensing [6, 7] applications.

Despite the ever-developing applications and wide-ranging research on BDD's properties, several aspects of its electrochemical efficiency remain unclear and need to be clarified for us to harness its full potential as an electrode. Aside from boron concentration and distribution, many factors have been shown to affect the electrochemical performance of BDDs, including surface termination [8–10], sp^2 carbon impurities [11], defects, and crystallographic orientation [12, 13]. The problem lies

F. C. I. Catalan · Y. Kim (✉)
Surface and Interface Science Laboratory, RIKEN 2-1 Hirosawa, Wako 351-0198, Saitama, Japan
e-mail: ykim@riken.jp

© Springer Nature Singapore Pte Ltd. 2022

Y. Einaga (ed.), *Diamond Electrodes*,
https://doi.org/10.1007/978-981-16-7834-9_3

https://www.twirpx.org & http://chemistry-chemists.com

in the compounded effects of these factors to the BDD electrode, which makes it difficult to determine the distinct role that each factor plays in the electrochemical activity of BDD especially when analyzed in the macroscopic scale.

This chapter aims to provide insights into the correlation of the *local* surface morphology and electrochemical activity of BDD electrodes. In particular, the focus is on the local characterization of BDD (100) and (111) facets to explain the crystallographic-orientation dependence of the electrochemical performance of BDD. The chapter begins with the micro-Raman analysis of polycrystalline BDD electrode film as it undergoes anodization. Combined with high-resolution optical microscopy, Raman spectroscopic imaging maps the chemical inhomogeneity and local changes on the BDD surface due to corrosion, allowing for a better understanding of the mechanisms behind anodic degradation in BDD electrodes [14]. For an even more localized characterization of BDD beyond the limit of optical detection, scanning tunneling microscopy (STM) is utilized to investigate BDD at the *atomic level* (Sect. 3). After a short review of the STM studies of undoped and boron-doped diamond measured at room temperature, atomic structures on the BDD surface obtained via STM at cryogenic temperatures are discussed. Attention is given to the surface structures unique to BDD (111), which may explain the electrochemical superiority of the (111) facet over (100) [12].

2 High-Resolution Micro-Raman Analysis: Anodic Corrosion in BDD

2.1 Degradation of BDD Electrodes

Despite diamond's intrinsic strength and chemical stability, considerable degradation has been reported in BDD electrodes when it undergoes high current density anodic treatments. In ultra-nanocrystalline BDD, surface oxidation has been shown to generate delamination and textural changes at a current density of 1 A cm^{-2} [15]. Anodic corrosion in micro-polycrystalline BDD films is enhanced with lower pH level [16], presence of organic compounds [16, 17], and increased doping levels [18]. More importantly, along with morphological changes, the electrochemical stability of BDD electrodes is significantly reduced with corrosion [19–21]. It is therefore imperative to understand the mechanisms of anodic corrosion in BDD in order to aid its development as an electrode for various applications.

Sp^2-hybridized carbon is known to initiate corrosion in BDD electrodes [16, 22]. These sites on the surface may have been formed during the chemical vapor deposition (CVD) growth process or as a product of subsequent treatments and interaction with the surroundings. In addition, oxygenated functional groups have been shown to affect electrochemical activity [23, 24], and the adsorption of certain surface groups seems to depend on the crystallographic orientation of the BDD surface [25, 26]. To understand the mechanisms that govern these observations and their consequent

https://www.twirpx.org & http://chemistry-chemists.com

roles in corrosion, morphological and chemical properties of the BDD surface as it undergoes anodization are investigated using high-resolution Raman spectroscopy, complemented by X-ray photoelectron spectroscopy (XPS).

2.2 Polarized Micro-Raman Study of Corrosion in BDD

Raman spectroscopy is regarded as one of the most versatile tools to characterize carbon-based materials. Compared to scanning electron microscopy or optical microscopy, Raman spectroscopy is very sensitive to the chemical species on or near the surface of the sample, providing comprehensive information about a material's composition and how it interacts with the environment. Raman spectra are specially informative and useful in BDD analysis as they are sensitive to the amount of boron dopants [27], crystallinity [28], presence of non-diamond carbon species, and diamond lattice defects. When combined with confocal and optical polarization-sensitive configurations, a spatial resolution of <1 μm and sensitivity to crystallographic orientation of diamond grains can be achieved [29], making Raman spectroscopy a valuable tool to analyze localized grain-dependent surface changes in polycrystalline BDD.

Characterization of pristine BDD

The BDD electrodes investigated and discussed in this section are polycrystalline, highly doped BDD thin films (B/C ratio = 1%, thickness = 4.2 ± 0.29 μm) deposited on a Si (111) wafer by microwave plasma-assisted CVD facility. As optical imaging shows (Fig. 1a), the pristine BDD film is characterized by discrete, well-distinguishable grains, with an average grain size of 4.0 ± 0.84 μm. The various-shaped grains are randomly distributed and closely-packed, which is expected of a highly doped BDD.

Raman spectroscopic measurements were carried out at room temperature using linearly polarized light from a 532-nm solid-state laser focused onto the sample with a 100x, NA 0.9 objective. Combined with a confocal pinhole (Φ = 150 μm) to spatially filter out unwanted scattered light from out-of-focus regions, the configuration generated a sampling spot size of 0.70 μm. This spatial resolution is well below the average size of a single grain on the sample, which indicates that grain-dependent localized spectroscopic measurements can be obtained with this configuration. The Raman signal was collected using the same focusing objective in a backscattering geometry and guided to a spectrometer equipped with a liquid nitrogen-cooled charge coupled device (CCD) detector. Optical polarization-sensitive measurements were performed by using a fixed analyzer with the polarization directed into the spectrometer while rotating the Raman signal polarization via a half-wave plate positioned prior to the analyzer. More details on the experimental set-up can be found in [14].

Figure 1b shows Raman spectra that were measured at the center of three different grains denoted in Fig. 1a. All spectra show features typical of highly doped BDD films: (1) a broad, non-uniform background caused by intra-band hole scattering

https://www.twirpx.org & http://chemistry-chemists.com

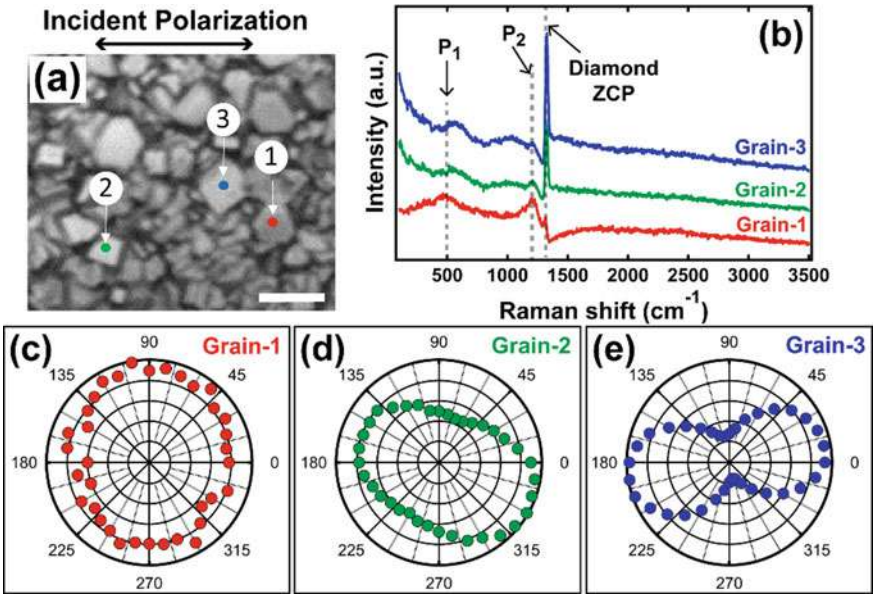

Fig. 1 Polarized Raman spectroscopy of various grains on the polycrystalline BDD: **a** Optical image of the polycrystalline BDD. Scale bar corresponds to 10 μm. **b** Raman spectra and **c**–**e** the corresponding polarization dependence of the diamond ZCP peak (~1332 cm −1) measured at 3 different grains. The spectra have been offset vertically from each other for clarity. Reprinted with permission from [14]. Copyright (2017) American Chemical Society

[30]; (2) a broad peak around 500 cm^{-1} (P_1) attributed to the presence of boron pairs in the diamond lattice [31, 32]; (3) a small ~ 1200 cm^{-1} peak, P_2, denoting crystal deformation due to single boron atoms substitutionally incorporated in the diamond lattice [33]; and, the diamond zone center phonon (ZCP) peak, which is positioned at 1332 cm^{-1} for undoped diamond. No sp^2 carbon is detected (G-mode at 1580 cm^{-1}), indicating a high-quality BDD film with negligible graphitic species.

Boron concentration, [B], may be quantified for each grain by fitting the P_1 peak with a combination of Lorentzian and Gaussian functions (details of the fitting parameters are discussed in [14]). The position of the Lorentzian peak ($\omega_{L,P1}$) is empirically known to be correlated to [B] by the following equation:

$$[B] = 8.44x10^{30}\exp\left(-0.048\omega_{L,P1}\right) \quad (1)$$

where [B] is in cm^{-3} and $\omega_{L,P1}$ is in cm^{-1} [27]. From Eq. 1, it is thus expected that a P_1 peak that is located at a lower wavenumber indicates a higher [B]. Using Eq. 1, we calculated the amount of boron in Grain-1, 2, and 3 as $[B]_1 = 9.8 \times 10^{20}$ cm^{-3}, $[B]_2 = 8.2 \times 10^{20}$ cm^{-3}, and $[B]_1 = 8.0 \times 10^{20}$ cm^{-3}, respectively.

The spectral features of the ZCP peak are also indicative of [B]—as more boron is incorporated into the diamond lattice, the ZCP peak becomes more asymmetric,

https://www.twirpx.org & http://chemistry-chemists.com

mimicking a Fano function rather than a Lorentzian. The Fano line shape comes from the quantum interference between the discrete diamond phonon mode and the continuum of electronic states caused by the dopants [34]. The dopant-induced asymmetry of the ZCP peak is accompanied by a shift of the peak position (ω_{ZCP}) toward a lower wavenumber and decrease in peak intensity. The more pronounced asymmetry and lower intensity of the ZCP peak in Grain-1's Raman spectra confirm a degraded crystalline quality due to a higher [B] compared to Grains 2 and 3 [14]. As the ZCP peak is a clear indicator of the crystallinity of the diamond grain, it is also very sensitive to the crystallographic orientation of the BDD grains and can therefore be used to precisely determine which facet each grain has. The peak is fitted with a Fano function, and the fitted peak intensity is plotted as a function of the rotation angle difference between the incident polarizer and the analyzer (θ). As a reference, when $\theta = 0^{\circ}$, the polarizer and the analyzer are parallel. Figures 1c–e show the optical polarization dependence of the diamond ZCP peak for Grains 1, 2, and 3, respectively. Clearly, the ZCP peak of Grain-1 has a weaker polarization dependence compared to Grains 2 and 3. On the basis of the Raman tensor [29], Grain-1 can be assigned as (111)-oriented, Grain-2 as (100)-oriented, and Grain-3 as (110)-oriented facet. Further discussions are focused on (111) and (100) grains as these facets are most abundant in CVD-grown polycrystalline diamond films [35]. The higher [B] in (111)-oriented Grain-1 confirms previous reports that boron is more efficiently incorporated into (111) facets than in (100) [36].

Temporal evolution of the BDD surface undergoing corrosion

Electrochemical treatments were carried out in a single-compartment polytetrafluoroethylene (PTFE) electrochemical cell with Pt wire counter electrode and Ag/AgCl (saturated KCl) reference electrode. The BDD film served as an anode in 3 M acetic acid (CH_3COOH) aqueous solution with 1 M perchloric acid ($HClO_4$) as supporting electrolyte. Constant current electrolysis were conducted with a potentiostat at a current density of 0.25 A/cm^2 for a total of 12 h. To clarify the corrosion mechanism in BDD, the morphological and chemical properties of the film electrode were systematically analyzed ex situ after 0.5, 2, 6, and 12 h using polarized Raman point spectroscopy, Raman imaging, and XPS.

The surface morphology and Raman spectral features of the (111)- and (100)-oriented facets are observed to evolve differently with electrolysis time (Fig. 2). For the (111)-facet (Grain-1), no significant modifications are observed in both the optical images (Fig. 2a–e), highlighted by a *circle*) and the Raman spectra (Fig. 2f). The precise positions of the P_1 and ZCP peaks indeed do not change significantly as the electrolysis time is increased up to 12 h (Table 1).

On the other hand, visible temporal changes in the relative intensity of the (100)-facet can be observed in the optical images (Grain-2, highlighted by a *square*). As the anodic treatment time is increased to a total of 12 h, a defect (crack) is even evident at the center of the grain, indicating severe etching due to corrosion. Figure 2g shows the temporal evolution of the Raman spectra of the (100)-facet (Grain-2). After just 0.5 h of anodic treatment, sp^2 carbon peak (G-band at 1580 cm^{-1}) is observed, as well as a notable increase in the spectral background especially at the high wavenumber

https://www.twirpx.org & http://chemistry-chemists.com

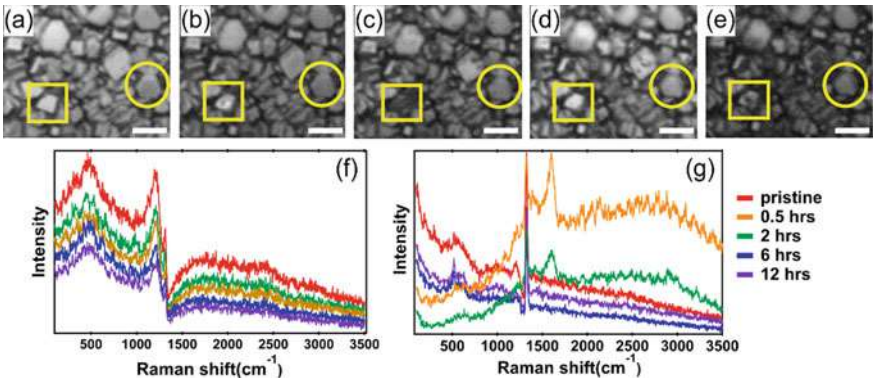

Fig. 2 Corrosion-induced changes in BDD as a function of electrolysis time: optical images of BDD surface **a** before anodic treatment and after **b** 0.5 h, **c** 2 h, **d** 6 h, and **e** 12 h of treatment. Scale bar corresponds to 5 μm. Time evolution of the Raman spectra at **f** (111)-grain (Grain-1) and **g** (100)-grain (Grain-2). (100) and (111) grains are highlighted in the optical images by the yellow square and circle, respectively. Reprinted with permission from [14]. Copyright (2017) American Chemical Society

Table 1 Raman shift in the P_1 peak and the diamond ZCP peak as a function of electrolysis time. (Adapted with permission from [14]. Copyright (2017) American Chemical Society.)

Electrolysis time (h)	P_1 peak position $\omega_{L,P1}$ (cm^{-1})	Boron concentration, [B] × 10^{20} (cm^{-3})	diamond ZCP peak position, ω_{ZCP} (cm^{-1})
Grain-1: (111)-facet			
0	476.6	9.8	1318.9
0.5	476.7	9.8	1319.2
2	478.5	8.9	1320.2
6	479.9	8.4	1319.9
12	478.1	9.1	1318.3
Grain-2: (100)-facet			
0	480.3	8.2	1317.6
0.5	480.5	8.1	1317.8
2	481.9	7.6	1318.7
6	499.8	3.2	1326.7
12	510.0	1.9	1326.2

region. The broad luminescence stems from a continuous distribution of electronic states within the optical bandgap of diamond that are introduced by various disordered forms of amorphous sp^2 carbon species [37, 38]. After two hours, the sp^2 carbon G-band peak and the broad luminescence disappear, suggesting that non-sp^3 carbon species are removed by corrosion [16, 22]. Moreover, a small, broad peak around 2900 cm^{-1} (full width at half maximum, FWHM ~ 150 cm^{-1}) can be observed in

https://www.twirpx.org & http://chemistry-chemists.com

the (100)-grain after 2 h treatment. The appearance of this peak, which is associated to the stretching mode of CH_x species after anodization, have also been reported previously [39, 40]. For this particular (100)-oriented grain (Grain-2), [B] decreases significantly by a factor of four (from 8.2×10^{20} cm^{-3} to 1.9×10^{20} cm^{-3}) after 12 h of treatment, as evidenced by the shift in the P_1 peak (Table 1). This indicates a depletion of boron with longer electrolysis time. This assertion is confirmed by the spectral shift of the diamond ZCP peak toward a higher wavenumber, indicating a relaxation of the tensile stress on the crystal lattice due to the decrease in the amount of dopants.

Raman spectral mapping of several large areas within the sample confirms the facet-dependent corrosion on the BDD surface. We monitored the spectral features in four different areas in the sample and observed a similar trend in the temporal evolution of (111) and (100)-facets [14]. The spectral shift of the P_1 peak is especially notable in all investigated areas in the sample. Figure 3 shows the trend of the average [B] calculated from four different areas. Each measured area consists of 400 pixels × 80 pixels (90 × 18 μm) comprising of 32,000 spectra. As the treatment is prolonged, the average [B] is reduced in all areas. In Area A, for example, the average [B] continuously decreased from 4.7×10^{20} cm^{-3} in its pristine state to 1.5×10^{20} cm^{-3} after 12 h. The corrosion-induced doping concentration reduction may explain the diminished electrochemical activity of BDD electrodes as reported previously [15, 20, 21].

As a complement to the chemical information provided by micro-Raman spectroscopy, high-resolution core level C 1 s XPS measurements were also systematically carried out after 2, 6, and 12 h or anodic treatment [14]. Although the spatial resolution of XPS is poor (1 μm) compared to Raman spectroscopy, it benefits from its extreme sensitivity to elemental composition on the surface.

In its pristine state, the main component at the surface is sp^3 carbon species, corresponding to the C–C bond in diamond. A very small contribution from C–O groups was also observed which may be ascribed to the natural oxidation of the film due to its exposure to air. No sp^2 C = C peak was observed, confirming the Raman measurements. However, after 2 h of electrolysis, a significant amount of sp^2 C = C species is detected, replacing some sp^3 surface carbon, as evidenced by the decrease

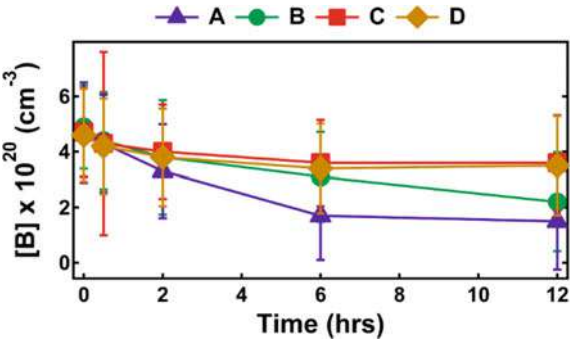

Fig. 3 Temporal evolution of the average boron concentration [B] calculated from the mean Raman shift of the P_1 peak measured at four different locations on the BDD film. Bars represent the standard deviation. Reprinted with permission from [14]. Copyright (2017) American Chemical Society

https://www.twirpx.org & http://chemistry-chemists.com

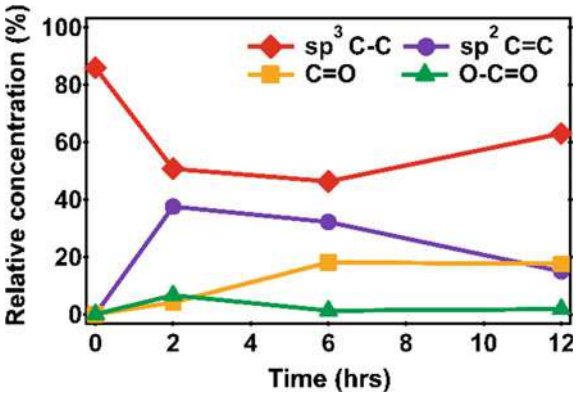

Fig. 4 Temporal evolution of the surface functional groups measured by XPS. Reprinted with permission from [14]. Copyright (2017) American Chemical Society

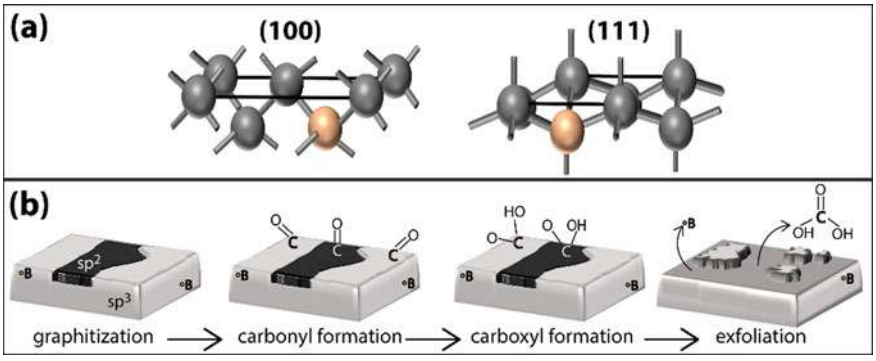

Fig. 5 **a** Schematic diagram of the idealized diamond (100) and (111) facets showing carbon dangling bonds. Black and peach spheres represent carbon and substitutional boron atoms, respectively. **b** Proposed mechanism for anodic corrosion of diamond. Reprinted with permission from [14]. Copyright (2017) American Chemical Society

in the relative concentration of the sp^3 C–C. As the anodic treatment is prolonged, the amount of sp^2 C = C species declines but not completely disappears, suggesting a non-uniform sp^2 etching within the measured area. The slight increase in the sp^3 C–C species after 12 h indicates that the surface has been etched, revealing sp^3 carbon atoms that were initially in the subsurface.

Detection of carbonyl (C = O) species as anodization progressed is also revealing and aids the comprehensive understanding of the facet-dependent corrosion in BDD. The corresponding XPS peak only appears after electrochemical treatment and increases in concentration at longer treatment times. Due to the single dangling bonds present in the unreconstructed diamond (111) surface, it has been previously shown that carbonyl cannot reasonably exist on the (111) facet [41, 42]. Therefore,

https://www.twirpx.org & http://chemistry-chemists.com

the presence and evolution of the C = O species must be related to the preferential corrosion of the (100) grains, as observed in the Raman studies. Another oxidized species, O–C = O, was also measured in smaller amounts. This functional group species may arise from carboxyl (COOH) which is shown to be a likely intermediate in the corrosion process of BDD [19].

Corrosion mechanism in BDD

The electrochemical oxidation of acetic acid has been previously explained using differential electrochemical mass spectrometry [43]. Successive H-abstractions by hydroxyl radicals (·OH) lead to the oxidation of CH_3COOH to CO_2. In the process, methyl radicals (CH_3·) are formed as intermediates. These methyl radicals have been shown to be an initial step in the corrosion process [16]. The small manifestation of the CH_x Raman peak measured after anodic treatment along with other spectral changes confirm its importance in the process.

In parallel, hydroxyl radicals also reacts with the BDD to create an OH-terminated surface. Based on the Raman and XPS measurements, it can be deduced that the subsequent interactions of the ·OH in the aqueous electrolyte with the BDD surface lead to two possible pathways: (1) direct graphitization of the diamond surface, leading to etching, or (2) further oxidation, leading to the formation of carbonyl bonds on the BDD surface. The first pathway is well-known and well-studied by researchers investigating corrosion in BDD. Here, the facet-dependent Raman results indicate that carbonyl formation is actually a very important step in the corrosion process, as carbonyl serves as intermediates for carboxyl to form, and further cause exfoliation by forming into carbonic acid [19]. This exposes the subsurface layer, and if boron atoms are present, allows for the boron to detach from the lattice as well, leading to a reduction in the average [B] in the BDD electrode. Similar reduction in boron content after 12 h anodic treatment was also observed near the surface region using glow discharge optical emission spectroscopy [16].

The observed grain orientation dependence of the corrosion process offers new and important insights, not only to aid our understanding of BDD electrode degradation, but also of the surface chemistry happening of the BDD surface. With these new information, future works can be geared toward minimizing degradation without sacrificing BDD electrochemical efficiency.

3 Scanning Tunneling Microscopy (STM): Atomic-Scale Imaging of BDD

3.1 STM Studies of Diamond Films

Our understanding of the mechanisms behind BDD remains to be incomplete mostly because of the intricate and intertwined correlation among the different factors affecting the properties of the BDD surface. One way to circumvent this complexity

https://www.twirpx.org & http://chemistry-chemists.com

is to observe the BDD at an even more localized level—*atomic level*—such that the compounded effects are minimized and the local property of the investigated surface is truly revealed.

The development of scanning tunneling microscopy (STM) [44] has provided us with the possibility of obtaining an atomically resolved view of solid surfaces. STM works by scanning a very sharp metal tip very close to the probed surface such that the wave functions of the tip and the surface atoms overlap [44, 45]. Applying a bias voltage (V_b) between the tip and the sample generates a tunneling current (I_t), which reflects the electron state densities and is highly dependent on the tip-sample gap distance. STM imaging, therefore, simultaneously provides information on surface topography and local electronic structure with sub-nanometer precision.

Clearly, for STM to be properly utilized as an imaging tool, the investigated sample surface has to be conductive, atomically flat, clean, and, ideally, well-ordered. Diamond, being an inherent insulator, is therefore not an easy and ideal sample for STM studies. For BDD, it means that the sample must have a considerable amount of boron dopants to yield enough conductivity on the surface. However, BDD growth using CVD with high boron doping usually leads to a rough surface, characterized by numerous defects, domains, and grain boundaries. Thus, highly doped BDD samples are likewise not ideal for STM investigations because of the limited working range of the z piezo scanner of the STM. Nevertheless, with appropriate growth parameters and pre-imaging treatments, BDD is a very interesting surface to analyze using STM.

As early as 1991, STM has been utilized to investigate diamond surfaces, mainly to clarify the CVD growth and nucleation mechanisms of epitaxial diamond films [46, 47]. The motivation later shifted toward understanding surface conductivity [48–50], superconductivity [51, 52], and electron field emission [53–55]. Most of the initial reports dealt with *undoped* single crystalline diamond films with hydrogen-terminated surfaces [47, 56–60], suggesting that hydrogenation is important not only for surface stabilization but also for rendering p-type surface conductivity to diamond [2, 61]. In diamond (100) films, elongated dimer rows of (2 × 1) monohydride surface reconstruction have been consistently observed [58, 62, 63]. On the other hand, STM imaging of hydrogenated diamond (111) surface reveals several structures including the ideal (1 × 1) rows [59, 60, 64], reconstructed Pandey (2 × 1) chain rows [65], and $\sqrt{3}x\sqrt{3}R30^\circ$ reconstruction [59, 64].

For boron-doped diamond films, STM reports have been limited to hydrogenated (100)-oriented single crystalline films due to the smoothness of the resulting film at substrate temperatures (T ~ 1000 K) compared to other facets [66]. Interestingly, no substantial differences were observed in the STM images of undoped diamond and BDD (100) films [58]. Considering the BDD community-accepted assertion that boron incorporation efficiency and electrochemical activity are facet-dependent, i.e., BDD (111) is superior over (100), STM characterization of BDD (111) is necessary to understand the role of boron in the BDD electrode.

In the following section, atomically resolved imaging of hydrogenated BDD (111) and (100) is demonstrated using ultrahigh vacuum (UHV) STM at cryogenic temperature (T = 5 K). Previous STM investigations of BDD films have been performed only at ambient temperature, which does not fully harness the resolving power that STM

https://www.twirpx.org & http://chemistry-chemists.com

can achieve. The low temperature and vacuum-like environment ensures a controlled surface environment with minimal temperature effects in both the surroundings (thermal drift during imaging) and the sample (lattice expansion). Moreover, such experimental conditions allow for precise measurements of the local electronic structure of the sample by monitoring the change in the tunneling current as a function of the bias voltage (scanning tunneling spectroscopy). The result is a clearer, more accurate atomic view of the BDD surface provided by STM measurements with unprecedented quality and precision.

3.2 Atomic Imaging at Cryogenic Temperature

Experimental details

Sample preparation and characteristics

The samples discussed in this section are single crystalline (100) and (111)-oriented BDD thin films grown via microwave-assisted CVD on heteroepitaxial diamond substrates with comparable doping (B/C ratio = 1%) and growth conditions. The carbon and boron sources are methane (CH_4) and trimethylborane ($B(CH_3)_3$), respectively. To ensure good surface morphology, the growth was implemented in a multi-step process followed by hydrogenation, which was performed by exposing the films to H_2 plasma. The samples were then fixed on tantalum sample holders with tantalum tape (Fig. 6a). A multimeter was used to ensure good contact between the sample and the holder and to measure the conductivity. Electrical resistivity of less than 200 Ω at room temperature was measured for all samples, which indicates conductivity high enough for low-temperature STM measurements to be achieved.

Optical and micro-Raman measurements were carried out before the samples were introduced into the STM UHV chamber. In the microscopic scale, the BDD (111) and (100) film surfaces show a pitted appearance as shown in Fig. 6c and d, respectively. Despite the apparent unevenness of the surfaces, micro-Raman measurements confirm that the crystallinity and boron concentration are generally uniform for both samples, with negligible graphitic species (sp^2 carbon, G-band at 1580 cm^{-1}) (Fig. 6e). The average boron concentration, [B], calculated using Eq. 1 in Sect. 2.2 are $[B]_{111} = 1.2 \times 10^{20}$ cm^{-3} and $[B]_{100} = 2.9 \times 10^{-19}$ cm^{-3}. In the BDD (100) surface, isolated dark spots are also observed (Fig. 6d). These areas appear to be highly-doped areas ($[B] \sim 9 \times 10^{20}$ cm^{-3}) and are generally avoided during STM measurements because the surface is very rough and may contain sp^2 carbon (Fig. 6b).

STM experimental parameters

STM measurements were performed in a low-temperature STM system operated at UHV conditions (base pressure $= 5 \times 10^{-11}$ Torr). BDD samples were degassed up to 750 ˚C by filament heating in the UHV chamber to remove unwanted adsorbates that may be on the surface. Heating was done slowly, carefully ensuring that the annealing

https://www.twirpx.org & http://chemistry-chemists.com

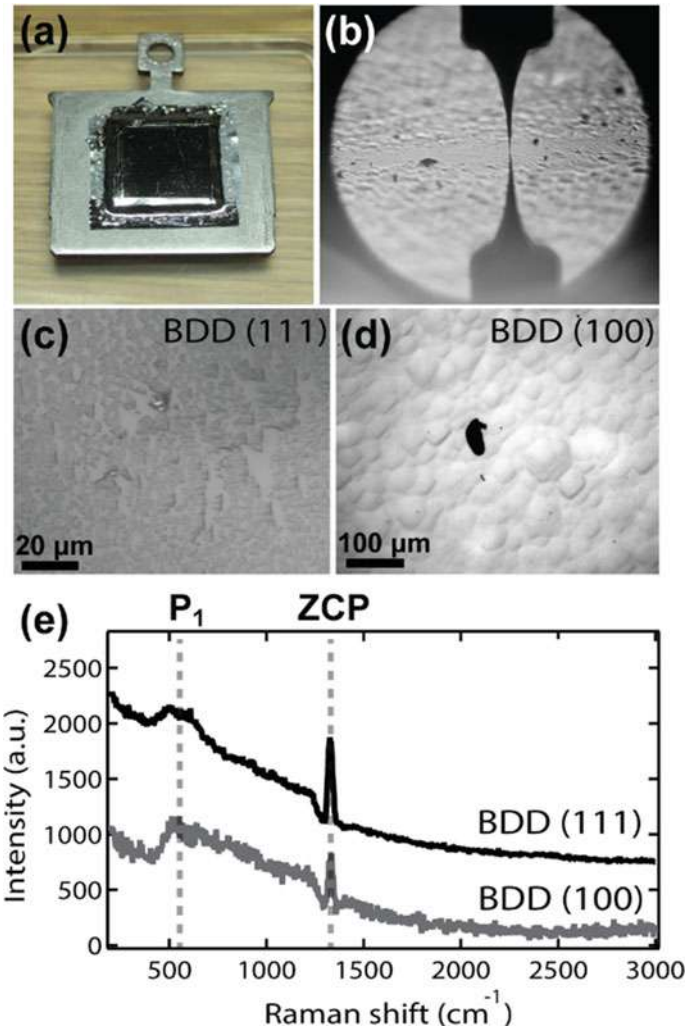

Fig. 6 **a** BDD (100) sample mount-ed on a tantalum STM holder plate. **b** STM tip (and its reflection) approached very near the BDD (100) surface. Optical images **c** and **d** and representative Raman spectra **e** of the BDD (100) and BDD (111) films

temperature does not exceed 1000 ˚C to avoid possible dopant redistribution and dehydrogenation of the surface [66]. The temperature was measured by monitoring the sample holder temperature using an infrared pyrometer. All STM images were collected at T = 5.0 K using an electrochemically etched tungsten tip (Fig. 6b). Prior to STM measurements of the BDD surfaces, tips were cleaned and characterized on metal substrates with well-defined properties.

https://www.twirpx.org & http://chemistry-chemists.com

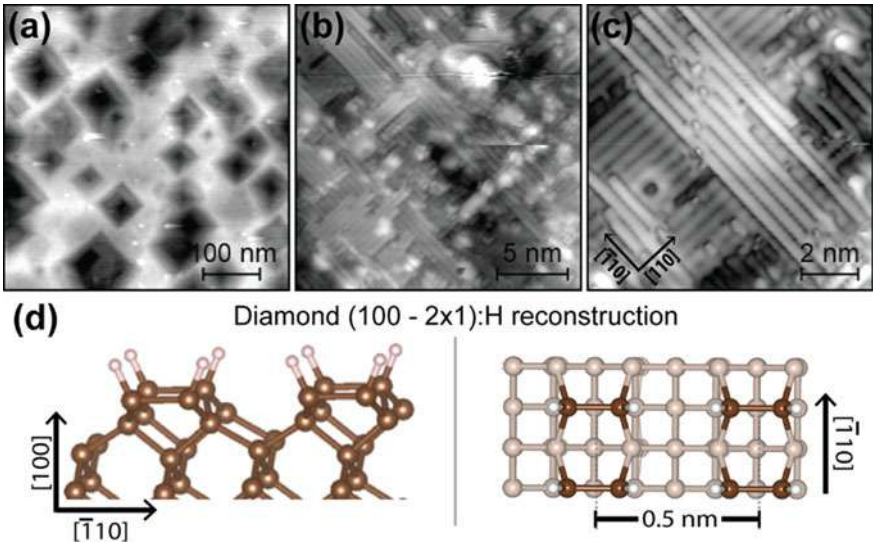

Fig. 7 STM imaging of BDD (100). **a** Large-scale topographic image shows deep square-shaped pits (V_b = 0.8 V, It = 0.5 nA). **b** 20 x 20 nm^2 and **c** 10 x 10 nm^2 STM images show the (2 x 1) CH-CH dimer rows (V_b = -0.5 V, I_t = 1 nA). **d** Side (left) and top (right) views of the (2 x 1):H dimer reconstruction model of diamond (100). Carbon and hydrogen atoms are represented by brown and white balls, respectively. To highlight the surface dimers in the top view of the model (right), dark and light-colored balls represent the surface carbon and subsurface/bulk carbon atoms, respectively

BDD (100)

In large-area scans (500 × 500 nm^2, Fig. 7a), BDD (100) looks unsmooth with random pits scattered on the surface. These square-shaped pits have an average depth of 3 nm and are attributed to the etching effect of hydrogen plasma on CVD-grown surfaces [48]. In higher-resolution scans of the flat areas (Fig. 7b–c), it can be observed that the surface is dominated by parallel rows forming domains that are rotated relative to each other by 90°. The rows have a (2 × 1) reconstruction with a row–row distance of 0.50 nm, representing monohydride carbon dimer rows similar to previous reports [47, 57, 63, 67]. The distance between the rows corresponds well with the calculated distance (0.504 nm) between C–C dimer rows of the (2 × 1) reconstructed diamond surface [68] (Fig. 7d). Moreover, inhomogeneities, characterized by row vacancies and bright protrusions, are abundant on the surface, as expected of CVD-grown films [69]. The bright protrusions are observed to proliferate on the surface when the samples are taken out of the UHV chamber and exposed to the ambient environment for a prolonged period, indicating that these represent adsorbates from the surroundings.

BDD (111)

Figure 8a shows a typical large-area topographic scan of the BDD (111) surface

https://www.twirpx.org & http://chemistry-chemists.com

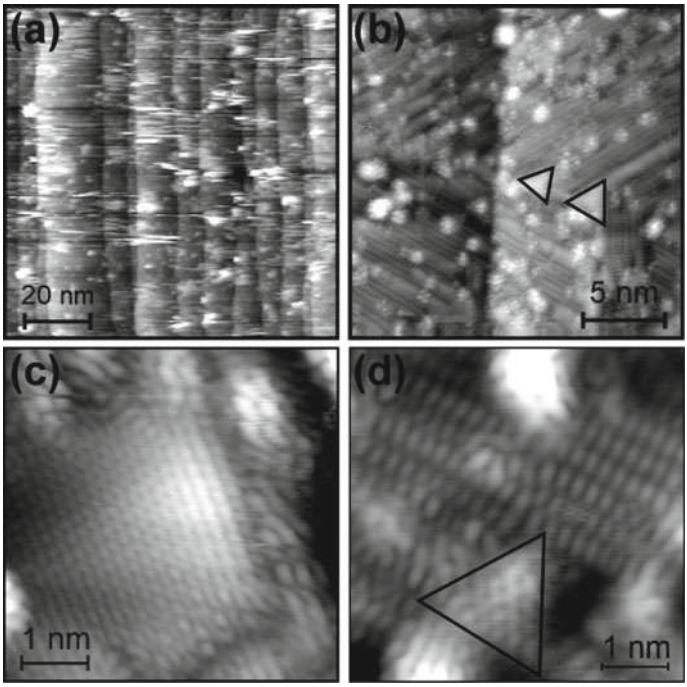

Fig. 8 **a** Terraces dominate the large-area STM images of BDD (111) ($V_b = 1.0$ V, $I_t = 1.0$ nA). Well-defined rows **b** and two types of triangu-lar features **c**, **d** charac-terize the surface. ($V_b = -1.0$ V, $I_t = 3–5$ nA)

imaged by STM. Flat terraces are separated by monoatomic steps along the [-110] direction and, similar to BDD (100) sample, are littered randomly with bright protrusions. A closer look at the terraces shows that the dominant structures on the surface are rows composed of well-defined oval protrusions (Fig. 8b and d). The rows are separated by an average distance of 4.1 ± 0.2 Å and form domains that are rotated by 120° with respect to each other. Each protrusion has a size of 2.5×1.0 Å. Aside from the rows, triangular areas can also be observed on the surface. Based on their average size, these areas can be categorized into two types. The first type, shown in Fig. 8c, has an average side length of 4 nm and is rarely observed on the surface. The other type, which is outlined by black lines in Fig. 8b and d, has an average side length of 2.0 nm. These unique features are superimposed on top of the rows and are inclined to be near step edges. As measured from several STM images taken from different sample areas, these structures cover 1–1.5% of the total sample area, which agrees well with the doping amount in the sample—an indication that this feature is related to incorporation of boron atoms in the diamond lattice. Notably, these features were only found in BDD (111) and not in BDD (100).

Four types of surface reconstructions can be observed on atomically resolved STM images of BDD (111) (Fig. 9). The oval protrusions that form the rows are

https://www.twirpx.org & http://chemistry-chemists.com

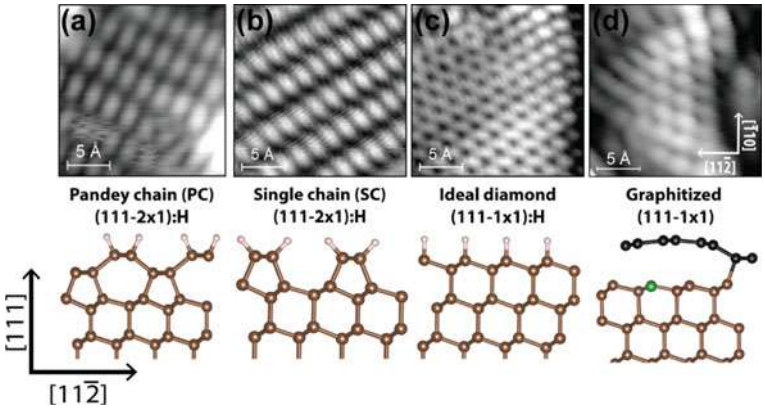

Fig. 9 Atomic-scale topographic images showing four types of surface reconstructions found in BDD (111): **a** hydrogenated Pandey chain (2x1), **b** hydrogenated single chain (2x1), **c** hydrogenated ideal diamond (1x1), and **d** (1x1) reconstruction with a graphitized surface (surface represented by black balls)

characterized by a (2 × 1) reconstruction, where the distance between neighboring spots along each row is 2.3 ± 0.2 Å. However, as Fig. 9a and b reveal, there are actually two types of inter-row arrangements, i.e., the oval protrusions form either (1) a rectangular surface cell (Fig. 9a), or (2) shifted rows (Fig. 9b). Theoretically, two reconstruction models for the diamond (111) surface are known to have a (2 × 1) symmetry—the Pandey chain (PC) reconstruction [70] and the single chain (SC) reconstruction [65]. Although the former is more commonly referred to especially in interpreting STM images, density functional theory (DFT) calculations indicate that the difference in surface energy between the two symmetries is actually minimal, implying that both are possibly occurring on the surface. The oval spots indicate the C–C σ-bonds between the top surface carbon atoms [65]. The atomic-scale STM image in Fig. 9c, which describes the *larger* triangular structure in Fig. 8c, shows a sixfold symmetry with a periodicity of 2.0 ± 0.1 Å. The perceived symmetry depicts the C–C bonds between the hydrogen-terminated surface carbon and second-layer carbon atoms in an ideal (111–1 × 1) diamond surface.

On the other hand, the symmetry shown in Fig. 9d, representing the *smaller* boron-related triangular feature, resembles a graphitized surface. Local density of states (LDOS) measurements at this area using scanning tunneling spectroscopy (STS) reveal an electronic structure with several states within the bandgap 71, which may be responsible for the superior electrochemical activity of BDD (111) over other facets. The localized and unique attributes of this feature suggest that these areas reflect the position of dopants on BDD (111), manifesting as localized graphitization on the surface. The effect is enhanced in BDD (111) due to the similarity of the stacking order of diamond (111) to graphite.

https://www.twirpx.org & http://chemistry-chemists.com

4 Chapter Summary and Outlook

Localized measurements of boron-doped diamond (BDD) are very important to unfold the complex mechanisms that govern BDDs. In this chapter, we have shown that high-resolution imaging and spectroscopy can provide a precise correlation between the surface structure of BDD and its electrochemical properties. With its high sensitivity to chemical composition and crystallographic orientation, high-resolution polarized Raman spectroscopy allowed for a comprehensive study of the facet-dependent chemical changes on the BDD surface resulting from interactions with its surroundings. Scanning tunneling microscopy (STM) goes a step further by providing an *atomic* view of the BDD surface morphology. Distinct local structures on BDD (111) surface gives us a preliminary explanation as to why the (111) surface is more electrochemically active and efficient compared to BDD (100).

The experimental demonstrations shown in this chapter about the use of Raman spectroscopy and STM for BDD investigations are only the beginning, setting the groundwork for further localized BDD measurements. A systematic STM study of the effects of doping type and concentration is a very important step to confirm the role of dopants in the conductivity of diamond. Another particularly promising direction to take is to investigate BDD using a method called STM-based tip-enhanced Raman spectroscopy (STM-TERS), which combines the chemical specificity of Raman spectroscopy and the atomic resolution of STM. Recent works on single molecule studies using STM-TERS in low-temperature UHV setting [72] and liquid environment [73] gives us a glimpse into how the method can be used to probe the chemical properties and electrochemical activity of functional materials including BDD.

Acknowledgements The experimental works mentioned in this chapter are supported by the Japan Science and Technology Agency (JST) under the ACCEL project entitled, "Fundamentals and Applications of Diamond Electrodes."

References

1. Macpherson JV (2015) A practical guide to using boron doped diamond in electrochemical research. Phys Chem Chem Phys 17:2935–2949. https://doi.org/10.1039/C4CP04022H
2. Pakes CI, Garrido JA, Kawarada H (2014) Diamond surface conductivity: properties, devices, and sensors. MRS Bull 39:542–548. https://doi.org/10.1557/mrs.2014.95
3. Yang N, Yu S, MacPherson JV et al (2019) Conductive diamond: synthesis, properties, and electrochemical applications. Chem Soc Rev 48:157–204. https://doi.org/10.1039/c7cs00757d
4. Einaga Y (2018) Development of electrochemical applications of boron-doped diamond electrodes. Bull Chem Soc Jpn 91:1752–1762. https://doi.org/10.1246/bcsj.20180268
5. Alfaro MAQ, Ferro S, Martínez-Huitle CA, Vong YM (2006) Boron doped diamond electrode for the wastewater treatment. J Braz Chem Soc 17:227–236. https://doi.org/10.1590/S0103-50532006000200003
6. Suzuki A, Ivandini TA, Yoshimi K et al (2007) Fabrication, characterization, and application of boron-doped diamond microelectrodes for in vivo dopamine detection. Anal Chem 79:8608–8615. https://doi.org/10.1021/ac071519h

https://www.twirpx.org & http://chemistry-chemists.com

7. Ogata G, Ishii Y, Asai K et al (2017) A microsensing system for the in vivo real-time detection of local drug kinetics. Nat Biomed Eng 1:654–666. https://doi.org/10.1038/s41551-017-0118-5
8. Hassan MM, Larsson K (2014) Effect of surface termination on diamond (100) surface electrochemistry effect of surface termination on diamond (100) surface electrochemistry. J Phys Chem C 118:22995–23002
9. Chou JP, Retzker A, Gali A (2017) Nitrogen-terminated diamond (111) surface for room-temperature quantum sensing and simulation. Nano Lett 17:2294–2298. https://doi.org/10.1021/acs.nanolett.6b05023
10. Mayrhofer L, Moras G, Mulakaluri N et al (2016) Fluorine-terminated diamond surfaces as dense dipole lattices: the electrostatic origin of polar hydrophobicity. J Am Chem Soc 138:4018–4028. https://doi.org/10.1021/jacs.5b04073
11. Watanabe T, Honda Y, Kanda K, Einaga Y (2014) Tailored design of boron-doped diamond electrodes for various electrochemical applications with boron-doping level and sp2-bonded carbon impurities. Phys Status Solidi 211:2709–2717. https://doi.org/10.1002/pssa.201431455
12. Ivandini TA, Watanabe T, Matsui T et al (2019) Influence of surface orientation on electrochemical properties of. J Phys Chem C 123:5336–5344. https://doi.org/10.1021/acs.jpcc.8b10406
13. Pleskov YV, Evstefeeva YE, Krotova MD et al (2006) Synthetic semiconductor diamond electrodes: Electrochemical behaviour of homoepitaxial boron-doped films orientated as (1 1 1), (1 1 0), and (1 0 0) faces. J Electroanal Chem 595:168–174. https://doi.org/10.1016/j.jelechem.2006.07.010
14. Catalan FCI, Hayazawa N, Yokota Y et al (2017) Facet-dependent temporal and spatial changes in boron-doped diamond film electrodes due to anodic corrosion. J Phys Chem C 121:26742–26750. https://doi.org/10.1021/acs.jpcc.7b06085
15. Chaplin BP, Wyle I, Zeng H et al (2011) Characterization of the performance and failure mechanisms of boron-doped ultrananocrystalline diamond electrodes. J Appl Electrochem 41:1329–1340. https://doi.org/10.1007/s10800-011-0351-7
16. Kashiwada T, Watanabe T, Ootani Y et al (2016) A study on electrolytic corrosion of boron-doped diamond electrodes when decomposing organic compounds. ACS Appl Mater Interfaces 8:28299–28305. https://doi.org/10.1021/acsami.5b11638
17. Griesbach U, Zollinger D, Pütter H, Comninellis C (2005) Evaluation of boron doped diamond electrodes for organic electrosynthesis on a preparative scale. J Appl Electrochem 35:1265–1270. https://doi.org/10.1007/s10800-005-9038-2
18. Katsuki N, Takahashi E, Toyoda M et al (1998) Water electrolysis using diamond thin-film electrodes. J Electrochem Soc 145:2358–2362. https://doi.org/10.1149/1.1838643
19. Chaplin BP, Hubler DK, Farrell J (2013) Understanding anodic wear at boron doped diamond film electrodes. Electrochim Acta 89:122–131. https://doi.org/10.1016/j.electacta.2012.10.166
20. Chen G (2004) Electrochemical technologies in wastewater treatment. Sep Purif Technol 38:11–41. https://doi.org/10.1016/j.seppur.2003.10.006
21. Anglada A, Urtiaga A, Ortiz I (2009) Contributions of electrochemical oxidation to waste-water treatment: fundamentals and review of applications. J Chem Technol Biotechnol 84:1747–1755. https://doi.org/10.1002/jctb.2214
22. Kavan L, Vlckova Zivcova Z, Petrak V et al (2015) Boron-doped diamond electrodes: electrochemical, atomic force microscopy and Raman study towards corrosion-modifications at nanoscale. Electrochim Acta 179:626–636. https://doi.org/10.1016/j.electacta.2015.04.124
23. Notsu H, Yagi I, Tatsuma T et al (2000) Surface carbonyl groups on oxidized diamond electrodes. J Electroanal Chem 492:31–37. https://doi.org/10.1016/S0022-0728(00)00254-0
24. Rao TN (1999) Band-edge movements of semiconducting diamond in aqueous electrolyte induced by anodic surface treatment. J Electrochem Soc 146:680. https://doi.org/10.1149/1.1391662
25. John P, Polwart N, Troupe CE, Wilson JIB (2003) The oxidation of diamond: the geometry and stretching frequency of carbonyl on the (100) surface. J Am Chem Soc 125:6600–6601. https://doi.org/10.1021/ja029586a

https://www.twirpx.org & http://chemistry-chemists.com

26. Ghodbane S, Ballutaud D, Omnes F, Agnes C (2010) Comparison of the XPS spectra from homoepitaxial 111}, {100 and polycrystalline boron-doped diamond films. Diam Relat Mater 19:630–636. https://doi.org/10.1016/j.diamond.2010.01.014
27. Bernard M, Deneuville A, Muret P (2004) Non-destructive determination of the boron concentration of heavily doped metallic diamond thin films from Raman spectroscopy. Diam Relat Mater 13:282–286. https://doi.org/10.1016/j.diamond.2003.10.051
28. Prawer S, Nugent KW, Weiser PS (1994) Polarized Raman spectroscopy of chemically vapor deposited diamond films. Appl Phys Lett 65:2248–2250. https://doi.org/10.1063/1.112778
29. Loudon R (1964) Advances in physics the Raman effect in crystals. Adv Phys 13:423–482. https://doi.org/10.1080/00018736400101051
30. Bustarret E, Gheeraert E, Watanabe K (2003) Optical and electronic properties of heavily boron-doped homo-epitaxial diamond. Phys Status Solidi Appl Res 199:9–18. https://doi.org/10.1002/pssa.200303819
31. Pruvost F, Bustarret E, Deneuville A (2000) Characteristics of homoepitaxial heavily boron-doped diamond films from their Raman spectra. Diam Relat Mater 9:295–299. https://doi.org/10.1016/S0925-9635(99)00241-1
32. Bernard M, Baron C, Deneuville A (2004) About the origin of the low wave number structures of the Raman spectra of heavily boron doped diamond films. Diam Relat Mater 13:896–899. https://doi.org/10.1016/j.diamond.2003.11.082
33. Niu L, Zhu J-Q, Han X et al (2009) First principles study of structural, electronic and vibrational properties of heavily boron-doped diamond. Phys Lett A 373:2494–2500. https://doi.org/10.1016/j.physleta.2009.05.008
34. Pruvost F, Deneuville A (2001) Analysis of the Fano in diamond. Diam Relat Mater 10:531–535. https://doi.org/10.1016/S0925-9635(00)00378-2
35. Nebel CE, Ristein J (2003) Semiconductors and semimetals: thin-film diamond I. Elsevier, Netherlands
36. Ushizawa K, Watanabe K, Ando T et al (1998) Boron concentration dependence of Raman spectra on 100 and 111 facets of B-doped CVD diamond. Diam Relat Mater 7:1719–1722. https://doi.org/10.1016/S0925-9635(98)00296-9
37. Bergman L, McClure MT, Glass JT, Nemanich RJ (1994) The origin of the broadband luminescence and the effect of nitrogen doping on the optical properties of diamond films. J Appl Phys 76:3020–3027. https://doi.org/10.1063/1.357508
38. Donato MG, Faggio G, Marinelli M et al (2001) High quality CVD diamond: a Raman scattering and photoluminescence study. Eur Phys J B-Condensed Matter 20:133–139
39. Bernard M, Deneuville A, Bustarret E (2002) Detection of CHx bonds from micro Raman spectroscopy on polycrystalline boron doped diamond electrodes. Diam Relat Mater 11:662–666. https://doi.org/10.1016/S0925-9635(01)00547-7
40. Ricci PC, Anedda A, Carbonaro CM et al (2005) Electrochemically induced surface modifications in boron-doped diamond films: a Raman spectroscopy study. Thin Solid Films 482:311–317. https://doi.org/10.1016/j.tsf.2004.11.169
41. Loh KP, Xie XN, Yang SW, Zheng JC (2002) Oxygen adsorption on (111)-oriented diamond: a study with ultraviolet photoelectron spectroscopy, temperature- programmed desorption, and periodic density functional theory. Phys Chem B 106:5230–5240
42. De-Theije FK, Reedijk MF, Arsic J et al (2001) Atomic structure of diamond {111} surfaces etched in oxygen water vapor. Phys Rev B Condens Matter Mater Phys 64:085403/1–7. https://doi.org/10.1103/PhysRevB.64.085403
43. Comninellis C, Kapalka A, Malato S et al (2008) Advanced oxidation processes for water treatment: advances and trends for R&D. J Chem Technol Biotechnol 83:769–776. https://doi.org/10.1002/jctb
44. Binnig G, Rohrer H, Gerber C, Weibel E (1982) Surface studies by scanning tunneling microscopy. Phys Rev Lett 49:58–60
45. Oura K, Lifshits VG, Saranin A et al (2003) Surface science—an introduction. Springer-Verlag, Berlin, Heidelberg

https://www.twirpx.org & http://chemistry-chemists.com

46. Turner KF, Legrice YM, Stoner BR et al (1991) Surface topography and nucleation of chemical vapor deposition diamond films on silicon by scanning tunneling microscopy. J Vac Sci Technol B 9:914–919
47. Tsuno T, Imai T, Nishibayashi Y et al (1991) Epitaxially grown diamond (001) 2x1/1x2 surface investigated by scanning Tunneling microscopy in air. Jpn J Appl Phys 30:1063–1066
48. Cannaerts M, Nesladek M, Haenen K et al (2001) Reversible switching of the surface conductance of hydrogenated CVD diamond films. Phys Status Solidi Appl Res 186:235–240. https://doi.org/10.1002/1521-396X(200108)186:2%3c235::AID-PSSA235%3e3.0.CO;2-Q
49. Bobrov K, Mayne A, Comtet G et al (2003) Atomic-scale visualization and surface electronic structure of the hydrogenated diamond C(100)-(2x1): H surface. Phys Rev B 68:8. https://doi.org/10.1103/PhysRevB.68.195416
50. Hellner L, Mayne AJ, Bernard R, Dujardin G (2005) Hydrogenated diamond crystal C(100) conductivity studied by STM. Diam Relat Mater 14:1529–1534. https://doi.org/10.1016/j.diamond.2005.04.006
51. Nishizaki T, Takano Y, Nagao M et al (2006) Scanning tunneling microscopy and spectroscopy studies of superconducting boron-doped diamond films. Sci Technol Adv Mater 7:22–26. https://doi.org/10.1016/j.stam.2005.11.015
52. Nishizaki T, Sasaki T, Kobayashi N et al (2013) Spatial variation of tunneling spectra in (111)-oriented films of boron-doped diamond probed by Stm/Sts. Int J Mod Phys B 27:1362014. https://doi.org/10.1142/S0217979213620142
53. Kim YD, Choi W, Wakimoto H et al (1999) Direct observation of electron emission site on boron-doped polycrystalline diamond thin films using an ultra-high-vacuum scanning tunneling microscope. Appl Phys Lett 75:3219–3221. https://doi.org/10.1063/1.125283
54. Krauss AR, Auciello O, Ding MQ et al (2001) Electron field emission for ultrananocrystalline diamond films. J Appl Phys 89:2958–2967. https://doi.org/10.1063/1.1320009
55. Rakhimov AT, Suetin NV, Soldatov ES et al (2000) Scanning tunneling microscope study of diamond films for electron field emission. J Vac Sci Technol B Microelectron Nanom Struct 18:76. https://doi.org/10.1116/1.591154
56. Busmann HG, Zimmermann-Edling W, Sprang H et al (1992) Surface views of polycrystalline diamond films: microtwins and flat faces, constricted and free atomic layer motion. Diam Relat Mater 1:979–988. https://doi.org/10.1016/0925-9635(92)90120-D
57. Stallcup RE, Aviles AF, Perez JM (1995) Atomic resolution ultrahigh vacuum scanning tunneling microscopy of epitaxial diamond (100) films. Appl Phys Lett 66:2331. https://doi.org/10.1063/1.113973
58. Kawarada H, Sasaki H, Sato A (1995) Scanning-tunneling-microscope observation of the homoepitaxial diamond (001) 2×1 reconstruction observed under atmospheric pressure. Phys Rev B 52:11351–11358. https://doi.org/10.1103/PhysRevB.52.11351
59. Sasaki H, Kawarada H (1993) Structure of chemical vapor deposited diamond (111) surfaces by Scanning Tunneling Microscopy. Jpn J Appl Phys 32:L1771–L1774
60. Tsuno T, Tomikawa T, Shikata SI, Fujimori N (1994) Diamond homoepitaxial growth on (111) substrate investigated by scanning tunneling microscope. J Appl Phys 75:1526–1529. https://doi.org/10.1063/1.356389
61. Kawarada H (1996) Hydrogen-terminated diamond surfaces and interfaces. Surf Sci Rep 26:205–206. https://doi.org/10.1016/S0167-5729(97)80002-7
62. Zimmermann-Edling W, Busmann HG, Sprang H, Hertel IV (1992) Imaging polycrystalline CVD diamond films on the micrometer and nanometer scale by STM and AFM. Ultramicroscopy 42–44:1366–1371. https://doi.org/10.1016/0304-3991(92)90450-X
63. Bobrov K, Mayne AJ, Dujardin G (2001) Atomic-scale imaging of insulating diamond through resonant electron injection. Nature 413:616–619. https://doi.org/10.1038/35098053
64. Busmann H-G, Lauer S, Hertel IV et al (1993) Observation of (sqrt(3) x sqrt(3)) R30 diamond (111) on vapour-grown polycrystalline films. Surf Sci 295:340–346
65. Kohler T, Sternberg M, Porezag D, Frauenheim T (1996) Surface properties of diamond (111): 1x1, 2x1, and 2x2 reconstructions. Phys Status Solidi A 156

https://www.twirpx.org & http://chemistry-chemists.com

66. Stallcup RE, Perez JM (2001) Scanning tunneling microscopy studies of temperature-dependent etching of diamond (100) by atomic hydrogen. Phys Rev Lett 86:3368–3371. https://doi.org/10.1103/PhysRevLett.86.3368
67. Bobrov K, Mayne AJ, Hoffman A, Dujardin G (2003) Atomic-scale desorption of hydrogen from hydrogenated diamond surfaces using the STM. In: Surface Science, pp 138–143
68. Furthmüller J, Hafner J, Kresse G (1996) Dimer reconstruction and electronic surface states on clean and hydrogenated diamond (100) surfaces. Phys Rev B 53:7334–7351. https://doi.org/10.1016/0039-6028(96)00192-6
69. Kuang Y, Wang Y, Lee N et al (1995) Surface structure of homoepitaxial diamond (100) films, a scanning tunneling microscopy study. Appl Phys Lett 67:3721
70. Pandey KC (1982) New dimerized-chain model for the reconstruction of the diamond (111)-(2 × 1) surface. Phys Rev B 25:4338–4341. https://doi.org/10.1103/PhysRevB.25.4338
71. Catalan FCI, The Anh L, Oh J et al (2021) Localized graphitization on diamond surface as a manifestation of dopants. Adv Mater 33:2103250
72. Jaculbia RB, Miwa K, Hayazawa N (2016) STM-Tip-enhanced Raman spectroscopy toward single molecule scale. In: ACS Symposium Series, pp 139–181
73. Yokota Y, Hayazawa N, Yang B et al (2019) Systematic assessment of benzenethiol self-assembled monolayers on Au(111) as a standard sample for electrochemical tip-enhanced raman spectroscopy. J Phys Chem C 123:2953–2963. https://doi.org/10.1021/acs.jpcc.8b10829

https://www.twirpx.org & http://chemistry-chemists.com

Electrochemical Image of BDD

Yasufumi Takahashi, Makarova Marina, Tomohiro Ando, and Takeshi Fukuma

Keywords Electrochemical imaging · Chemical sensing · Microelectrode

1 Scanning Electrochemical Microscopy (SECM)

Scanning electrochemical microscopy (SECM) is scanning probe microscopy, which uses an ultramicroelectrode (UME) as a probe for characterizing sub-microscale chemical profile and electrochemical reactivity mapping of various samples [1–3]. After the scanning, the oxidation/reduction current detected by the scanning UME and the current value and position information of the UME are reconstructed to visualize the chemical concentration or electrochemical reactivity at the sample surface. Electrode miniaturization improves the spatial resolution and offers several other advantages, such as low double-layer charging currents, low ohmic drops, fast mass transport, and a diffusion rate-limiting steady-state current. The steady-state current of the voltammogram of the UME is described as follows:

$$i = 4nFDCa \tag{1}$$

where F is Faraday's constant, D and C are the diffusion coefficient and bulk concentration of the redox species, respectively, and a is the radius of the UME.

Numerous electrochemical systems such as electrodes, [4] semiconductors, [5] insulator surfaces, [4] nanomaterials, [6] liquid/liquid interfaces, [7] catalytic materials, [8] corrosion, [9] and life science materials have been analyzed by SECM [10].

Y. Takahashi (✉) · M. Marina · T. Ando · T. Fukuma
WPI Nano Life Science Institute (WPI-NanoLSI), Kanazawa University, Kanazawa 920-1192, Japan
e-mail: yasufumi@se.kanazawa-u.ac.jp

© Springer Nature Singapore Pte Ltd. 2022

Y. Einaga (ed.), *Diamond Electrodes*,
https://doi.org/10.1007/978-981-16-7834-9_4

https://www.twirpx.org & http://chemistry-chemists.com

Here, we describe the measurement principles and setup of SECM and the application of SECM to carbon materials.

2 Instrumentation

An SECM system consists of four major components: an electrochemical cell (including the UME and a counter/reference electrode), a current detector (current amplifier or potentiostat), a micro/nano-positioner, and a data acquisition system (Fig. 1). During such high-resolution measurements, the system must be isolated from vibrations by an anti-vibration table. In a typical SECM measurement, a two-electrode setup is employed because the redox current is extremely small (pA–nA) and the *IR* drop is negligible. If an external bias is required, it must be supplied by a bipotentiostat. The UME or sample is scanned by a micro/nano-positioner. A piezo stage and stepping motor-based stage are used for nanoscale and microscale scanning, respectively. Data acquisition is performed by a conventional analog-to-digital (A/D)/digital-to-analog (D/A) converter or a field-programmable gate array board. The scanning area of the sample is selected by observing the sample position under an inverted optical microscope or a digital microscope.

2.1 Measurement Principle and Application

Feedback mode

Feedback (FB) mode is used to evaluate electrochemical reactivity on a sample surface quantitatively. In FB mode measurement, an electrochemical mediator, which

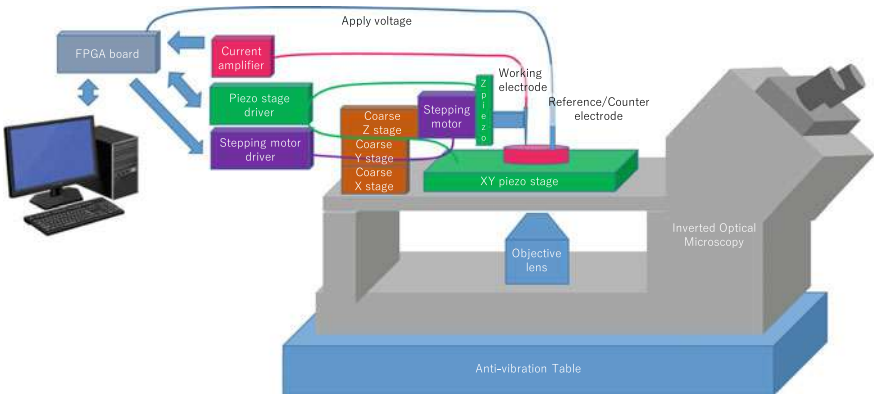

Fig. 1 Experimental setup of SECM

https://www.twirpx.org & http://chemistry-chemists.com

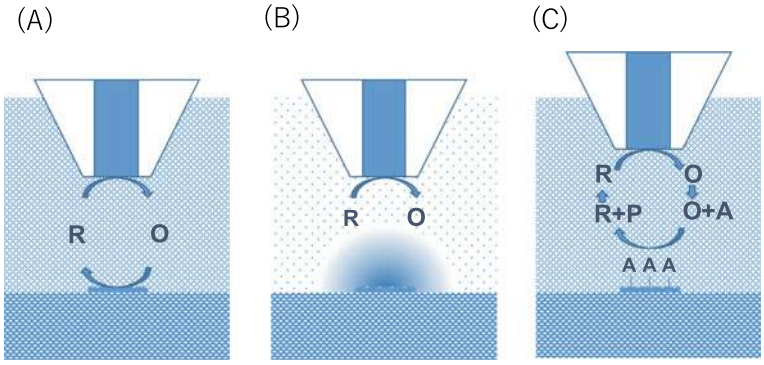

Fig. 2 Schematics of **a** feedback mode SECM, **b** generation collection-mode SECM, and **c** surface interrogation mode SECM

shuttles the electron transfer between UME and sample, is added in advance and the electrochemical mediator is oxidized/reduced by the UME and diffused to the sample surface. Then, the electrochemical mediator is reduced/oxidized and regenerated on the sample surface (Fig. 2a). The regenerated electrochemical mediator reacts on the UME and the current enhancement is observed by repeating this redox process. This process is called a redox cycle and the current enhancement is called a positive FB effect. The magnitude of the current enhancement depends on the UME–sample distance. The rate constant of the SECM FB mode is typically determined from the current–distance profile (approach curve) [4]. When the sample surface is inert, the redox cycle does not occur and the diffusion state of the electrochemical mediator is physically blocked as the UME approaches the sample surface. Consequently, the current is lower than in bulk measurements. This phenomenon is called the negative FB effect.

In FB mode, the electrochemical mediator first reacts at the UME, then diffuses to the sample surface where it is regenerated. In other words, the reaction-start timing can be controlled by the UME. As the redox cycle strongly depends on the sample–UME distance, FB mode has a higher spatial resolution than the generation collection (GC) mode (explained below). Therefore, a thin insulating sheath (RG = rg/a, where rg and a are the radii of the insulating sheath and electrode, respectively) is valid to bring the UME close to the sample surface.

As an example of SECM operated in FB mode, the heterogeneously doped state of boron-doped diamond (BDD) is introduced here. Bard's group used $Ru(NH_3)_6^{3+/2+}$ as the redox mediator and characterized electrochemical reactivity of the low concentration (0.5 to 10 ppm) boron-doped hydrogen-terminated diamonds [11]. They estimated the effective kinetic rate constants k_{eff} s of the BDDs with different boron densities by fitting the SECM approach curves to theoretical curves (Fig. 3). Using conductive atomic force microscopy (C-AFM), they characterized the relationship of conductivity and electrochemical reactivity.

https://www.twirpx.org & http://chemistry-chemists.com

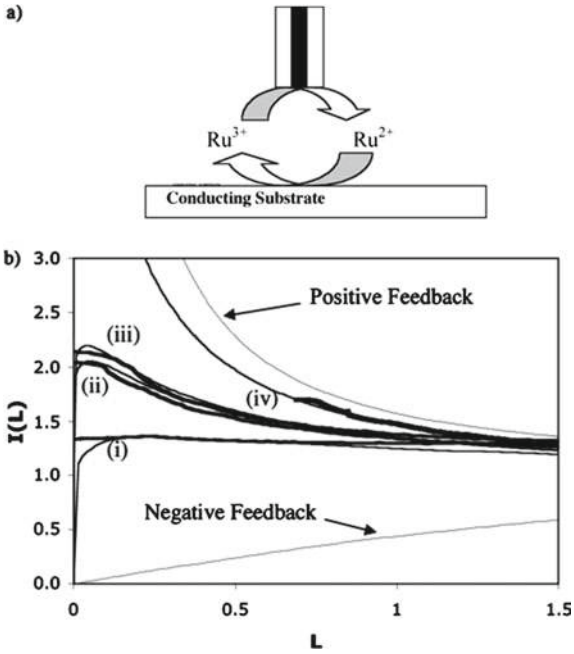

Fig. 3 **a** Schematic of positive feedback at a conductive substrate in SECM. **b** Experimental approach curves (thick black lines) obtained by a 25 μm-diameter Pt tip approaching the BDD substrates. Measurements were performed in 1.3 mM $Ru(NH_3)_6^{3+}$ in 0.1 M KCl, with a tip potential of −0.4 V versus Ag/AgCl and a substrate potential of 0.0 V versus Ag/AgCl and different concentrations of doped BDD: (i) 0.5, (ii) 1, (iii) 5, and (iv) 10 ppm. Theoretical curves (gray lines) with different effective rates k_{eff}: 0.010, (ii) 0.019, (iii) 0.021, and (iv) 0.072 cm/s. Thin black lines are the predicted approach curves in pure positive and negative FB modes, respectively. Adapted with permission from reference 11, Copyright 2004 American Chemical Society

Macpherson's group also characterized BDDs by FB mode SECM [12]. Their BDDs were heavily doped ($\sim 5 \times 10^{20}$ atoms cm^{-3}) and exhibited metal-like conductivity. The authors performed a correlative analysis of SECM, C-AFM, and cathodoluminescence (CL). The C-AFM and CL imaging revealed that the conductivity and boron uptake were nonuniform across the BDD surface. Although the conductivity difference between the grain boundaries with resistances of ca. 100 kΩ and ca. 50 MΩ was difficult to distinguish by C-AFM, it was easily detected by SECM, which characterizes the conductivity difference as a redox current.

Generation collection-mode

In generation collection (G/C) mode, the chemicals produced by sample/UME are detected by UME/sample (Fig. 2b). In this mode, the two main measurement styles are substrate generation-tip collection (SG-TC) mode, and tip generation-substrate collection (TG-SC) mode. In SG-TC mode, the UME detects the redox species generated by a substrate electrode and obtains high-sensitivity measurements because the

https://www.twirpx.org & http://chemistry-chemists.com

background current is usually very low. This mode images the concentration profiles of redox species and evaluates the fluxes of redox species generated from a sample. In TG-SC mode, the redox species are generated by the UME tip and are collected by the substrate electrode. The difference between TG-SC mode and FB mode is that the redox species is not reversible in TG-SC SECM.

As an application of the G/C-mode SECM, Bard and coworkers detected the $CO_2^{\cdot -}$ radical anion using TG-SC mode SECM [13]. The CO_2 reduction reaction is an attractive application for BDD and investigated how the boron doping level and sp^2 content of BDDs influenced the formic-acid production reaction [14, 15]. In the case of radical anion detection using TG-SC mode SECM, the generated radical have to react by substrate immediately. For this reason, the separation distance between the UME and sample surface is critical. Bard and colleagues determined that the radical anion $CO_2^{\cdot -}$ dimerizes to form oxalate ($C_2O_4^{2-}$) with a half-lifetime of 10 ns and a rate constant of 6.0×10^8 M^{-1} s^{-1}. Therefore, SECM can effectively identify and quantify the reactivities of highly reactive species with short lifetimes in solution.

Surface interrogation-SECM (SI-SECM)

Recently, adsorbed intermediates on the sample surface have been investigated by SI-SECM. The adsorbed intermediates react with the oxidized/reduced electrochemical mediator introduced by the UME; afterward, the regenerated mediator reacts on the UME again. This approach is similar to FB mode, but the current associated with the adsorbed intermediates is enhanced while the adsorbed intermediates react on the sample and mediator (Fig. 2c). SI-SECM has characterized the oxygen evolution reaction of "CoPi" oxygen-evolving catalyst (OEC), [16] the hydrogen evolution reactions of Ni [17] and molybdenum disulfide (MoS_2), [18] and the $^{\cdot}OH_{(ads)}$ reactions of $SrTiO_3$, [19] TiO_2, [5] and Ir [20].

Lopez and coworkers performed a kinetic analysis of water oxidation reaction on BDDs using SI-SECM [21]. After investigating the effect of electrolyte type and pH on the water oxidation reaction, they found that sulfate electrolytes at pH 11.0 maximize the water oxidation rate. They also found two kinetically distinct surface intermediates. One of these intermediates adsorbed at two orders of magnitude faster than the other but desorbed more slowly. The molar surface densities of the intermediates adsorbed at the faster and slower rates were 4–7 $\times$ 10^{-5} and 3–4.4 $\times$ 10^{-5} mol/cm^2, respectively. The SI-SECM imaging suggested that as the product generation progresses, the electron transfer rates slow down because limited surface sites are available for bonding the intermediates.

Bard's group characterized adsorbed CO ($CO_{(ads)}$) by SI-SECM [22]. They detected the $CO_{(ads)}$ using bromine (Br_2) as the electrochemical mediator, which yielded CO_2 and Br^- on polycrystalline platinum in aqueous H_2SO_4 (0.5 M). Besides providing support for $CO_{(ads)}$, the platinum acted as a heterogeneous catalyst for the oxidation process, as observed by scanning electrochemical cell microscopy (SECCM, discussed next).

https://www.twirpx.org & http://chemistry-chemists.com

3 Scanning Electrochemical Cell Microscopy

SECCM is a new electrochemical imaging tool developed by Patrick Uniwin's group [23]. In SECCM, the probe is a nanopipette filled with the electrolyte solution, which forms a meniscus-state electrochemical cell at the sample surface. The SECCM nanopipette can be easily and reliably fabricated at the nanoscale size and achieves high-resolution electrochemical imaging because the sample does not need to be immersed in the solution. The small electrochemical cell of SECCM avoids the chemical diffusion problem of SECM imaging, which depends on the UME–sample distance, and limits the resolution of SECM imaging (Fig. 4a). Previously, SECCM has characterized BDDs, [24–28] single-walled carbon nanotubes, [29–31] highly oriented pyrolytic graphite (HOPG)/graphene, [32–37] nanoparticles, [29, 38, 39] polycrystalline platinum [40–42], MoS_2, [43–46] and lithium-ion battery materials [47–49].

3.1 Measurement Principle of SECCM

In SECCM, the glass nanopipette is used for scanning probe and form the electrochemical cell at the sample surface. There are two main measurement styles. The double-barrel nanopipette is the most used SECCM measurement style (Fig. 4b) [23]. Each barrel (diameter <500 nm) of the tapered theta pipette is filled with an electrolyte solution and an Ag/AgCl electrode. A voltage applied between the Ag/AgCl electrode generates an ionic current across the thin meniscus of the solution at the end of the pipette. The ionic current provides a FB signal for controlling the sample–pipette distance. Furthermore, the electrochemical measurement can be performed because the sample surface can be connected as a working electrode, with one of the electrodes in the nanopipette serving as a quasi-reference electrode. This method can analyze not only conductive samples but also semiconducting and insulating samples.

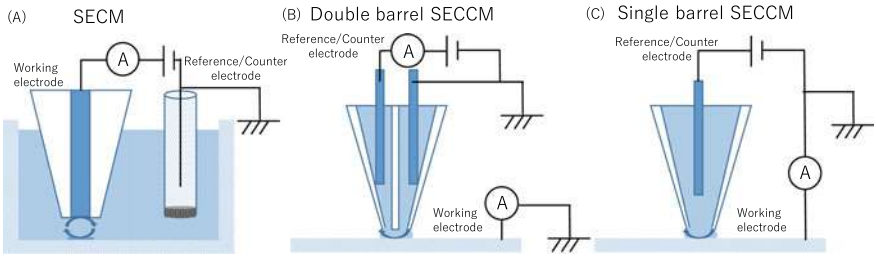

Fig. 4 Schematic of **a** feedback mode SECM, **b** generation collection-mode SECM, and **c** surface interrogation mode SECM

https://www.twirpx.org & http://chemistry-chemists.com

The other main measurement style uses a single-barreled nanopipette [49] filled with an electrolyte solution and an Ag/AgCl electrode (Fig. 4c). The nanopipette was brought into close contact with a sample electrode surface via a liquid meniscus at the nanopipette end. When the meniscus just contacts the surface, the nanopipette is halted by a small capacitive current. The tip height at this point is recorded and electrochemical measurement is performed. Single-barreled SECCM provides high-resolution images because the nanopipette is easily and reliably miniaturized, but is limited to conductive samples.

3.2 *Measurement Principle and Application*

MacPherson and coworkers characterized the facet-dependent heterogeneous electron transfer rate and the boron-doped level of polished polycrystalline BDD (pBDD) electrodes by SECCM and field-emission scanning electron microscopy [24]. They used three types of electrochemical mediators: outer-sphere (one-electron oxidation of ferrocenylmethyltrimethylammonium ($FcTMA^+$)), inner-sphere (one-electron oxidation of Fe^{2+}), and complex processes with coupled electron transfer and chemical reactions (oxidation of serotonin). Regardless of the mediator, the facet-dependent boron doping level dominantly affected the electrochemical reactivity of the electrodes (Fig. 5). One advantage of SECCM characterization is the prevention of fouling of the scanning probe during the imaging. Recall that SECCM

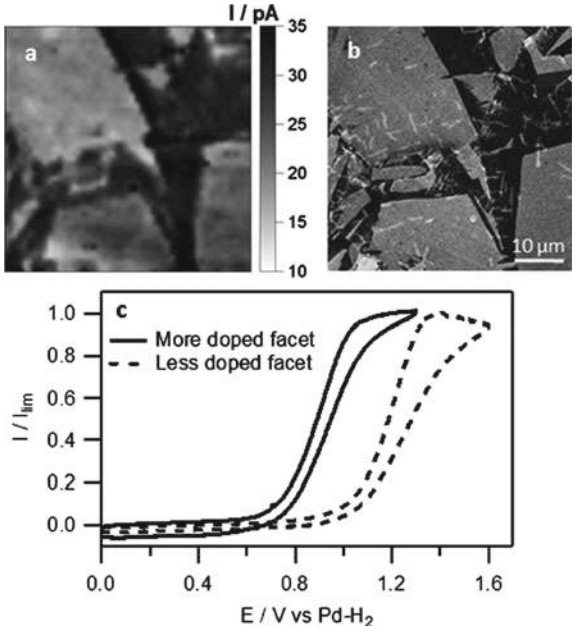

Fig. 5 **a** SECCM image (50 µm × 50 µm) of the oxidation of 2 mM Fe2 + in 0.5 M H2SO4 at 1.2 V versus Pd − H2 (ω = 470 mV). **b** Corresponding field-emission scanning electron microscope image of the same area. **c** CVs recorded on a more- and less-boron-doped facet scanned at 100 mV/s. Adapted with permission from reference 24, Copyright 2016 American Chemical Society

https://www.twirpx.org & http://chemistry-chemists.com

forms a mobile nanoscale electrochemical cell for electrochemical imaging. In microelectrode probing by SECM, the products of serotonin oxidation block the electrode surface and deteriorate the electrodes. In SECCM, serotonin is used as the electrochemical mediator for imaging.

MacPherson's group also characterized the chloride-containing aqueous solvent (electrolyte) window of the pBDD electrodes by SECCM, electron backscatter diffraction, and Raman microscopy [26]. They related the doping level to the termination state and reactivity and found a wider solvent window on an H-terminated surface than on an O-terminated one. On the O-terminated surface, the anodic potential window was greatly diminished by chloride electro-oxidation.

SECCM is a useful tool not only for electrochemical imaging but also for local electrochemical surface modification. MacPherson and coworkers locally oxidized a BDD surface by SECCM, which electrochemically converted the H-terminated surface to an–O-terminated surface [28]. During the BDD oxidation, they applied + 1.5 V at a scan speed of 1.0 mm/s (see left panel of Fig. 6). The electrochemical reactivity was then characterized by scanning the sample surface. As shown in the right panel of Fig. 6, anodic treatment measurably reduced the current of the $Ru(NH)_6^{3+}$ reduction because it partially removed the H-termination layer.

We have developed hopping-mode SECCM for visualizing the facet-dependent electrochemical reactivities of single crystal and unpolished polycrystalline BDDs [50]. Figure 7a shows the measurement scheme of hopping-mode SECCM measurement of the single crystal BDD. To overcome the electrochemical cell distortion introduced by the sample tile effect, a linear sweep voltammogram was measured at all measurement points for characterizing the half-wave potential ($E_{1/2}$) of the facet-dependent reactivity difference. Figure 7b shows the SECCM topography and

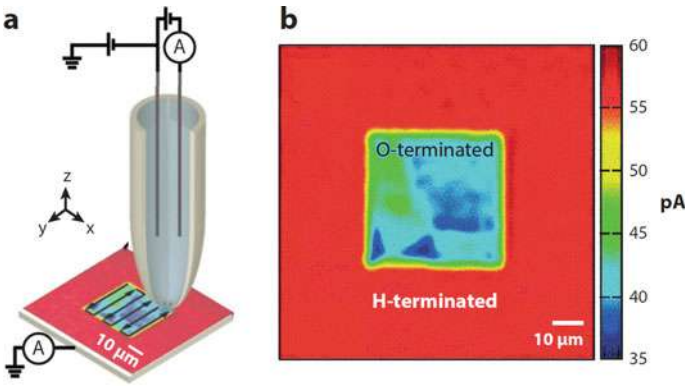

Fig. 6 **a** SECCM setup, showing how a micron-sized capillary locally oxidizes the surface (write: convert H to O) and subsequently reads the resulting surface change. **b** Electrochemical (read) scan of an O-terminated square region on the H-terminated polycrystalline surface by SECCM. The surface was anodically oxidized by biasing at +1.5 V (write) and imaged (read) at −0.3 V using an SECCM probe filled with 2 mM $Ru(NH_3)_6^{3+}$ in 50 mM KNO_3. Adapted with permission from reference 28, with Copyright 2015 The Royal Society of Chemistry

https://www.twirpx.org & http://chemistry-chemists.com

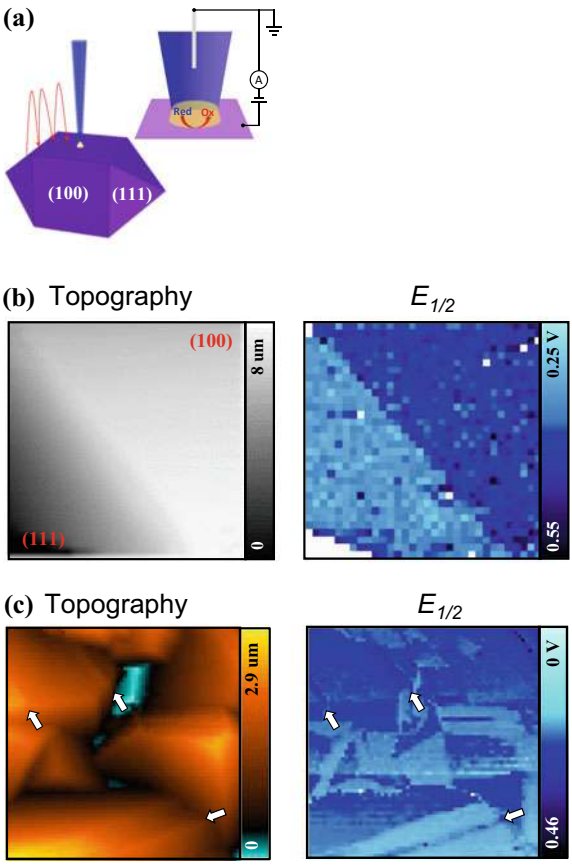

Fig. 7 **a** Schematic of the Hopping-mode SECCM measurements of single-crystal BDDs. (**b**, **c**) Topography (left) and half-wave potential (right) SECCM images on **b** single crystal BDD and **c** polycrystalline H-BDD. Nanopipette filled with 4 mM $K_4[Fe(CN)_6]$ in 0.1 M KCl. Scan sizes were **b** 6 × 6 μm^2 and **c** 10 × 10 μm^2. The CV scan rate was **b** 1 V/s and **c** 10 V/s. Adapted with permission from reference 52, Copyright 2021 American Chemical Society

$E_{1/2}$ images of a single crystal BDD. A larger $E_{1/2}$ was observed on the (100) facet compared to that on the (111) facet, indicative of slower electron-transfer kinetics. This reactivity difference is attributed to boron dopant concentration differences and concurred with those of previous reports [51, 52]. We also characterized the facet-dependent reactivity difference on the unpolished polycrystalline BDD surface. While interrogation of the single crystal surface is extremely useful for fundamental studies, the vast majority of researchers employ polycrystalline BDD. Nearly all SECM and SECCM studies have been carried out on the freestanding polished surface, with limited SECM success on the as-grown material due to the lack of topographical control. Figure 7c shows the SECCM image of the polycrystalline BDD. By the Hopping mode SECCM, we could visualize the microscale surface height difference and the two clear reactivity different responses corresponding to the (100) and (111) facets on the unpolished BDD polycrystalline. In the future, SECCM will be used for unveiling crystal facet-dependent product selectivity of CO_2 reduction reaction on the polycrystalline BDD.

https://www.twirpx.org & http://chemistry-chemists.com

4 Conclusions

This chapter introduced recent progress and applications of SECM and SECCM in the characterization of BDD electrodes. The electrochemical reactivity of BDDs depends on the facet, boron-doped density, surface terminated state, and sp^2 content of the BDDs. Accordingly, SECM and SECCM are useful tools for visualizing the electrochemical reactivity and analyzing the kinetics rate constant of BDDs. Boron doping provides both electrode conductivity and emergent reaction sites on the surface. Observing the electrochemical activity of unpolished BDD, we verified a clear activity difference among the different facets and high reactivity at the grain boundaries. Guidelines for producing proper crystal facets and surface modifications, enabling efficient chemical reactions of BDDs, are expected in the future.

References

1. Takahashi Y, Kumatani A, Shiku H, Matsue T (2017) Scanning probe microscopy for nanoscale electrochemical imaging. Anal Chem 89(1):342–357
2. Bentley CL, Edmondson J, Meloni GN, Perry D, Shkirskiy V, Unwin PR (2019) Nanoscale electrochemical mapping. Anal Chem 91(1):84–108
3. Polcari D, Dauphin-Ducharme P, Mauzeroll J (2016) Scanning electrochemical microscopy: a comprehensive review of experimental parameters from 1989 to 2015. Chem Rev 116(22):13234–13278
4. Amphlett JL, Denuault G (1998) Scanning electrochemical microscopy (SECM): an investigation of the effects of tip geometry on amperometric tip response. J Phys Chem B 102(49):9946–9951
5. Zigah D, Rodriguez-Lopez J, Bard AJ (2012) Quantification of photoelectrogenerated hydroxyl radical on TiO2 by surface interrogation scanning electrochemical microscopy. Phys Chem Chem Phys 14(37):12764–12772
6. Kim J, Renault C, Nioradze N, Arroyo-Currás N, Leonard KC, Bard AJ (2016) Electrocatalytic activity of individual pt nanoparticles studied by nanoscale scanning electrochemical microscopy. J Am Chem Soc 138(27):8560–8568
7. Wei C, Bard AJ, Mirkin MV (1995) Scanning electrochemical microscopy. 31. Application of SECM to the study of charge transfer processes at the liquid/liquid interface. J Phys Chem 99(43):16033–16042
8. Fernández JL, Walsh DA, Bard AJ (2005) Thermodynamic guidelines for the design of bimetallic catalysts for oxygen electroreduction and rapid screening by scanning electrochemical microscopy. M−Co (M:Pd, Ag, Au). J Am Chem Soc 127(1):357–365
9. Fernández-Pérez BM, Izquierdo J, González S, Souto RM (2014) Scanning electrochemical microscopy studies for the characterization of localized corrosion reactions at cut edges of coil-coated steel. J Solid State Electr 18(11):2983–2992
10. Takahashi Y, Shevchuk AI, Novak P, Babakinejad B, Macpherson J, Unwin PR, Shiku H, Gorelik J, Klenerman D, Korchev YE, Matsue T (2012) Topographical and electrochemical nanoscale imaging of living cells using voltage-switching mode scanning electrochemical microscopy. Proc Natl Acad Sci 109(29):11540
11. Holt KB, Bard AJ, Show Y, Swain GM (2004) Scanning electrochemical microscopy and conductive probe atomic force microscopy studies of hydrogen-terminated boron-doped diamond electrodes with different doping levels. J Phys Chem B 108(39):15117–15127

https://www.twirpx.org & http://chemistry-chemists.com

12. Wilson NR, Clewes SL, Newton ME, Unwin PR, Macpherson JV (2006) Impact of grain-dependent boron uptake on the electrochemical and electrical properties of polycrystalline boron doped diamond electrodes. J Phys Chem B 110(11):5639–5646
13. Kai T, Zhou M, Duan Z, Henkelman GA, Bard AJ (2017) Detection of CO_2—in the electrochemical reduction of carbon dioxide in N, N-dimethylformamide by scanning electrochemical microscopy. J Am Chem Soc 139(51):18552–18557
14. Xu J, Natsui K, Naoi S, Nakata K, Einaga Y (2018) Effect of doping level on the electrochemical reduction of CO_2 on boron-doped diamond electrodes. Diam Relat Mater 86:167–172
15. Xu J, Einaga Y (2020) Effect of sp2 species in a boron-doped diamond electrode on the electrochemical reduction of CO_2. Electrochem Commun 115:106731
16. Ahn HS, Bard AJ (2015) Surface interrogation of CoPi water oxidation catalyst by scanning electrochemical microscopy. J Am Chem Soc 137(2):612–615
17. Liang Z, Ahn HS, Bard AJ (2017) A study of the mechanism of the hydrogen evolution reaction on nickel by surface interrogation scanning electrochemical microscopy. J Am Chem Soc 139(13):4854–4858
18. Ahn HS, Bard AJ (2016) Electrochemical surface interrogation of a MoS2 hydrogen-evolving catalyst: In Situ determination of the surface hydride coverage and the hydrogen evolution kinetics. J Phys Chem Lett 7(14):2748–2752
19. Simpson BH, Rodríguez-López J (2015) Electrochemical imaging and redox interrogation of surface defects on operating SrTiO3 photoelectrodes. J Am Chem Soc 137(47):14865–14868
20. Arroyo-Currás N, Bard AJ (2015) Iridium oxidation as observed by surface interrogation scanning electrochemical microscopy. J Phys Chem C 119(15):8147–8154
21. Counihan MJ, Setwipatanachai W, Rodríguez-López J (2019) Interrogating the surface intermediates and water oxidation products of boron-doped diamond electrodes with scanning electrochemical microscopy. ChemElectroChem 6(13):3507–3515
22. Wang Q, Rodriguez-Lopez J, Bard AJ (2009) Reaction of Br 2 with adsorbed CO on Pt, studied by the surface interrogation mode of scanning electrochemical microscopy. J Am Chem Soc 131(47):17046–17047
23. Ebejer N, Schnippering M, Colburn AW, Edwards MA, Unwin PR (2010) Localized high resolution electrochemistry and multifunctional imaging: scanning electrochemical cell microscopy. Anal Chem 82(22):9141–9145
24. Patten HV, Lai SCS, Macpherson JV, Unwin PR (2012) Active sites for outer-sphere, inner-sphere, and complex multistage electrochemical reactions at polycrystalline boron-doped diamond electrodes (pBDD) revealed with scanning electrochemical cell microscopy (SECCM). Anal Chem 84(12):5427–5432
25. Tomlinson LI, Patten HV, Green BL, Iacobini J, Meadows KE, McKelvey K, Unwin PR, Newton ME, Macpherson JV (2016) Intermittent-contact scanning electrochemical microscopy (IC-SECM) as a quantitative probe of defects in single crystal boron doped diamond electrodes. Electroanal 28(10):2297–2302
26. Liu DQ, Chen CH, Perry D, West G, Cobb SJ, Macpherson JV, Unwin PR (2018) Facet-resolved electrochemistry of polycrystalline boron-doped diamond electrodes: microscopic factors determining the solvent window in aqueous potassium chloride solutions. ChemElectroChem 5(20):3028–3035
27. Patten HV, Meadows KE, Hutton LA, Iacobini JG, Battistel D, McKelvey K, Colburn AW, Newton ME, Macpherson JV, Unwin PR (2012) Electrochemical mapping reveals direct correlation between heterogeneous electron-transfer kinetics and local density of states in diamond electrodes. Angew Chem Int Ed 51(28):7002–7006
28. Patten HV, Hutton LA, Webb JR, Newton ME, Unwin PR, Macpherson JV (2015) Electrochemical "read-write" microscale patterning of boron doped diamond electrodes. Chem Commun (Camb) 51(1):164–167
29. Lai SC, Dudin PV, Macpherson JV, Unwin PR (2011) Visualizing zeptomole (electro)catalysis at single nanoparticles within an ensemble. J Am Chem Soc 133(28):10744–10747
30. Guell AG, Ebejer N, Snowden ME, McKelvey K, Macpherson JV, Unwin PR (2012) Quantitative nanoscale visualization of heterogeneous electron transfer rates in 2D carbon nanotube networks. Proc Natl Acad Sci USA 109(29):11487–11492

https://www.twirpx.org & http://chemistry-chemists.com

31. Guell AG, Meadows KE, Dudin PV, Ebejer N, Byers JC, Macpherson JV, Unwin PR (2014) Selection, characterisation and mapping of complex electrochemical processes at individual single-walled carbon nanotubes: the case of serotonin oxidation. Faraday Discuss 172:439–455
32. Guell AG, Ebejer N, Snowden ME, Macpherson JV, Unwin PR (2012) Structural correlations in heterogeneous electron transfer at monolayer and multilayer graphene electrodes. J Am Chem Soc 134(17):7258–7261
33. Patel AN, Collignon MG, O'Connell MA, Hung WO, McKelvey K, Macpherson JV, Unwin PR (2012) A new view of electrochemistry at highly oriented pyrolytic graphite. J Am Chem Soc 134(49):20117–20130
34. Patel AN, McKelvey K, Unwin PR (2012) Nanoscale electrochemical patterning reveals the active sites for catechol oxidation at graphite surfaces. J Am Chem Soc 134(50):20246–20249
35. Kirkman PM, Guell AG, Cuharuc AS, Unwin PR (2014) Spatial and temporal control of the diazonium modification of sp2 carbon surfaces. J Am Chem Soc 136(1):36–39
36. Guell AG, Cuharuc AS, Kim YR, Zhang G, Tan SY, Ebejer N, Unwin PR (2015) Redox-dependent spatially resolved electrochemistry at graphene and graphite step edges. ACS Nano 9(4):3558–3571
37. Zhang G, Tan SY, Patel AN, Unwin PR (2016) Electrochemistry of Fe(3+/2+) at highly oriented pyrolytic graphite (HOPG) electrodes: kinetics, identification of major electroactive sites and time effects on the response. Phys Chem Chem Phys 18(47):32387–32395
38. Lai SCS, Lazenby RA, Kirkman PM, Unwin PR (2015) Nucleation, aggregative growth and detachment of metal nanoparticles during electrodeposition at electrode surfaces. Chem Sci 6(2):1126–1138
39. Chen CH, Ravenhill ER, Momotenko D, Kim YR, Lai SC, Unwin PR (2015) Impact of surface chemistry on nanoparticle-electrode interactions in the electrochemical detection of nanoparticle collisions. Langmuir 31(43):11932–11942
40. Aaronson BDB, Chen CH, Li HJ, Koper MTM, Lai SCS, Unwin PR (2013) Pseudo-single-crystal electrochemistry on polycrystalline electrodes: visualizing activity at grains and grain boundaries on platinum for the Fe2+/Fe3+ redox reaction. J Am Chem Soc 135(10):3873–3880
41. Chen CH, Meadows KE, Cuharuc A, Lai SC, Unwin PR (2014) High resolution mapping of oxygen reduction reaction kinetics at polycrystalline platinum electrodes. Phys Chem Chem Phys 16(34):18545–18552
42. Chen CH, Meadows KE, Cuharuc A, Lai SCS, Unwin PR (2014) High resolution mapping of oxygen reduction reaction kinetics at polycrystalline platinum electrodes. Phys Chem Chem Phys 16(34):18545−18552
43. Chen CH, Jacobse L, McKelvey K, Lai SCS, Koper MTM, Unwin PR (2015) Voltammetric scanning electrochemical cell microscopy: dynamic imaging of hydrazine electro-oxidation on platinum electrodes. Anal Chem 87(11):5782–5789
44. Bentley CL, Kang M, Maddar FM, Li F, Walker M, Zhang J, Unwin PR (2017) Electrochemical maps and movies of the hydrogen evolution reaction on natural crystals of molybdenite (MoS2): basal vs. edge plane activity. Chem Sci 8(9):6583–6593
45. Bentley CL, Unwin PR (2018) Nanoscale electrochemical movies and synchronous topographical mapping of electrocatalytic materials. Faraday Discuss 210:365–379
46. Daviddi E, Gonos KL, Colburn AW, Bentley CL, Unwin PR (2019) Scanning electrochemical cell microscopy (SECCM) chronopotentiometry: development and applications in electroanalysis and electrocatalysis. Anal Chem 91(14):9229–9237
47. Takahashi Y, Kobayashi Y, Wang Z, Ito Y, Ota M, Ida H, Kumatani A, Miyazawa K, Fujita T, Shiku H, Korchev YE, Miyata Y, Fukuma T, Chen M, Matsue T (2020) High-resolution electrochemical mapping of the hydrogen evolution reaction on transition-metal dichalcogenide nanosheets. Angew Chem Int Ed 59(9):3601–3608
48. Tao B, Yule LC, Daviddi E, Bentley CL, Unwin PR (2019) Correlative electrochemical microscopy of Li-Ion (De)intercalation at a series of individual LiMn2 O4 particles. Angew Chem 58(14):4606–4611
49. Inomata H, Takahashi Y, Takamatsu D, Kumatani A, Ida H, Shiku H, Matsue T (2019) Visualization of inhomogeneous current distribution on ZrO2-coated LiCoO2 thin-film electrodes using scanning electrochemical cell microscopy. Chem Commun 55(4):545–548

https://www.twirpx.org & http://chemistry-chemists.com

50. Takahashi Y, Kumatani A, Munakata H, Inomata H, Ito K, Ino K, Shiku H, Unwin PR, Korchev YE, Kanamura K, Matsue T (2014) Nanoscale visualization of redox activity at lithium-ion battery cathodes. Nat Commun 5:5450
51. Liu D-Q, Chen C-H, Perry D, West G, Cobb SJ, Macpherson JV, Unwin PR (2018) Facet-resolved electrochemistry of polycrystalline boron-doped diamond electrodes: microscopic factors determining the solvent window in aqueous potassium chloride solutions. Chemelectrochem 5(20):3028−3035
52. Ando T, Asai K, Macpherson JV, Einaga Y, Fukuma T, Takahashi Y (2021) Nanoscale reactivity mapping of a single-crystal boron-doped diamond particle. Anal Chem. https://doi.org/10.1021/acs.analchem.1c00053
53. Yang N, Yu S, Macpherson JV, Einaga Y, Zhao H, Zhao G, Swain GM, Jiang X (2019) Conductive diamond: synthesis, properties, and electrochemical applications. Chem Soc Rev 48(1):157–204
54. Ivandini TA, Watanabe T, Matsui T, Ootani Y, Iizuka S, Toyoshima R, Kodama H, Kondoh H, Tateyama Y, Einaga Y (2019) Influence of surface orientation on electrochemical properties of boron-doped diamond. J Phys Chem C 123(9):5336–5344

https://www.twirpx.org & http://chemistry-chemists.com

Computational Aspects of Surface and Interface of BDD Electrode

Yoshitaka Tateyama, Zdenek Futera, Yusuke Ootani, Shota Iizuka, and Le The Anh

Abstract Boron-doped diamond (BDD) has attracted much attention from various viewpoints such as superconductivity and electrochemical applications. To understand these characters, first-principles calculation studies based on density functional theory (DFT) have been performed in some decades. Associated with the BDD superconductivity, many calculations of bulk BDD characters such as the electronic states, Boron configurations inside and so on were carried out, providing a reasonable superconductivity mechanism. In contrast, mechanisms of the electrochemical behaviors remain mostly unresolved. Due to the heavy computational costs, most studies examined BDD surfaces in vacuum and the adsorption of some water molecules. These provided some meaningful aspects, but were insufficient to understand the interfacial redox (electron transfer) reactions between the BDD electrode and the aqueous solution. Recently, DFT molecular dynamics calculations of the BDD/water interfaces were performed, which indicated the equilibrium structures and electronic states of the BDD/water interfaces as well as their dependence on the BDD electrode termination. Besides, a theory to understand the interfacial electron transfer mechanism was provided, on the basis of the DFT results. In this chapter, these theoretical analyses via DFT calculations of BDD bulk, surfaces in vacuum and interfaces with water are surveyed. This will give a useful perspective for the future theoretical and computational studies of electrochemical reactions of the BDD electrode, and the other electrode materials as well.

Keywords Boron-doped diamond · Density functional theory · Electrochemistry · Electron transfer · Surface termination

Y. Tateyama (✉) · S. Iizuka · L. T. Anh
Center for Green Research On Energy and Environmental Materials (GREEN), National Institute for Materials Science (NIMS), 1-1 Namiki, Tsukuba 305-0044, Ibaraki, Japan
e-mail: TATEYAMA.Yoshitaka@nims.go.jp

Z. Futera
Faculty of Science, University of South Bohemia, Branisovska 1760, 370 05, Ceske Budejovice, Czech Republic

Y. Ootani
Institute for Materials Research, Tohoku University, 2-1-1 Katahira, Aoba-ku, Sendai 980-8577, Japan

© Springer Nature Singapore Pte Ltd. 2022

Y. Einaga (ed.), *Diamond Electrodes*,
https://doi.org/10.1007/978-981-16-7834-9_5

https://www.twirpx.org & http://chemistry-chemists.com

1 Introduction

1.1 Characteristics of BDD

Carbon diamond is intrinsically an electrical insulator. When Boron with one less electron is doped into the diamond, boron-doped diamond (BDD) can show a p-type semiconductor behavior. Such a semiconductor character has been known for decades. In 2004, it was discovered that the highly doped BDD exhibits the superconductivity with T_c of 4K [1]. Stimulated by this discovery, several computational studies based on density functional theory (DFT) have been conducted to clarify the superconductivity mechanism in bulk BDD [2–7].

There is another class of characteristic in BDD; electrode applications for electrochemical reactions such as electro catalysis, sensors, etc. [8, 9]. BDD has various interesting properties such as large electrochemical window, chemical stability and so on. This electrochemical application was initiated by the works by Swain et al. in the 1990s [10, 11], earlier than the superconductivity trend in fact. In the theoretical side, however, the early stage of DFT calculation studies on the electrochemical aspects has appeared after 2005. This is because, ideally, the interfaces between the BDD electrode and electrolyte solution are to be properly modeled in the calculation, which has been computationally demanding. In fact, most of the computational works so far used the surface models, not explicit interface models. Even the surface models need computational resources, and the DFT calculation analyses have become feasible only about 15 years ago.

In this chapter, we focus on the DFT calculations studies of surfaces and interfaces of BDD electrode from the electrochemical viewpoint. We address the comprehensive survey of this field to indicate what critical issues remain, and to facilitate many future works.

1.2 First-Principles Density Functional Theory Calculation

Before the survey of the BDD calculation results, we briefly explain first-principles calculations based on DFT and Kohn–Sham (KS) scheme. DFT and its extension to the KS equation was developed by Kohn et al. [12, 13]. This theory gives total energy, $E[\{\boldsymbol{R}_\mathrm{I}\}]$, of many-body electron systems in condensed matter as follows.

$$E[\{R_I\}] = \sum_i \left\langle \phi_i \mid -\frac{\nabla^2}{2} \mid \phi_i \right\rangle + \frac{1}{2}\int\int dr dr' \frac{n(r)n(r')}{|r-r'|} + E_{xc}[n] + \sum_I \int dr \frac{Z_I n(r)}{|r-R_I|} + \sum_{I<J} \frac{Z_I Z_J}{|R_I - R_J|} + E_{ext},$$

https://www.twirpx.org & http://chemistry-chemists.com

where ϕ_i and $n(\boldsymbol{r})$ are i-th KS orbital and electron density, respectively. Z_I denotes charge of the I-th ion. $\boldsymbol{r}$ and $\boldsymbol{R}_I$ correspond to the coordinates of electron and I-th ion, respectively. The terms in the right-hand side mean the electronic kinetic energy, electrostatic energy, exchange–correlation energy, electron–ion interaction energy, ion-ion interaction energy and external interaction energy, respectively. One can get the electronic ground state energy by improving KS orbitals to minimize the total energy or solve the KS equation: $\left(-\frac{\nabla^2}{2} + V_{eff}(r)\right)\phi_i(r) = \varepsilon_i\phi_i(r)$, where ε_i is the KS orbital energy.

Once the total energy is obtained for the given atomic structure, the forces exerted on the atoms are calculated. Using these forces, one can relax the structure. The flowchart is summarized in Fig. 1a. In this geometry optimization procedure, no temperature effect is involved so that it is regarded as 0 K simulation. If molecular dynamics (MD) is performed based on the forces at finite temperature, one can get more or less equilibrium atomic configurations at the temperature, which is schematically shown in the upper panel of Fig. 1b. This allows the molecular fluctuations and thus is crucial in dealing with solution like water, where many shallow local minima exist in the potential energy surface (lower panel of Fig. 1b).

There are in fact two streams of the DFT calculation codes; physics side and chemistry side. The DFT codes for the condensed matter physics usually use periodic boundary condition (PBC). This PBC allows the exact treatment of large singe crystal lattice, exploiting the crystal periodicity. However, when lattice defects are examined, the PBC may introduce spurious interactions between the defects. To avoid such artifact, a larger supercell containing many primitive cells is necessary. Therefore, calculation of point defects in bulk BDD may need more than 64 carbon sites, and

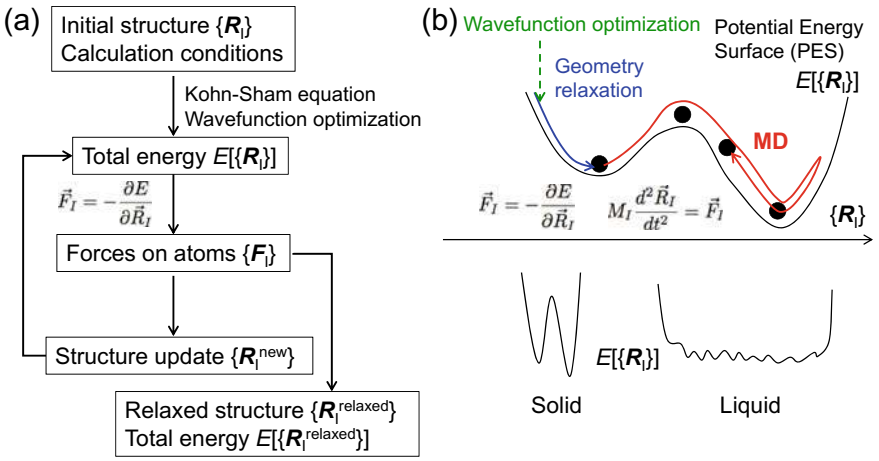

Fig. 1 **a** Flowchart of typical first-principles calculation for geometry relaxation. E, $\{\boldsymbol{R}_I\}$, $\{\boldsymbol{F}_I\}$ denote the total energy, a set of atomic coordinates, a set of forces exerted on atoms, respectively. **b** Potential energy surface (PES) picture for wavefunction optimization, geometry relaxation and molecular dynamics (MD). The lower panel shows the typical PES shapes in solid and liquid

https://www.twirpx.org & http://chemistry-chemists.com

more sites and vacuum region (solution region) are essential for the surface (interface) studies. Yet, DFT calculations provide reasonably accurate relaxed structures. One can calculate the electronic states like the position of the valence band maximum (VBM) and conduction band minimum (CBM) in energy via KS orbital energies, although the choice of the exchange–correlation functional ($E_{xc}[n]$) may affect the accuracy of the band gap. Therefore, a caution is needed when the metal–insulator transition is discussed. However, the typical *p*-type and *n*-type semiconductors can be treated without such care.

2 Computational Analysis of BDD Bulk

2.1 Boron Complex in BDD Bulk

As noted, Boron is an acceptor to carbon diamond for the *p*-type semiconductor. In 2004, it was discovered that highly doped BDD exhibits the superconductivity with T_c of 4K[1]. After the discovery, many DFT-based computational studies have been conducted mainly for understanding the superconductivity mechanism. Most of the works focused on the substitutional doping of boron in the bulk diamond (Fig. 2a) and the electron–phonon coupling on the basis of BCS superconducting theory [2–5]. The papers examined the coupling of phonon with holes at the top of the σ-bonding VBM, in a way similar to another superconducting material MgB_2, which was also found around the same time. However, the three-dimensional nature of the sp^3-hybridized carbon network in diamond leads to a density of states at the Fermi level much weaker than in the quasi-two-dimensional MgB_2 compound. This results in a lower coupling constant in diamond.

As another important issue, the Boron state in the bulk diamond has attracted attention. In addition to substitutional Boron and interstitial Boron, the forms of dimer, cluster, aggregate and the complex with defects have been investigated [6, 14–17]. It is reported that the interstitial Boron is unstable [6] while stable Boron

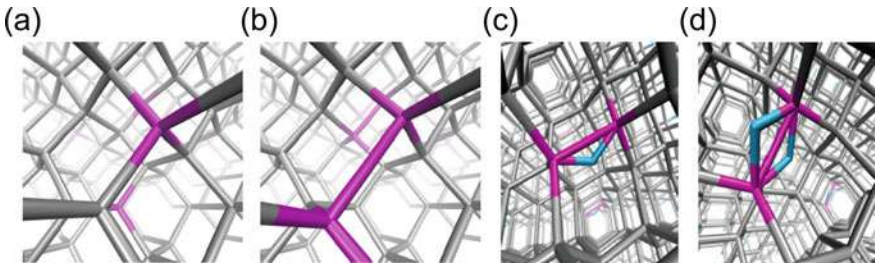

Fig. 2 Schematic pictures of Boron states in bulk carbon diamond; **a** Substitutional single Boron, **b** Boron dimer, **c** B-H-B complex, and **d** B-2H-B complex, where purple and sky-blue pipes correspond to B and H, respectively

https://www.twirpx.org & http://chemistry-chemists.com

dimer (Fig. 2b) is inactive both electronically and vibrationally [14, 16, 17]. Goss et al. demonstrated that certain complexes provide shallower acceptors than substitutional B and the pair of B interstitials does not give rise to the required carriers [18]. The presence of Boron–Hydrogen pair was also suggested as well. It was recently suggested that B-H-B or B-2H-B complexes (Fig. 2c & d) may exist as well thermodynamically, considering the CVD synthesis conditions with large amount of hydrogen, and the former can give the hole carrier [17]. In summary, introduction of substitutional individual Boron is most effective for increasing the whole carriers. Thus, the superconducting transition temperature T_c is not only determined by the B concentration, but also by Boron configurations in the BDD bulk.

3 Computational Analysis of BDD Surface

3.1 Structural and Electronic Properties of BDD Surface

BDD has been used as an electrode in the electrochemical applications. BDD has several characteristics such as wide electrochemical window, low background current, good chemical stability and hardness. The latter three can be originated from bulk modulus and the energy band gap of undoped diamond. There are arguments correlating the large band gap with the electrochemical window. However, this argument is not correct as the band gap does not correspond to the voltage window. Note that even Pt metal surface with no gap has a certain width of window. Hence, the electrochemical window and reactions are rather associated with the surface states.

There have been many DFT-based computational works on carbon diamond surfaces. The representative orientations are (100) and (111) surfaces, and their bare and H-terminated surfaces were well understood. The (100) surface has the dimer-row reconstructions in both bare and H-terminated cases (Fig. 3a & b). The bare (111) surface is known that the Pandy model is the most stable, while (1 × 1) surface is more probable for the H-termination (Fig. 3c & d). Hence, understanding the effects of orientation and termination is the first step of the studies on the BDD surfaces. Then, the dependence of Boron state and position near the surface should be taken into account.

The DFT calculation studies of the BDD surfaces in the early stage used very approximated methods and models: DFT methods with empirical parameters were applied to the H-terminated (100) surface, and slab thickness for the surface model was insufficient. In addition, only the limited conditions were examined so that it is difficult to make a substantial comparison with the experimental observations.

First reasonable DFT calculation studies of the BDD surface were reported by the groups of Tateyama and Larsson in 2014. Futera et al. provided the surface phase diagrams of (100) and (111) surfaces with respect to the H and O chemical potentials. In addition to the bare (100) and (111) surfaces, structural stabilities of major H-, O- and OH-terminations (Fig. 3e & f) were all calculated with the reasonable calculation

https://www.twirpx.org & http://chemistry-chemists.com

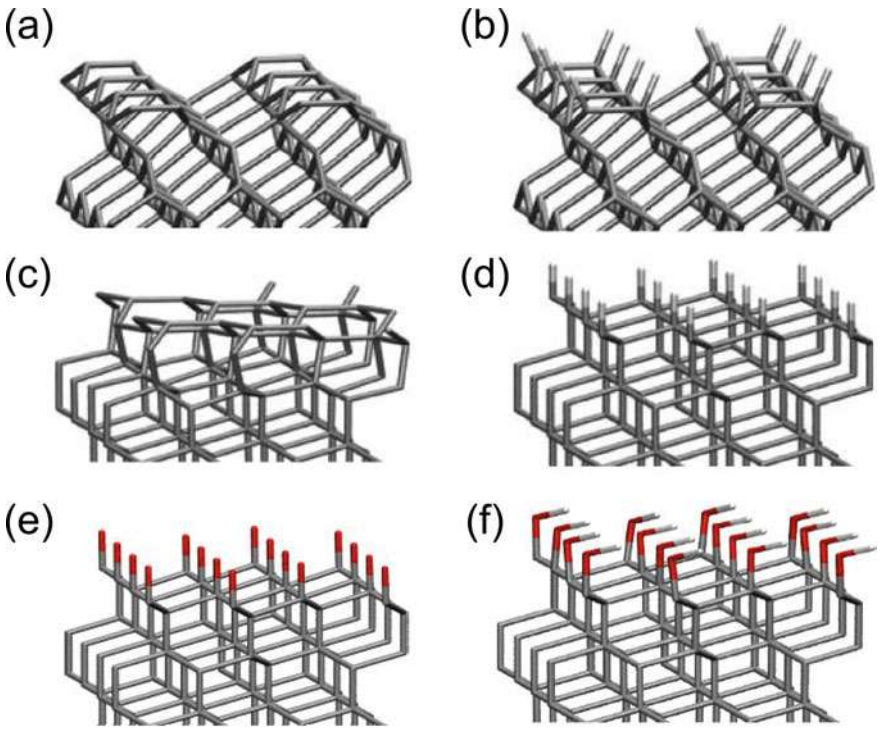

Fig. 3 Schematic pictures of typical diamond surface structures; **a** bare (100)-2 × 1 surface (dimerized surface), **b** H-terminated (100)-2 × 1 surface, (c) bare (111)-2 × 1 surface (Pandy structure), **d** H-terminated (111)-1 × 1 surface, **e** O-terminated (111)-1 × 1 surface and **f** OH-terminated (111)-1 × 1 surface. Carbon, Oxygen and Hydrogen are shown as gray, red and white pipes, respectively

conditions and the slab thickness [17]. Besides, the mixed terminations among H-, O- and OH- were also provided. They also evaluated the band positions of BDD (111) surfaces with respect to the vacuum level and suggested that H-terminated BDD has higher band position in energy than the oxidized ones (O-, OH- terminations). Hassan et al. calculated H-, O (ontop)-, O(bridge)-, OH and NH_2- terminations of BDD (100) surfaces with adsorptions of multiple water molecules (water monolayer) plus the possible reactants [19]. Although the slab thickness looks insufficient, the authors also observed the electron transfer from the H-terminated BDD (100) surface to water adlayer, which is consistent with the band position analysis by Futera et al. [17].

Since then, the Larsson group reported several papers of BDD surfaces; B-position dependence of H adsorption energy on the H-terminated (110) and (111) surfaces, bare (111) surfaces and the surface graphitization, bare and H-terminated (111) surfaces, and O-terminated (111)-1 × 1 surfaces [20–23]. These works focus on the termination stability associated with Boron, rather than mimicking water environment. It should be also noted that the slab thickness of 3–4 bi-layers might be

https://www.twirpx.org & http://chemistry-chemists.com

insufficient for the target effects. The Tateyama group also made some reports on the BDD surfaces in collaboration with the experimentalists [24–27]. The electrolytic corrosion behavior of BDD under the oxidative condition was elucidated via the removal of the OH termination [26]. The mechanism of surface hydrogenation of BDD by cathodic reduction below ca. -2 V versus SHE (standard hydrogen electrode) was discussed with the reaction with the generated H atom radical [27]. The reconstruction stability of BDD (111) surfaces depending on the Boron position in the depth direction was recently examined [28].

The other groups also provided interesting DFT calculation results. Graphitization of bare BDD (111) surfaces induced by B-doping was demonstrated by Lu et al. [29]. Though the supercell used in the calculations is rather small, the proposed concept was very interesting. Yao et al. discussed the Boron dimer stability on the (100)-2 × 1 and (111)-2 × 1 surfaces [30]. Shen et al. examined the electron affinity of BDD (100) surfaces depending on the terminations including B-termination, and proposed that B-terminated oxidized diamond (001) surface might have negative electron affinity (NEA) [31].

3.2 Water Adsorption on BDD Surface

The electrochemical measurement usually utilizes aqueous solution. In this respect, a certain coverage of water molecules on top of the surface termination is essential for understanding the microscopic mechanisms. Herein, the DFT calculations studies with such modeling are briefly introduced.

As mentioned above, Hassan et al. used the calculation models with the H_2O monolayer on the terminations [19]. Futera et al. examined more realistic BDD (111) surface/water interfaces, which will be described in the next section. Jaimes et al. examined the H_2O molecule adsorption on the H-terminated BDD (111)-1 × 1 surfaces and confirmed the hydrophobic nature [32]. However, as described above, the DFT calculation analyses of the realistic interfaces with water are still quite lacking.

4 Computational Analysis of BDD / Water Interface

4.1 BDD / Water Interface Under Equilibrium

The electrochemical reaction usually needs electrolyte solution as well as electrode. For the former, the aqueous solution is the most representative. Before the electrochemical reaction, the interfacial region between the BDD electrode and water is expected to reach thermal equilibrium. The computational simulations should reproduce this equilibrium situation. At finite temperature, water molecules always

https://www.twirpx.org & http://chemistry-chemists.com

fluctuate so that the water dynamics is to be taken into account. In this respect, MD sampling simulation of realistic interface system is indispensable. Around the solid / liquid interfaces, the local interfacial dipole may affect the behaviors of the space charge layer in the BDD electrode side and the electric double layer in the aqueous solution side. As the classical force field (FF) cannot treat such charge polarization properly, MD simulation based on the DFT total energy and force is ideal, whereas DFT-MD simulations are computationally demanding. Therefore, only limited studies have addressed DFT-MD analyses of realistic BDD / water interface systems.

Futera et al. first reported a comprehensive investigation of BDD / water interface systems via extensive DFT-MD simulations [17]. They examined (111) and (100) interfaces with water by using supercells with ca. 1 nm × 1 nm × 5 nm edges, which contain 256 Carbon sites, 105 water molecules and the termination moieties. For the terminations, H-, O-, OH-terminations and their mixtures were treated. The size of the water region was controlled by referring the water density at the ambient condition. The supercells with H- and OH- terminations are shown in Fig. 4a. These procedures provide a general workflow for the reasonable simulations of solid/liquid interfaces. In addition, they examined the dependence of the Boron concentration between ca. 0.8% (2B substitution) and 5.5% (14B substitution). To reproduce the

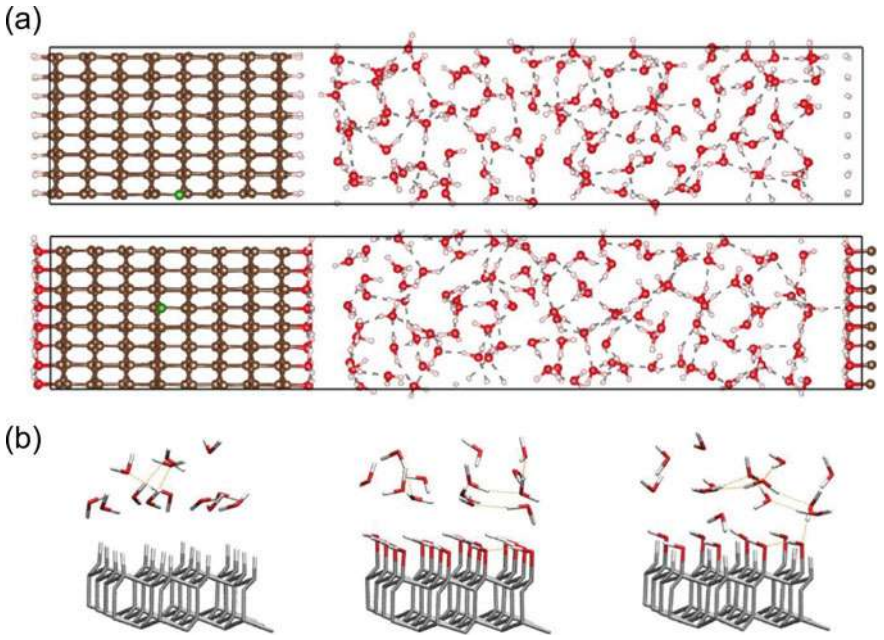

Fig. 4 **a** Schematic pictures of supercells for the first-principles calculations of the BDD (111) / water interfaces with H- and OH-terminations. **b** Snapshots of the equilibrium states of the BDD(111) / water interfaces; (left) H-termination, (center) OH-termination, (right) (OH, H) half-and-half termination

https://www.twirpx.org & http://chemistry-chemists.com

high electronic conductivity, they adopted scattered single B doping via substitution. Choice of the DFT calculation condition for the electronic states is also crucial for the accurate sampling. In their work, BLYP functional, known to be good for water, was used for the exchange–correlation functional [33, 34]. To simulate the room temperature condition, Nose thermostat at 298.15 K was used [35].

Firstly, the termination phase diagram depending on the H and O chemical potentials was calculated in the vacuum BDD surfaces, and then the energetically probable surface terminations were evaluated. The evaluation of the phase diagram for the BDD/water interface systems was then carried out, where H-, O-, OH- terminations as well as the half-and-half terminations of (H, O), (H, OH) and (O, OH) of the (111) interfaces were examined via DFT-MD sampling. The radial distribution analyses between the BDD terminations and the water molecules demonstrated that H-termination does not have hydrogen bonding with the interfacial water, suggesting the hydrophobic character. The 100% OH termination also looks hydrophobic because the flat hydrogen bonding network is formed within the termination. In the other cases, there are more or less hydrogen bonding between the termination and the interfacial water so that the hydrophilic character appears (Fig. 4b). Such hydrophobicity and hydrophilicity were used for how close the reactant in aqueous solution can approach to the BDD electrode, which may influence the redox performance.

4.2 Redox Reactivity of BDD Electrode in Aqueous Solution

Direct DFT-MD simulations of the solid/liquid interfaces provide the characteristics of the interfacial electronic states, related to the space charge layer and the electric double layer. The ideal set-up is using larger supercell containing salt such as NaCl under control of artifact net dipole in the system, which is still difficult with the typical computational resources nowadays. However, the electronic states of the solid/liquid interfaces without salt can provide useful information about the interfacial redox reactions. Note that methods that can deal with the salt concentration and the bias effects via continuum models have been recently proposed [36], which may give more detailed insights in future.

The DFT-MD investigations demonstrated that the interfacial potential and the interfacial band offset between BDD and bulk water significantly change, depending on the terminations [17, 25]. In the H-termination case, the BDD band position in energy is higher than the other terminations. The VBM and CBM of BDD are approximately located at above −4 and 0 eV with respect to the approximate vacuum level. This means that the H-terminated BDD (111) surface may have a capability of reducing proton and NEA. In fact, it is well known that the NEA exhibits upon the H-terminated (111) diamond. The equilibrium structural and electronic properties at probable BDD/water interfaces were clarified theoretically with this paper [17].

On top of that, Futera et al. provided a way of understanding the possibility of electrochemical reaction, using the equilibrium band offset and the hypothetical bias effect. With the band edge pinning assumption in which the VBM relation between

https://www.twirpx.org & http://chemistry-chemists.com

the BDD electrode and water are kept around the interfaces (black circles in Fig. 5a & b), the application of bias can be regarded as the change of the Fermi energy of the BDD bulk part (Fig. 5b). As BDD is a p-type semiconductor, the Fermi energy is basically close to the VBM. Thus, bias effect can be approximated by the change of the VBM position in the BDD bulk region (Fig. 5b).

The authors also treated the interfacial electron transfer in terms of Fermi golden rule: When the energies of initial and final states match with each other, the electron transfer, in other words redox reaction occurs. When the target redox reaction has the redox potential between 0 and 1.2 V versus SHE (standard hydrogen electrode), the VBM of H-terminated BDD is already close to this redox energy level (H-BDD in Fig. 5a). Therefore, the band bending is expected to be small for these redox reactions (H-BDD in Fig. 5b), indicating that smooth reversible redox reaction can realize. On the other hand, oxidized BDD has a deeper VBM position in energy (OH-BDD in Fig. 5a). Thus, for the electron transfer, a large upper shift of VBM is necessary, which leads to the larger band bending (OH-BDD in Fig. 5b). In this case, the distance of electron tunneling becomes longer so that the interfacial electron transfer is suppressed. This explanation is a promising theory to explain the experimental observations of termination dependence of BDD for the interfacial redox reactions.

In the work by Futera et al., the experimental results of $[Fe(CN)_6]^{4-/3-}$ redox reactions were referred. In this case, the correlation between the negatively charged

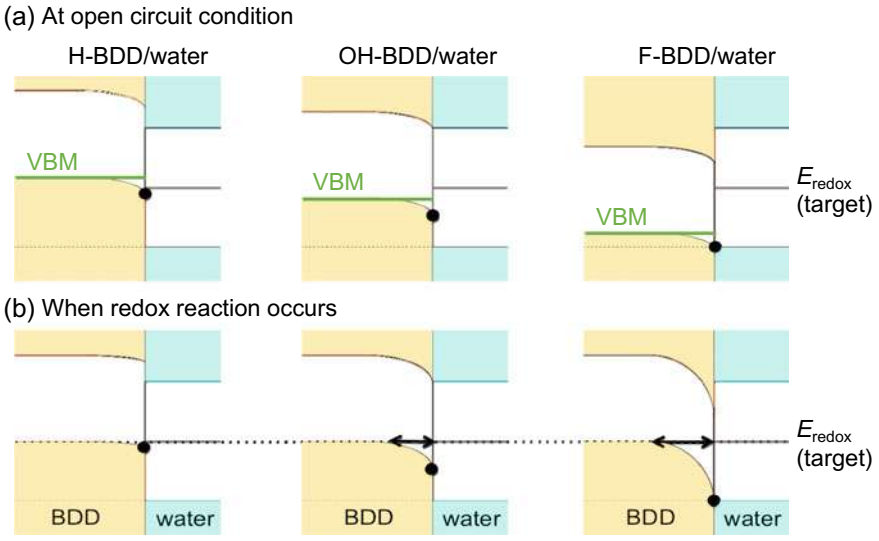

Fig. 5 Schematic pictures of the alignment of the electronic band structures at the BDD (111) / water interfaces; **a** at the open circuit condition, and **b** when redox reaction occurs. The target redox potential is shown by E_{redox}. Black circle shows the pining position of the BDD valence band maximum (VBM) at the interface. When the bias is applied to induce the redox reactions, the Fermi energy (~ VBM) is shifted to match with E_{redox}. The arrows in (**b**) indicate the band bending widths, corresponding to the barriers for electron tunneling

https://www.twirpx.org & http://chemistry-chemists.com

ion and the surface termination was inferred as well. As oxidized BDD surfaces are expected to be slightly negative, the anion cannot approach to the BDD electrode so that the interfacial redox reaction is suppressed. This is a different mechanism from the band offset aspect. If this mechanism is dominant, the BDD electrochemical behavior with the cation redox species should be opposite.

To prove which mechanism is dominant between the band offset theory and the surface charge effect, Yamaguchi et al. performed the crucial comparative experiment as well as DFT-MD analyses [25]. The authors used dopamine (DA), 4-ethylcatecol (EC), 3,4-dihydroxyphenylacetic acid (DOPAC) which has the same moiety with the same redox potential, while the terminations have positive, neutral and negative charges, respectively (Fig. 6a). The experimental cyclic voltammogram (CV) was shown in Fig. 6b. In this work, as grown H-terminated, oxidized (mainly OH-terminated) and Fluorine (F)-terminated BDD surfaces were compared. The main difference among the CV curve is the termination dependence, not the charge of the redox species. The redox irreversibility is larger in the F-terminated BDD than the H-terminated one. The anodic peak current also decreases in the order of H-, OH- and F-terminated BDD. Besides, no peak was observed in the measured potential range for DOPAC on the F-terminated BDD. These imply that the band offset effect depending on the termination plays a major role.

The authors then performed the DFT-MD calculations of the BDD/water interfaces with the targeted three-types (H-, OH-, and F-) of terminations, where the 100% termination was assumed. The supercells were shown in Fig. 4a. The radial distribution functions from terminated H or F to water hydrogen and oxygen indicate that F-BDD has more hydrophobicity than the others. The origin is likely to be the electrostatic repulsion between the terminated F and water oxygen, which increases

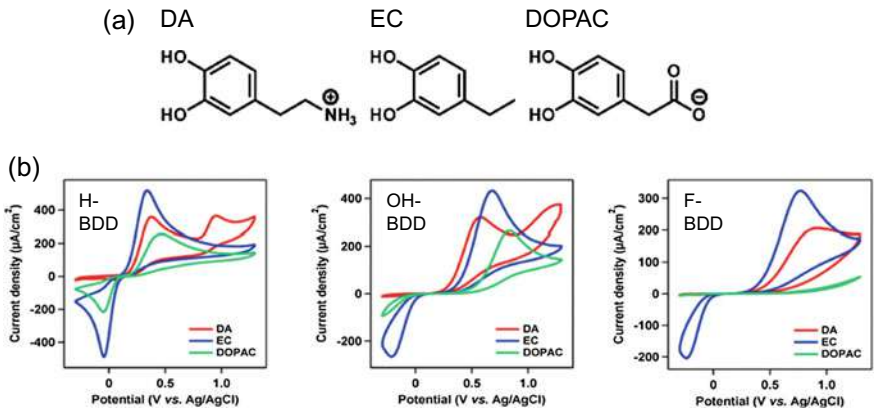

Fig. 6 **a** Molecular structures of dopamine (DA), 4-ethylcatechol (EC), and 3,4-dihydroxyphenylacetic acid (DOPAC), examined in the experiment [25]. These have catechol structure in common, leading to the same redox potential. On the other hand, the charges are +1, 0 and -1, thus different. **b** Cyclic voltammogram of DA, EC, and DOPAC with the BDD electrode with hydrogenated-, oxidized- and fluorinated terminations

https://www.twirpx.org & http://chemistry-chemists.com

the spatial gap across the interface. This argument can hold for the anionic analyte, DOPAC, accounting for the considerable positive shift of anodic current peak and increase in the irreversibility for the F-BDD electrode.

Besides, the calculated projected densities of states (PDOSs) suggest the electronic origin as well. As shown in Fig. 5a, compared to the water band, the H-BDD band position is so high, while the F-BDD band is very low. If the band edge pinning scheme, as described above, is hold, the "interfacial" band bending, shown by the black arrows in Fig. 5b, is much larger in F-BDD when the Fermi energy aligns with the target redox potential (Fig. 7a, b). This long tunneling region (Fig. 7) for electron in the BDD subsurface suppresses the interfacial electron transfer between BDD and the target redox species, and thus increases the irreversibility in the CVs. At present, these scenarios account for most of the observations.

Comparison between the (100) and (111) interfaces was also carried in the same group. Ivanti et al. indicated that the H-terminated (111)-1 × 1 interfaces has slightly higher band position of BDD, leading to intrinsic electron transfer to water region and thus demonstrated the surface transfer doping models [24]. The calculated O- and OH-terminated interfaces increase the difference between the (111) and (100) orientation, and the band edge position of the (100) is found sufficiently lower than the (111). Following the band bending scenario described above, the oxidized (100) surfaces are less reactive than the (111), which is in qualitative agreement with the experiments.

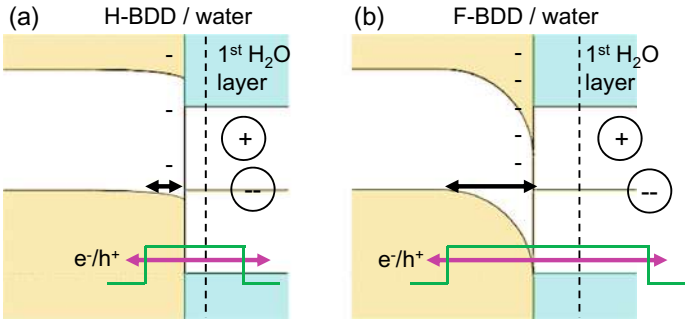

Fig. 7 Schematic picture of interfacial redox (electron transfer) mechanism based on the Fermi golden rule. The dominant factor is the band bending width in the BDD side, which is related to the length of electron tunneling (black arrow). H-terminated BDD will have shorter length than F-terminated on due to the intrinsic band alignment. In the solution side, hydrophobicity and hydrophilicity can affect the tunneling length, and the electrostatic interaction between the surface charge and the charge of the reactant may also affect

https://www.twirpx.org & http://chemistry-chemists.com

5 Summary

In this chapter, we introduce the DFT calculation studies to date of BDD properties, especially focusing on the surfaces and the aqueous interfaces of BDD electrodes from the electrochemical viewpoints.

We first present the basics of first-principles calculations and briefly introduce the studies of the BDD bulk for understanding of the superconductivity mechanisms and exploration of the Boron states. For the latter, substitutional, interstitial, dimerized, aggregated and hydrogen-complexed Boron were examined. To keep the electronic conductivity, it is suggested that increase of substitutional Boron or metastable B-H-B complex by control of the synthesis condition is suggested to be desirable.

In the DFT surface studies, structural stability of the surface reconstruction in the vacuum, the dependence of termination and Boron position were examined so far. The electronic states related to the electron transfer were also discussed. The H-terminated BDD surface is found to have high position of the band structure in energy, which is connected to NEA.

Finally, the first-principles calculation studies with realistic interface models are introduced. It is suggested that the band alignment between the BDD electrode and water significantly depends on the termination as well as the orientations of the BDD surfaces. In general, H-terminated BDD has higher band position in energy, while oxidized or fluorinated terminations show the lower position. To explain the electrochemical reactivity, the band bending scheme coupled with Fermi golden rule is proposed: The bias control to the target redox potential is connected to the variation of the Fermi energy in the BDD bulk, together with the band alignment pinning at the BDD/water interface. This will imply the width of the band bending (a sort of space charge layer), which plays a barrier role for the electron tunneling. The charge of the surface termination affects the distance of interfacial water from the surface (a sort of electric double layer), which can contribute to the barrier as well. The evaluation of electron transfer ability based on this theory reasonably demonstrated the experimental observation; higher reversibility and reactivity for H-terminated BDD, while lower in F-terminated BDD.

The surface termination of the BDD electrode has a great influence on its electrochemical properties, so it is important to control the surface to be suitable for each application. Furthermore, surface modification by functional molecules is also important not only for better understanding of BDD's fundamentals but also for a variety of applications.

References

1. Ekimov EA, Sidorov VA, Bauer ED, Mel'nik NN, Curro NJ, Thompson JD, Stishov SM (2004) Superconductivity in diamond. Nature 428(6982):542–545. https://doi.org/10.1038/nature02449

https://www.twirpx.org & http://chemistry-chemists.com

2. Lee KW, Pickett WE (2004) Superconductivity in boron-doped diamond. Phys Rev Lett 93(23):1–4. https://doi.org/10.1103/PhysRevLett.93.237003
3. Boeri L, Kortus J, Krogh Andersen O (2006) Normal and superconducting state properties of b-doped diamond from first-principles. Sci Technol Adv Mater 7(SUPPL. 1):S54–S59. https://doi.org/10.1016/j.stam.2006.04.009
4. Shirakawa T, Horiuchi S, Ohta Y, Fukuyama H (2007) Theoretical study on superconductivity in boron-doped diamond. J Phys Soc Japan 76(1):1–9. https://doi.org/10.1143/JPSJ.76.014711
5. Moussa JE, Cohen ML (2008) Constraints on T(c) for superconductivity in heavily boron-doped diamond. Phys Rev B 77(6). https://doi.org/10.1103/PhysRevB.77.064518
6. Oguchi T (2006) Electronic structure of B-doped diamond: a first-principles study. Sci Technol Adv Mater 7(SUPPL. 1):S67–S70. https://doi.org/10.1016/j.stam.2006.03.008
7. Klein T, Achatz P, Kacmarcik J, Marcenat C, Gustafsson F, Marcus J, Bustarret E, Pernot J, Omnes F, Sernelius BE, Persson C, da Silva AF, Cytermann C (2007) Metal-insulator transition and superconductivity in boron-doped diamond. Phys Rev B 75(16). https://doi.org/10.1103/PhysRevB.75.165313
8. Fujishima A, Einaga Y, Rao TN, Tryk DA (2005) Diamond electrochemistry. Elsevier Inc
9. Einaga Y (2010) Diamond electrodes for electrochemical analysis. J Appl Electrochem 40(10):1807–1816. https://doi.org/10.1007/s10800-010-0112-z
10. Swain GM, Ramesham R (1993) The electrochemical activity of boron-doped polycrystalline diamond thin film electrodes. Anal Chem 65(4):345–351. https://doi.org/10.1021/ac00052a007
11. Swain GM (1994) The use of CVD diamond thin films in electrochemical systems. Adv Mater 6(5):388–392. https://doi.org/10.1002/adma.19940060511
12. Kohn W, Sham LJ (1965) Self-consistent equations including exchange and correlation effects. Phys Rev 140:A1133. https://doi.org/10.1103/PhysRev.140.A1133
13. Parr RG, Yang W (1989) Density-functional theory of atoms and molecules. Oxford University Press
14. Bourgeois E, Bustarret E, Achatz P, Omnes F, Blase X (2006) Impurity dimers in superconducting B-doped diamond: experiment and first-principles calculations. Phys Rev B 74(9). https://doi.org/10.1103/PhysRevB.74.094509
15. Oguchi T (2008) Electronic structure of boron-doped diamond with B-H complex and B pair. Sci Technol Adv Mater 9(4):20–24. https://doi.org/10.1088/1468-6996/9/4/044211
16. Long R, Dai Y, Guo M, Yu L, Huang B, Zhang R, Zhang W (2008) Effect of B-complexes on lattice structure and electronic properties in heavily boron-doped diamond. Diam Relat Mater 17(3):234–239. https://doi.org/10.1016/j.diamond.2007.12.019
17. Futera Z, Watanabe T, Einaga Y, Tateyama Y (2014) First principles calculation study on surfaces and water interfaces of boron-doped diamond. J Phys Chem C 118(38):22040–22052. https://doi.org/10.1021/jp506046m
18. Goss JP, Briddon PR (2006) Theory of boron aggregates in diamond: first-principles calculations. Phys Rev B 73(8). https://doi.org/10.1103/PhysRevB.73.085204
19. Hassan MM, Larsson K (2014) Effect of surface termination on diamond (100) surface electrochemistry. J Phys Chem C 118(40):22995–23002. https://doi.org/10.1021/jp500685q
20. Zou Y, Larsson K (2016) Effect of boron doping on the CVD growth rate of diamond. J Phys Chem C 120(19):10658–10666. https://doi.org/10.1021/acs.jpcc.6b02227
21. Zhao S, Larsson K (2019) First principle study of the attachment of graphene onto different terminated diamond (111) surfaces. Adv Condens Matter Phys. https://doi.org/10.1155/2019/9098256
22. Wang X, Wang C, Shen X, Larsson K, Sun F (2019) DFT calculations of energetic stability and geometry of O-terminated B- and N-doped diamond (1 1 1)-1 × 1 surfaces. J Phys Condens Matter 31(26). https://doi.org/10.1088/1361-648X/ab152f
23. Wang X, Song X, Wang H, Qiao Y, Larsson K, Sun F (2020) Selective control of oxidation resistance of diamond by dopings. ACS Appl Mater Interfaces 12(37):42302–42313. https://doi.org/10.1021/acsami.0c11215
24. Ivandini TA, Watanabe T, Matsui T, Ootani Y, Iizuka S, Toyoshima R, Kodama H, Kondoh H, Tateyama Y, Einaga Y (2019) Influence of surface orientation on electrochemical properties

https://www.twirpx.org & http://chemistry-chemists.com

of boron-doped diamond. J Phys Chem C 123(9):5336–5344. https://doi.org/10.1021/acs.jpcc.8b10406
25. Yamaguchi C, Natsui K, Iizuka S, Tateyama Y, Einaga Y (2019) Electrochemical properties of fluorinated boron-doped diamond electrodes: via fluorine-containing plasma treatment. Phys Chem Chem Phys 21(25):13788–13794. https://doi.org/10.1039/c8cp07402j
26. Kashiwada T, Watanabe T, Ootani Y, Tateyama Y, Einaga Y (2016) A study on electrolytic corrosion of boron-doped diamond electrodes when decomposing organic compounds. ACS Appl Mater Interfaces 8(42):28299–28305. https://doi.org/10.1021/acsami.5b11638
27. Kasahara S, Natsui K, Watanabe T, Yokota Y, Kim Y, Iizuka S, Tateyama Y, Einaga Y (2017) Surface hydrogenation of boron-doped diamond electrodes by cathodic reduction. Anal Chem 89(21):11341–11347. https://doi.org/10.1021/acs.analchem.7b02129
28. Le TA, Catalan FCI, Kim Y, Einaga Y, Tateyama Y (2021) Boron position-dependent surface reconstruction and electronic states of boron-doped diamond (111) surfaces: an Ab-Initio study. Phys Chem Chem Phys 23(29):15628–15634. https://doi.org/10.1039/d1cp00689d
29. Lu C, Yang H, Xu J, Xu L, Chshiev M, Zhang S, Gu C (2017) Spontaneous formation of Graphene on diamond (111) driven by B-doping induced surface reconstruction. Carbon NY 115:388–393. https://doi.org/10.1016/j.carbon.2017.01.030
30. Yao X, Feng Y, Hu Z, Zhang L, Wang EG (2013) Dimerization of boron dopant in diamond (100) epitaxy induced by strong pair correlation on the surface. J Phys Condens Matter 25(4). https://doi.org/10.1088/0953-8984/25/4/045011
31. Shen W, Pan Y, Shen S, Li H, Zhang Y, Zhang G (2019) Electron affinity of boron-terminated diamond (001) surfaces: a density functional theory study. J Mater Chem C 7(31):9756–9765. https://doi.org/10.1039/c9tc02517k
32. Jaimes R, Vazquez-Arenas J, González I, Galván M (2016) Delimiting the boron influence on the adsorptive properties of water and OH radicals on H-terminated boron doped diamond catalysts: a density functional theory analysis. Surf Sci 653:27–33. https://doi.org/10.1016/j.susc.2016.04.018
33. Becke AD (1988) Density-fnnctional exchange-energy approximation with correct asymptotic behavior. J Chem Phys 38(6):3098–3100. https://doi.org/10.1063/1.1749835
34. Lee C, Yang W, Parr RG (1988) Development of the Colle-Salvetti correlation-energy formula into a functional of the electron density. Phys Rev B 37(2):785–789. https://doi.org/10.1103/PhysRevB.37.785
35. Nosé S (1984) A unified formulation of the constant temperature molecular dynamics methods. J Chem Phys 81(1):511–519. https://doi.org/10.1063/1.447334
36. Nishihara S, Otani M (2017) Hybrid solvation models for bulk, interface, and membrane: reference interaction site methods coupled with density functional theory. Phys Rev B 96(11):115429. https://doi.org/10.1103/PhysRevB.96.115429

https://www.twirpx.org & http://chemistry-chemists.com

Porous Diamond Electrodes and Application to Electrochemical Capacitors

Takeshi Kondo

Fabrication methods of boron-doped diamond (BDD) electrodes with large specific surface areas are reviewed specifically in terms of their application to electrochemical capacitors including an electric double-layer capacitor (EDLC) or supercapacitor. As a bottom–up approach, quartz glass fibers were employed as a removable template for BDD deposition to obtain BDD hollow fiber membrane/wool. As a top–down approach, two-step heat treatment was developed as a simple and versatile method for the fabrication of porous BDD electrodes. This technology can be used for the fabrication of porous BDD whisker pillar arrays having a hierarchical nanostructured surface. In addition, BDD powder and boron-doped nanodiamond (BDND) were prepared as conductive diamond powders with a large specific surface area. The cyclic voltammetry of BDND electrodes with a symmetric two-electrode system in 1 M H_2SO_4 showed a cell voltage of 1.8 V, which was much larger than that of activated carbon (AC), whereas the double-layer capacitance was at a similar level. In addition, a decrease in the capacitance was suppressed at the BDND electrode compared with the AC electrode. Based on these properties, the BDND electrode was found to be useful as an electrode material of an aqueous EDLC with high energy and power densities.

1 Introduction

An electric double-layer capacitor (EDLC) is also called a supercapacitor and is an energy storage device with a simple structure in which an electrolyte and a separator are sandwiched between two electrodes (Fig. 1). When voltage is applied between the

T. Kondo (✉)
Department of Pure and Applied Chemistry, Faculty of Science and Technology, Tokyo University of Science, Noda, Japan
e-mail: t-kondo@rs.tus.ac.jp

© Springer Nature Singapore Pte Ltd. 2022

Y. Einaga (ed.), *Diamond Electrodes*,
https://doi.org/10.1007/978-981-16-7834-9_6

https://www.twirpx.org & http://chemistry-chemists.com

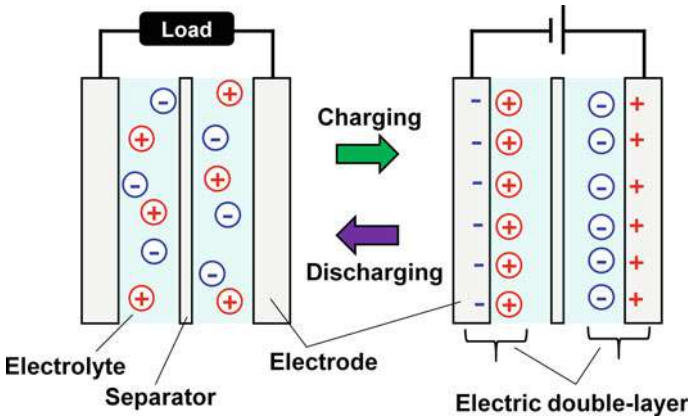

Fig. 1 Schematic illustration of charging/discharging of EDLC

electrodes, electrolyte ions are adsorbed on the electrode surface and electric double-layers are formed to store the electric charge to the device. The accumulated charge can be easily discharged by the desorption of the adsorbed ions from the electrode surface. Based on this mechanism, the EDLC exhibits several advantages such as rapid charging–discharging, high power density, and long cycle-life durability. This is in contrast to secondary batteries in which charging–discharging occurs based on the redox reaction of the active material at the electrode [1–4]. However, EDLCs generally have a disadvantage of low energy density, and thus, improvement of the energy density is desired. Since the energy that can be stored in an EDLC is represented by $CV^2/2$ (C: electric double-layer capacitance and V: cell voltage), to obtain a higher energy density, both the capacitance and cell voltage must be increased. Since the capacitance is directly proportional to the electrode surface area where adsorption of the electrolyte ions occurs, activated carbon (AC) with a large specific surface area is commonly used as the electrode material. Additionally, to increase the cell voltage, organic electrolytes having a wide potential window (such as a propylene carbonate solution) are used. In contrast, the use of an aqueous electrolyte for EDLC has some advantages, such as large capacitance, high conductivity, safety due to nonflammability of the electrolyte solution, and durability to invasion of water to the device [4, 5]. However, the aqueous electrolyte has a significant drawback that the potential window is narrow and the cell voltage is smaller than that when the organic electrolyte is used.

Boron-doped diamond (BDD) is known to exhibit a wide potential window in aqueous electrolytes [6–8]. Therefore, if the BDD can be used as an electrode material for EDLC, a large cell voltage can be expected even when an aqueous electrolyte is used for a device with high energy and power densities. However, a BDD thin-film electrode is basically flat with a small specific surface area and cannot be practically applied to the EDLC. Honda has developed nanohoneycomb diamond electrodes by performing the oxygen plasma etching of a flat BDD electrode surface using a

https://www.twirpx.org & http://chemistry-chemists.com

highly ordered nanoporous alumina membrane as a mask [7, 9–11]. Although such a treatment may cause increased defects on the surface of a diamond electrode, the characteristic of a wide potential window was maintained. The double-layer capacitance (C_{dl}) of the nanohoneycomb diamond electrode estimated by electrochemical impedance spectroscopy in 0.1 M H_2SO_4 was 1.97×10^{-3} F cm^{-2}, which was improved greatly from that of the as-deposited BDD electrode (1.29×10^{-5} F cm^{-2}), whereas the potential window estimated by cyclic voltammetry (CV) was basically unchanged [7]. Therefore, it is considered that the enhancement of specific surface area by an appropriate method is effective for creating a diamond electrode exhibiting a large double-layer capacitance, while maintaining a wide potential window in an aqueous solution. BDD is a very hard material and not easy to process. In addition, there are severe limitations in the synthesis method (i.e., chemical vapor deposition (CVD)) and its conditions. BDD with a large specific surface area is not obtained easily by direct synthesis. In this chapter, BDD materials with large specific surface areas toward application to EDLC fabricated by template methods (bottom–up approach) and etching methods (top–down approach) are introduced. In addition, conductive diamond powder materials, e.g., BDD powder (BDDP) and boron-doped nanodiamond (BDND), and their electrochemical properties for EDLC are described.

2 Fabrication of Porous BDD by Bottom-Up Approach

2.1 Preparation of Porous BDD Using Template Substrate Materials

The use of a three-dimensional template substrate is one effective way to fabricate a BDD material with a large specific surface area. Usually, a polycrystalline BDD thin-film with a thickness of several micrometers to several tens of micrometers is grown on a flat substrate via CVD. When a substrate material having a three-dimensional structure is used instead of a flat substrate, it is considered that a porous BDD electrode that reflects the shape of the substrate material can be produced, although the thickness of the BDD thin-film to be formed on the substrate must be rather thin compared to the dimension of the template structure. Thus, materials of micrometer-sized structures with sufficient thermal and chemical stabilities that can withstand the CVD process are considered to be suitable for a template substrate [12–21].

https://www.twirpx.org & http://chemistry-chemists.com

2.2 Preparation of BDD Hollow Fibers Using Quartz Glass Fiber Materials as Substrates

BDD hollow fiber membrane (BDD–HFM) [22] and BDD hollow fiber wool (BDD–HFW) [23] were prepared using a quartz glass filter and wool, respectively, as a porous substrate having high thermal and chemical stability. The quartz glass filter used in this study was commercially available and consisted of quartz glass fibers with a diameter of 0.4–2 μm and a length of 100 μm or longer. The quartz glass wool consisted of quartz glass fiber with a diameter of 3–3.5 μm. Although these materials could sustain the CVD process, they can be removed chemically by immersion in hydrofluoric acid after BDD film deposition, so that they can be used as a removable template.

The quartz glass filter paper was immersed in 0.5 g/L nanodiamond dispersion for seeding, and then BDD thin-film was deposited on the quartz glass fiber surface by a microwave plasma-assisted CVD method (MPCVD) with a microwave power of 1300 W and a carrier hydrogen gas flow rate of 400 sccm and a pressure of 50 Torr. A mixed solution of 70% trimethoxyborane/methanol and acetone (B/C atomic concentration ratio was 20,000 ppm) was used as the carbon/boron source. The CVD stage temperature was 500 and 800 °C for BDD–HFM and –HFW, respectively. After BDD deposition, the quartz glass fiber of the substrate was removed by immersion in a concentrated HF/HNO_3 solution (1:1, mol/mol) (Fig. 2) [22, 23].

Figure 3 shows the scanning electron microscopy (SEM) images of BDD–HFM [22]. It can be seen that the BDD hollow fibers did not separate from each other even after the quartz glass fiber template was removed by etching, and the hollow fibers were coalesced to form a continuous network structure. The inner diameter of the hollow fiber was constant, reflecting the diameter of the quartz fiber substrate, and the outer diameter increased with BDD deposition time. The wall thickness of the hollow fiber was relatively large at the upper part (plasma side) of the membrane and decreased toward the lower part during the CVD process. This is likely because the carbon source concentration in the gas phase of the voids between the quartz fibers during CVD decreases with the depth from the top surface of the membrane. On the other hand, in the case of BDD–HFW, BDD was found to be deposited on the quartz fiber surface in the entire quartz glass wool. This is likely because the gap between the quartz glass fibers of the wool was sufficiently wide (Fig. 4). Thus, it was confirmed that quartz glass fiber is useful as a removable template material for BDD deposition by MPCVD.

To investigate the electrochemical properties of BDD–HFM and –HFW, test electrodes were prepared by attaching these materials to a conductive carbon tape, and then CV was recorded in 0.1 M H_2SO_4. From the result of CV at 10 mV s^{-1}, the BDD–HFM and –HFW were found to show a large C_{dl} of about 13 F g^{-1} [22, 23]. Thus, it was confirmed that these materials can be used as electrochemical electrodes with a large specific surface area. However, the potential window in the aqueous electrolyte estimated in the three-electrode system was about 1.5–2 V, which is considerably smaller than that expected as a BDD electrode (ca. 3.5 V). This is due to the presence

https://www.twirpx.org & http://chemistry-chemists.com

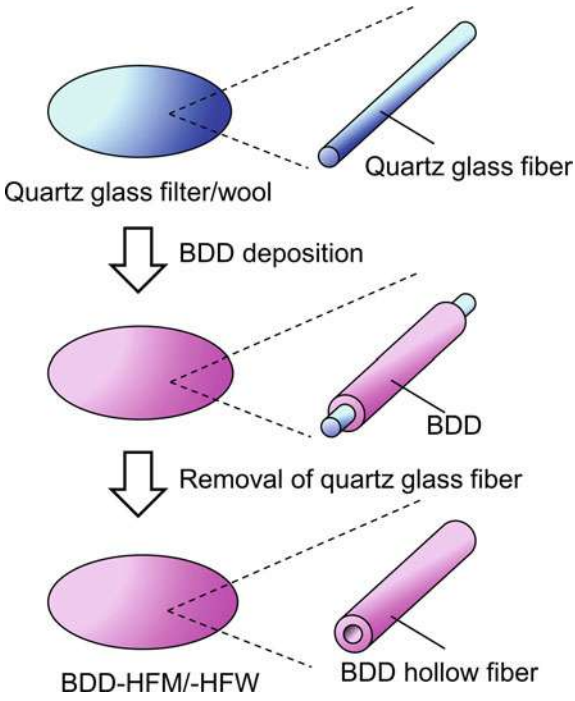

Fig. 2 Fabrication of BDD-HFM/HFW. Reprinted from [23], Copyright 2012, with permission from Materials Research Society of Japan

of a large amount of sp^2 carbon impurities, which cannot be effectively removed by etching with hydrogen plasma during the CVD process due to the three-dimensional structure.

Although fabrication of a BDD electrode with a large specific surface area using a template substrate is a simple method, there is a problem that the growth rate and crystal quality of BDD tend to be inhomogeneous due to the complicated shape of the substrate causing inhomogeneous contact with the hydrogen plasma, carbon concentration in the gas phase, and local temperature during CVD. In addition, whether or not the shape of the template can be reflected to the final product depends on the thickness of the BDD thin-film deposited on the template. Therefore, if the conditions for deposition of a high-quality, and thin BDD thin-film can be achieved, it may be possible to fabricate a BDD electrode with a large specific surface area using a template material having a submicrometer-sized porous structure.

https://www.twirpx.org & http://chemistry-chemists.com

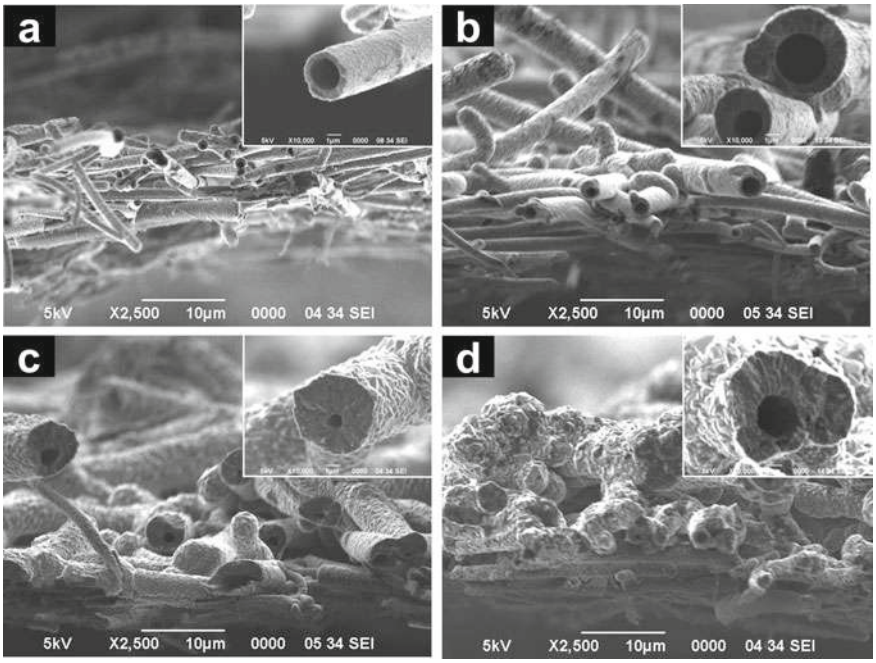

Fig. 3 SEM images of BDD-HFM. Reprinted from [22], Copyright 2009, with permission from Elsevier

3 Fabrication of Porous BDD via Top–Down Approach

3.1 Fabrication of Porous BDD by Etching Treatments

In contrast to the bottom-up approach using a template substrate, top–down approaches using etching treatments of a flat BDD thin-film surface are also an effective way to fabricate BDD electrodes with a large specific surface area. Diamond is a chemically inert material; however, its surface can be decomposed by oxidation, e.g., a reaction with oxygen to form carbon dioxide. For example, a diamond surface can be oxidized by contact with oxygen plasma to form oxygen termination, but decomposition of diamond can proceed in the depth direction by long-term oxygen plasma treatment and can be applied to fabrication of micro-/nanostructures on the surface. A nanohoneycomb diamond electrode can be obtained by etching a BDD surface with oxygen plasma using a highly ordered nanoporous alumina membrane mask [7, 9–11]. It has also been reported that vertically aligned diamond nanowires can be fabricated using diamond nanoparticles as a mask dispersed on the surface of a BDD thin-film [24]. Vertically aligned diamond whiskers prepared by reactive ion etching (RIE) of a flat BDD surface without a mask have also been reported by Terashima [25]. Steam activation [26] and catalytic etching [27, 28] have been reported for the

https://www.twirpx.org & http://chemistry-chemists.com

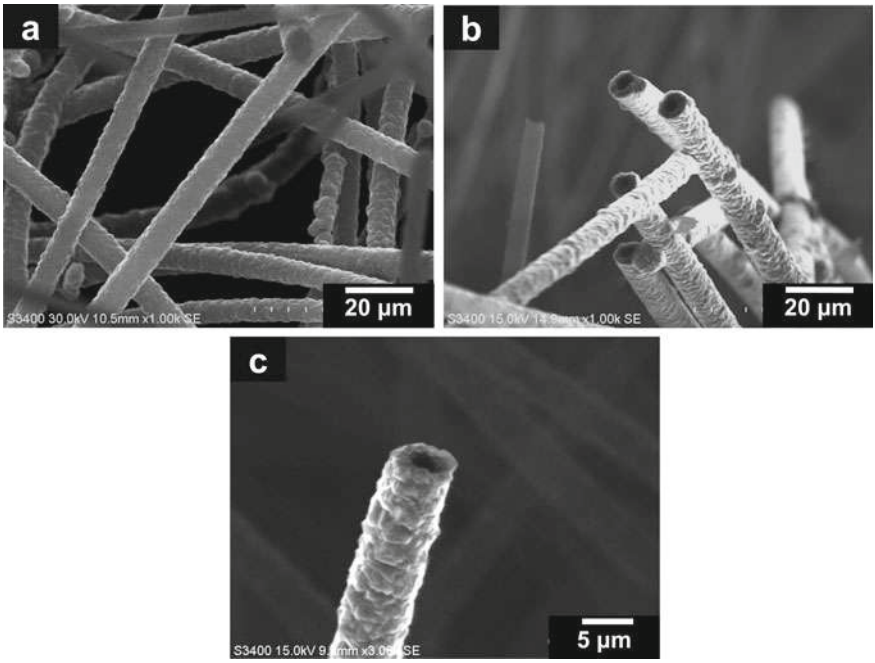

Fig. 4 SEM images of BDD-HFW. Reprinted from [23], Copyright 2012, with permission from Materials Research Society of Japan

fabrication of porous BDD surfaces. Since a conventional (flat) BDD thin-film is used as a starting material of such a top–down method, porous BDD electrodes with relatively high crystal quality containing little sp^2 carbon impurities are expected to be generated. In addition, it is advantageous that a submicrometer-sized structure can be introduced by top–down methods.

3.2 Preparation of a Porous BDD Electrode by a Two-Step Heat Treatment Method

Although etching treatments using an appropriate mask is useful for fabrication of porous BDD electrodes with good reproducibility, the size of the mask limits the area of the electrodes produced. In this respect, a fabrication method without using a mask is useful. Therefore, we have developed a two-step heat treatment method to fabricate porous BDD electrodes [8]. In the two-step heat treatment method, the surface of the BDD is first graphitized by heat treatment in an argon atmosphere, and then the graphitic component is decomposed by oxidation via heat treatment in air to obtain a porous BDD electrode (Fig. 5a) [8].

https://www.twirpx.org & http://chemistry-chemists.com

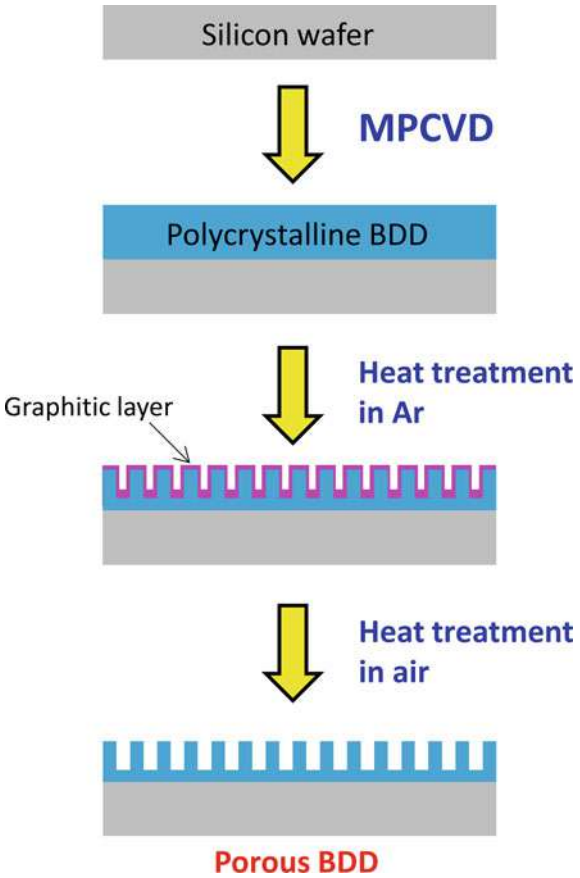

Fig. 5 Schematic illustration of porous BDD electrode fabrication process via two-step heat treatment. Reprinted from [8], Copyright 2014, with permission from Elsevier

At first, a BDD thin-film prepared by MPCVD was heat-treated at 1000 °C in an argon gas flow using a quartz tube furnace to graphitize the BDD surface. In addition to obvious changes in morphology of the BDD surface observed from the SEM images (not shown), the Raman spectra showed a remarkable increase in the D (1330 cm^{-1}) and G (1590 cm^{-1}) bands derived from the formation of sp^2 carbon components after the first heat treatment (Fig. 5b) [8]. After subsequent heat treatment in air at 425 °C with a muffle furnace, the sample surface was found to be porous, and the Raman spectra showed decreases in the D and G band intensities, suggesting that the sp^2 carbon component formed by the first heat treatment was selectively removed by the second heat treatment.

Figure 6 shows the SEM images of the porous BDD thin-film prepared by various durations of the first heat treatment (graphitization) [8]. The surface was found to be roughened in homogeneously depending on the crystallographic orientation of the facet even when the treatment time was 3 h. After an 8-h treatment, roughening with a triangular texture and the formation of reverse-pyramidal pits were observed

https://www.twirpx.org & http://chemistry-chemists.com

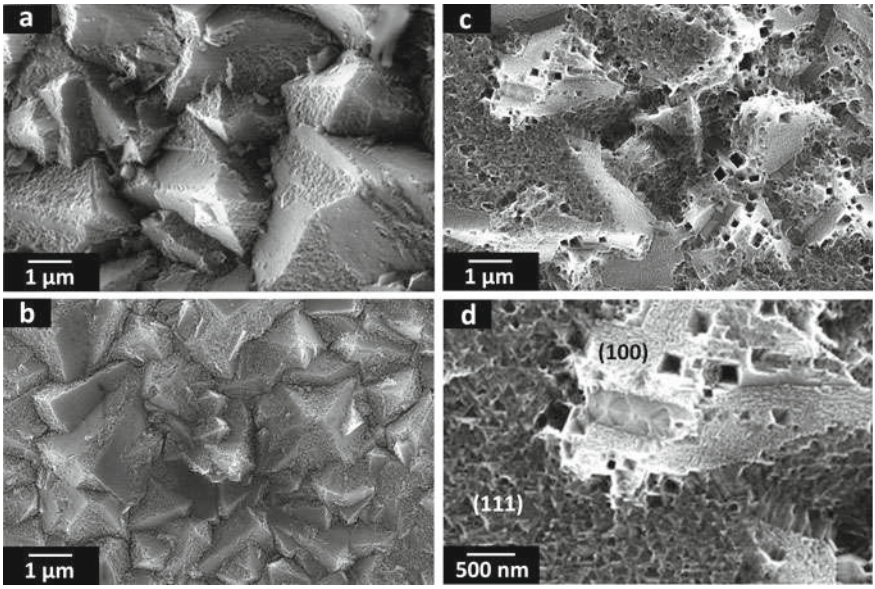

Fig. 6 SEM images of porous BDD electrode surface after graphitization for **a** 3, **b** 6, and **c** and **d** 8 h. Reprinted from [8], Copyright 2014, with permission from Elsevier

on the (111) and (100) crystal facets. It is considered that this behavior is based on the anisotropic phase transition of the diamond surface to graphite in the first heat treatment with respect to the crystal facet. It has been proposed that heat graphitization of diamond (111) planes undergo C (111)-(2 × 1) structure and then transition to graphite (001) planes [29, 30]. This transition is considered to occur at both the (111) and (100) facets, also in the present case, resulting in the crystal face-dependent morphological changes described above [8]. This two-step heat treatment contains only simple processes and has several advantages as a fabrication method for porous BDD electrodes: no mask, catalysis, or residual chemicals are used, no pretreatment or posttreatment is required, and no special instrument is needed. Moreover, unlike plasma etching methods, heat treatment is basically an isotropic process, and thus the diamond surface is expected to be treated uniformly even though the treated diamond material has a three-dimensional structure.

Figure 7a shows the CV of an as-deposited BDD electrode and a porous BDD electrode prepared by the two-step heat treatment (graphitization treatment time was 12 h) in 1 M Na_2SO_4 [8]. The potential window of the porous BDD electrode was as wide as ca. 3 V, slightly narrower than that of the as-deposited BDD electrode. This could be because the amount of sp^2 carbon impurities is minor and the active sites for oxygen and hydrogen evolution reactions are few on the surface of the porous BDD electrode prepared by this method. In contrast, the double-layer charging current was found to remarkably increase after the treatment, indicating that the increase in specific surface area was reflected in the electrochemical properties of the

https://www.twirpx.org & http://chemistry-chemists.com

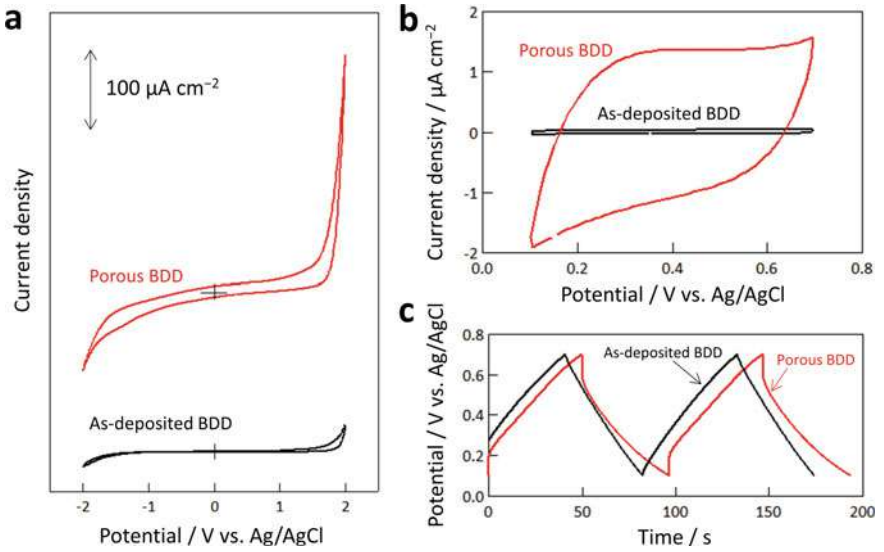

Fig. 7 **a** and **b** CV curves for as-deposited and porous BDD electrodes measured in 1 M Na_2SO_4 at potential sweep rate of 10 mV s^{-1}. Potential sweep region was **a** from − 2 to + 2 V and **b** from + 0.1 to + 0.7 V versus Ag/AgCl. **c** Galvanostatic charge–discharge curve for as-deposited and porous BDD electrode measured in 1 M Na_2SO_4 at constant current of 3.5 nA (as-deposited BDD) and 100 nA (porous BDD). Reprinted from [8], Copyright 2014, with permission from Elsevier

electrode. The C_{dl} of the porous BDD electrode was calculated from the CV recorded in the potential range from +0.1 to +0.7 V versus Ag/AgCl to be 137 μF cm^{-2}, much greater than that of the as-deposited BDD electrode (3.5 μF cm^{-2}) (Fig. 7b) [8]. The C_{dl} calculated from the slope of the galvanostatic charge–discharge curve (Fig. 7c) was 4.7 μF cm^{-2} for the as-deposited BDD electrode (constant current: 3.5 nA and dV/dt: 10.6 mV s^{-1}), and 140 μF cm^{-2} for the porous BDD electrode (constant current: 100 nA and dV/dt: 10.1 mV s^{-1}) [8], which were equivalent to those estimated from CV. From the above results, it is shown that the two-step heat treatment method is a simple and highly flexible method for increasing the specific surface area of a diamond electrode and thus increases the electric double-layer capacitance, while maintaining a comprehensive potential window.

3.3 Fabrication of Diamond Electrodes with Hierarchical Nanostructures

Preparation of porous BDD electrodes using a template substrate material (bottom-up approach) is useful for creating a micrometer-sized three-dimensional structure. On the other hand, top–down approaches, e.g., using plasma etching can impart a submicrometer-sized structure to the BDD thin-film surface. Thus, combining these

https://www.twirpx.org & http://chemistry-chemists.com

two approaches is considered to be an effective way to fabricate a BDD electrode surface with hierarchical nanostructures [31]. To examine whether such an idea is effective, a BDD pillar array (BDD-PA) was prepared by deposition of a BDD thin-film on a silicon pillar array substrate, followed by pore formation by the two-step heat treatment, and nanowhisker formation by RIE to obtain a hierarchically nanostructured BDD electrode. The silicon pillar array was prepared by depositing a mask pattern via photolithography and performing RIE with a SF_6 plasma using a deep RIE system. Typically, the prepared pillars have a diameter of 10 μm, a height of 50 μm, and a pitch between pillars of 20 μm [31]. A BDD thin-film was then deposited by MPCVD on the silicon pillar array substrate to obtain BDD-PA. The BDD-PA was subjected to two-step heat treatment to form a porous surface to prepare porous BDD-PA (P-BDD-PA). Nanowhiskers were formed on the BDD, P-BDD, BDD-PA and P-BDD-PA surfaces using RIE with O_2 plasma according to the report by Terashima [25] to obtain BDD whiskers (BDDW), P-BDDW, BDDW-PA, and P-BDDW-PA, respectively. Figure 8 shows SEM images of BDD, P-BDD, BDDW, and P-BDDW [31]. Submicrometer-sized pores are seen to be formed on the surface of the polycrystalline BDD having micrometer-sized grains after the two-step heat treatment. Furthermore, RIE with O_2 plasma was found to form nanowhiskers with a size of several tens of nanometers on the treated BDD surface. From this result, it was found that hierarchical nanostructures can be imparted by performing the two-step heat treatment, followed by nanowhisker formation. Figure 9 shows SEM images of BDD-PA, P-BDD-PA, and P-BDDW-PA prepared using the silicon pillar array substrate [31]. Pore formation by a two-step heat treatment and nanowhisker formation by RIE were confirmed on both the upper and side surfaces of the BDD

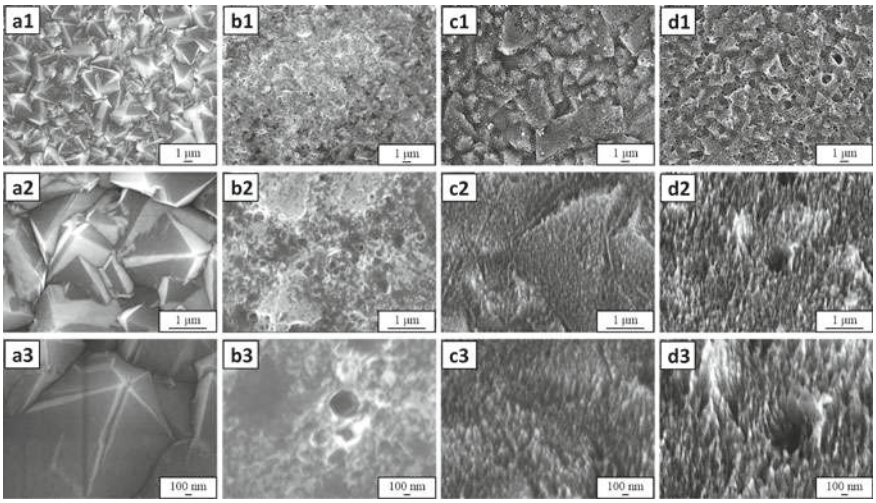

Fig. 8 SEM images of (a1-a3) BDD, (b1-b3) P-BDD, (c1-c3) BDDW, and (d1-d3) P-BDDW surfaces with various magnifications. Reprinted from [31], Copyright 2017, with permission from Elsevier

https://www.twirpx.org & http://chemistry-chemists.com

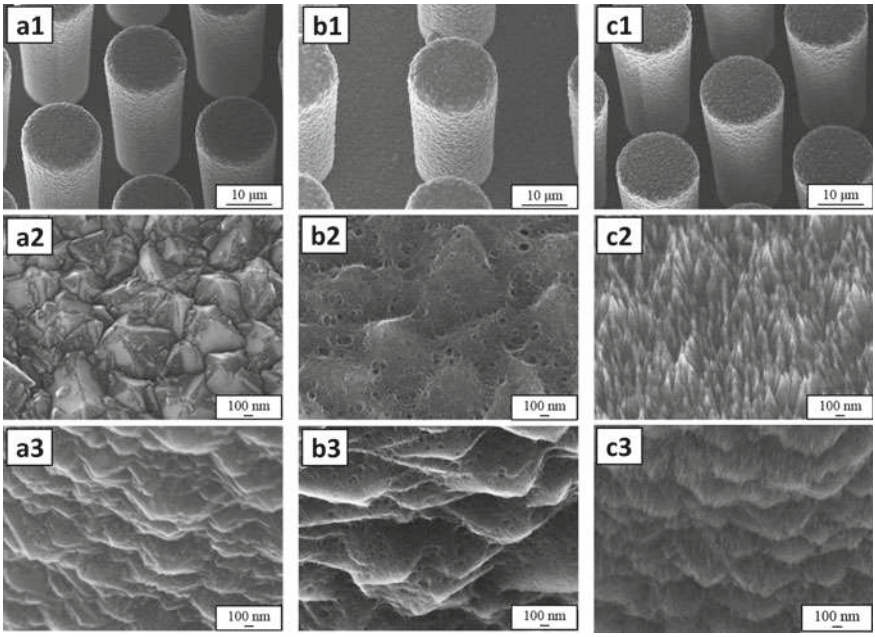

Fig. 9 SEM images of (a1-a3) BDD-PA, (b1-b3) P-BDD, and (c1-c3) P-BDDW-PA. (a1, b1, c1) Low-magnification images, (a2, b2, c2) top surface of a pillar, and (a3, b3, c3) side surface of a pillar. Reprinted from [31], Copyright 2017, with permission from Elsevier

pillars, and it was found that these nanostructures can be generated on the entire BDD-PA surface.

Figure 10 shows CVs of BDD-PA, P-BDD-PA and P-BDDW-PA electrodes in 1 M Na_2SO_4 [31]. Even after the two-step heat treatment and nanowhisker formation, a wide potential window of 3 V and flat electric double-layer charging current was found to be shown, indicating that the characteristics of the BDD electrode were maintained after these treatments. On the other hand, the current value in the double-layer region increased as the two-step heat treatment and nanowhisker formation were found to be enhanced. The C_{dl} of BDD, BDD-PA, P-BDD-PA, and P-BDDW-PA calculated using the CV anodic current at + 0.2 V versus Ag/AgCl were 15, 75, 350, and 2809 $\mu F\,cm^{-2}$, respectively. Therefore, the specific surface areas of the BDD materials were shown to be effectively increased by imparting hierarchical nanostructures and enabling large electric double-layer capacitance, while maintaining a wide potential window up to 3 V in aqueous electrolytes.

https://www.twirpx.org & http://chemistry-chemists.com

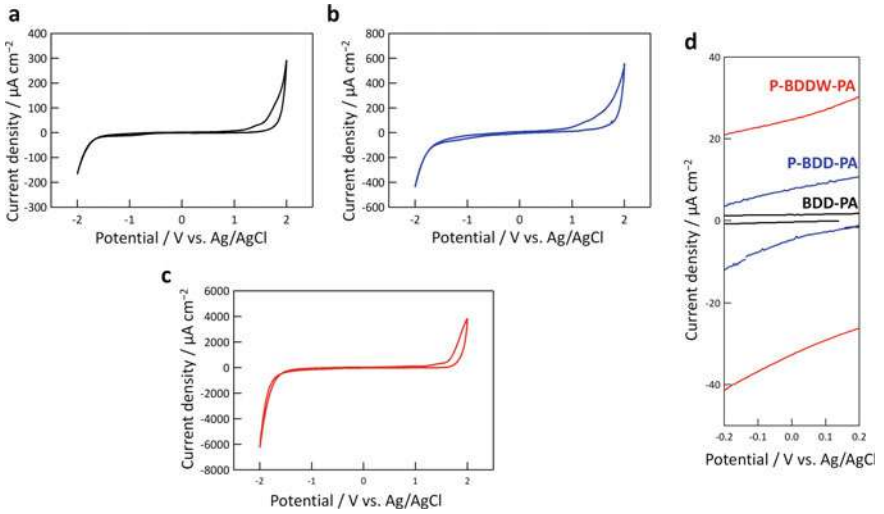

Fig. 10 CV curves measured in 1 M Na_2SO_4 for the **a** BDD-PA, **b** P-BDD-PA, and **c** P-BDDW-PA electrodes. The potential sweep rate was 10 mV s^{-1}. **d** Comparison of CV curves measured for the BDD-PA, P-BDD-PA and P-BDDW-PA electrodes in a narrow potential range (double-layer region). Reprinted from [31], Copyright 2017, with permission from Elsevier

4 Applications of Conductive Diamond Powders and Nanoparticles to EDLC

4.1 Application of BDD Powder (BDDP) to EDLC

We have described various methods for the fabrication of porous BDD electrodes including template substrates and etching technologies. Although these methods have been shown to be effective in increasing the specific surface area of BDD electrodes, they are not sufficiently practical for applications of BDD to an electrode material for EDLC widely. Since diamond is a hard material, it is difficult to fabricate devices with various shapes and sizes even if a large specific surface area material can be obtained based on BDD thin-films. Therefore, we prepared BDDP and boron-doped nanodiamond (BDND) as conductive diamond powder materials and investigated their electrochemical properties for applications to EDLC. BDDP and BDND have a relatively large specific surface area, and electrodes can be produced by coating an ink containing BDDP or BDND on a current collector, so that devices with various shapes and sizes can be fabricated. They are also suitable for flexible devices. Briefly, BDDP was obtained by deposition of a BDD layer on the surface of a commercially available diamond powder substrate by MPCVD [32–34]. A detailed fabrication method and characterization of BDDP are described in Chap. 7.

A test electrode for electrochemical investigations of BDDP was prepared as follows. First, BDDP was dispersed in a 30% ethanol aqueous solution to prepare an

https://www.twirpx.org & http://chemistry-chemists.com

ink, which was cast on a glassy carbon electrode, a current collector. After drying, a Nafion solution was cast on the outermost surface to obtain a test electrode. A test electrode of AC was also prepared using an ink containing AC and acetylene black (8:1, w/w) [34].

Figure 11 shows CV in 1 M H_2SO_4 with a symmetric two-electrode system using AC and BDDP (particle sizes were 150, 350, and 3500 nm denoted here as BDDP-150, -350, and -3500, respectively) electrodes [34]. In the case of AC, the cell voltage can be applied up to 0.8 V without causing a Faradaic reaction, however, when a voltage higher than that was applied, a reaction current due to the electrolysis of water was observed. On the other hand, it was found that BDDP can apply the cell voltage up to 1.5 V without Faradaic current. This is considered to reflect the feature of BDD showing a wide potential window in aqueous electrolytes. Figure 12a features a plot showing the C_{dl} calculated from the CV with respect to the scan rate. As the particle size of BDDP decreases, the C_{dl} was found to increase due to the increase in the specific surface area. However, the C_{dl} of BDDPs were quite small compared to that of AC with a very large specific surface area. Figure 12b shows the scan rate dependence of the relative capacitance when the capacitance at 10 mV s^{-1} is 100. While the relative capacitance of AC decreased significantly with

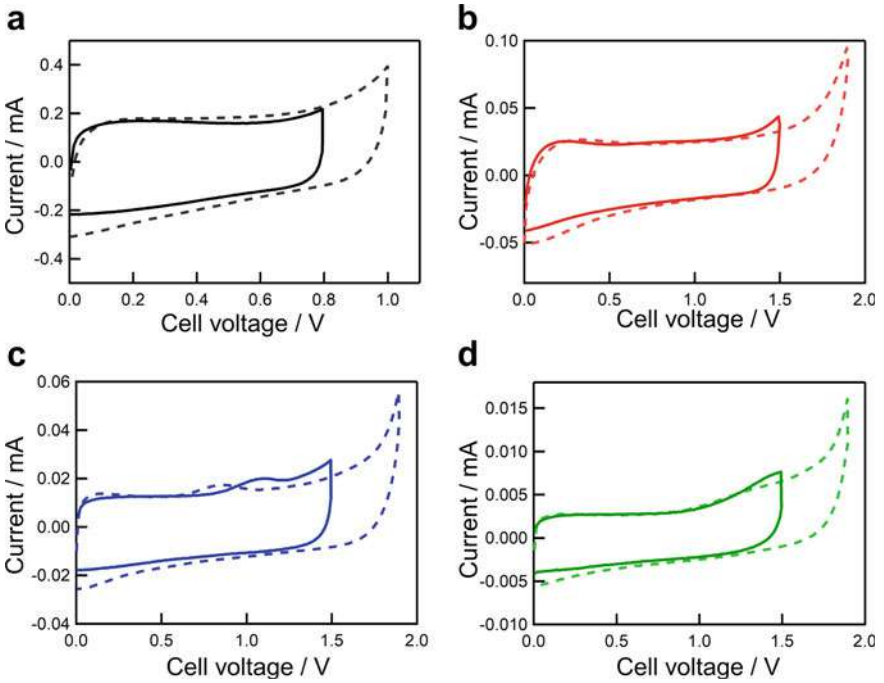

Fig. 11 CVs in 1.0 M H_2SO_4 with a symmetric two-electrode system. **a** AC, **b** BDDP-150, **c** BDDP-350, and **d** BDDP-3500. Scan rate was 10 mV s^{-1}. Solid and dashed lines indicate CV curves with different switching potentials. Reprinted from [34] by The Authors licensed under CC BY 4.0

https://www.twirpx.org & http://chemistry-chemists.com

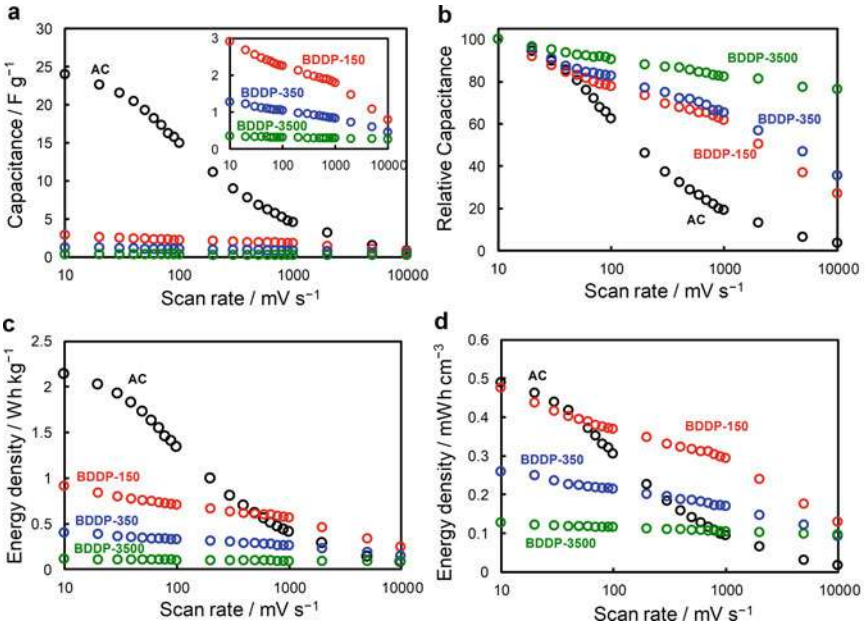

Fig. 12 **a** Capacitance of AC and BDDP electrode cells as a function of scan rate. Inset indicates magnification. **b** Relative capacitance of AC and BDDP electrodes as a function of scan rate. **c** Gravimetric and **d** volumetric energy density of AC and BDDP electrodes as a function of scan rate. Capacitance was estimated from CV in 1.0 M H_2SO_4 with a symmetric two-electrode system. Reprinted from [34] by The Authors licensed under CC BY 4.0

scan rate, those of BDDPs decreased moderately. Since AC has well-developed pores including micropores inside the particles, when the scan rate increases, formation of an electric double-layer on the inner surface of the deep pores cannot follow the potential change. This behavior can cause a decrease in capacitance with increased scan rate. On the other hand, since BDDP is a nonporous material, the capacitance decrease is considered to be suppressed even with a rapid charging–discharging.

Figure 12c shows the energy density per unit weight of the electrode active material with respect to the scan rate [34]. The energy density E was calculated by the relationship $E = C_{dl}V^2/2$, and $V = 0.8$ V and 1.5 V were used for AC and BDDP, respectively. The BDDP showed a very small C_{dl} compared to AC, however, since a large cell voltage up to 1.5 V can be applied, the resulting energy density was relatively large. Especially in the rapid charge–discharge region of 500 mV s^{-1} or more, the energy density of the BDDP-150 electrodes was found to exceed that of AC. In addition, while AC is a bulky material, BDDP has a larger bulk density than AC, and should be more advantageous when the charge–discharge performance with respect to the device volume matters. Figure 12d shows the energy density per unit volume of the electrode layer of the BDDP and AC electrodes [34]. The energy densities of BDDP-150 and AC electrodes were found to be equivalent even in the scan rate

https://www.twirpx.org & http://chemistry-chemists.com

region slower than 100 mV s^{-1}, and that of BDDP-150 became larger in the higher scan rate region than that of AC.

Figure 13 features Ragone plots showing the energy and power densities per unit weight of the electrode active material and per unit volume of the electrode layer of the BDDP and AC electrodes. The AC electrode showed a higher energy density in the region where the charge–discharge rate was slow. However, especially in the plot for the volumetric performance (Fig. 13b), the BDDP-150 electrode showed larger energy and power densities than the AC version in the region where the charge–discharge rate was high. This result suggests that BDDPs are suitable for compact EDLC devices that can handle rapid charging–discharging.

Since BDDP is a powder material, an ink containing it can be prepared and applied to a current collector to fabricate various types of EDLC devices such as laminate, cylinder, and coin types, or microsupercapacitors with coplanar electrodes. This should be a major difference of such BDD powder/nanoparticles from thin-film-based porous BDD materials. It was also confirmed that the amount of sp^2 carbon impurities

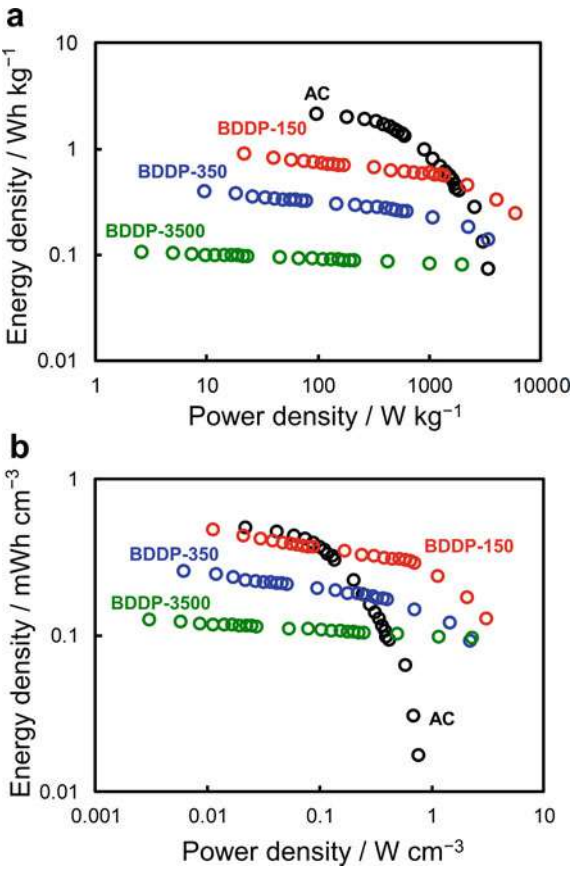

Fig. 13 Ragone plots showing **a** gravimetric and **b** volumetric energy density versus power density of AC and BDDP electrode cells. Reprinted from [34] by The Authors licensed under CC BY 4.0

https://www.twirpx.org & http://chemistry-chemists.com

contained in the BDDP increased by reducing the particle size [35], however, the presence of the sp^2 carbon components did not cause considerable narrowing of the potential window. Therefore, the use of BDDP with a smaller particle size is considered to be suitable for better performance, i.e., both large capacitance and cell voltage, for an electrode material of aqueous EDLC.

4.2 Preparation of Boron-Doped Nanodiamond (BDND) Particles

Boron-doped nanodiamond (BDND) particle was developed with the aim of further reducing the particle size of conductive diamond powder to increase the specific surface area [36]. Nanodiamond (ND) particles with a particle size of about 5 nm (provided by Daicel Corporation) were used as a substrate material. ND was then subjected to MPCVD with a mixture solution of trimethoxyborane/methanol and acetone (B/C atomic ratio: 20,000 ppm) as a carbon/boron source of the BDD layer deposited on the ND substrate. After the CVD process, the sample contains a large amount of sp^2 carbon component as a by-product, so the sample is subjected to thermal oxidation treatment in air at 425 °C for 8 h to minimize the amount of sp^2 carbon content in the BDND (heat-treated BDND).

The sp^2 carbon component remained even after the thermal oxidation treatment, showing no obvious difference in the Raman spectra before and after the treatment [36]. However, from the observation with transmission electron microscopy (TEM), the sp^2 carbon component was suggested to be reduced by thermal oxidation (Fig. 14) [36]. Figure 15a shows the Brunauer–Emmett–Teller (BET) specific surface areas of ND and BDND obtained by nitrogen sorption measurement [36]. From this result, it was found that the specific surface area was reduced by the CVD process, but then greatly increased by the subsequent thermal oxidation treatment. The BDND fabrication process considered from these results is proposed in Fig. 15b [36]. The primary particle size of ND was about 5 nm; however, since it was handled in a dry state, the ND is considered to be in an agglomerated state during the CVD process. The BDD and sp^2 carbon components are then deposited on the surfaces of the agglomerates, so that the voids between the primary ND particles on the agglomerate surface are filled and the specific surface area decreases. In the subsequent thermal oxidation treatment, the vulnerable sp^2 carbon components are selectively decomposed, leaving stable sp^2 carbon structures, which is supported by the TEM observation showing the presence of graphene-like structures on the heat-treated BDND. Such a residual component may result in a significant increase in the specific surface area of the BDND after heat treatment.

https://www.twirpx.org & http://chemistry-chemists.com

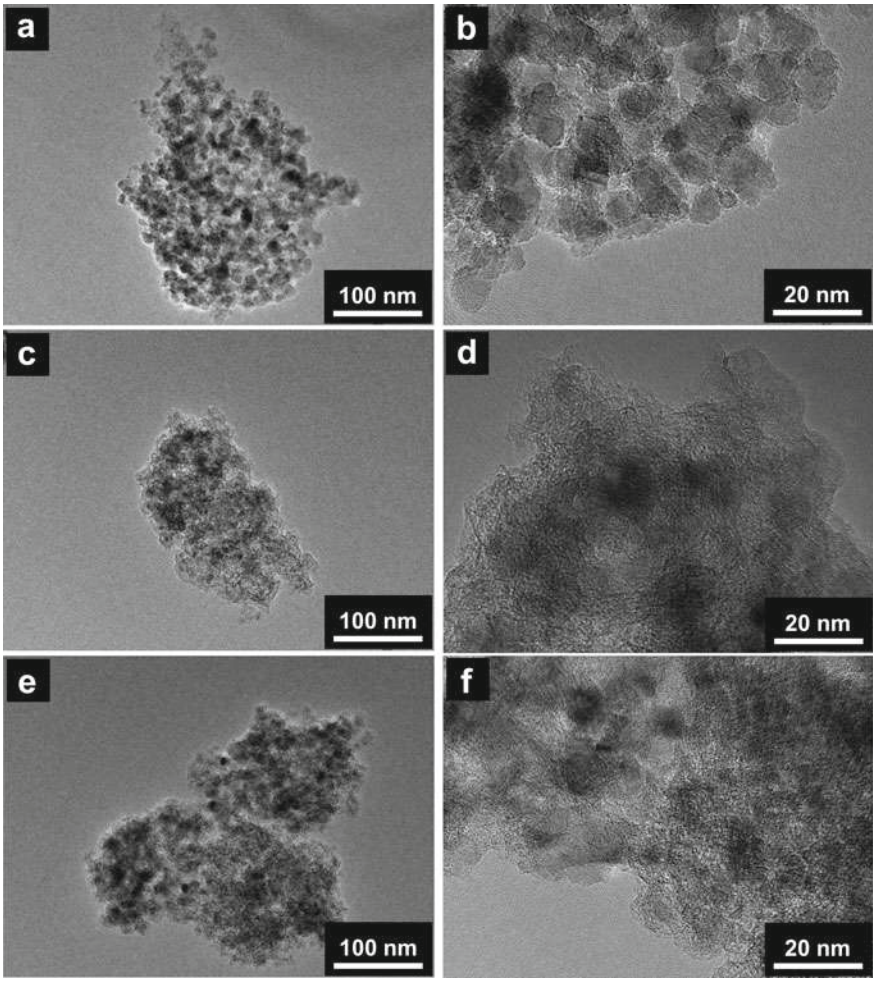

Fig. 14 TEM images of the **a**, **b** ND, **c**, **d** as-deposited BDND, and **e**, **f** heat-treated BDND. Reprinted from [36] by The Authors licensed under CC BY 4.0

4.3 Electrochemical Properties of BDND

The electrochemical characteristics of the prepared BDND were evaluated by CV with test electrodes prepared as described above. Figure 16 shows the CV measured in 1 M H_2SO_4 with a symmetric two-electrode system [36]. In contrast to the case of the AC electrode with a potential window (cell voltage) of 0.8 V, the BDND electrode exhibited a large cell voltage of 1.8 V without Faradaic current. This result confirms that the BDND can show a wide potential window, and is expected to be useful for an aqueous EDLC with a large cell voltage. In addition, the CV current of the BDND

https://www.twirpx.org & http://chemistry-chemists.com

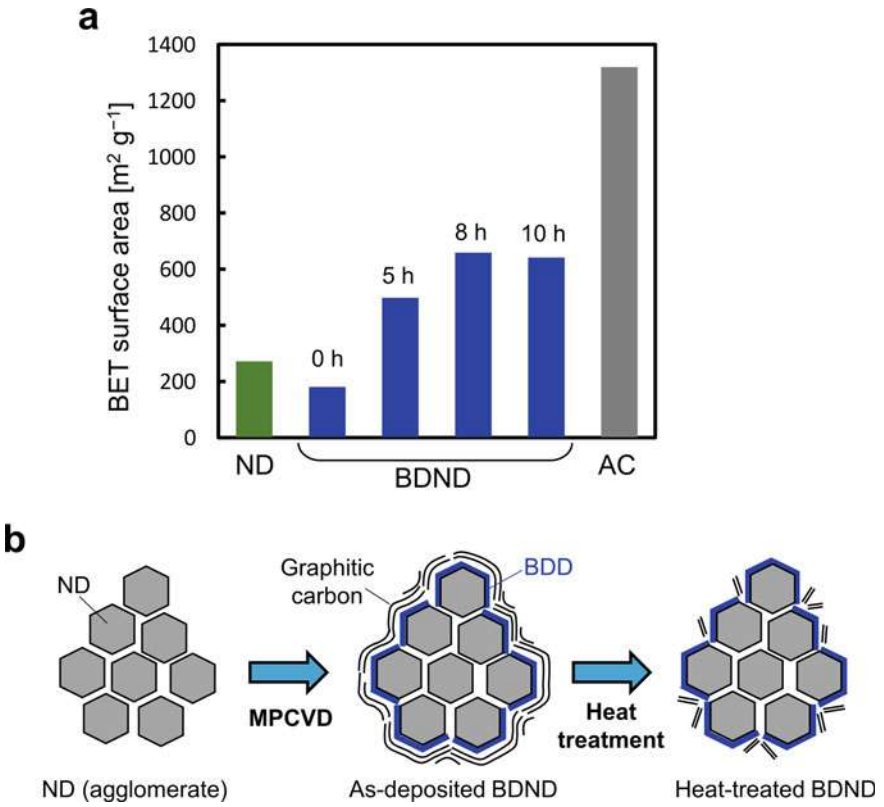

Fig. 15 **a** BET specific surface area of AC, ND, and BDND with various heat treatment times (0, 5, 8, and 10 h); **b** A proposed schematic illustration of the BDND preparation. Reprinted from [36] by The Authors licensed under CC BY 4.0

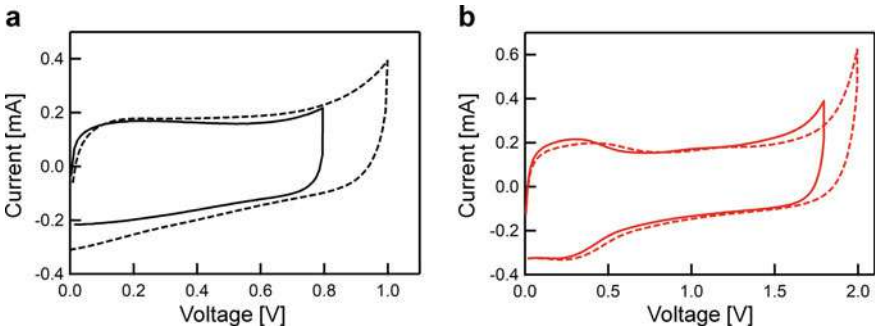

Fig. 16 CVs in 1 M H_2SO_4 with a symmetric two-electrode system: **a** AC and **b** BDND electrodes. The scan rate was 10 mV s^{-1}. Reprinted from [36] by The Authors licensed under CC BY 4.0

https://www.twirpx.org & http://chemistry-chemists.com

electrode was almost the same order as the AC electrode. In these test electrodes, 0.4 mg of electrode active material (AC or BDND) was deposited, and the C_{dl} was calculated to be 20 and 15 F g^{-1} for the AC and BDND electrodes, respectively. Therefore, it was confirmed that the BDND is an electrode material to which a large cell voltage can be applied while exhibiting a capacitance equivalent to that of AC in an aqueous electrolyte.

Figure 17 shows the scan rate dependence of the capacitance per unit weight of the electrode active material calculated from the CV current [36]. At scan rates slower than 100 mV s^{-1}, the AC electrode showed a larger C_{dl} than the BDND electrode, whereas the C_{dl} was larger at the BDND electrode than the AC electrode at scan rates above 200 mV s^{-1}. As described above, C_{dl} of the AC electrode remarkably decreased as the scan rate increased due to the well-developed pore structure of AC. On the other hand, since BDND does not have such pores like AC, though interparticle space among primary particles may function as pores, it is considered that electrolyte ion transfer is relatively fast even at fast scan rates, and the decrease in C_{dl} can be suppressed compared to that of the AC electrode. Figure 17c shows plots of energy density calculated from the C_{dl} (Fig. 17a) as a function of scan rate

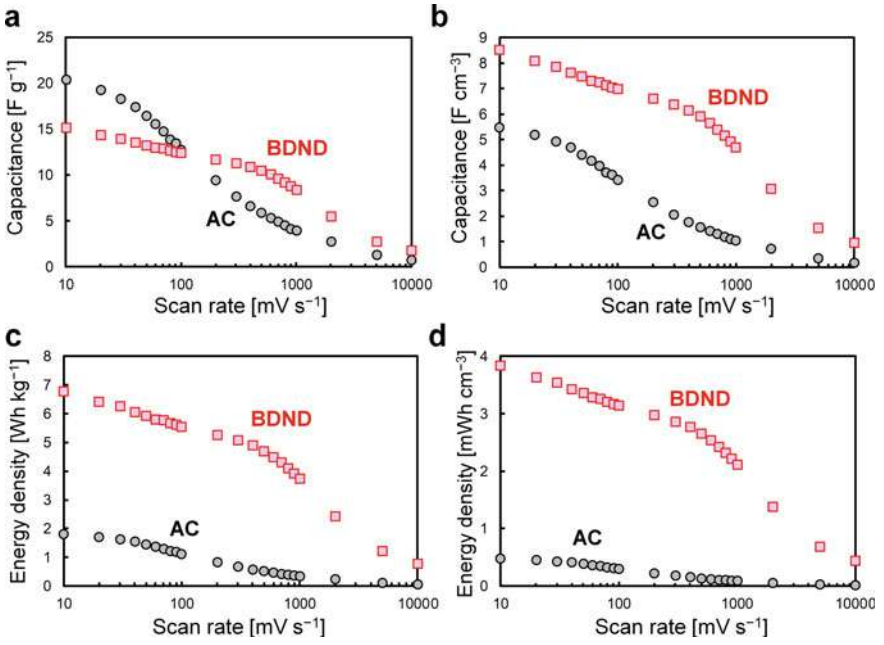

Fig. 17 Capacitance **a** per unit weight of the active material and **b** per unit volume of the electrode layer; and the energy density **c** per unit weight of the active material and **d** per unit volume of the electrode layer as a function of the scan rate. The capacitance was estimated based on CV data recorded in 1 M H_2SO_4 with a symmetric two-electrode system. The energy density was calculated based on the capacitance (panels a and b) and cell voltage (0.8 V and 1.8 V for AC and BDND, respectively). Reprinted from [36] by The Authors licensed under CC BY 4.0

https://www.twirpx.org & http://chemistry-chemists.com

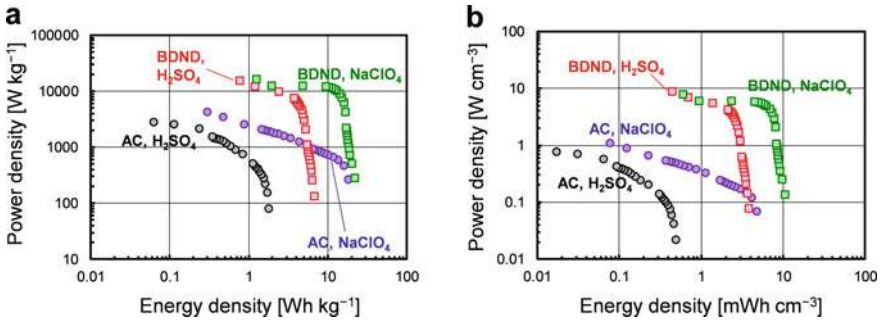

Fig. 18 Ragone plots showing the power density versus energy density **a** per unit weight of the active material and **b** per unit volume of the electrode layer of the AC and BDND electrode cell. The electrolytes used were 1 M H_2SO_4 and saturated $NaClO_4$. Reprinted from [36] by The Authors licensed under CC BY 4.0

[36]. The cell voltages used for the calculation were 0.8 and 1.8 V for the AC and BDND electrodes, respectively. As mentioned earlier, the energy density is directly proportional to the square of the cell voltage, so the energy density was found to be larger at the BDND electrode than at the AC electrode in this scan rate region (10–1000 mV s^{-1}).

Bulk densities of AC and BDND were calculated from the volume and weight of the electrode active material layer to be 0.23 and 0.52 g cm^{-3}, respectively. This fact indicates that the BDND should be suitable for a compact EDLC device. Figure 17b and d shows the C_{dl} and energy density per unit volume of the electrode active material layer calculated using these bulk densities [36]. The BDND electrode showed a larger C_{dl} than the AC electrode in the scan rate range of 10–1000 mV s^{-1}, and the difference in the volumetric energy density was greater than the gravimetric one. The results show that BDND is useful for production of more compact or thinner aqueous EDLC devices than those using AC when the energy density of the device is the same.

Figure 18 shows the Ragone plots when the electrode materials were BDND and AC, and the electrolytes are 1 M H_2SO_4 and saturated $NaClO_4$ [36]. In the gravimetric plot (Fig. 18a), it can be seen that the performance was found to be better in terms of both energy and power densities at the BDND electrode than the AC one. The large energy densities are obtained based on the large cell voltage due to the use of an electrolyte and an electrode material leading a wide potential window (saturated $NaClO_4$ and BDND, respectively). In contrast, the large power densities seen when using BDND are due to the fact that the decrease in C_{dl} was suppressed even when the scan rate was fast, i.e., the charging–discharging was fast. Moreover, in the volumetric Ragone plot (Fig. 18b), the difference in performance between the BDND and AC electrodes is emphasized based on the larger bulk density of the BDND than that of AC. From the above results, it is expected that a compact and safe aqueous EDLC with high energy and power densities can be produced by using BDND as an electrode material.

https://www.twirpx.org & http://chemistry-chemists.com

5 Conclusions

Fabrication of various types of porous BDD electrodes aimed at applications for EDLC, and their electrochemical properties are described. As described in this chapter, the specific surface area of BDD electrodes can be increased using various methods such as bottom-up approaches using templates, top–down approaches using etching treatments, or the preparation of BDDP materials. These technologies are considered to be useful for expanding the application fields of BDD electrodes including electrochemical energy devices. For applications in electrochemical capacitors, surface modification with redox-active molecules and oxides, etc., should also be effective for increasing the capacitance by combining an increase in the specific surface area of the electrode. BDD electrodes, even after imparting micro/nanostructures, have been shown to have excellent properties as an electrode material for EDLC with a wide potential window in aqueous electrolytes. The continued development toward the mass production of BDD material with a large specific surface area is desired for practical use in EDLC applications.

Acknowledgements The author appreciates the support of this work by KAKENHI (Nos. 26410246 and 19K05064) grants from the Japan Society for the Promotion of Sciences (JSPS) , by Adaptable and Seamless Technology transfer Program through Target-driven R&D (A-STEP) from Japan Science and Technology Agency (JST), by Tokyo Ohka Foundation for the Promotion of Science and Technology, and by the Joint Usage/Research Program of the Photocatalysis International Research Center, Research Institute for Science and Technology, Tokyo University of Science.

References

1. Simon P, Gogotsi Y (2008) Materials for electrochemical capacitors. Nat Mater 7:845. https://doi.org/10.1038/nmat2297
2. Inagaki M, Konno H, Tanaike O (2010) Carbon materials for electrochemical capacitors. J Power Sources 195(24):7880–7903. https://doi.org/10.1016/j.jpowsour.2010.06.036
3. Wang G, Zhang L, Zhang J (2012) A review of electrode materials for electrochemical supercapacitors. Chem Soc Rev 41(2):797–828. https://doi.org/10.1039/C1CS15060J
4. Béguin F, Presser V, Balducci A, Frackowiak E (2014) Carbons and electrolytes for advanced supercapacitors. Adv Mater 26(14):2219–2251. https://doi.org/10.1002/adma.201304137
5. Burke A (2000) Ultracapacitors: why, how, and where is the technology. J Power Sources 91(1):37–50. https://doi.org/10.1016/S0378-7753(00)00485-7
6. Einaga Y (2010) Diamond electrodes for electrochemical analysis. J Appl Electrochem 40(10):1807–1816. https://doi.org/10.1007/s10800-010-0112-z
7. Honda K, Rao TN, Tryk DA, Fujishima A, Watanabe M, Yasui K, Masuda H (2000) Electrochemical characterization of the nanoporous honeycomb diamond electrode as an electrical double-layer capacitor. J Electrochem Soc 147(2):659–664. https://doi.org/10.1149/1.1393249
8. Kondo T, Kodama Y, Ikezoe S, Yajima K, Aikawa T, Yuasa M (2014) Porous boron-doped diamond electrodes fabricated via two-step thermal treatment. Carbon 77:783–789. https://doi.org/10.1016/j.carbon.2014.05.082

https://www.twirpx.org & http://chemistry-chemists.com

9. Honda K, Rao TN, Tryk DA, Fujishima A, Watanabe M, Yasui K, Masuda H (2001) Impedance characteristics of the nanoporous honeycomb diamond electrodes for electrical double-layer capacitor applications. J Electrochem Soc 148(7):A668. https://doi.org/10.1149/1.1373450
10. Honda K, Yoshimura M, Uchikado R, Kondo T, Rao TN, Tryk DA, Fujishima A, Watanabe M, Yasui K, Masuda H (2002) Electrochemical characteristics for redox systems at nano-honeycomb diamond. Electrochim Acta 47(27):4373–4385. https://doi.org/10.1016/S0013-4686(02)00511-X
11. Honda K, Yoshimura M, Kawakita K, Fujishima A, Sakamoto Y, Yasui K, Nishio N, Masuda H (2004) Electrochemical characterization of carbon nanotube/nanohoneycomb diamond composite electrodes for a hybrid anode of Li-Ion battery and super capacitor. J Electrochem Soc 151(4):A532. https://doi.org/10.1149/1.1649752
12. Gao F, Wolfer MT, Nebel CE (2014) Highly porous diamond foam as a thin-film micro-supercapacitor material. Carbon 80:833–840. https://doi.org/10.1016/j.carbon.2014.09.007
13. Zanin H, May PW, Fermin DJ, Plana D, Vieira SMC, Milne WI, Corat EJ (2014) Porous boron-doped diamond/carbon nanotube electrodes. ACS Appl Mater Interf 6(2):990–995. https://doi.org/10.1021/am4044344
14. Gao F, Lewes-Malandrakis G, Wolfer MT, Müller-Sebert W, Gentile P, Aradilla D, Schubert T, Nebel CE (2015) Diamond-coated silicon wires for supercapacitor applications in ionic liquids. Diam Relat Mater 51:1–6. https://doi.org/10.1016/j.diamond.2014.10.009
15. Hébert C, Scorsone E, Mermoux M, Bergonzo P (2015) Porous diamond with high electrochemical performance. Carbon 90:102–109. https://doi.org/10.1016/j.carbon.2015.04.016
16. Ruffinatto S, Girard HA, Becher F, Arnault JC, Tromson D, Bergonzo P (2015) Diamond porous membranes: a material toward analytical chemistry. Diam Relat Mater 55:123–130. https://doi.org/10.1016/j.diamond.2015.03.008
17. Sawczak M, Sobaszek M, Siuzdak K, Ryl J, Bogdanowicz R, Darowicki K, Gazda M, Cenian A (2015) Formation of highly conductive boron-doped diamond on TiO2 nanotubes composite for supercapacitor or energy storage devices. J Electrochem Soc 162(10):A2085–A2092. https://doi.org/10.1149/2.0551510jes
18. Aradilla D, Gao F, Lewes-Malandrakis G, Müller-Sebert W, Gentile P, Boniface M, Aldakov D, Iliev B, Schubert TJS, Nebel CE, Bidan G (2016) Designing 3D multihierarchical heteronanostructures for high-performance on-chip hybrid supercapacitors: Poly(3,4-(ethylenedioxy)thiophene)-coated diamond/silicon nanowire electrodes in an aprotic ionic liquid. ACS Appl Mater Interfaces 8(28):18069–18077. https://doi.org/10.1021/acsami.6b04816
19. Gao F, Nebel CE (2016) Diamond-based supercapacitors: realization and properties. ACS Appl Mater Interf 8(42):28244–28254. https://doi.org/10.1021/acsami.5b07027
20. Scorsone E, Gattout N, Rousseau L, Lissorgues G (2017) Porous diamond pouch cell supercapacitors. Diam Relat Mater 76:31–37. https://doi.org/10.1016/j.diamond.2017.04.004
21. Aradilla D, Gao F, Lewes-Malandrakis G, Müller-Sebert W, Gentile P, Pouget S, Nebel CE, Bidan G (2017) Powering electrodes for high performance aqueous micro-supercapacitors: diamond-coated silicon nanowires operating at a wide cell voltage of 3V. Electrochim Acta 242:173–179. https://doi.org/10.1016/j.electacta.2017.04.102
22. Kondo T, Lee S, Honda K, Kawai T (2009) Conductive diamond hollow fiber membranes. Electrochem Commun 11(8):1688–1691. https://doi.org/10.1016/j.elecom.2009.06.027
23. Kondo T, Kodama Y, Yuasa M (2012) Fabrication and electrochemical properties of boron-doped diamond hollow fiber wool. Trans Mater Res Soc Jpn 37(4):503–506. https://doi.org/10.14723/tmrsj.37.503
24. Yang N, Uetsuka H, Osawa E, Nebel CE (2008) Vertically aligned diamond nanowires for DNA sensing. Angew Chem Int Ed 47(28):5183–5185. https://doi.org/10.1002/anie.200801706
25. Terashima C, Arihara K, Okazaki S, Shichi T, Tryk DA, Shirafuji T, Saito N, Takai O, Fujishima A (2011) Fabrication of vertically aligned diamond whiskers from highly boron-doped diamond by oxygen plasma etching. ACS Appl Mater Interfaces 3(2):177–182. https://doi.org/10.1021/am1007722

https://www.twirpx.org & http://chemistry-chemists.com

26. Ohashi T, Zhang J, Takasu Y, Sugimoto W (2011) Steam activation of boron doped diamond electrodes. Electrochim Acta 56(16):5599–5604. https://doi.org/10.1016/j.electacta.2011.04.005
27. Ohashi T, Sugimoto W, Takasu Y (2009) Catalytic roughening of surface layers of BDD for various applications. Electrochim Acta 54(22):5223–5229. https://doi.org/10.1016/j.electacta.2009.04.021
28. Shi C, Li C, Li M, Li H, Dai W, Wu Y, Yang B (2016) Fabrication of porous boron-doped diamond electrodes by catalytic etching under hydrogen–argon plasma. Appl Surf Sci 360:315–322. https://doi.org/10.1016/j.apsusc.2015.11.028
29. Pandey KC (1982) New dimerized-chain model for the reconstruction of the diamond (111)-(2 × 1) surface. Phys Rev B 25(6):4338–4341
30. Petukhov AV, Passerone D, Ercolessi F, Tosatti E, Fasolino A (2000) (Meta)stable reconstructions of the diamond (111) surface: Interplay between diamond and graphitelike bonding. Phys Rev B 61(16):R10590–R10593
31. Kondo T, Yajima K, Kato T, Okano M, Terashima C, Aikawa T, Hayase M, Yuasa M (2017) Hierarchically nanostructured boron-doped diamond electrode surface. Diam Relat Mater 72:13–19. https://doi.org/10.1016/j.diamond.2016.12.004
32. Fischer AE, Swain GM (2005) Preparation and characterization of boron-doped diamond powder. J Electrochem Soc 152(9):B369. https://doi.org/10.1149/1.1984367
33. Ay A, Swope VM, Swain GM (2008) The physicochemical and electrochemical properties of 100 and 500 nm diameter diamond powders coated with boron-doped nanocrystalline diamond. J Electrochem Soc 155(10):B1013. https://doi.org/10.1149/1.2958308
34. Kondo T, Kato T, Miyashita K, Aikawa T, Tojo T, Yuasa M (2019) Boron-doped diamond powders for aqueous supercapacitors with high energy and high power density. J Electrochem Soc 166(8):A1425–A1431. https://doi.org/10.1149/2.0381908jes
35. Kondo T, Nakajima K, Osasa T, Kotsugai A, Shitanda I, Hoshi Y, Itagaki M, Aikawa T, Tojo T, Yuasa M (2018) Effect of substrate size on the electrochemical properties of boron-doped diamond powders for screen-printed diamond electrode. Chem Lett 47(12):1464–1467. https://doi.org/10.1246/cl.180672
36. Miyashita K, Kondo T, Sugai S, Tei T, Nishikawa M, Tojo T, Yuasa M (2019) Boron-doped nanodiamond as an electrode material for aqueous electric double-layer capacitors. Sci Rep 9(1):17846. https://doi.org/10.1038/s41598-019-54197-9

https://www.twirpx.org & http://chemistry-chemists.com

Boron-Doped Diamond Powder

Takeshi Kondo

Abstract In this chapter, preparation of boron-doped diamond (BDDP) and its application to screen-printed electrodes and cathode catalyst supports were described. Screen-printed diamond electrodes using ink containing BDDP and polyester resin binder can be used as highly sensitive and disposable electrodes for electrochemical sensors, demonstrating sensitive detection of ciprofloxacin in artificial urine. Pt-supported BDDP is expected to be useful for a highly durable polymer electrolyte fuel cell cathode catalyst based on the corrosion resistance of BDDP to highly positive potentials.

Boron-doped diamond powder (BDDP) was developed to expand the range of applications of diamond electrodes. In this chapter, preparation of BDDP and its application to screen-printed electrodes and cathode catalyst supports were described. BDDP is a conductive diamond powder obtained by deposition of a boron-doped diamond (BDD) layer on a diamond powder (DP) substrate surface via chemical vapor deposition method. The particle size of BDDP can be arbitrarily selected depending on the particle size of the DP substrate, ranging at least from several hundreds of nanometers to several micrometers. Screen-printed diamond electrodes using ink containing BDDP and polyester resin binder can be used as highly sensitive and disposable electrodes for electrochemical sensors, demonstrating sensitive detection of ciprofloxacin in artificial urine. The characteristics of the BDDP-printed electrodes were shown to be controlled by surface termination of BDDP and binder-to-BDDP ratio in the ink. Pt-supported BDDP is expected to be useful for a highly durable polymer electrolyte fuel cell cathode catalyst. BDDP is a highly versatile functional electrode material that can be made into ink and paste and can be combined with other compounds, expanding widely the application of diamond electrodes.

T. Kondo (✉)
Department of Pure and Applied Chemistry, Faculty of Science and Technology, Tokyo University of Science, Noda, Japan
e-mail: t-kondo@rs.tus.ac.jp

© Springer Nature Singapore Pte Ltd. 2022

Y. Einaga (ed.), *Diamond Electrodes*,
https://doi.org/10.1007/978-981-16-7834-9_7

https://www.twirpx.org & http://chemistry-chemists.com

1 Introduction

Boron-doped diamond (BDD) electrodes exhibit a wide potential window in aqueous and nonaqueous electrolytes and low background current with extreme physical and chemical stability. Based on these excellent properties, they can be used for electrochemical sensor with high sensitivity and stability and can be also applied as an electrode material for highly efficient electrolysis with excellent durability. However, since the BDD electrode is usually prepared by chemical vapor deposition (CVD) method using a flat plate substrate of a limited type of material such as silicon and niobium, it can be obtained as a hard and flat plate electrode with a relatively small size (e.g., 2 inches in diameter). Therefore, it is difficult to obtain an electrode having an arbitrary shape or a three-dimensional structure. Moreover, since the size of the CVD apparatus for preparation of BDD is also limited, it is not easy to obtain a BDD electrode with a large size. In order to overcome such restrictions of direct BDD synthesis onto the substrate, the use of powdered BDD can be a candidate. If BDD powder (BDDP) that exhibits a wide potential window, low background current, and physical/chemical stability similar to those of the BDD thin-film electrode can be obtained, it can be made into ink or paste to form electrodes. It can be printed or painted to form a diamond electrode using a substrate with various sizes and types of materials. This strategy enables creation of novel diamond electrodes that are lightweight, inexpensive, flexible, and large size, which cannot be directly fabricated by the CVD method. In addition, BDDP has a large specific surface area and can be applied to a fuel cell catalyst support and an electrode material for electrochemical capacitors.

BDDP can be obtained through direct synthesis by high-pressure and high-temperature method [1], by milling a BDD thin-film prepared by CVD [2], and by deposition of a BDD layer on the surface of a diamond powder (DP) substrate [3, 4]. Among these, BDDP prepared by the third method should be suitable for electrochemical applications because it exhibits sufficient conductivity and should be feasible to mass production. In this method, DP commercially available as an abrasive with a controlled size can be used for the substrate, and only the surface thereof needs to be coated with a BDD layer. The size of the DP substrate can be widely selected at least from several hundreds of nanometers to several micrometers, and thus BDDP with a desired particle size can be obtained [5]. This chapter describes the fabrication and electrochemical properties of BDDP prepared by BDD deposition on a DP substrate. In addition, electrochemical applications of BDDP including screen-printed diamond electrodes enabling highly sensitive electrochemical detection and platinum-supported BDDP (Pt/BDDP) for highly durable polymer electrolyte fuel cell (PEFC) cathode catalysts are also introduced.

https://www.twirpx.org & http://chemistry-chemists.com

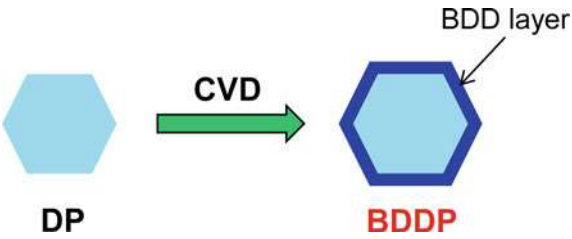

Fig. 1 Schematic illustration of preparation of BDDP

2 Preparation and Basic Properties of BDDP

2.1 Preparation of BDDP

BDDP can be obtained by deposition of a BDD layer by the CVD method on the surface of a DP substrate that is commercially available as an abrasive (Fig. 1) [6]. 0.8 g of cleaned DP (Micron + MDA, Element Six) was placed on a CVD molybdenum susceptor (2 inches in diameter), and a BDD layer was grown on the DP surface by microwave plasma-assisted CVD method. Mixed solution of 70% trimethoxyborane/methanol and acetone (B/C atomic concentration ratio was 20,000 ppm) was used as a carbon/boron source. The CVD process was performed with a microwave power of 1,300 W, a carrier H_2 gas flow rate of 400 sccm, a pressure of 50 Torr, a stage temperature of 800 °C, and a deposition time of 8 h. After the CVD process, sp^2 carbon impurities were removed by heat treatment in air at 425 °C for 5 h. This treatment can reduce sp^2 carbon impurities [7] and simultaneously oxidize the BDDP surface (O-BDDP). If necessary, the BDDP surface can be converted to hydrogen termination (H-BDDP) by hydrogen plasma treatment. The hydrogen plasma treatment was carried out using a CVD apparatus with a microwave power of 500 W, a carrier H^2 gas flow rate of 100 sccm, a pressure of 20 Torr, and a stage temperature of 800 °C for 1 h [8].

2.2 Effect of Particle Size

Figure 2 shows scanning electron microscopy (SEM) images of the DP substrates with various particle sizes and the corresponding BDDP [5]. Comparing the SEM images of the DP substrates with particle sizes of 301, 436, 1,647, and 2,650 nm (denoted as DP-300, DP-450, DP-1600, and DP-2600, respectively) and the corresponding BDDP (denoted as BDDP-350, -650, -2000, -3500, respectively), no obvious change was observed in terms of particle size and shape before and after BDD layer growth by CVD. However, when magnified images of DP-300 and BDDP-350 surfaces were compared, the DP-300 surface was found to be relatively smooth,

https://www.twirpx.org & http://chemistry-chemists.com

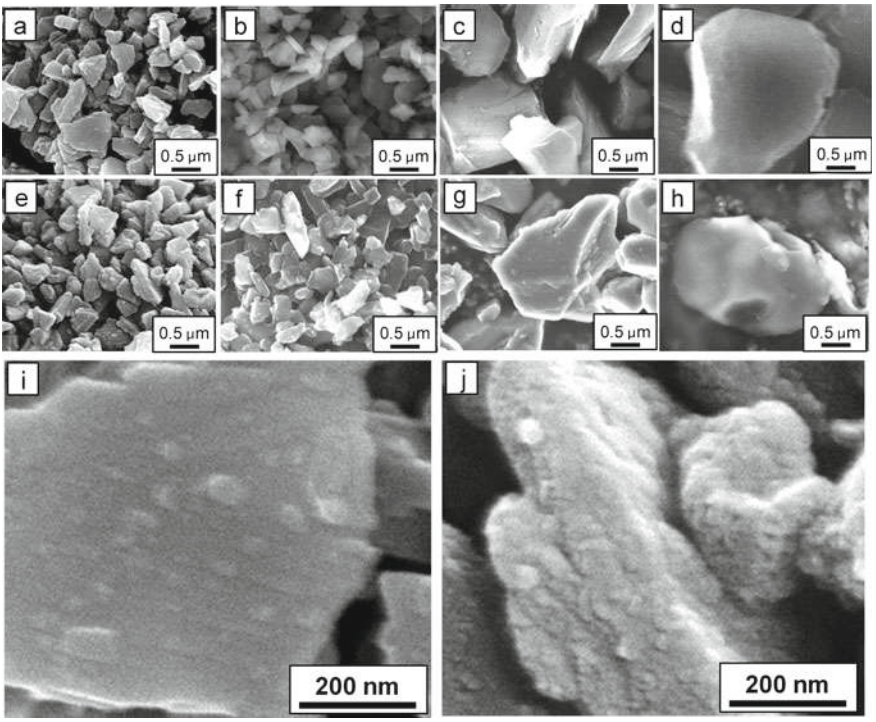

Fig. 2 SEM images of DP cores (**a**–**d**) and the corresponding BDDPs (**e**–**h**). **a** DP-300, **b** DP-450, **c** DP-1600, **d** DP-2600, **e** BDDP-350, **f** BDDP-650, **g** BDDP-2000 and **h** BDDP-3500. Magnified images of **i** DP-300 and **j** BDDP-350. Reprinted from [5], Copyright 2018, with permission from The Chemical Society of Japan

whereas the BDDP-350 has a rough surface consisting of grains with a size of 2–50 nm (Fig. 2i, j) [5]. This result suggested that nanocrystalline BDD was grown on the DP substrate surface by CVD.

Figure 3a–h shows the particle size distribution of DP and BDDP obtained by dynamic light scattering method [5]. BDDP showed a monomodal distribution similar to the DP substrates, and average particle size was found to slightly increase after the BDD layer growth by CVD (Table 1 and Fig. 2i) [5]. Since the increment of average particle size after CVD was much smaller than DP core particle size, it can be concluded that a single BDDP was formed from a single DP. Therefore, BDDP having a desired particle size can be obtained by selecting a DP with the corresponding size as the substrate. The apparent BDD layer thickness defined as half of the difference between average particle sizes of BDDP and the corresponding DP was plotted as a function of DP particle size (Fig. 2j) [5]. As a result, the BDD layer thickness, that is the growth rate, was found to increase as the particle size of the DP substrate increased. In addition, results from Raman spectroscopy showed that the larger the particle size, the smaller the intensity ratio between the G band (1600 cm^{-1}) and

https://www.twirpx.org & http://chemistry-chemists.com

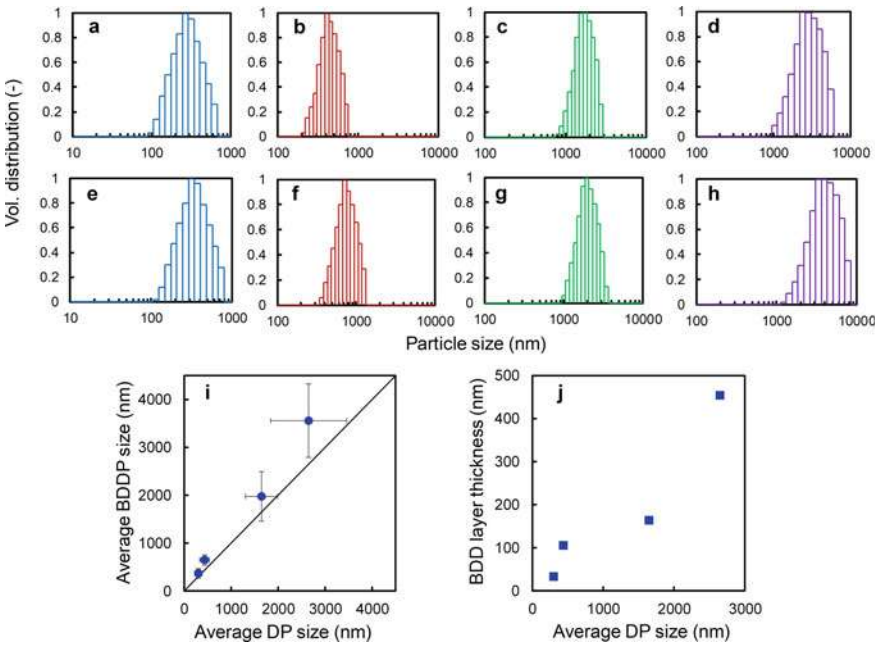

Fig. 3 Particle size distribution of DP cores (**a**–**d**) and the corresponding BDDPs (**e**–**h**). **a** DP-300, **b** DP-450, **c** DP-1600, **d** DP-2600, **e** BDDP-350, **f** BDDP-650, **g** BDDP-2000, and **h** BDDP-3500. **i** Plot of average BDDP size versus average DP core size. **j** Plot of BDD layer thickness versus average DP core size. Reprinted from [5], Copyright 2018, with permission from The Chemical Society of Japan

Table 1 Average particle size, conductivity, and I_G/I_{dia} of BDDP with various DP core size

Average DP core size/nm	Average BDDP size/nm	Conductivity/S cm^{-1}	I_G/I_{dia}
301	367	0.34	0.092
436	647	0.35	0.083
1647	1975	0.83	0.034
2650	3558	0.62	0.005

the diamond peak (1333 cm^{-1}) (I_G/I_{dia}) and the higher the crystal quality of BDD (Fig. 3, Table 1) [5]. The G band should be derived from sp^2 carbon impurities present at the grain boundaries of the BDD layer. Since the grain boundaries become tighter as BDD grows, I_G/I_{dia} in BDDP with thicker BDD layers and larger grain size should decrease. In addition, the conductivity of BDDP calculated from DC resistance between both ends of a BDDP cylinder filled in a glass tube (1 mm in inner diameter) was in the order of 0.1 S cm^{-1}. Thus, it was confirmed that BDDP can be used as an electrochemical electrode material (Fig. 4).

https://www.twirpx.org & http://chemistry-chemists.com

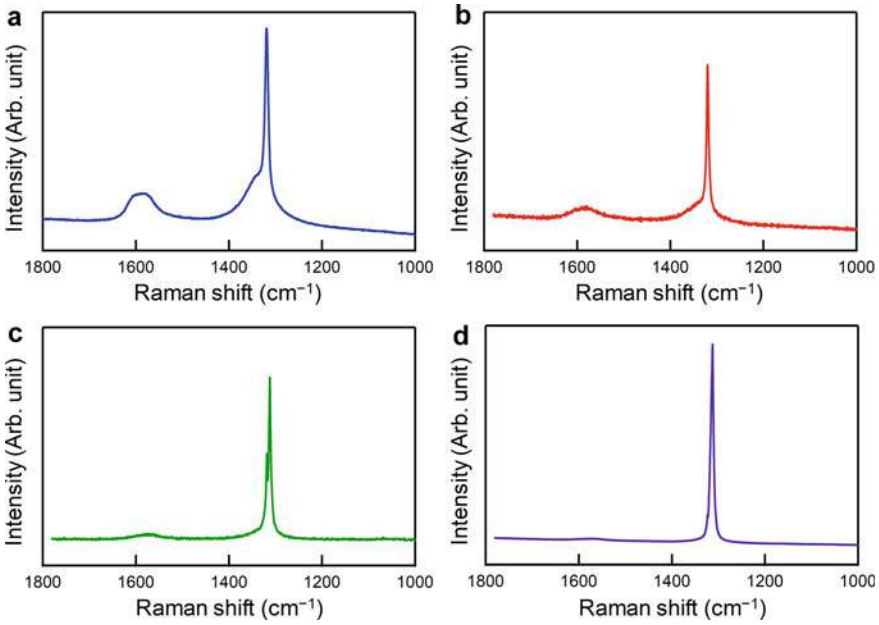

Fig. 4 Raman spectra of **a** BDDP-350, **b** BDDP-650, **c** BDDP-2000, and **d** BDDP-3500. Reprinted from [5], Copyright 2018, with permission from The Chemical Society of Japan

BDDP of any particle size can be prepared by selecting the particle size of the DP substrate. BDDP showed good conductivity and thus can be used as an electrode material regardless of the particle size in the range of several hundreds of nanometers to several micrometers. However, as the particle size became smaller, the content of sp^2 carbon component tended to increase. For example, when used for applications such as electroanalysis where the presence of sp^2 carbon impurities deteriorates the performance, it is necessary to use BDDP having a relatively large particle size (e.g., several micrometers). On the other hand, for applications such as electrochemical capacitors where the influence of sp^2 carbon impurities is not significant and large specific surface area is useful, it is better to use BDDP with a smaller particle size (e.g., several hundreds of nanometers or smaller).

3 Screen-Printed Diamond Electrode

3.1 Fabrication of Screen-Printed Diamond Electrode

Screen-printed electrode is one type of electrodes that can be mass produced at low cost and is used as a disposable electrode such as a personal glucose sensor. In particular, screen-printed carbon electrodes are used as a platform for sensing

https://www.twirpx.org & http://chemistry-chemists.com

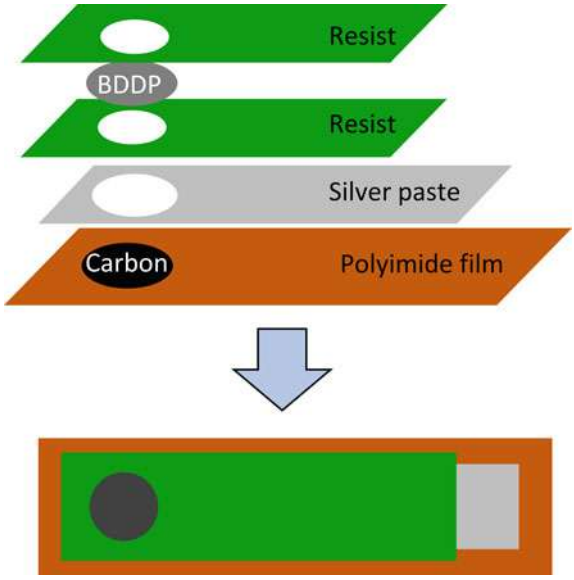

Fig. 5 Schematic illustration of the procedure for fabrication of the BDDP-printed electrode. Reprinted with permission from [14]. Copyright 2016 American Chemical Society

devices in a wide range of fields, such as clinical/biological, pharmaceutical, environmental, and food analyses, and can be modified with mediators, metal nanoparticles, enzymes, and antibodies to enable analyte-specific detection [9–13]. Screen-printed diamond electrodes using BDDP as an electrode material are considered to be useful as a lightweight, inexpensive, mass-producible, and highly sensitive electrochemical sensing platform, which can be used in a variety of electrochemical applications.

BDDP ink for screen-printed electrode was prepared by adding 100 mg of BDDP to 2-butanone/isophorone solution, where 30 mg of polyester resin (binder) was dissolved. Then, a screen-printed diamond electrode was fabricated on a polyimide substrate by printing carbon ink (current collector), silver ink (electrical lead), resist ink (insulation mask), BDDP ink, and resist ink in this order by using a screen printer (Fig. 5) [14]. The screen-printed diamond electrode showed a good electrochemical response, whereas the background current was smaller than that of the screen-printed carbon electrode [6], indicating that a highly sensitive electrochemical detection with a large signal-to-background (S/B) ratio can be obtained by using the screen-printed diamond electrode.

3.2 Sensitive Electrochemical Detection of Ciprofloxacin

We investigated the detection of ciprofloxacin (CIP) as an application of screen-printed diamond electrodes to a highly sensitive electrochemical detection [8]. CIP is a fluoroquinolone antibiotic and is used for the treatment of various infectious

https://www.twirpx.org & http://chemistry-chemists.com

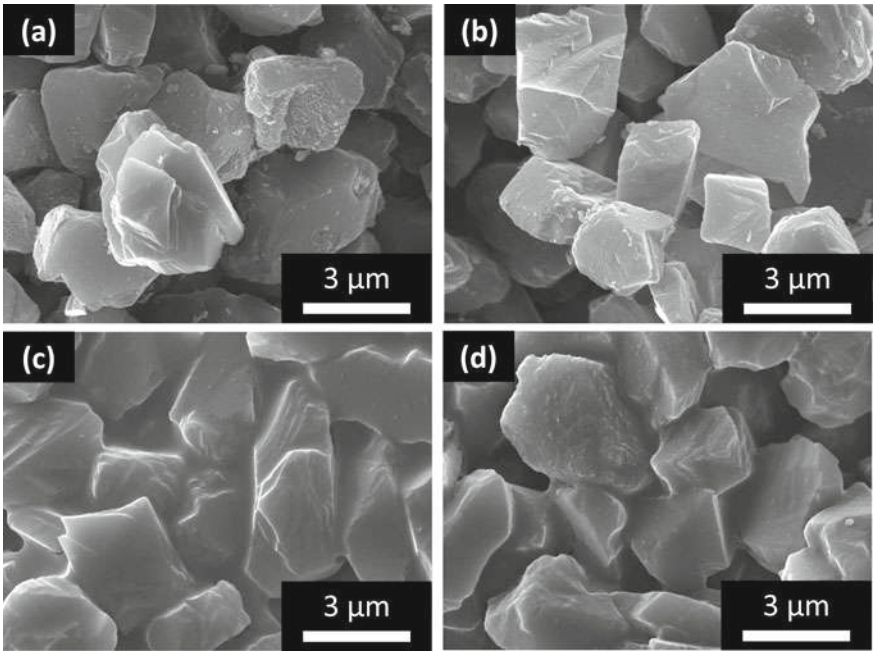

Fig. 6 SEM images of **a** H-BDDP, **b** O-BDDP, **c** H-BDDP-printed, and **d** O-BDDP-printed electrode surface. Reprinted from [8], Copyright 2020, with permission from Elsevier

diseases [15]. It is known that antibiotics are excreted from the body of an administered patient via urine for example and can be discharged into environmental waters [16]. This can cause the development of antibiotic-resistant bacteria, and therefore, highly sensitive detection of antibiotics from urine or environmental water is desired.

To examine suitable conditions for the detection of CIP with high sensitivity, screen-printed electrodes were prepared using H-BDDP and O-BDDP. Figure 6 shows the SEM images of H-BDDP and O-BDDP and those of H-BDDP- and O-BDDP-printed electrode surfaces [8]. The shape, size, and surface morphology of H-BDDP and O-BDDP were almost unchanged. On the other hand, when comparing the surface of screen-printed electrodes, it was suggested that H-BDDP-printed electrode had a higher miscibility to the binder (polyester resin) than O-BDDP-printed electrode because the voids between the particles on H-BDDP-printed electrode were filled with the binder more than those on O-BDDP-printed electrode. This should be because the O-BDDP surface has a significant amount of polar oxygen-containing functional groups exhibiting hydrophilic properties, whereas the H-BDDP surface has few such functional groups and is rich in hydrophobic C–H groups.

Figure 7a, b shows the linear sweep voltammograms (LSVs) of CIP at various concentrations on H-BDDP- and O-BDDP-printed electrodes [8]. It was found that O-BDDP-printed electrode showed a clear anodic peak and the electrochemical response was found to be better than that of H-BDDP-printed electrode. Although

https://www.twirpx.org & http://chemistry-chemists.com

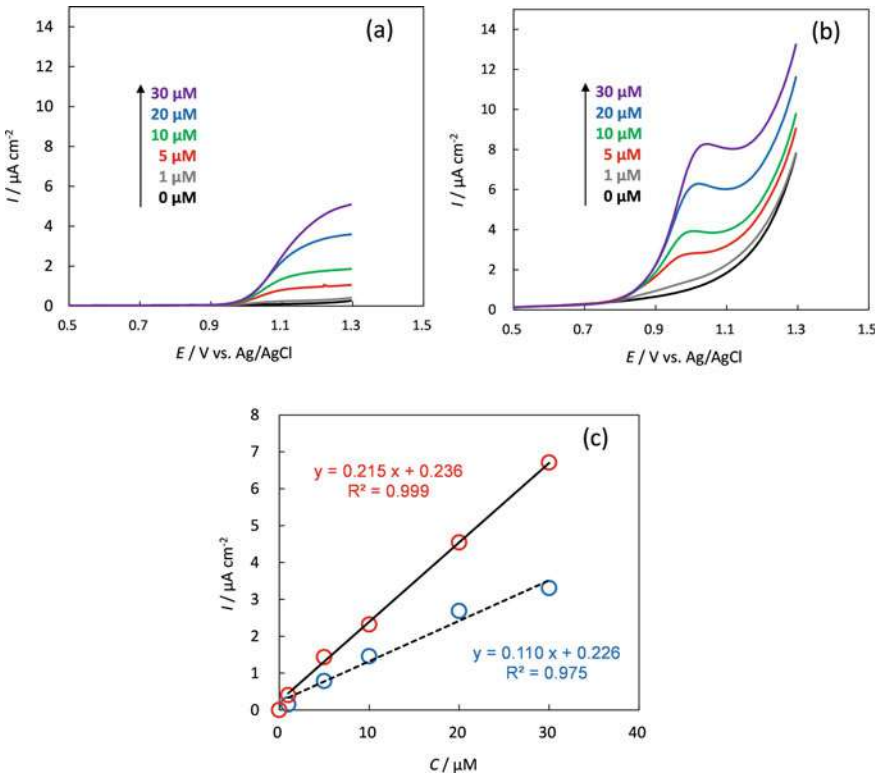

Fig. 7 LSVs of CIP in 1/15 M PBS at **a** H-BDDP-printed, and **b** O-BDDP-printed electrodes. Potential sweep rate was 10 mV s^{-1}. **c** Calibration curves of CIP detection by LSV at O-BDDP-printed (solid line) and H-BDDP-printed electrodes (dotted line). Reprinted from [8], Copyright 2020, with permission from Elsevier

the calibration curve for CIP detection showed a linear response in the concentration range of 1–30 µM at both electrodes, the slope of the calibration curve was larger for O-BDDP-printed electrode than that for H-BDDP one. H-BDDP was considered to have a higher affinity with the binder, so that the contact between the BDDP surface and the electrolyte solution was poor, and the apparent electron-transfer rate should be low compared to that of O-BDDP-printed electrode [8]. The slope of the calibration curve for O-BDDP-printed electrode was comparable to that for conventional H-BDD thin-film electrode [8], indicating that O-BDDP-printed electrode can be used as a highly sensitive and disposable electrode for CIP detection.

In order to simulate the detection of CIP in the human urine, CIP in artificial urine was detected using O-BDDP-printed electrode. Figure 8 shows the LSVs of CIP in artificial urine diluted 100-fold with 1/15 M phosphate buffer solution (PBS) [8]. A clear anodic peak was observed at + 1.0 V versus Ag/AgCl, and a good linear calibration curve was obtained in the CIP concentration range of 1–30 µM. According to a report by Wagenlehner et al., CIP of 407 mg/L (1,221 µM) was

https://www.twirpx.org & http://chemistry-chemists.com

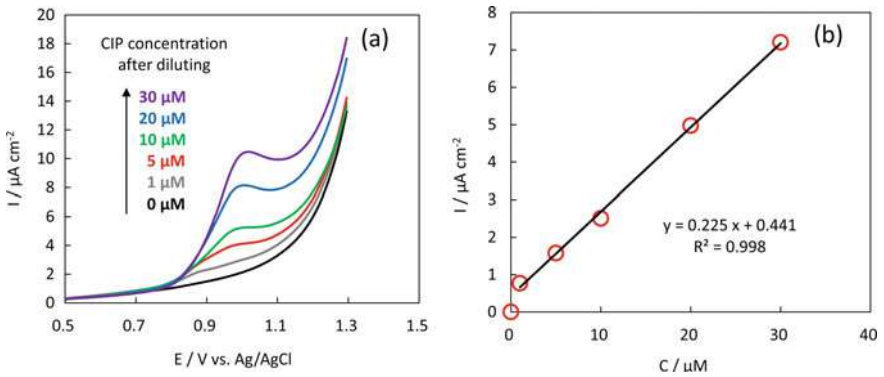

Fig. 8 **a** LSVs of CIP in artificial urine diluted 100 times in 1/15 M PBS at the O-BDDP-printed electrode. Potential sweep rate was 10 mV s^{-1}. **b** Calibration curve created from the data in panel a. Final concentrations (after dilution) are indicated in (a). Reprinted from [8], Copyright 2020, with permission from Elsevier

detected in the urine of healthy volunteers who received CIP [17]. Therefore, if urine contains CIP at this concentration level, CIP in urine can be measured from a sample diluted 100-fold with PBS at O-BDDP-printed electrode. Since CIP with a final concentration of 1–30 μM could be detected even from artificial urine diluted 10 times, the CIP in urine at a concentration range of 10–3,000 μM can be determined by adjusting the dilution ratio appropriately. From the above studies, it was shown that O-BDDP-printed electrode can be used as a disposable electrode exhibiting a highly sensitive detection of CIP.

3.3 Random Microelectrode Array Effect for Highly Sensitive Detection

BDDP inks for screen-printed diamond electrodes contain BDDP and an insulating binder (PES). In this case, the working electrode fabricated by printing is a composite film consisting of BDDP and PES. Thus, the conductive domain (BDDP) and the insulating domain (PES) are exposed to the electrolyte solution. In order to increase the total area of the conductive domain in contact with the electrolyte, the PES-to-BDDP (PES/BDDP) ratio should be as low as possible to the extent that a stable electrode layer can be formed. On the other hand, when the proportion of insulating domains is extremely large and the conductive domains having a size in the order of micrometers are isolated from each other, the individual conductive domains should behave as microelectrodes, and the entire printed electrode is expected to function as a microelectrode array. In this case, faradaic current at such an electrode (i.e., with a large PES/BDDP ratio) should be smaller than at conventional printed electrodes regarded as a planar electrode (i.e., with a small PES/BDDP ratio), but the S/B ratio

https://www.twirpx.org & http://chemistry-chemists.com

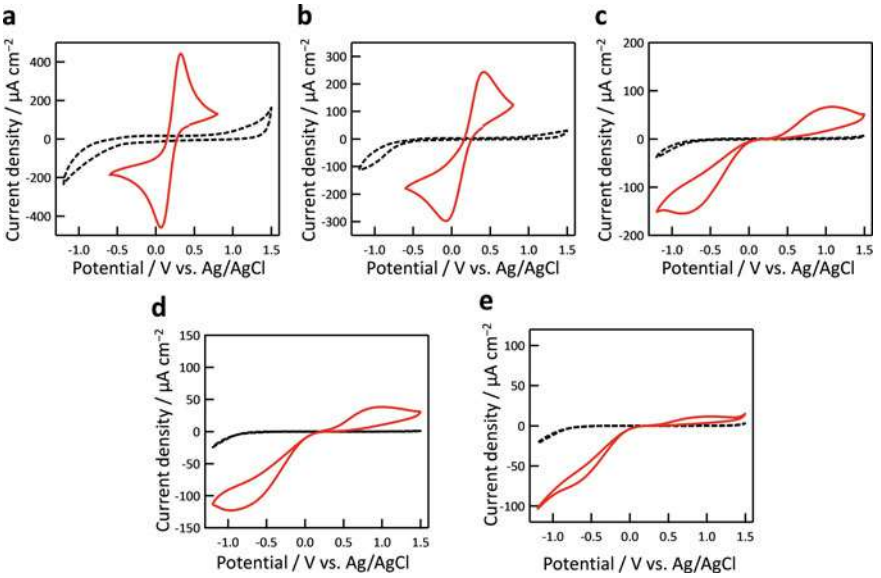

Fig. 9 CV for 5 mM $K_3Fe(CN)_6$ in 0.1 M Na_2SO_4 at the BDDP-printed electrodes with various PES/BDDP ratios of **a** 0.3, **b** 0.5, **c** 1.0, **d** 1.5, and **e** 2.0. Dashed lines indicate the background current. Potential sweep rate was 100 mV s^{-1}. Reprinted with permission from [14]. Copyright 2016 American Chemical Society

for the detection at the former electrode should be large due to very low background current. As a result, BDDP-printed electrodes with a large PES/BDDP ratio are expected show a highly sensitive electrochemical detection.

Figure 9 shows the CV of $K_3Fe(CN)_6$ at BDDP-printed electrodes prepared using BDDP inks with PES/BDDP ratios of 0.3, 0.5, 1.0, 1.5, and 2.0 [14]. When the PES/BDDP ratio was 0.3, the CV behavior was typical of a planar electrode showing a symmetrical redox peak pair. As the PES/BDDP ratio was increased, the peak separation of the redox peak pair increased, the peak current density decreased, and the asymmetry between anodic and cathodic peak currents became more pronounced. When the PES/BDDP ratio was 2.0, almost no anodic current was observed with a sigmoidal cathodic peak, which is a typical behavior of a microelectrode. This transition in the CV behavior was considered to be based on the transition of the type of diffusion layer: when the PES/BDDP ratio was small (0.3–0.5) and a linear diffusion layer was formed on the electrode surface as a planar electrode. However, as the PES/BDDP ratio increased, partially overlapped (PES/BDDP ratio of 1.0–1.5) and isolated hemispherical diffusion layers (PES/BDDP ratio of 2.0) were formed (Fig. 10) [14]. Figure 11 shows SEM and copper elemental map images obtained by energy-dispersive X-ray spectroscopy of the surface of BDDP-printed electrodes with PES/BDDP ratios of 0.5, 1.5, and 2.0 after the electrodeposition of copper from copper sulfate solution [14]. When the PES/BDDP ratio was 1.5 or 2.0, it was confirmed that the conductive domains with a size of several tens of micrometers were

https://www.twirpx.org & http://chemistry-chemists.com

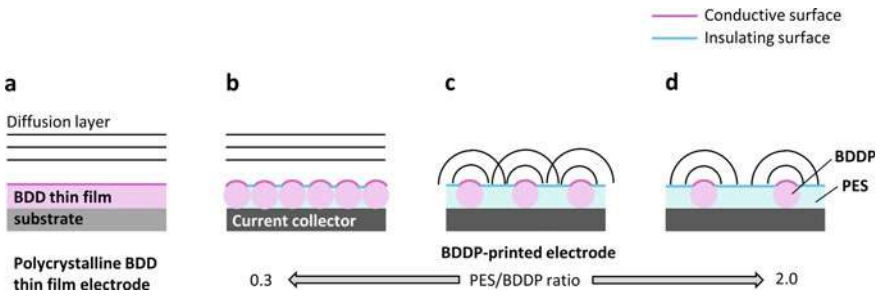

Fig. 10 Schematic illustration of the diffusion layers on polycrystalline BDD thin-film and BDDP-printed electrodes. Reprinted with permission from [14]. Copyright 2016 American Chemical Society

isolated from each other to form a sea-island structure (Fig. 11d, f) [14]. Therefore, it was found that a random microelectrode array based on such a sea-island structure consisting of insulating and conductive domains was formed on BDDP-printed electrode with a large PES/BDDP ratio.

Figure 12a–c shows differential pulse voltammograms (DPVs) in 0.1 M Na_2SO containing 8-hydroxy-2′-deoxyguanosine (8-OHdG) at various concentrations at polycrystalline BDD thin-film electrode and BDDP-printed electrodes (PES/BDDP ratios of 0.3 and 1.0) [14]. 8-OHdG is known to be an oxidative stress marker generated by oxidative DNA damage [18], and thus oxidative stress can be evaluated, for example, by measuring the concentration of 8-OHdG in urine [19–21]. At polycrystalline BDD thin-film electrode and BDDP-printed electrode with a PES/BDDP ratio of 0.3, a well-shaped anodic peak was observed and the peak current was confirmed to increase linearly with the concentration in the range of 3–35 μM. Comparing the S/B ratios of 8-OHdG detection from the DPV data, BDDP-printed electrode was found to show a larger S/B ratio than conventional polycrystalline BDD thin-film electrode (Fig. 12d) [14]. Although the peak current density at BDDP-printed electrode was smaller than that at BDD thin-film electrode, the very small background current at the printed electrode was more effective, resulting in a larger S/B ratio. In the case of BDDP-printed electrode with a PES/BDDP ratio of 1.0, the shape of the DPV anodic peak was distorted, the current value became smaller, and the peak shifted to positive potentials. However, the S/B ratio of 8-OHdG detection was larger than that of BDD thin-film or BDDP-printed electrode with a PES/BDDP of 0.3, and it was found that BDDP-printed electrode with a PES/BDDP of 1.0 enabled the most sensitive electrochemical detection among these electrodes. This was also based on the effect of the very low background current due to the small total surface area of the conductive domain on the electrode. Therefore, it was shown that BDDP-printed electrode with a large PES/BDDP ratio exhibits a random microelectrode array effect and is suitable for application to highly sensitive electrochemical analysis.

https://www.twirpx.org & http://chemistry-chemists.com

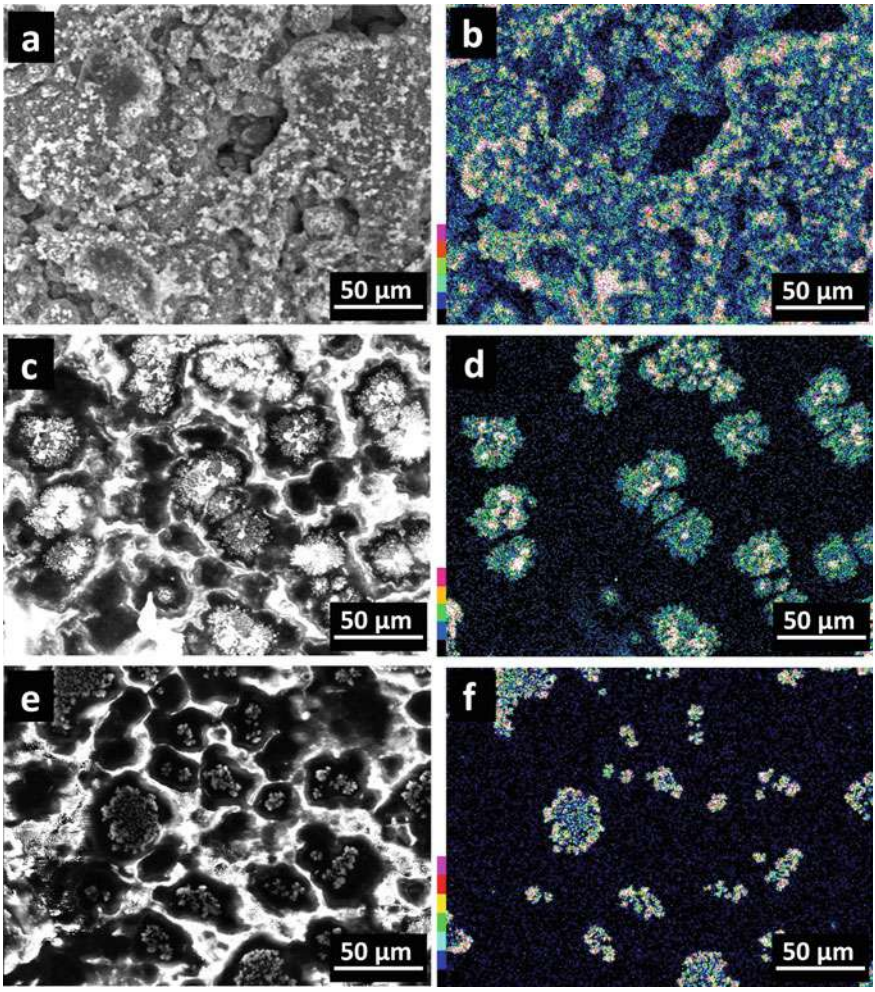

Fig. 11 **a**, **c**, **e** SEM images and **b**, **d**, **f** EDS elemental Cu maps of BDDP-printed electrode surfaces with PES/BDDP ratios of **a**, **b** 0.5, **c, d** 1.5 and **e**, **f** 2.0. Reprinted with permission from [14]. Copyright 2016 American Chemical Society

3.4 Other Applications

One of the advantages of preparing electrodes using BDDP ink is that it is easy to combine with other compounds and materials. For example, bare BDDP-printed electrodes cannot be used for electrochemical detection of hydrogen peroxide due to large over potential for the anodic reaction. However, CVs at printed electrodes prepared using BDDP ink containing cobalt phthalocyanine (CoPc) as an electrocatalyst showed a clear anodic peak for hydrogen peroxide oxidation [22]. Further,

https://www.twirpx.org & http://chemistry-chemists.com

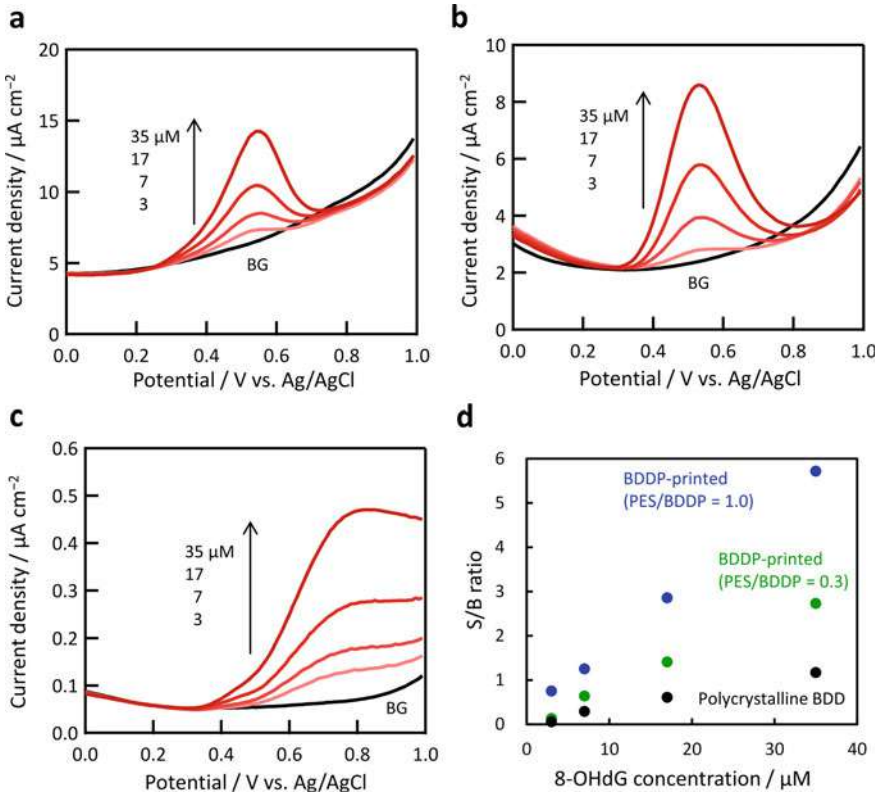

Fig. 12 DPV for 0.1 M Na_2SO_4 containing various concentrations of 8-OHdG using **a** the polycrystalline BDD thin film electrode, and BDDP-printed electrodes with PES/BDDP ratios of **b** 0.3 and **c** 1.0. Potential sweep rate, pulse height, and pulse width were 100 mV s^{-1}, 50 mV and 100 ms, respectively. **d** S/B ratio for 8-OHdG detection as a function of the 8-OHdG concentration. Reprinted with permission from [14]. Copyright 2016 American Chemical Society

a glucose sensor could be fabricated by coating the CoPc/BDDP-printed electrode surface with a glucose oxidase-immobilized layer [22].

In addition to screen printing, the use of a stencil is another and easy way to fabricate electrodes using BDDP ink. Nantaphol et al. developed microfluidic and electrochemical paper-based analytical devices (μPADs and ePADs) by using BDDP ink as the electrode material [23, 24]. They are inexpensive and disposable devices and can be applied to electrochemical detection of neurotransmitters and heavy metal ions with high sensitivity. In this way, it is possible to manufacture inexpensive analytical devices using various substrates by printing BDDP ink to form electrodes. It is considered that mass production of lightweight, inexpensive, and highly functional printed diamond electrodes becomes possible by optimizing the ink conditions (e.g., binder content, addition of catalyst).

https://www.twirpx.org & http://chemistry-chemists.com

4 Application to Cathode Catalyst Support for PEFC

4.1 Durable Support for PEFC Cathode Catalyst

PEFC is a promising power generation system that can be used for portable devices and electric vehicles and have the advantages of low operating temperature, high-theoretical energy efficiency, and fast start-up [25, 26]. Platinum-supported carbon (Pt/C) is commonly used as a cathode catalyst of PEFC. One of the major issues of the Pt/C catalyst is corrosion of carbon support that can limit the durability of PEFC. Especially when applied to automobiles, the cathode is exposed to a highly positive potential during frequent start–stop operations, which causes oxidative corrosion of the carbon support [25, 27, 28]. There are several reports on durable cathode catalyst support such as SnO_2, Nb–SnO_2 [29], TiO_x, TiN [30], and polymer-coated CNTs [31] with excellent oxidation resistance. BDDP is also a candidate for highly durable catalyst support. Spătaru et al. reported the development of a highly active and durable methanol oxidation catalyst using BDDP or surface-modified BDDP as a support [32–34]. In this study, we prepared a Pt/BDDP catalyst with platinum nanoparticles supported on the BDDP surface and evaluated its electrochemical properties toward application to cathode catalyst for PEFC. Catalytic activity for oxygen reduction reaction (ORR) and durability to highly positive potentials were investigated.

4.2 Preparation of Pt/BDDP

Pt/BDDP was prepared via the nanocapsule method described in literature [35, 36]. Briefly, platinum acetylacetonate ($Pt(acac)_2$) was incorporated in reverse micelles consisting of surfactants (oleylamine and oleic acid) formed in organic solvent (diphenyl ether containing 1,2-hexadecanediol). After adding BDDP, $NaBH_4$, a reducing agent, was added into the solution to obtain Pt/BDDP. Figure 13 shows transmission electron microscopy (TEM) images of Pt/BDDP. Platinum nanoparticles were confirmed to have a particle diameter of 2–5 nm and were dispersed densely and supported on the BDDP surface. The particle size estimated from the diffraction peaks of Pt in the X-ray diffraction pattern using the Scherrer equation was 4.5 nm, which was consistent with the result of TEM observation [36]. From the results above, the nanocapsule method was confirmed to be suitable as a method for preparation of Pt/BDDP with relatively small Pt nanoparticles being densely supported on the BDDP surface.

https://www.twirpx.org & http://chemistry-chemists.com

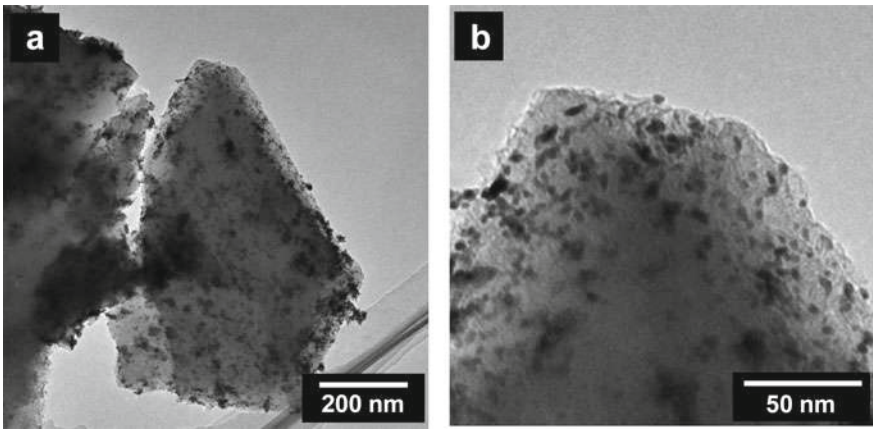

Fig. 13 TEM images of **a** Pt/BDDP-300. Panel **b** is magnified image of a. Reprinted from [36] by The Authors licensed under CC BY 4.0

4.3 Electrochemical Properties of Pt/BDDP

Figure 14 shows CVs in 1.0 M HClO4 of Pt/C (commercially available 10 wt% Pt-supported carbon black) and of Pt/BDDP-300 and Pt/BDDP-200 prepared using BDDP with an average particle size of 300 and 200 nm, respectively [36]. Redox peaks typical of platinum were observed in all CVs, confirming that the Pt nanoparticles supported on BDDP were electrochemically active. Figure 15 shows LSVs recorded by rotating disk electrode (RDE) method in O_2- saturated 1.0 M $HClO_4$ [36]. At bare BDDP-300, no cathodic current for ORR was observed. In contrast, the cathodic current for ORR was observed at Pt/BDDP-300 with an onset potential similar to Pt/C. From this result, Pt nanoparticles supported on the BDDP surface were confirmed to have a sufficient catalytic activity for ORR.

4.4 Durability Test

In order to evaluate the durability of Pt/BDDP as a PEFC cathode catalyst, a potential cycle test in a highly positive potential range (from + 1.0 to + 1.5 V versus NHE at a scan rate of 0.5 V s^{-1}) simulating the start–stop operation of a fuel cell was performed in argon-purged 1.0 M $HClO_4$. The durability of the catalyst was evaluated using electrochemically active surface area (ECA). ECA was calculated from the following equation using the charge amount Q_H (in microcoulombs) of the reductive adsorption peak of H_2 (typically ca. + 0.1 to + 0.3 V vs. NHE) of CV in 1.0 M $HClO_4$, weight of platinum contained in Pt/BDDP wPt (in grams), and hydrogen adsorption charge amount on a smooth polycrystalline platinum surface (210 μC cm^{-2}) [37]:

$$\text{ECA}\ [\text{m}^2\ \text{g-Pt}^{-1}] = Q_H/(210 \times 10^4\ \mu\text{C m}^{-2} \times w_{Pt}).$$

https://www.twirpx.org & http://chemistry-chemists.com

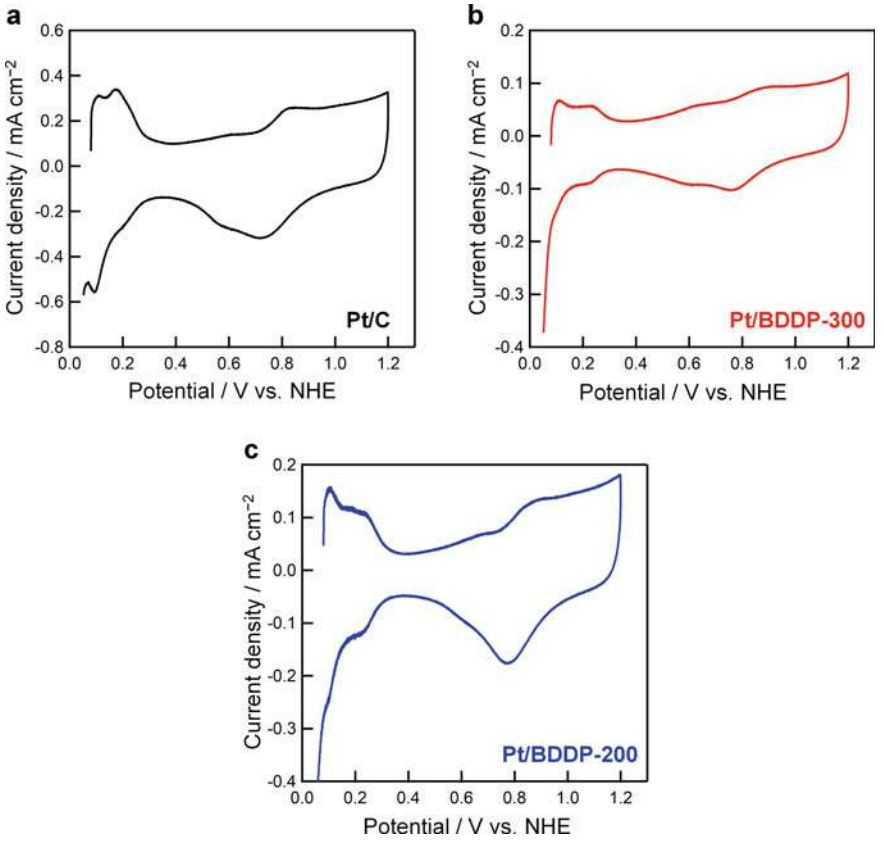

Fig. 14 CV in 1.0 M $HClO_4$ at **a** Pt/C, **b** Pt/BDDP-300, and **c** Pt/BDDP-200 electrodes. Potential sweep rate was 30 mV s^{-1}. Reprinted from [36] by The Authors licensed under CC BY 4.0

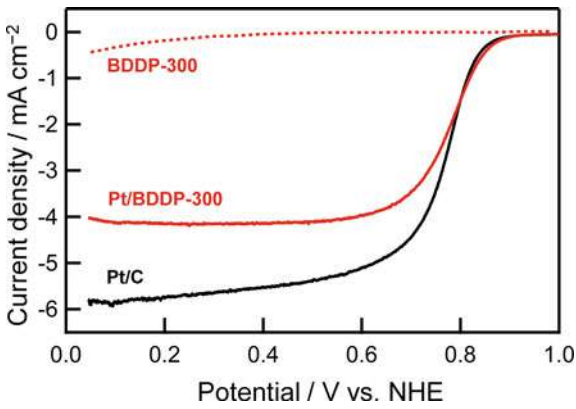

Fig. 15 LSV in O_2-satrated 1.0 M $HClO_4$ at BDDP-300, Pt/BDDP-300, and Pt/C electrodes recorded by the RDE method. Rotation speed was 1,000 rpm. Potential sweep rate was 10 mV s^{-1}. Reprinted from [36] by The Authors licensed under CC BY 4.0

https://www.twirpx.org & http://chemistry-chemists.com

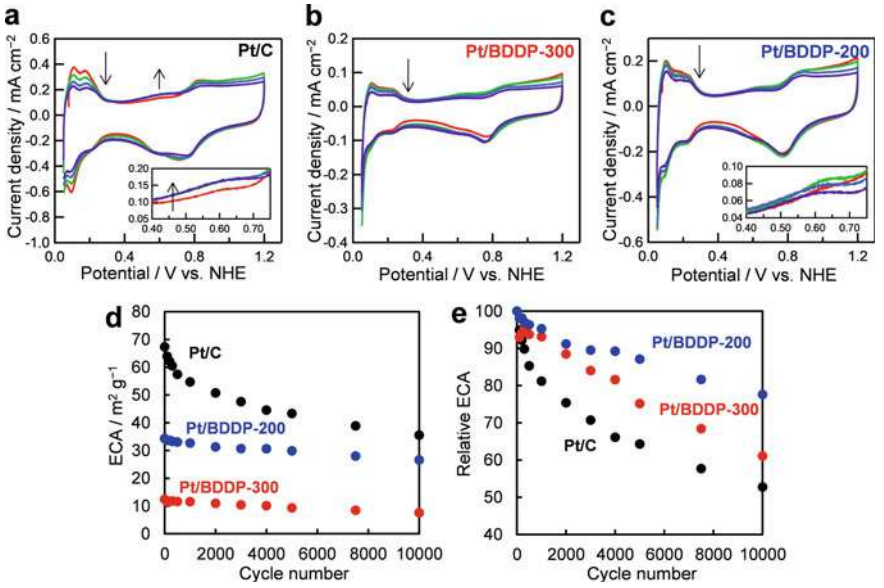

Fig. 16 CV in 1.0 M $HClO_4$ at **a** Pt/C, **b** Pt/BDD-300, and **c** Pt/BDDP-200 electrodes before and after the potential cycle test (1,000, 5,000, and 10,000 cycles). Arrows indicate this order of the curves. Potential sweep rate was 30 mV s^{-1}. Insets indicate the magnified curves of the anodic scan. **d** ECA and **e** normalized ECA evaluated from the CV as a function of potential cycle test cycle number. Reprinted from [36] by The Authors licensed under CC BY 4.0

Figure 16a–c shows the CVs measured before and after 1,000, 5,000, and 10,000 cycles of the test [36]. In the CV of Pt/C, the current density of the redox peak derived from the platinum surface (+0.1 to + 0.3 V vs. NHE) decreased with increasing cycle number. It was also found that the current density of the redox peak possibly for quinone/hydroquinone group on the carbon surface at +0.6 V versus NHE increased as the potential cycle number increased. This suggested that the potential cycles at a highly positive potential range caused corrosion of the carbon support and desorption of platinum from the surface. On the other hand, no change in the CV shape for Pt/BDDP due to such a change in the surface of the support was observed, suggesting sufficient stability of BDDP to application of highly positive potentials. Focusing on the change in ECA with respect to the potential cycle, Pt/C tended to decrease rapidly by 1,000 cycles and then gradually (Fig. 16d, e) [36]. On the other hand, in the case of Pt/BDDP, there was no such rapid decrease in ECA at the initial stage. Comparing ECA after 10,000 cycles, the ECA at Pt/C decreased to 53% of the initial ECA, while that at Pt/BDDP-300 and at Pt/BDDP-200 was 61% and 78%, respectively. The initial deterioration of ECA at Pt/C was considered caused by the aggregation and desorption of Pt particles due to carbon corrosion [38]. On the other hand, corrosion of the BDDP should hardly occur. The decrease in ECA was considered to be due to aggregation of platinum particles on the BDDP surface during the test. The platinum particles on the BDDP surface have basically the same activity as those on the carbon

https://www.twirpx.org & http://chemistry-chemists.com

support, and it was found that BDDP functions as a support with excellent corrosion resistance. Therefore, if platinum can be supported more strongly on the BDDP surface, a more durable cathode catalyst is expected to be obtained for improvement in PEFC durability.

5 Conclusions

The fabrication of BDDP, a conductive diamond powder, and its applications including screen-printed electrodes and PEFC cathode catalysts were described. BDDP is an electrode material that basically exhibits the basic characteristics typical of diamond electrodes (e.g., wide potential window, low background current, excellent stability). Thus, BDDP can replace and exceed conventional carbonaceous powder as a conductive powder material in some situations. BDDP is a basic material that can be obtained with an arbitrary particle size to some extent and can be used widely in the fields of electrochemical sensors, electrolysis, and electrochemical energy devices (e.g., fuel cells, electrochemical capacitor), by making it into paste or ink to form electrodes and by combining it with other materials for functionalization. It is also possible to manufacture electrodes and devices with BDDP using lightweight, inexpensive, and flexible substrates like resin films and papers. Development of mass production of high-quality BDDP should enable its practical use in a wide range of electrochemical application fields.

Acknowledgements The author appreciates the support of this work by KAKENHI (No. 26410246) grants from the Japan Society for the Promotion of Sciences (JSPS) , by Tokyo Ohka Foundation for the Promotion of Science and Technology, and by the Joint Usage/Research Program of the Photocatalysis International Research Center, Research Institute for Science and Technology, Tokyo University of Science.

References

1. Shakhov FM, Abyzov AM, Takai K (2017) Boron doped diamond synthesized from detonation nanodiamond in a C-O-H fluid at high pressure and high temperature. J Solid State Chem 256:72–92. https://doi.org/10.1016/j.jssc.2017.08.009
2. Heyer S, Janssen W, Turner S, Lu Y-G, Yeap WS, Verbeeck J, Haenen K, Krueger A (2014) Toward deep blue nano hope diamonds: heavily boron-doped diamond nanoparticles. ACS Nano 8(6):5757–5764. https://doi.org/10.1021/nn500573x
3. Fischer AE, Swain GM (2005) Preparation and characterization of boron-doped diamond powder. J Electrochem Soc 152(9):B369. https://doi.org/10.1149/1.1984367
4. Ay A, Swope VM, Swain GM (2008) The physicochemical and electrochemical properties of 100 and 500 nm diameter diamond powders coated with boron-doped nanocrystalline diamond. J Electrochem Soc 155(10):B1013. https://doi.org/10.1149/1.2958308
5. Kondo T, Nakajima K, Osasa T, Kotsugai A, Shitanda I, Hoshi Y, Itagaki M, Aikawa T, Tojo T, Yuasa M (2018) Effect of substrate size on the electrochemical properties of boron-doped

https://www.twirpx.org & http://chemistry-chemists.com

diamond powders for screen-printed diamond electrode. Chem Lett 47(12):1464–1467. https://doi.org/10.1246/cl.180672
6. Kondo T, Sakamoto H, Kato T, Horitani M, Shitanda I, Itagaki M, Yuasa M (2011) Screen-printed diamond electrode: a disposable sensitive electrochemical electrode. Electrochem Commun 13(12):1546–1549. https://doi.org/10.1016/j.elecom.2011.10.013
7. Osswald S, Yushin G, Mochalin V, Kucheyev SO, Gogotsi Y (2006) Control of sp(2)/sp(3) carbon ratio and surface chemistry of nanodiamond powders by selective oxidation in air. J Am Chem Soc 128(35):11635–11642. https://doi.org/Doi10.1021/Ja063303n
8. Matsunaga T, Kondo T, Osasa T, Kotsugai A, Shitanda I, Hoshi Y, Itagaki M, Aikawa T, Tojo T, Yuasa M (2020) Sensitive electrochemical detection of ciprofloxacin at screen-printed diamond electrodes. Carbon 159:247–254. https://doi.org/10.1016/j.carbon.2019.12.051
9. Albareda-Sirvent M, Merkoçi A, Alegret S (2000) Configurations used in the design of screen-printed enzymatic biosensors. Review Sens Actuat B Chem 69 (1):153–163. doi:https://doi.org/10.1016/S0925-4005(00)00536-0
10. Heller A, Feldman B (2008) Electrochemical glucose sensors and their applications in diabetes management. Chem Rev 108(7):2482–2505. https://doi.org/10.1021/cr068069y
11. Tudorache M, Bala C (2007) Biosensors based on screen-printing technology, and their applications in environmental and food analysis. Anal Bioanal Chem 388(3):565–578. https://doi.org/10.1007/s00216-007-1293-0
12. Darain F, Park S-U, Shim Y-B (2003) Disposable amperometric immunosensor system for rabbit IgG using a conducting polymer modified screen-printed electrode. Biosens Bioelectron 18(5):773–780. https://doi.org/10.1016/S0956-5663(03)00004-6
13. Shitanda I, Takamatsu S, Watanabe K, Itagaki M (2009) Amperometric screen-printed algal biosensor with flow injection analysis system for detection of environmental toxic compounds. Electrochim Acta 54(21):4933–4936. https://doi.org/10.1016/j.electacta.2009.04.005
14. Kondo T, Udagawa I, Aikawa T, Sakamoto H, Shitanda I, Hoshi Y, Itagaki M, Yuasa M (2016) Enhanced sensitivity for electrochemical detection using screen-printed diamond electrodes via the random microelectrode array effect. Anal Chem 88(3):1753–1759. https://doi.org/10.1021/acs.analchem.5b03986
15. Martin Santos A, Wong A, Araújo Almeida A, Fatibello-Filho O (2017) Simultaneous determination of paracetamol and ciprofloxacin in biological fluid samples using a glassy carbon electrode modified with graphene oxide and nickel oxide nanoparticles. Talanta 174:610–618. https://doi.org/10.1016/j.talanta.2017.06.040
16. Johnson AC, Keller V, Dumont E, Sumpter JP (2015) Assessing the concentrations and risks of toxicity from the antibiotics ciprofloxacin, sulfamethoxazole, trimethoprim and erythromycin in European rivers. Sci Total Environ 511:747–755. https://doi.org/10.1016/j.scitotenv.2014.12.055
17. Wagenlehner FME, Wydra S, Onda H, Kinzig-Schippers M, Sörgel F, Naber KG (2003) Concentrations in Plasma, urinary excretion, and bactericidal activity of linezolid (600 Milligrams) versus those of ciprofloxacin (500 Milligrams) in healthy volunteers receiving a single oral dose. Antimicrob Agents Chemother 47(12):3789–3794. https://doi.org/10.1128/aac.47.12.3789-3794.2003
18. Loft S, Vistisen K, Ewertz M, Tjønneland A, Overvad K, Poulsen HE (1992) Oxidative DNA damage estimated by 8-hydroxydeoxyguanosine excretion in humans: influence of smoking, gender and body mass index. J Article 13(12):2241–2247
19. Kato D, Komoriya M, Nakamoto K, Kurita R, Hirono S, Niwa O (2011) Electrochemical determination of oxidative damaged DNA with high sensitivity and stability using a nanocarbon film. Anal Sci 27(7):703–707
20. Wu LL, Chiou C-C, Chang P-Y, Wu JT (2004) Urinary 8-OHdG: a marker of oxidative stress to DNA and a risk factor for cancer, atherosclerosis and diabetics. Clin Chim Acta 339(1–2):1–9. https://doi.org/10.1016/j.cccn.2003.09.010
21. Yao Q-H, Mei S-R, Weng Q-F, Zhang P-d, Yang Q, Wu C-y, Xu G-W (2004) Determination of urinary oxidative DNA damage marker 8-hydroxy-2′-deoxyguanosine and the association with cigarette smoking. Talanta 63(3):617–623. https://doi.org/10.1016/j.talanta.2003.12.024

https://www.twirpx.org & http://chemistry-chemists.com

22. Kondo T, Horitani M, Sakamoto H, Shitanda I, Hoshi Y, Itagaki M, Yuasa M (2013) Screen-printed modified diamond electrode for glucose detection. Chem Lett 42(4):352–354. https://doi.org/10.1246/cl.121242
23. Nantaphol S, Channon RB, Kondo T, Siangproh W, Chailapakul O, Henry CS (2017) Boron doped diamond paste electrodes for microfluidic paper-based analytical devices. Anal Chem 89(7):4100–4107. https://doi.org/10.1021/acs.analchem.6b05042
24. Nantaphol S, Kava AA, Channon RB, Kondo T, Siangproh W, Chailapakul O, Henry CS (2019) Janus electrochemistry: simultaneous electrochemical detection at multiple working conditions in a paper-based analytical device. Anal Chim Acta 1056:88–95. https://doi.org/10.1016/j.aca.2019.01.026
25. Yu X, Ye S (2007) Recent advances in activity and durability enhancement of Pt/C catalytic cathode in PEMFC: Part II: degradation mechanism and durability enhancement of carbon supported platinum catalyst. J Power Sources 172(1):145–154. https://doi.org/10.1016/j.jpowsour.2007.07.048
26. Wee J-H, Lee K-Y, Kim SH (2007) Fabrication methods for low-Pt-loading electrocatalysts in proton exchange membrane fuel cell systems. J Power Sources 165(2):667–677. https://doi.org/10.1016/j.jpowsour.2006.12.051
27. Roen LM, Paik CH, Jarvi TD (2004) Electrocatalytic corrosion of carbon support in PEMFC Cathodes. Electrochem Solid-State Lett 7(1):A19–A22. https://doi.org/10.1149/1.1630412
28. Meyers JP, Darling RM (2006) Model of carbon corrosion in PEM fuel cells. J Electrochem Soc 153(8):A1432–A1442. https://doi.org/10.1149/1.2203811
29. Tsukatsune T, Takabatake Y, Noda Z, Daio T, Zaitsu A, Lyth SM, Hayashi A, Sasaki K (2014) Platinum-Decorated tin oxide and niobium-doped tin oxide PEFC electrocatalysts: oxygen reduction reaction activity. J Electrochem Soc 161(12):F1208–F1213. https://doi.org/10.1149/2.0431412jes
30. Shintani H, Kakinuma K, Uchida H, Watanabe M, Uchida M (2015) Performance of practical-sized membrane-electrode assemblies using titanium nitride-supported platinum catalysts mixed with acetylene black as the cathode catalyst layer. J Power Sources 280(Supplement C):593–599. doi:https://doi.org/10.1016/j.jpowsour.2015.01.132
31. Berber MR, Hafez IH, Fujigaya T, Nakashima N (2015) A highly durable fuel cell electrocatalyst based on double-polymer-coated carbon nanotubes. Sci Rep 5:16711. https://doi.org/10.1038/srep16711
32. Preda L, Kondo T, Spataru T, Marin M, Radu M, Osiceanu P, Fujishima A, Spataru N (2017) Enhanced activity for methanol oxidation of platinum particles supported on iridium oxide modified boron-doped diamond powder. ChemElectroChem 4(8):1908–1915. https://doi.org/10.1002/celc.201700155
33. Spătaru T, Kondo T, Anastasescu C, Balint I, Osiceanu P, Munteanu C, Spătaru N, Fujishima A (2017) Silica veils-conductive diamond powder composite as a new propitious substrate for platinum electrocatalysts. J Solid State Electrochem 21(4):1007–1014. https://doi.org/10.1007/s10008-016-3454-6
34. Spătaru N, Calderon-Moreno JM, Osiceanu P, Kondo T, Terashima C, Popa M, Radu MM, Culiţă D, Preda L, Mihai MA, Spătaru T (2020) Conductive diamond powder inclusion in drop-casted graphene for enhanced effectiveness as electrocatalyst substrate. Chem Eng J 402:126258. https://doi.org/10.1016/j.cej.2020.126258
35. Yano H, Kataoka M, Yamashita H, Uchida H, Watanabe M (2007) Oxygen reduction activity of carbon-supported Pt−M (M = V, Ni, Cr Co, and Fe) alloys prepared by nanocapsule method. Langmuir 23(11):6438–6445. https://doi.org/10.1021/la070078u
36. Kondo T, Kikuchi M, Masuda H, Katsumata F, Aikawa T, Yuasa M (2018) Boron-doped diamond powder as a durable support for platinum-based cathode catalysts in polymer electrolyte fuel cells. J Electrochem Soc 165(6):F3072–F3077. https://doi.org/10.1149/2.0111806jes

https://www.twirpx.org & http://chemistry-chemists.com

37. Binninger T, Fabbri E, Kötz R, Schmidt TJ (2014) Determination of the electrochemically active surface area of metal-oxide supported platinum catalyst. J Electrochem Soc 161(3):H121–H128. https://doi.org/10.1149/2.055403jes
38. Monzo J, van der Vliet DF, Yanson A, Rodriguez P (2016) Elucidating the degradation mechanism of the cathode catalyst of PEFCs by a combination of electrochemical methods and X-ray fluorescence spectroscopy. Phys Chem Chem Phys 18(32):22407–22415. https://doi.org/10.1039/C6CP03795J

https://www.twirpx.org & http://chemistry-chemists.com

Electrogenerated Chemiluminescence at Diamond Electrode

Irkham, Andrea Fiorani, and Yasuaki Einaga

Abstract Electrogenerated chemiluminescence (also known as *electrochemiluminescence* and abbreviated ECL) is a complex phenomenon of luminescence triggered by electrochemical reactions where the heterogeneous electron transfer, then ECL as consequence, is affected by the electrode materials which is crucial in the signal development and intensity. Among electrode materials, doped diamond electrodes are still underdeveloped for ECL application especially compared to the more commons noble metals and other carbon-based. After a brief and general introduction on electrochemiluminescence, this chapter will focus on several studies and developments of doped diamond electrodes by taking advantage on its own unique properties as the electrode for ECL.

1 Introduction

Electrochemiluminescence is the process of photons emission from a molecular specie (the luminophore) that undergo homogenous electron transfer (ET) in solution, which is triggered by a heterogeneous electrochemical reaction [1, 2]. The development of ECL started in the mid-1960s with the pioneering works of Hercules [3], Chandross [4] and Bard [5].

Generally, the ECL process starts with two species, an electron donor and an electron acceptor, that are produced at the surface of electrode which later undergo

Irkham (✉) · A. Fiorani · Y. Einaga
Department of Chemistry, Keio University, 3-14-1 Hiyoshi, Yokohama 223−8522, Japan
e-mail: irkham@unpad.ac.id

A. Fiorani
e-mail: andrea.fiorani@keio.jp

Y. Einaga
e-mail: einaga@chem.keio.ac.jp

Irkham
Department of Chemistry, Padjadjaran University, Jalan Raya Bandung Sumedang Km. 21, Sumedang 45363, Indonesia

© Springer Nature Singapore Pte Ltd. 2022

Y. Einaga (ed.), *Diamond Electrodes*,
https://doi.org/10.1007/978-981-16-7834-9_8

https://www.twirpx.org & http://chemistry-chemists.com

a homogeneous ET to generate the excited state. The formation of the excited stated instead of the fundamental state has been rationalized by Marcus theory of ET [1, 2, 6]. Depending on the generation pathways, it is possible to recognize two types of ECL: annihilation and coreactant mechanisms.

In annihilation ECL, the luminophore is either oxidized and reduced by a transient electrochemical technique or by two separate electrodes in close proximity. When the two radicals encounter in the diffusion layer, a homogeneous ET results in the formation of the excided state. Although the approach is generally simple, only the luminophore is needed, annihilation ECL requires a high energy to generated both radicals (in the range of 2–3 eV), which is usually difficult to achieved in an aqueous solution due to the narrow potential window of water [7].

On the other hand, in coreactant ECL a sacrificial molecule (coreactant) is used in combination with the luminophore. Subsequent to its oxidation or reduction, the coreactant undergoes a chemical decomposition to form a highly reducing or oxidizing intermediate. The ET between this coreactant radical intermediate and the luminophore, also in its oxidized or reduced form, lead to the excited state of the luminophore. Consequently, the coreactant ECL emission can be achieved by a single potential step (either oxidation or reduction) and within the limited potential window of aqueous solutions which paved the way for analytical applications.

Through the years, ECL developed into a powerful transduction technique for analytical applications, mainly but not limited to important biological targets [8–10], and recently to imaging of cells and nanomaterials [11–14].

Some features of ECL include (i) an excellent signal-to-noise ratio with typical detection limit of pM; (ii) broad dynamic range of more than 6 order magnitude; (iii) rapid measurement; small working volume (tens of μL), which could be achieved thanks to the combination of electrochemical stimulus and luminescent response.

Since ECL is primary triggered by a heterogeneous electron transfer, electrode materials are crucial in the signal development and intensity [15–17]. Among electrode materials, doped diamond electrodes are still underdeveloped for ECL applications especially compared to the more commons noble metals (i.e., Pt, Au) and other carbon-based electrode such as glassy carbon (GC), carbon nanotubes or graphene [18]. The fact that doped diamond electrode, typically boron-doped diamond (BDD), has several advantages in the aqueous solution compared to over mentioned electrode (wide potential window, low background current, high stability and durability) should make BDD also a suitable candidate for ECL applications. In this chapter, we will focus on several studies and development of the BDD electrode which take advantage of its own unique properties.

The research on ECL at diamond electrodes deals mainly with the coreactant mechanism, which is categorized in "oxidative-reduction" and "reductive-oxidation" ECL.

https://www.twirpx.org & http://chemistry-chemists.com

2 Oxidative-Reduction ECL

Generally, in the oxidative-reduction ECL, the light is generated by oxidation in a single potential step or sweep. The mechanism starts with both luminophore and coreactant oxidation. The oxidized form of the coreactant then generates a strong reducing radical via a chemical step (e.g., bond cleavage, deprotonation). An electron transfer between this radical and the oxidized luminophore leads to ECL. The most investigated luminophore and coreactant couple for oxidative-reduction ECL, including at diamond electrodes, is $Ru(bpy)_3^{2+}$ and tri-*n*-propylamine (TPrA) [19–21]. In fact, it is the only couple able to give ECL without $Ru(bpy)_3^{2+}$ oxidation, but only TPrA oxidation [22–24], and the only couple that is used in commercial ECL applications. Other coreactant such as oxalate [25] and hydroxyl radicals [26] have also been reported for oxidative-reduction ECL at diamond electrodes.

2.1 TPrA Coreactant System

The ECL of TPrA coreactant coupled with $Ru(bpy)_3^{2+}$ on BDD was compared with the more common Pt and GC electrodes [20]. Figure 1 shows the electrochemical and ECL behavior by cyclic voltammetry of as-deposited boron-doped diamond, GC and Pt electrodes. At diamond electrode, ECL starts around 1.0 V with three ECL waves at 1.30 V, 1.89 and 2.33 V. The first ECL peak corresponds to the potential of $Ru(bpy)_3^{2+}$ oxidation, following the catalytic route mechanism of Eqs. 1–5.

$$Ru(bpy)_3^{2+} - e^- \nabla Ru(bpy)_3^{3+} \tag{1}$$

$$Ru(bpy)_3^{3+} + TPrA \nabla Ru(bpy)_3^{2+} + TPrA^{\bullet+} \tag{2}$$

$$TPrA^{\bullet+} \nabla TPrA^{\bullet} + H^+ \tag{3}$$

$$Ru(bpy)_3^{3+} + TPrA^{\bullet} \nabla Ru(bpy)_3^{2+\prime} + Pr_2N^+ = CHCH_2CH_3 \tag{4}$$

$$Ru(bpy)_3^{2+\prime} \nabla Ru(bpy)_3^{2+} + hv \tag{5}$$

The second ECL peak is related with direct oxidation of TPrA at the BDD electrode (Eq. 6), in fact the second voltammetric wave is obtained at ca. 1.8 V, the same potential as the second ECL peak, following the mechanism of Eqs. 1, 6, 3–5.

$$TPrA - e^- \nabla + TPrA^{\bullet+} \tag{6}$$

https://www.twirpx.org & http://chemistry-chemists.com

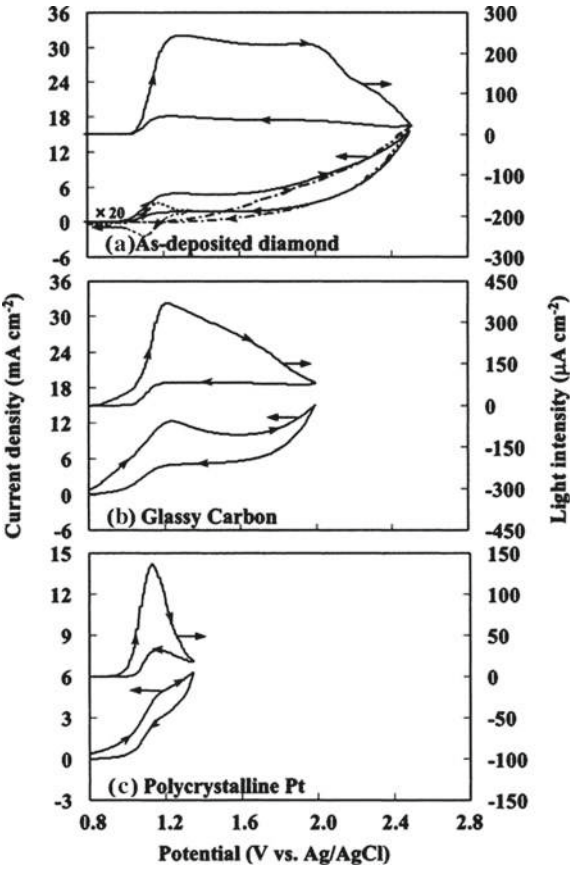

Fig. 1 Cyclic voltammograms and ECL curves at **a** as-deposited boron-doped diamond, **b** glassy carbon, and **c** polycrystalline Pt electrodes in 200 mM phosphate buffer solution containing 300 μM $Ru(bpy)_3^{2+}$ and 100 mM TPrA. The dotted line is without TPrA, the dot-dashed line is without $Ru(bpy)_3^{2+}$. Reprinted (Adapted or Reprinted in part) with permission from [20]. Copyright 2003 American Chemical Society

The higher overpotential, compared to GC, is due to the fact that redox species with inner sphere electron transfer are oxidized at relatively higher potential on diamond electrodes (as in the case of oxygen evolution from water oxidation).

For this reason, it is believed that the mechanism with direct oxidation of TPrA plays a small role in the first ECL peak.

The third ECL shoulder is related to the direct oxidation of the dealkylation products of TPrA, since secondary and primary amines are supposed to undergo oxidation at higher potential than a tertiary amine. The mechanism would be similar to that described in Eqs. 1, 6, 3–5. Instead of TPrA, the secondary and primary amines will act as the coreactant.

The long-term behavior, of ECL for the $Ru(bpy)_3^{2+}$/TPrA system, was compared for BDD, GC, and Pt electrodes by cycling up to 1000 times, to evaluate the relative stability (Fig. 2).

BDD electrode shows the highest persistence of ECL intensity, nearly constant at 90%. In contrast, ECL at GC decreases dramatically, reaching 23% of the initial value, while at Pt, the relative ECL intensity decreases linearly with the cycle number

https://www.twirpx.org & http://chemistry-chemists.com

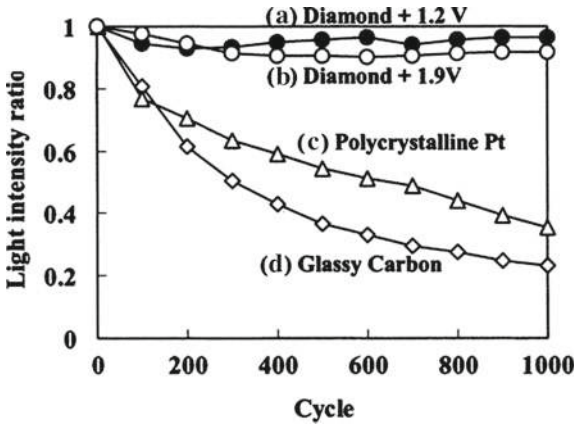

Fig. 2 Correlation of the relative ECL peak intensity and the number of the potential cycling. The ECL peak of polycrystalline Pt (C) and for the GC (D) electrodes is at 1.2 V versus Ag/AgCl. Reprinted (Adapted or Reprinted in part) with permission from [20]. Copyright 2003 American Chemical Society

reaching 35% at the end of the cycling. The low adsorption properties of BDD and resistance to fouling are most likely the reasons for this high stability compared to GC and Pt [27].

ECL, from electroanalytical technique can be turned to a powerful imaging technique if coupled with optical microscopy [11–13, 21, 23, 28–30]. When applied on BBD, ECL imaging enables to visualize the heterogeneity in electrochemical activity of the polycrystalline diamond surface [31].

Figure 3 shows the imaging of ECL emission for (100), (111) and randomly oriented growth sectors of BDD, with the plotted ECL intensity lines for the three different zone represented in Fig. 4.

The ECL emission at (100)-oriented microcrystallite shows the lowest intensity, which is approximately 50% of that for (111), while the ECL intensity for the (111) growth sector is similar to the ECL intensity at randomly oriented BDD. The ECL intensity for the (100) growth sector increases linearly with increasing potential, and it requires more overpotential than other regions to drive the ECL reaction. This suggests a remarkably lower conductivity at (100)-oriented microcrystallite than that for (111). This results from the microcrystallite-based heterogeneity of boron concentration, since heavily doped polycrystalline diamond contains microcrystals with different boron doping levels, i.e., semiconductor and semi-metallic diamond microcrystals. The microstructural heterogeneity of boron concentration leads to electrochemical reactivity heterogeneity at the heavily doped polycrystalline diamond.

The highest ECL peaks at the edges of the (100) and (111) facet are ascribed to diffusion effects. The ridges of microcrystallite form pointed-edge lines toward the solution and the reactant molecules could be supplied to the ridge regions by semispherical diffusion, enhancing the reaction rate of ECL.

https://www.twirpx.org & http://chemistry-chemists.com

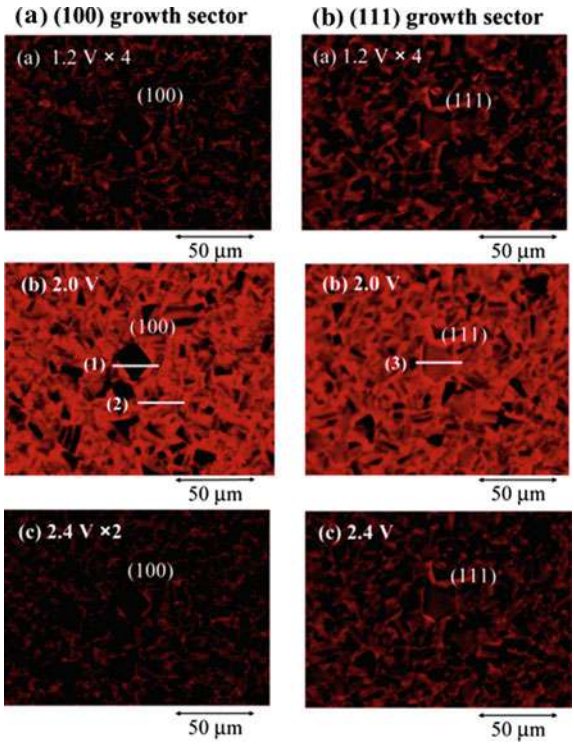

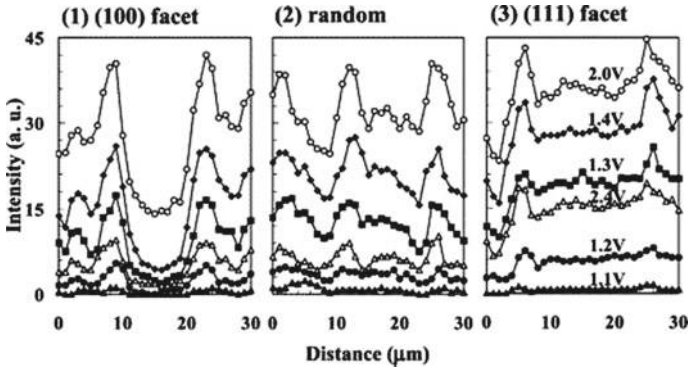

Fig. 3 ECL images of the boron-doped polycrystalline diamond electrode during chronoamperometric measurements at **a** 1.2, **b** 2.0, and **c** 2.4 V for 5 s, in 200 mM phosphate buffer solution containing 300 µM $Ru(bpy)_3^{2+}$ and 100 mM TPrA. First step at 0.4 V. Reprinted (Adapted or Reprinted in part) with permission from [31]. Copyright 2004 American Chemical Society

Fig. 4 ECL intensity as a function of applied potential for three selected regions of the boron-doped polycrystalline diamond surface. The three selected regions are presented in Fig. 3 as horizontal bars. Reprinted (Adapted or Reprinted in part) with permission from [31]. Copyright 2004 American Chemical Society

https://www.twirpx.org & http://chemistry-chemists.com

2.2 Hydroxyl Radical Coreactant System

The ability of BBD electrodes to carry out the oxidation of organic molecules mediated by the hydroxyl radical (OH•) generated upon water oxidation, was explored for novel ECL coreactant reactions [26]. In this way, it is possible to generate the reducing species by hydrogen abstraction from the coreactant. A class of compounds that can easily form this radical through the hydrogen abstraction are molecules with hydroxyl groups.

The first studied has been ascorbic acid (AA) and the ECL is reported for BDD, GC and Pt (Fig. 5). All three electrode show the first peak at 1.25 V, BDD and GC show the second peak at 2.1 V and 2.3 V, respectively, and BDD only shows a third peak at 3.7 V.

The first peak is related to the catalytic mechanism, while the second ECL peak is ascribed to direct oxidation of AA, similar to TPrA [26].

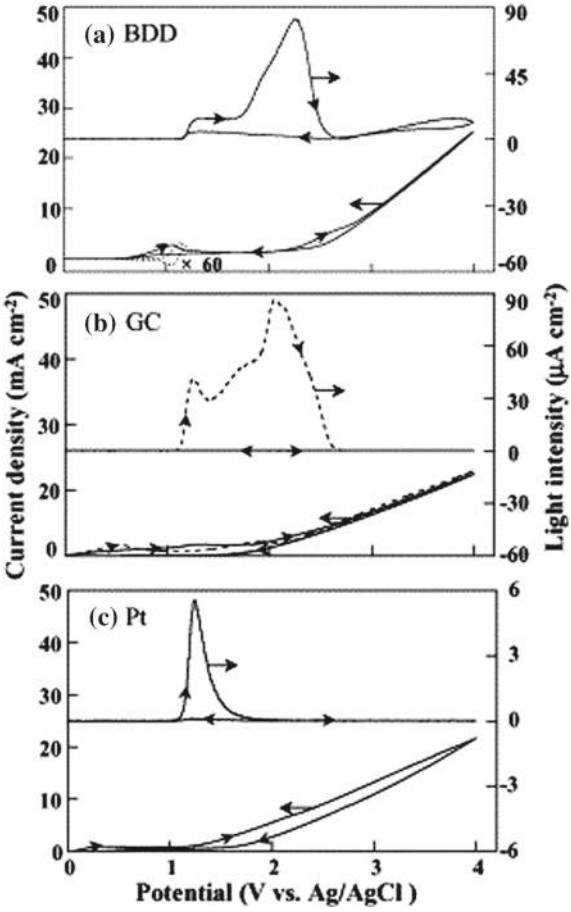

Fig. 5 Cyclic voltammograms and ECL curves at: **a** BDD; **b** GC; **c** polycrystalline Pt electrodes in 100 mM phosphate buffer solution containing 200 μM $Ru(bpy)_3^{2+}$ and 20 mM AA. The dotted line for (**a**) represents the data in the absence of AA. The dotted line for (**b**) represents the data of the first cycle and the solid line represents the second cycle. Reprinted from [26], Copyright 2005, with permission from Elsevier

https://www.twirpx.org & http://chemistry-chemists.com

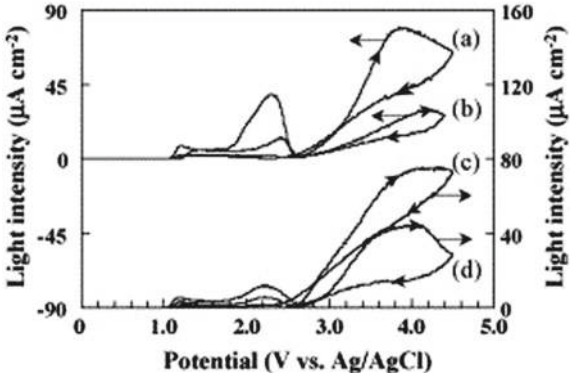

Fig. 6 Voltage–ECL curves in 100 mM phosphate buffer solution containing 100 μM $Ru(bpy)_3^{2+}$ and 30 mM coreactant. The coreactants are THF **a**, AA **b**, 2-propanol **c** and 1-propanol **d**. Reprinted from [26], Copyright 2005, with permission from Elsevier

Concerning the third ECL peak, the constant onset potential (approximately 2.6 V) (Fig. 6) suggests the formation of the coreactant radicals by the reaction between intermediates of oxygen evolution and the coreactant itself.

Since this ECL reaction was observed only at BDD electrodes, the products or intermediates involved in this mechanism are hydroxyl radicals that are well known to be easily generated during oxygen evolution reaction at the BDD surface [32]. The initial step of water discharge is the formation of adsorbed hydroxyl radicals on the electrode surface (M(OH•)), which leads to O_2 evolution:

$$M + H_2O \nabla M(OH\bullet) + H^+ + e^- \quad (7)$$

$$M(OH\bullet) \nabla M + 1/2O_2 + H^+ + e^- \quad (8)$$

3 Reductive-Oxidation ECL

In the reductive-oxidation ECL, the light is generated by a reduction reaction upon the coreactant and luminophore. For analytical applications, this coreactant pathway is less popular because it can be easily hampered by hydrogen evolution reaction. In this context, the used of BDD electrodes could give a great advantage to the system since it has a high overpotential for hydrogen evolution in aqueous solutions. A coreactant used for generating ECL on BDD electrode by this pathway is peroxydisulfate ($S_2O_8^{2-}$) [33].

First the ECL of $Ru(bpy)_3^{2+}$/persulfate at BDD electrode was investigated by using CV and compared with Pt and GC electrode (Fig. 7). In contrast with Pt and GC, ECL signal at BDD electrode was observed with high intensity. This could be achieved due to the higher overpotential for hydrogen evolution (Fig. 7b), leading to

https://www.twirpx.org & http://chemistry-chemists.com

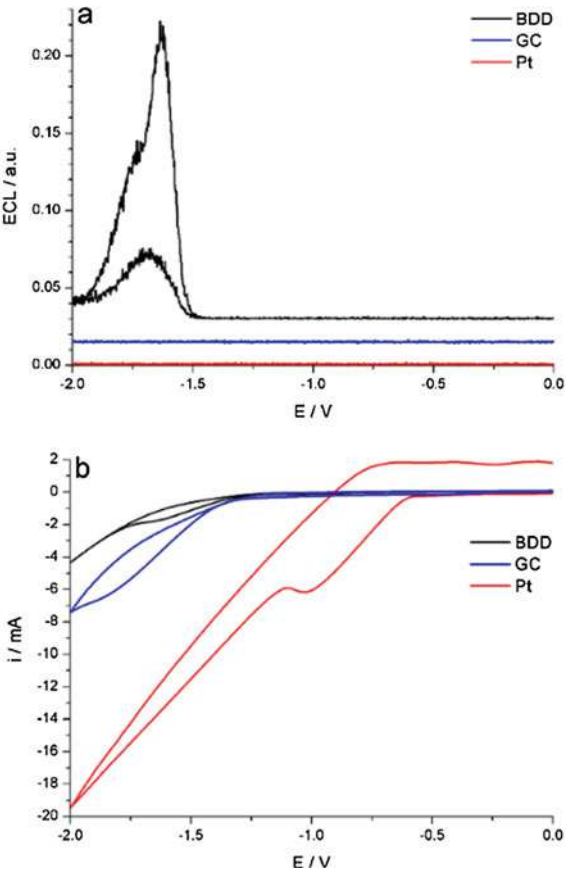

Fig. 7 Comparison of ECL (**a**) and CV (**b**) with BDD (black), GC (blue) and Pt (red) electrodes for 10 μM $Ru(bpy)_3^{2+}$ and 100 μM $S_2O_8^{2-}$ in 0.2 M PB. The scan rate is 100 mV/s and the pH 6.8. In (**a**), the curves are shifted for clarity. Reprinted (Adapted or Reprinted in part) with permission from [33]. Copyright 2018 American Chemical Society

higher reduction rate of both $Ru(bpy)_3^{2+}$ and $S_2O_8^{2-}$, and at the same time reducing the hindrance to the light emission.

The mechanism of ECL at BDD starting at -1.5 V is described as follow:

$$S_2O_8^{2-} + e^- \nabla S_2O_8^{\bullet 3-} \tag{9}$$

$$\left[Ru(bpy)_3\right]^{2+} + e^- \nabla \left[Ru(bpy)_3\right]^{+} \tag{10}$$

$$S_2O_8^{\bullet 3-} \nabla SO_4^{2-} + SO_4^{\bullet -} \tag{11}$$

$$[Ru(bpy)_3]^{+} + SO_4^{\bullet -} \nabla [Ru(bpy)_3]^{2+\prime} + SO_4^{2-} \tag{12}$$

$$[Ru(bpy)_3]^{2+\prime} \nabla [Ru(bpy)_3]^{2+} + hv \tag{13}$$

https://www.twirpx.org & http://chemistry-chemists.com

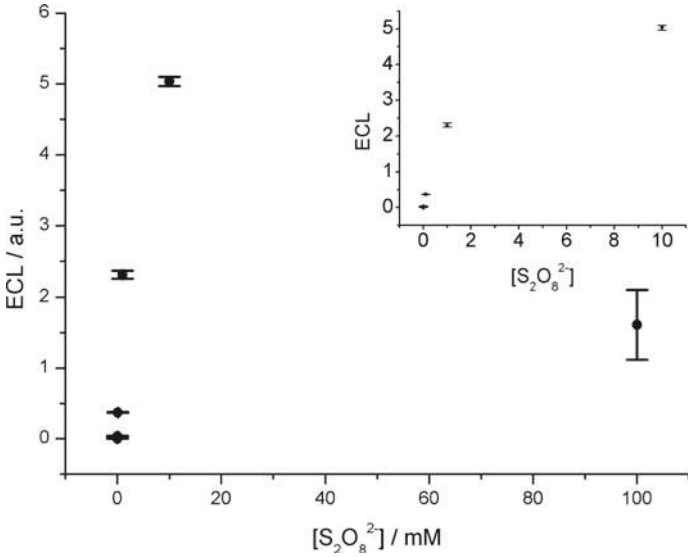

Fig. 8 Integrated ECL emission with a BDD electrode as a function of $S_2O_8^{2-}$ concentration, from 1 μM to 100 mM, by cyclic voltammetry. Inset: magnification of ECL response from 1 μM to 10 mM. Solution: 10 μM $Ru(bpy)_3^{2+}$ in 200 mM PB; scan rate: 100 mV/s; pH: 6.8. Reprinted (Adapted or Reprinted in part) with permission from [33]. Copyright 2018 American Chemical Society

The ECL response as a function of the $S_2O_8^{2-}$ concentration in the range from 1 μM to 100 mM was investigated (Fig. 8). It is found that the maximum ECL emission is at 10 mM of $S_2O_8^{2-}$ while at 100 mM the emission is much lower. This behavior is ascribed to the quenching of $S_2O_8^{2-}$ on the excited state of $Ru(bpy)_3^{2+}$ (Eq. 14) [34]. In this case, the ECL emission for $Ru(bpy)_3^{2+}/S_2O_8^{2-}$ ratio was found to be 1/1000 at BDD electrode which is lower compared to the data reported by White et al. [8] (at Pt electrode, water/acetonitrile solution) with a value of 1/20 and those from Yamazaki-Nishida et al. [35] which gave value of 1/200. This increase in the $S_2O_8^{2-}$ concentration range without the interference by the oxidative quenching would enable a wider range of $Ru(bpy)_3^{2+}$ detection.

$$[Ru(bpy)_3]^{2+\prime} + S_2O_8^{2-} \nabla [Ru(bpy)_3]^{3+} + SO_4^{2-} + SO_4^{\bullet -} \qquad (14)$$

4 In-Situ Generation of Coreactant ECL

Although the research is focused on coreactant approach for bioanalytical applications, the high concentration of coreactant might shows some disadvantages such

https://www.twirpx.org & http://chemistry-chemists.com

as toxicity and it may interfere with the target bio-analyte [36]. In order to maintain a more general analytical applicability, the in-situ generation of coreactant starting from a relatively unreactive precursor would however represent an alternative approach capable to keep the highly sensitive technique and, at the same time, to circumvent most of the aforementioned drawbacks [37]. In such a context, peroxide compound, i.e., $S_2O_8^{2-}$ and H_2O_2, offers some advantages with respect to amines due to the possibility to be prepared at will and in-situ, by applying a suitably positive potential in an aqueous solution.

BDD is a suitable electrode candidate for this strategy due to its ability to efficiently generate strong oxidants upon oxidation of inorganic salts such as sulfate and carbonate [38, 39]. This, combined with the high overpotential for hydrogen evolution reaction, lead to the realization of coreactant-free ECL system in aqueous solutions.

4.1 Sulfate Electrolyte System

Figure 9 shows the ECL-potential and its corresponding CV curves by scanning the potential from 0 V to 3.0 V, followed by a scan to negative potential to -2.0 V in 0.1 M Na_2SO_4 solution. The first positive scan was meant to generate $S_2O_8^{2-}$ (via oxidation of sulfate, Eq. 15–17) which later acts as the coreactant for the ruthenium to generate the ECL emission at the negative scan, where both $S_2O_8^{2-}$ and $Ru(bpy)_3^{2+}$ reduction take place (Eq. 9–13).

$$BDD + H_2O \nabla BDD(OH\bullet) + H^+ + e^- \quad (15)$$

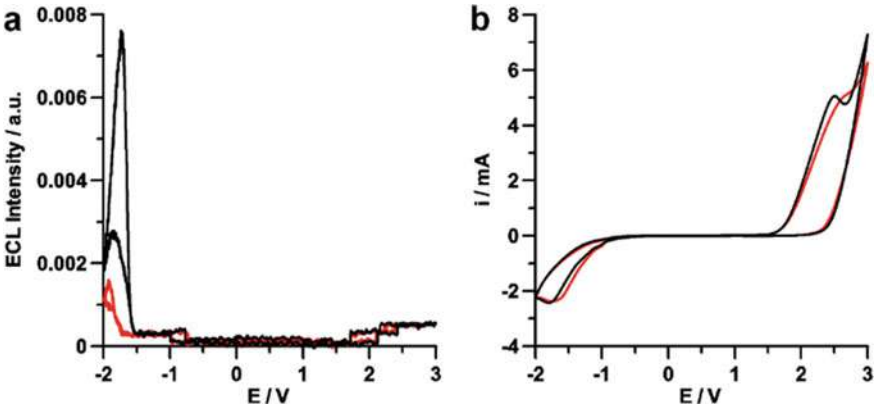

Fig. 9 Comparison of **a** ECL and **b** CV between 100 mM Na_2SO_4 (black) and 100 mM $KClO_4$ (red) measurement of 5 μM $Ru(bpy)_3Cl_2$ in water solvent. Reprinted (Adapted or Reprinted in part) with permission from [37]. Copyright 2016 American Chemical Society

https://www.twirpx.org & http://chemistry-chemists.com

$$BDD(OH\bullet) + SO_4^{2-} \nabla BDD\left(SO_4^{\bullet -}\right) + OH^- \quad (16)$$

$$BDD\left(SO_4^{\bullet -}\right) + SO_4^{2-} \nabla BDD + S_2O_8^{2-} + e^- \quad (17)$$

The ECL emission profile (Fig. 9a, black line) is similar to that obtained in the $Ru(bpy)_3^{2+}/S_2O_8^{2-}$ system which suggest that the coreactant $S_2O_8^{2-}$ is generate effectively during the first scan to the positive potential.

Interestingly, a weak emission was also obtained in the $NaClO_4$ solution where coreactant should not be generated (Fig. 9a, red line). A possible explanation for such an emission is therefore that ECL generation may also take place according to the annihilation route (Eq. 18), where $Ru(bpy)_3^{3+}$ generated in the positive scan (Eq. 1) may react with $Ru(bpy)_3^{+}$ generated in the negative scan (Eq. 10).

$$Ru(bpy)_3^{+} + Ru(bpy)_3^{3+} \nabla Ru(bpy)_3^{2+\prime} + Ru(bpy)_3^{2+} \quad (18)$$

This annihilation mechanism of $Ru(bpy)_3^{3+}/Ru(bpy)_3^{+}$ is usually unobserved in aqueous media where the prevailing HER prevents formation of the reduced species $Ru(bpy)_3^{+}$ [40], while it would be made possible in the present case by the high overpotential for HER on BDD [27, 41]. Notice that annihilation ECL for aqueous $Ru(bpy)_3^{2+}$ solutions was only previously reported in the case of interdigitated carbon microelectrode arrays, with 2 μm width spacing, working in a generation/collection biasing mode [42].

Using chronoamperometry measurement, the oxidation charge at 3.0 V increase linearly with the oxidation time both in the presence and absence of sulfate ion (Fig. 10a). By contrast, the integrated ECL signals (measured during the step at -2.0 V, Fig. 10b) decreases linearly with the square root of oxidation time (Fig. 10b, inset) indicating that the efficiency of overall ECL generation process is limited by diffusion electrogenerated peroxydisulfate toward the bulk of solution.

4.2 Carbonate Electrolyte System

Hydrogen peroxide (H_2O_2) is a common coreactant used in chemiluminescence, also in ECL. The reductive-oxidation mechanism of H_2O_2 coreactant has already been reported for $Ru(bpy)_3^{2+}$ [43]. On the other hand, hydrogen peroxide can be conveniently prepared by electro-oxidation of carbonate in aqueous solution at BDD electrode [39]. The strategy for generating the ECL emission is similar to the $Ru(bpy)_3^{2+}$/sulfate system, except in this time, carbonate is used as the source of the coreactant H_2O_2 which requires an hydrolysis reaction to generate the coreactant [44].

A high ECL emission could be observed in 0.1 M Na_2CO_3 aqueous solution at a BDD electrode by cyclic voltammetry from 0 V to 2.5 V, followed by a negative scan to -2.5 V, while parallel experiment in $NaClO_4$ only gives a weak signal of

https://www.twirpx.org & http://chemistry-chemists.com

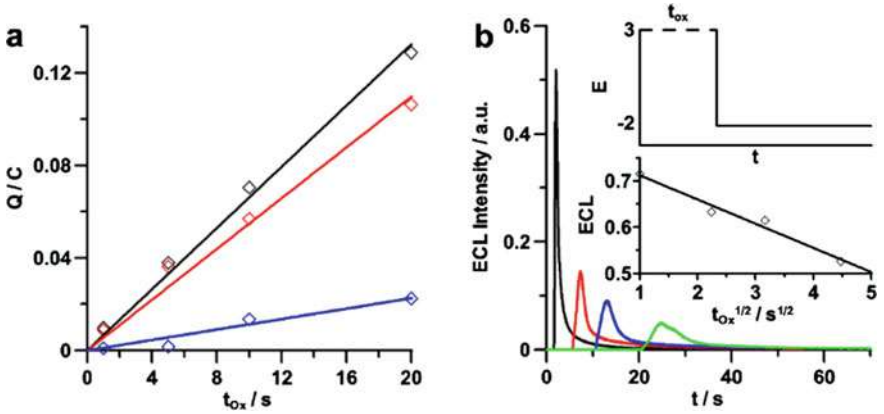

Fig. 10 **a** Integrated charge at 3.0 V for different oxidation times for 100 mM Na_2SO_4 (black), 100 mM $KClO_4$ (red), and (blue) their difference. **b** ECL intensity transients measured during chronoamperometric experiments carried out in a 5 μM $Ru(bpy)_3Cl_2$ and 100 mM Na_2SO_4 aqueous solution; first step from 0 to 3.0 V for $t_{ox} = 1, 5, 10$, or 20 s, followed by a step to −2.0 V for 50 s. Fig. b, inset: (top) potential program used in the chronoamperometric experiments; (bottom) integrated ECL intensity versus square root of time step duration t_{ox}. Reprinted (Adapted or Reprinted in part) with permission from [37]. Copyright 2016 American Chemical Society

the annihilation ECL of $Ru(bpy)_3^{2+}$ (Fig. 11). The first positive scan generated the peroxydicarbonate ($C_2O_6^{2-}$) from the oxidation of carbonate, which further reacts with water to produce H_2O_2 according to the following mechanism:

$$BDD + OH^- \nabla BDD(OH) + e^- \quad (19)$$

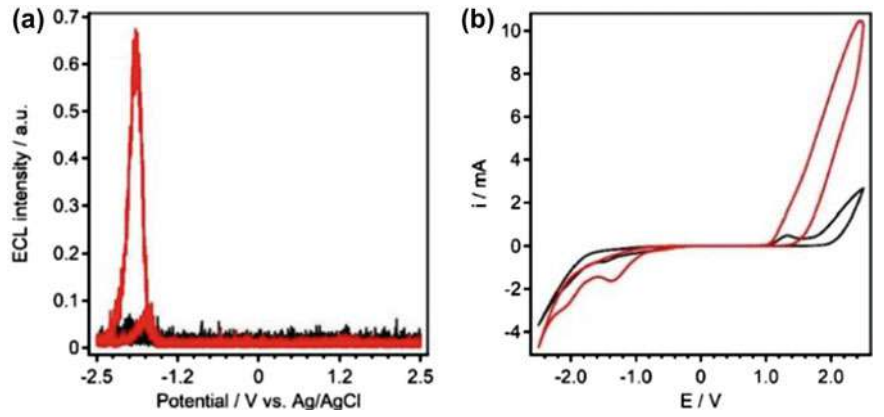

Fig. 11 Comparison between **a** the ECL measurements and **b** the CVs of 10 μM $Ru(bpy)_3Cl_2$ in aqueous solutions (pH 11.5) of 100 mM Na_2CO_3 (red) and 100 mM $NaClO_4$ (black). Reprinted (Adapted or Reprinted in part) with permission from [44]. Copyright 2019 American Chemical Society

https://www.twirpx.org & http://chemistry-chemists.com

$$2BDD(OH\bullet) + 2CO_3^{2-} \nabla 2BDD + C_2O_6^{2-} + 2OH^- \quad (20)$$

$$C_2O_6^{2-} + 2H_2O \nabla H_2O_2 + 2HCO_3^- \quad (21)$$

The CV in Na_2CO_3 shows a significantly higher anodic current compared to that in $NaClO_4$ (Fig. 11b), confirming the oxidation process of the carbonate. For both electrolytes, an onset oxidation potential of 1.1 V was observed, with a peak at 1.3 V in $NaClO_4$ solution. This was previously reported to be the oxidation of hydroxide ions at a BDD electrode (Eq. 19) [45], which mediates the oxidation of carbonate (Eq. 20). The second scan, toward negative potentials, generated the ECL after both H_2O_2 and $Ru(bpy)_3^{2+}$ are reduced, as proposed by Choi and Bard [43], with the following mechanism:

$$H_2O_2 + e^- \nabla OH^\bullet + OH^- \quad (22)$$

$$Ru(bpy)_3^{2+} + e^- \nabla Ru(bpy)_3^{+} \quad (23)$$

$$Ru(bpy)_3^{+} + OH^\bullet \nabla Ru(bpy)_3^{2+\prime} + OH^- \quad (24)$$

$$Ru(bpy)_3^{2+\prime} \nabla Ru(bpy)_3^{2+} + h\nu \quad (25)$$

The $Ru(bpy)_3^{2+}$/carbonate ECL system can work at a potential of 1.8 V, which is 500 mV lower than that previously mentioned $Ru(bpy)_3^{2+}$/sulfate system.

The effect of pH on the ECL signal was investigated using CV measurements (Fig. 12). The oxidation current, ascribed to carbonate, was found to decrease with the decreasing of pH, suggesting less $C_2O_6^{2-}$, and thus less H_2O_2, was generated. This is due to the effect of pH on the equilibrium of the carbonate species. In the neutral region, the concentration of carbonate is less dominant compared to the bicarbonate, and as the current decreases in the oxidation scan, it means that the carbonate ions is oxidized rather than bicarbonate or carbonic acid. However, the ECL signal increases as the pH decreases from 11.5, reaching a maximum at pH 7, while a further decrease down to pH 4 almost suppresses the ECL completely. In this case, the stability of the hydrogen peroxide generated in the solution seems to be the main factor for the ECL emission, since hydrogen peroxide is more stable when the pH is neutral or acidic [46–48]. In conclusion, the ECL emission peak at pH 7 is due to two trends, the decrease in carbonate oxidation current and the increase in H_2O_2 stability.

H_2O_2 is also a well-known coreactant for luminol which lead to the formation of 3-aminophthalate dianion in its triplet state [49–51]. After undergo triplet-singlet transition, it emits light at a wavelength from 424 to 510 nm, depending on the solvent [52–54]. It means that luminol could also be used in the carbonate system at BDD electrodes. Figure 13 shows this efficient H_2O_2 production for carbonate oxidation

https://www.twirpx.org & http://chemistry-chemists.com

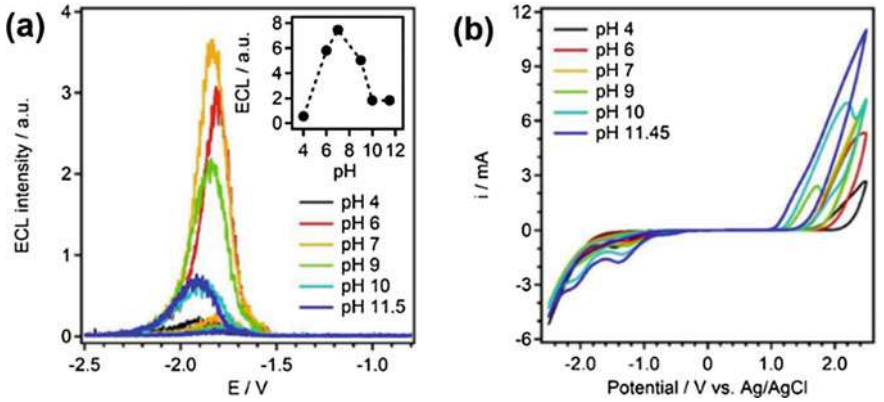

Fig. 12 **a** ECL intensity and **b** current by CV for 100 mM Na_2CO_3 and 10 μM $Ru(bpy)_3Cl_2$ with variation of pH. Potential was first swept to 2.5 V then -2.5 V. Inset: Plot of integrated ECL value as a function of pH. Reprinted (Adapted or Reprinted in part) with permission from [44]. Copyright 2019 American Chemical Society

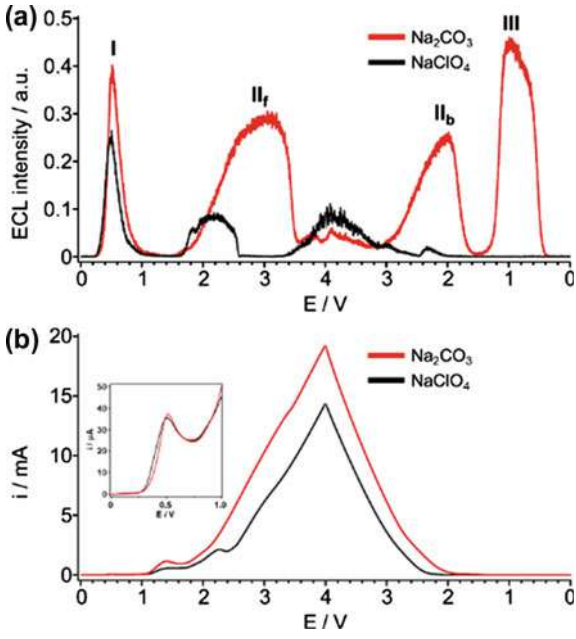

Fig. 13 **a** ECL intensity and **b** CV measurements of luminol 100 μM in 100 mM Na_2CO_3 (red), and in 100 mM $NaClO_4$ (black) at pH 12. For clarity, the potentials of forward and backward scans have been plotted consecutively, and peaks are named by roman numerals. Subscripts f and b stand for forward and backward, respectively. Reprinted (Adapted or Reprinted in part) with permission from [55]. Copyright 2020 American Chemical Society

(red trace) compared to water oxidation (black trace) which results in higher ECL emission and different emission signals [55]. From the ECL profiles obtained by CV (Fig. 13a), it is clear that the ECL emission in carbonate solution has (i) a higher intensity compared to water oxidation in $NaClO_4$ and (ii) one more peak, namely

https://www.twirpx.org & http://chemistry-chemists.com

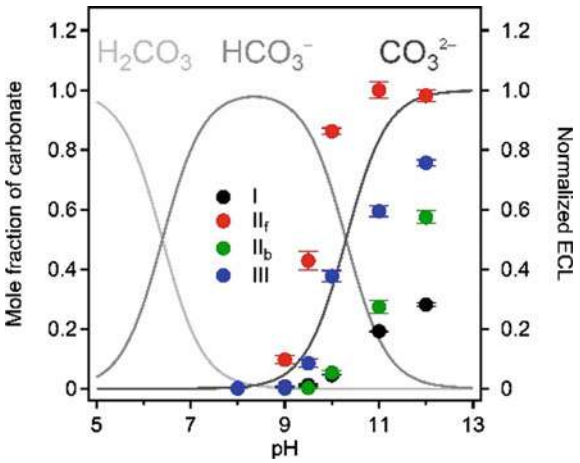

Fig. 14 Mole fraction of carbonate (left y-axis) and integral of ECL emission (right y-axis) as a function of pH. ECL by CV at 100 mVs^{-1}, 100 μM luminol in 100 mM Na_2CO_3. All ECL signals are normalized to the maximum of peak II_f. Reprinted (Adapted or Reprinted in part) with permission from [55]. Copyright 2020 American Chemical Society

peak III appeared. This highlights the role of carbonate in the H_2O_2 production at BDD electrode compared to direct water oxidation.

The first peak (I) starting at 0.3 V and reaching the maximum at 0.5 V is from direct luminol oxidation to 3-aminophthalate (Fig. 13b, inset), where the H_2O_2 is not involved. The second peak (II_f) starting at 1.6 V is affected by the electrolyte, as the oxidation of carbonate generates the coreactant H_2O_2 according to Eq. 19–21. At a basic pH [51], the H_2O_2 is partially deprotonated (pKa = 11.62) and can be oxidized to superoxide radical anion. This superoxide then further react with oxidized luminol to form 3-aminophthalate and lead to ECL emission. The decrease in peak II_f after 3.5 V is induced by water oxidation that hampering the light emission. The effect is reversed in the backward scan where the peak II_b starts to appear.

The last ECL peak (III) starts at 1.4 V until 0.4 V, after the II_b is completely turned off. Form the potential range of emission this has been associated to oxidized luminol and H_2O_2 [56, 57].

The pH effect on ECL revealed the role of carbonate on the ECL of luminol (Fig. 14). A clear correlation exists for the carbonate concentration and peak II_f. Since this peak is obtained directly by carbonate oxidation, the ECL emission reflects promptly the increase of its concentration. Furthermore, this reveals that electrochemical oxidation in carbonated solutions is upon the carbonate instead of the bicarbonate or both anions.

5 Summary

The electrogenerated chemiluminescence at doped diamond electrodes has shown how this material is capable to open new perspective in ECL applications as a result of its unique characteristics. First, it could improve the long established ECL system

https://www.twirpx.org & http://chemistry-chemists.com

of $Rubpy_3^{2+}/S_2O_8^{2-}$, due to its high stability and wide potential window, however, more investigations are needed for the $Rubpy_3^{2+}$/TPrA system. Second, it also offers a novel in-situ generation of coreactant approach, i.e., in sulfate or carbonate electrolytes, which could possibly find a viable application for bioanalytical application thanks to the unique ability to generate a strong oxidant from stable inorganic salt. This topic is still under development, and it can offer plenty of new applications to be investigated and new mechanisms to be uncovered.

References

1. Bard AJ (ed) (2004) Electrogenerated chemiluminescence. Marcel Dekker Inc, New York
2. Sojic N (ed) (2019) Analytical electrogenerated chemiluminescence: from fundamentals to bioassays. Royal Society of Chemistry, London
3. Hercules DM (1964) Chemiluminescence resulting from electrochemically generated species. Science 145:808–809
4. Visco RE, Chandross EA (1964) Electroluminescence in solutions of aromatic hydrocarbons. J Am Chem Soc 86:5350–5351
5. Santhanam KSV, Bard AJ (1965) Chemiluminescence of electrogenerated 9,10-diphenylanthracene anion radical. J Am Chem Soc 87:139–140
6. Marcus RA (1993) Electron transfer reaction in chemistry: theory and experiment. Angew Chem Int Ed Engl 32:1111–1121
7. Fiorani A, Irkham VG et al (2019) Diamond electrode for electrogenerated chemiluminescence. In: Yang N, Zhao G, Foord J (eds) Nanocarbon electrochemistry. Willey, New York, pp 285–321
8. Marquette CA, Blum LJ (2008) Electro-chemiluminescent biosensing. Anal Bioanal Chem 390:155–168
9. Muzyka K (2014) Current trends in the development of the electrochemiluminescent immunosensors. Biosens Bioelectron 54:393–407
10. Hu L, Xu G (2010) Application and trends in electrochemiluminescence. Chem Soc Rev 39:3275–3304
11. Zanut A, Fiorani A, Rebeccani S et al (2019) Electrochemiluminescence as emerging microscopy techniques. Anal Bioanal Chem 411:4375–4382
12. Hiramoto K, Villani E, Iwama T et al (2020) Recent advances in electrochemiluminescence-based systems for mammalian cell analysis. Micromachines 11:530–532
13. Fereja TH, Du F, Wang C et al (2020) Electrochemiluminescence imaging techniques for analysis and visualizing. J. Anal. Test. 4:76–91
14. Zhang J, Arbault S, Sojic N et al (2019) Electrochemiluminescence imaging for bioanalysis. Annu Rev Anal Chem 12:275–295
15. Valenti G, Fiorani A, Li H et al (2016) Essential role of electrode materials in electrochemiluminescence applications. ChemElectroChem 3:1990–1997
16. Valenti G, Fiorani A, Villani E et al (2020). In: Sojic N (ed) Analytical electrogenerated chemiluminescence: from fundamentals to bioassays. Royal Society of Chemistry, London, pp 159–175
17. Fiorani A, Eßmann V, Santos CS et al (2020) Enhancing electrogenerated chemiluminescence on platinum electrodes through surface modification. ChemElectroChem 7:1256–1260
18. Fiorani A, Merino JP, Zanut A et al (2019) Advanced carbon nanomaterials for elctrochemiluminescent biosensor applications. Curr Opin Electrochem 16:66–74
19. Leland JK, Powell MJ (1990) Electrogenerated chemiluminescence: an oxidative-reduction type ECL reaction sequence using tripropyl amine. J Electrochem Soc 137:3127–3131
20. Honda K, Yoshimura M, Rao TN et al (2003) Electrogenerated chemiluminescence of the ruthenium tris(2,2')bipyridyl/amines system on a boron-doped diamond electrode. J Phys Chem B 107:1653–1663

https://www.twirpx.org & http://chemistry-chemists.com

21. Sentic M, Virgilio F, Zanut A et al (2016) Microscopic imaing and tuning of electrogenerated chemiluminescence with boron-doped diamond nanoelectrode arrays. Anal Bioanal Chem 408:7085–7094
22. Miao W, Choi J, Bard AJ (2002) Electrogenerated chemiluminescence 69: The tris(2,2'-bipyridine)ruthenium(II), $(Ru(bpy)_3^{2+})$/tri-*n*-propylamine (TPrA) system revisited – A new route involving $TPrA^{\bullet+}$ cation radicals. J Am Chem Soc 124:14478–14485
23. Sentic M, Milutinovic M, Kanoufi F et al (2014) Mapping electrogenerated chemiluminescence reactivity in space: mechanistic insight into model system used in immunoassays. Chem Sci 4:2568–2572
24. Zanut A, Fiorani A, Canola S et al (2020) Insights into the mechanism of coeractant electrogeneratedchemiluminescence facilitating enhanced bioanalytical performance. Nat Commun 11:2668–2676
25. Yamanaka Y, Miyamoto M, Tanaka Y et al (2008) Development of the direct modification method of the ruthenium complex on conductive diamond surfaces and the selective detection of bio-related materials. Electrochim Acta 53:5397–5408
26. Honda K, Yamaguchi Y, Yamanaka Y et al (2005) Hydroxyl radical-related electrogenerated chemiluminescence reaction for a ruthenium tris(2,2')bipyridyl/co-reactants system at boron-doped diamond electrodes. Electrochim Acta 51:588–597
27. Macpherson JV (2015) A practical guide to using boron doped diamond in electrochemical research. Phys Chem Chem Phys 17:2935–2949
28. Pan S, Liu J, Hill CM (2015) Observation of local redox events at individual Au nanoparticles using electrogenerated chemiluminescence microscopy. J Phys Chem C 119:27095–27103
29. Wilson AJ, Marchuk K, Willets KA (2015) Imaging electrogenerated chemiluminescence at single gold nanowire electrodes. Nano Lett 15:6110–6115
30. Valenti G, Scarabino S, Goudeau B et al (2017) Single cell electrochemiluminescence imaging: from the proof-of-concept to disposable device-based analysis. J Am Chem Soc 139:16830–16837
31. Honda K, Noda T, Yoshimura M et al (2004) Microstructural heterogeneity for electrochemical activity in polycrystalline diamond thin films observed by electrogenerated chemiluminescence imaging. J Phys Chem B 108:16117–16127
32. Marsellia B, Garcia-Gomez J, Michauda P-A Rodrigo et al (2003) Electrogeneration of hydroxyl radicals on boron-doped diamond electrodes. J Electrochem Soc 150:79−83
33. Fiorani A, Irkham et al (2018) Electrogenerated chemiluminescence with peroxydisulfate as a coreactant using boron doped diamond electrodes. Anal Chem 90:12959–12963
34. White HS, Bard AJ (1982) Electrogenerated chemiluminescence. 41. Electrogenerated chemiluminescence and chemiluminescence of the $Ru(2,2'\text{-}bpy)_3^{2+}$-$S_2O_8^{2-}$ system in acetonitrile-water solutions. J Am Chem Soc 104:6891–6895
35. Yamazaki-Nishida S, Harima Y, Yamashita K (1990) Direct current electrogenerated chemiluminescence observed with $[Ru(bpz)_3]^{2+}$ in fully aqueous solution. Electroanal Chem Interfacial Electrochem 283:455–458
36. Xu J, Huang P, Qin Y et al (2016) Analysis of intracellular glucose at single cells using electrochemiluminescence imaging. Anal Chem 88:4609–4612
37. Irkham, Fiorani A et al (2016) Co-reactant-on-demand ECL: electrogenerated chemiluminescence by the in situ production of $S_2O_8^{2-}$ at boron-doped diamond electrodes. J Am Chem Soc 138:15636–15641
38. Khamis D, Mahé E, Dardoize F et al (2010) Peroxodisulfate generation on boron-doped diamond microelectrodes array and detection by scanning electrochemical microscopy. J Appl Electrochem 40:1829–1838
39. Velazquez-Peña S, Sáez C, Cañizares P et al (2013) Production of oxidants via electrolysis of carbonate solutions with conductive-diamond anodes. Chem Eng J 230:272–278
40. Tokel NE, Bard AJ (1972) Electrogenerated chemiluminescence. IX. Electrochemistry and emission from systems containing tris (2, 2'-bipyridine) ruthenium (II) dichloride. J Am Chem Soc 94:2862

https://www.twirpx.org & http://chemistry-chemists.com

41. Einaga Y (2010) Diamond electrodes for electrochemical analysis. J Appl Electrochem 40:1807–1816
42. Fiaccabrino GC, Koudelka-Hep M, Hsueh YT et al (1998) Electrochemiluminescence of tris(2,2‘-bipyridine)ruthenium in water at carbon microelectrodes. Anal Chem 70:4157–4161
43. Choi JP, Bard AJ (2005) Electrogenerated chemiluminescence (ECL) 79. Reductive-oxidation ECL of tris(2,2′-bipyridine) ruthenium(II) using hydrogen peroxide as a coreactant in pH 7.5 phosphate buffer solution. Anal Chim Acta 541:143–150
44. Irkham, Valenti G et al (2020) electrogenerated chemiluminescence by in situ production of coreactant hydrogen peroxide in carbonate aqueous solution at a boron-doped diamond electrode. J Am Chem Soc 142:1518–1525
45. Irkham EY (2019) Oxidation of hydroxide ions in weak basic solutions using boron-doped diamond electrodes: effect of the buffer capacity. Analyst 144:4499–4504
46. Thostenson JO, Ngaboyamahina E, Sellgren KL et al (2017) Enhanced H_2O_2 production at reductive potentials from oxidized boron-doped ultrananocrystalline diamond electrodes. ACS Appl Mater Interfaces 9:16610–16619
47. Martin HB (1996) Hydrogen and oxygen evolution on boron-doped diamond electrodes. J Electrochem Soc 143:133–136
48. Saha MS, Furuta T, Nishiki Y (2003) Electrochemical synthesis of sodium peroxycarbonate at boron-doped diamond electrodes. Electrochem Solid-State Lett 6:5–7
49. Cui H, Zou G-Z, Lin X-Q (2003) Electrochemiluminescence of luminol in alkaline solution at a paraffin-impregnated graphite electrode. Anal Chem 75:324–333
50. Sakura S (1992) Electrochemiluminescence of hydrogen peroxide-luminol at a carbon electrode. Anal Chim Acta 262:49–57
51. Garcia-Segura S, Centellas F, Brillas E (2012) Unprecedented electrochemiluminescence of luminol on a boron-doped diamond thin-film anode. enhancement by electrogenerated superoxide radical anion. J Phys Chem C 116:15500–15504
52. Giussani A, Farahani P, Martínez-Muñoz D et al (2019) Molecular basis of the chemiluminescence mechanism of luminol. Chem Eur J 25:5202–5213
53. Merényi G, Lind J, Eriksen TEJ (1990) Luminol chemiluminescence: chemistry, excitation, emitter. Biolumin Chemilumin 5:53–56
54. Baader WJ, Stevani CV, Bastos EL (2006) In the chemistry of peroxides, ed. Z. Rappoport, John Wiley & Sons Ltd, Chichester, pp 1211–1278
55. Irkham, Ivandini TA et al (2021) Electrogenerated chemiluminescence of luminol mediated by carbonate electrochemical oxidation at a boron-doped diamond. Anal Chem 93(4):2336–2341
56. Rose AL, Waite TD (2001) Chemiluminescence of luminol in the presence of iron(ii) and oxygen: oxidation mechanism and implications for its analytical use. Anal Chem 73:5909–5920
57. Lee J, Seliger HH (1972) Quantum yields of Luminol chemiluminescence reaction in aqueous and aprotic solvents. Photochem Photobiol 15:227–237

https://www.twirpx.org & http://chemistry-chemists.com

Photoelectrocatalytic and Photocatalytic Reduction Using Diamond

Kazuya Nakata and Chiaki Terashima

Abstract Diamond has excellent physical and chemical stability and exhibits unique electrochemical properties. This chapter focuses on the behavior of diamonds as a photoelectrochemical electrode and photocatalyst under light irradiation. Since diamond has a large band gap, long wavelength light such as visible light cannot excite electrons from valence band to the conduction band. However, when irradiated with short wavelength ultraviolet light, a photocurrent based on electron excitation can be observed. Thus, diamond can act as a photoelectrochemical electrode. And also, the generated excited electrons can also give an opportunity as a photocatalyst under no bias. Since the conduction band of diamond is large negative, especially in the case of hydrogen-terminated diamond, it shows a negative electron affinity under light irradiation, and it generates dissolved electrons in a solution, which should reduce inactive molecules to make useful substances. In this chapter, we introduce reduction reactions utilizing negative electron affinity and also describe the effect of modification of the diamond surface on the reduction reaction, and finally, hybridization with nanomaterials that enhances the light absorption efficiency of diamond.

Keywords Photoelectrocatalysis · Photocatalysis · Ammonia synthesis · CO_2 reduction

1 Introduction

Diamond is a material that has outstanding properties such as high hardness, thermal conductivity, and chemical stability. Diamond is originally an insulator, but it changes to semiconductor when doped impurities. For example, it is known that when boron

K. Nakata (✉)
Division of Science for Biological System, Institute of Agriculture, Tokyo University of Agriculture and Technology, 2-24-16 Naka-cho, Koganei, Tokyo 184-0012, Japan
e-mail: nakata@go.tuat.ac.jp

C. Terashima
Photocatalysis International Research Center, Research Institute for Science and Technology, Tokyo University of Science, 2641 Yamazaki, Noda 278-8510, Chiba, Japan

© Springer Nature Singapore Pte Ltd. 2022

Y. Einaga (ed.), *Diamond Electrodes*,
https://doi.org/10.1007/978-981-16-7834-9_9

https://www.twirpx.org & http://chemistry-chemists.com

is doped into diamond, it acts as a p-type semiconductor (boron-doped diamond, BDD). When BDD is used as an electrode, it not only has excellent characteristics such as a large hydrogen and oxygen overpotential and a small background current in an aqueous solution, but also exhibits a unique electrode reactions [1, 2]. Therefore, diamond is attracting attention as a unique carbon electrode material different from sp^2 carbon materials such as highly oriented pyrolytic graphite and glassy carbon in the fields of electrochemistry and photoelectrochemistry. In particular, since the conduction band of diamond is at a very high negative potential, it can be expected that the photoexcited electron has a very strong reduction ability that enables unique chemical reactions under mild conditions. In this chapter, unique properties of diamond as a photoelectrochemical electrode and photocatalyst under light irradiation are introduced.

2 Photocurrent of Diamond Electrode Under Light Irradiation

The photoelectrochemical behavior of diamond was firstly reported by Pleskov et al. [3]. They used non-doped polycrystalline diamond on a tungsten substrate. Figure 1 shows the dependence of dark and photocurrent on the potential when light is irradiated at regular intervals using a high mercury lamp. It was found that the diamond electrode is photo-sensitive because the photocurrent was observed under the light irradiation. When the experiment was conducted in an oxygen-free inert atmosphere, the observed photocurrent value was significantly reduced. This suggests that the photocurrent is associated with the electrochemical reduction of oxygen dissolved in the electrolyte. The band gap of diamond is 5.5 eV, and the light source used by the authors cannot generate carriers by inter-band transitions. Therefore, it is considered to be a transition of photoexcitation of electrons from impurity levels in the forbidden band to the conduction band. As a result of the spectral dependence of the cathodic photocurrent, it is assumed that the impurity level is at 2–3.5 eV below the bottom of the conduction band (Fig. 2).

Beside the non-doped diamond, Fujishima et al. reported that a cathodic photocurrent generates when BDD is irradiated with a 500 W Xe lamp, as shown in Fig. 3 [4]. This cathodic photocurrent is considered to be due to the reduction of protons in electrolyte, as confirmed that the pH increased during the light irradiation. Since the band-to-band excitation of electrons does not occur in the light source used at this time, the photocurrent was derived from the electrons being excited from the valence band to the impurity state in the band gap. The excited electrons are believed to go into solution, and the holes pass through the bulk and eventually cause an oxidation reaction at the counter electrode.

On the other hand, if the BDD electrode is irradiated with light having energy that causes band-to-band electronic excitation, a large photocurrent can be observed. Fujishima et al. conducted an experiment to observe the photocurrent by irradiating

https://www.twirpx.org & http://chemistry-chemists.com

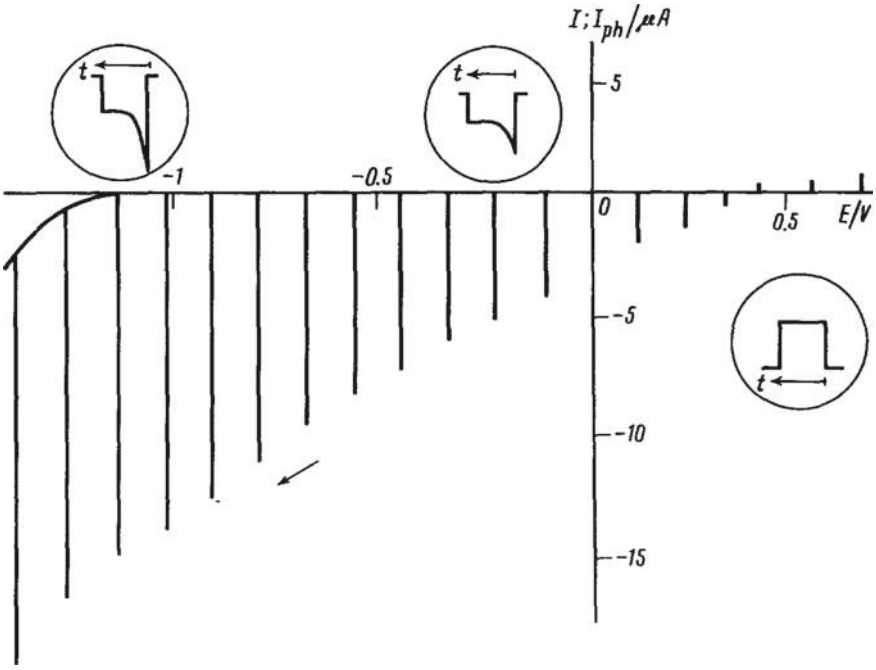

Fig. 1 Dependence of the dark current (solid curve) and the photocurrent upon intermittent illumination on the potential. Air atmosphere, 5 mV/s. The insets show schematically the transients of the photocurrent after the light is switched on and off in different potential ranges. Reprinted from [3], Copyright 1987, with permission from Elsevier

BDD electrodes with different types of laser light such as ArF (193 nm, 6.4 eV), KrF (248 nm, 5.0 eV), and XeF (351 nm, 3.53 eV), as shown in Fig. 4 [5]. When ArF excimer laser light was applied to the surface of BDD electrode, that hydrogen evolution occurred at a very positive potential of + 1 V versus SCE, which was very difficult to occur in the dark, whereas almost no photocurrent was observed in KrF (wavelength 248 nm/5.0 eV) and XeF (wavelength 351 nm/3.53 eV). From this result, when ArF is used, band-to-band excitation from the valence band to the conduction band of diamond occurs and much reduction electrons generated in the conduction band of diamond by photoexcitation reacts with a proton in water, resulting in hydrogen evolution. In addition, the impedance of this electrode was measured, and the flat band potential was calculated from the Mott-Schottky plot, which gives 0.9 ± 0.1 V versus SCE. This result offers the conduction band of diamond is about -4.20 V versus SCE (Fig. 5). Thus, BDD containing a small amount of boron has a high reduction ability by photoexcitation.

https://www.twirpx.org & http://chemistry-chemists.com

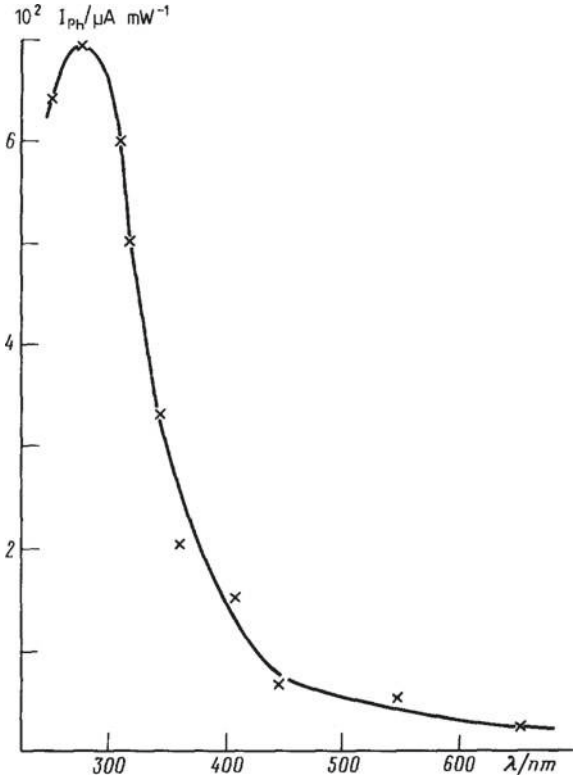

Fig. 2 Spectral dependence of the cathodic photocurrent. $E = -0.4$ V. Reprinted from [3], Copyright 1987, with permission from Elsevier

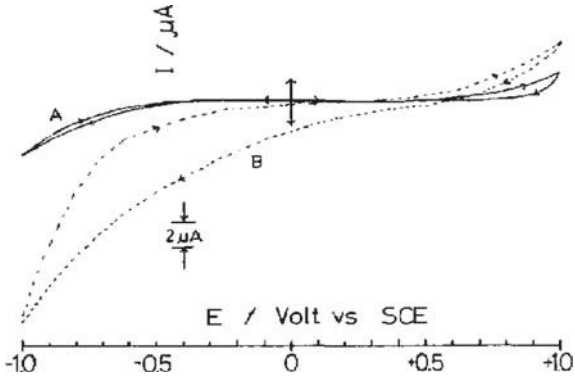

Fig. 3 *I-E* curves at boron-doped diamond electrode in the dark (curve A) and under illumination (curve B) (solution, 1.0 M KCl; scan speed, 10 mV s^{-1}; electrode area, 11 0.0 mm^2). Reprinted from [4], Copyright 1992, with permission from Elsevier

https://www.twirpx.org & http://chemistry-chemists.com

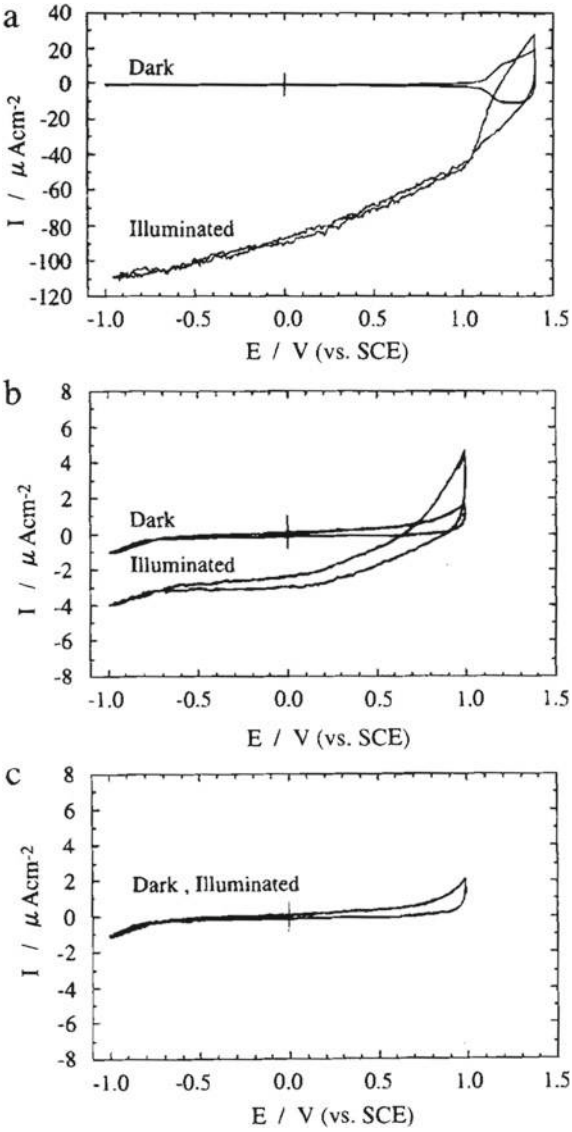

Fig. 4 Current–voltage curves at the semiconducting boron-doped diamond electrode with and without illumination from **a** ArF, **b** KrF, and **c** XeF excimer lasers, all at an average power of 80 mW cm^2 in 0.1 M KH_2PO_4. In part (c), the light and dark curves coincide. Reprinted from [5], Copyright 1997, with permission from IOP Publishing

3 Negative Electron Affinity for Reduction Reactions at Diamond Surface

In 1979, Himpsel et al. investigated natural diamond of type Ib by photoelectron spectroscopy using synchrotron radiation [6]. As a result, it was reported for the first time that the (111) surface has a negative electron affinity (NEA), that is, the lowest energy level of the conduction band of diamond is located higher than the vacuum

https://www.twirpx.org & http://chemistry-chemists.com

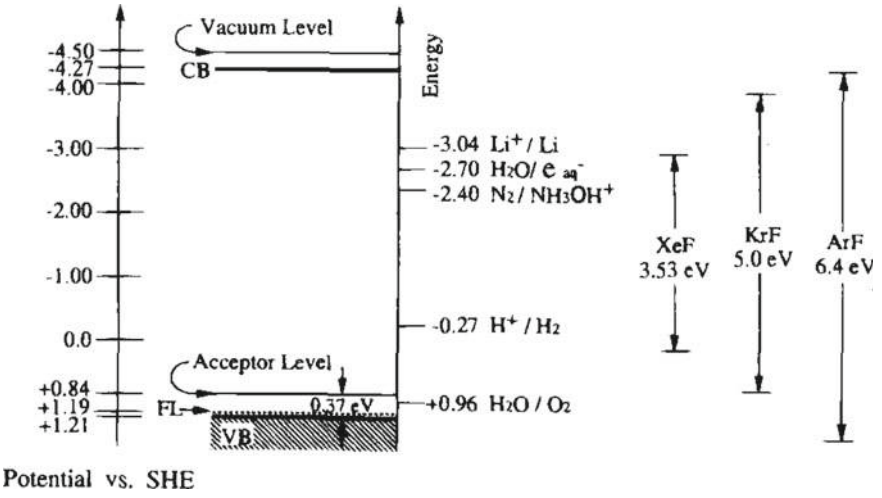

Fig. 5 Energy band diagram for BDD, showing for comparison the energies for the various excimer lasers used. Representative aqueous redox couples (at pH 4.5) are also shown. Reprinted from [5], Copyright 1997, with permission from IOP Publishing

level. On the hydrogen-terminated diamond surface, the conduction band exists ~0.8–1.3 eV above the vacuum level. In other words, when a hydrogen-terminated diamond surface is irradiated with light having an energy larger than 5.5 eV, the electrons excited to the conduction band diffuse to the surface and are directly emitted to the vacuum (Fig. 6). Although various studies have been reported on the emission of electrons from diamond to a vacuum, there have been few studies on the emission of electrons into a solution. The energy of the emitted electrons is very high, and it is about −5.5 V versus NHE. This has the potential to use the electrons generated by NEA as an excellent reducing agent.

Hamers et al. reported ammonia synthesis from nitrogen using reduction reaction caused by irradiation of hydrogen-terminated diamond [7]. In general, nitrogen is weakly absorbed on the catalyst surface, and it is necessary to form an high energy intermediate for the synthesis of ammonia. Industrially, ammonia is synthesized by reaction of nitrogen and hydrogen on the catalyst surface at a high temperature of 300–550 °C. In other words, it is difficult to synthesize them at room temperature and ambient pressure. Reduction of nitrogen requires a reduction reaction to form N_2H, which has a high energy barrier. Theoretical studies have predicted that dissolved dinitrogen anions ($N_{2(aq)}^-$) may form in water, indicating the possibility of forming N_2H through the reaction of $N_{2(aq)}^- + H^+$[8]. However, this requires high energy (−4.2 V vs. NHE), so it has not been observed so far. On the other hand, solvated electrons give important intermediates and can cause a reaction ($H_2O + e^- \sim e^-_{(aq)}$ ($E^0 = -2.86$ V vs. NHE)). Thus, the electrons emitted from diamond generate solvated electrons, which causes the reduction to H^+ to H•, which requires high energy, and the subsequent reduction from N_2 to N_2H.

https://www.twirpx.org & http://chemistry-chemists.com

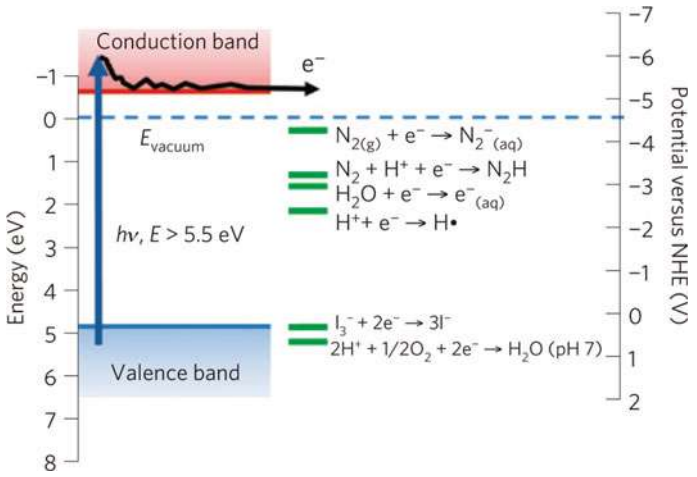

Fig. 6 Electronic energy level diagram of diamond. The valence band and conduction band of H-terminated diamond are compared with several relevant electrochemical reduction potentials, including both absolute energy scale (left) and the electrochemical energy scale (right) relative to the NHE. Potential for reduction of oxygen to water is shown for pH 7; other potentials shown are standard E^0 values. Reprinted from [7], Copyright 2013, with permission from Springer Nature

To observe solvated electrons, Hammers et al. measured transient absorption spectroscopy. The solvated electrons have a wide absorption band with a peak at 720 nm. The transient absorption was measured by exciting the diamond with a pulsed ultraviolet laser (213 nm). The transmitted 632 nm light was rapidly reduced by UV irradiation. The decreased intensity gradually recovered, and it is speculated that the solvated electrons were used for recombination and other reactions. No dissolved electrons were observed in the oxygen-terminated diamond. The quantum yield was ~ 0.6% at 211.5 nm and 0.15% at 223.5 nm for polycrystalline BDD.

Furthermore, Hammer et al. conducted two types of experiments to reduce N_2 with diamond. One is using a dual-component cell, BDD and platinum are used for cathode and anode, respectively. Another was using a single-component cell, in which only BDD was immersed in the electrolyte. In Fig. 7, ammonia was produced more efficiently using the dual-component cell than single-component cell. This is because the valence band of diamond is not so deep, so the oxidation power is poor, and in single-component cells, the reduction reaction of N_2 is limited by the slow oxidation of water. In addition, in order to confirm that the NH_3 generation is derived from N_2, an experiment was conducted using Ar instead of N_2, and as a result, NH_3 generation was suppressed. Therefore, it was suggested that the produced NH_3 was derived from N_2. Interestingly, it was also found that NH_3 was produced even when using cheap diamond that was used as a polishing agent (~125 nm average size).

Next, in order to investigate the relationship between the ammonia yield and the excitation wavelength, the irradiation wavelength dependence was investigated (Fig. 8). The highest ammonia yield was obtained when irradiated with light of all

https://www.twirpx.org & http://chemistry-chemists.com

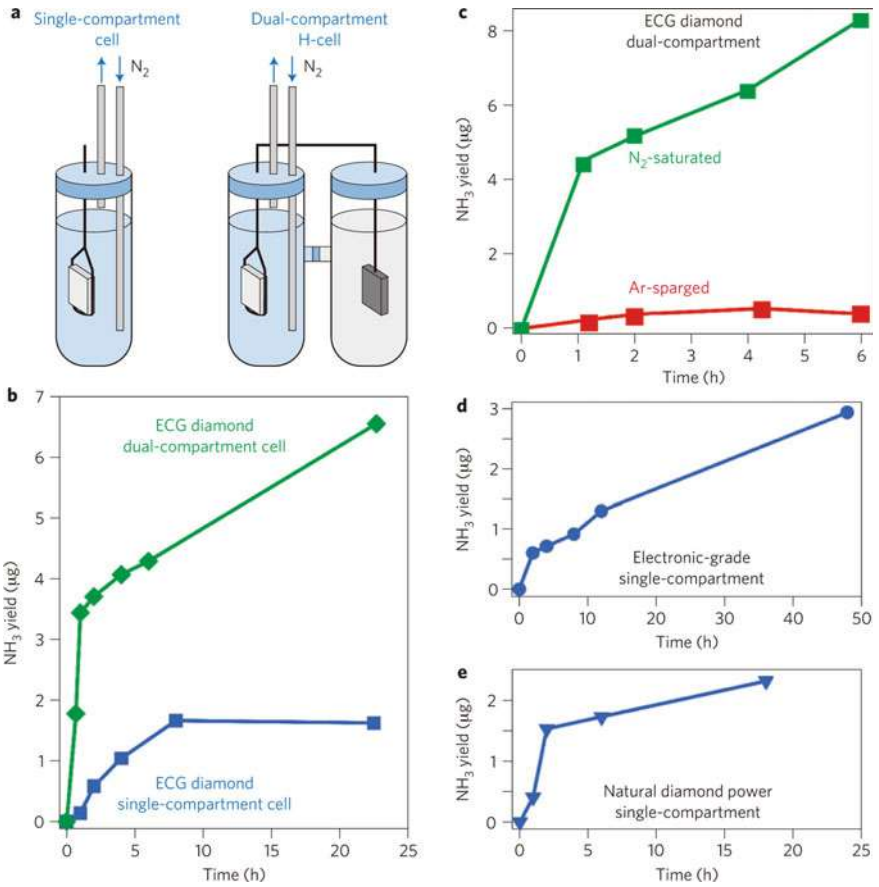

Fig. 7 Ammonia yields from photochemical reduction of N_2 at diamond surfaces. **a** Schematic diagram of reaction vessels. **b** Total ammonia yield from electrochemical grade (ECG) diamond in N_2-saturated water using single-compartment and dual-compartment cells. **c** Comparison of ammonia yield from ECG diamond in N_2-saturated water and argon-sparged water, using the H-cell geometry. **d** Yield from electronic-grade diamond. **e** Yield from natural diamond powder dispersed in water. Reprinted from [7], Copyright 2013, with permission from Springer Nature

wavelengths (>190 nm), but it was also active at >225 nm (energy < 5.5 eV) and > 280 nm (energy < 4.4 eV).

When the diamond surface is hydrogen-terminated, it has NEA, whereas, when it is oxygen-terminated, it has positive electron affinity. To investigate the effect of surface termination on the reduction of nitrogen, hydrogen- and oxygen-terminated diamonds were synthesized and compared. As a result, the hydrogen yield was higher in the hydrogen termination than in the oxygen termination, as shown in Fig. 8

There is great interest in reduction of CO_2, to produce useful chemicals. One-electron reduction is thought to be effective in reduction of CO_2, but it requires a high potential of -1.9 V versus SHE and exists at a position higher than the conduction band

https://www.twirpx.org & http://chemistry-chemists.com

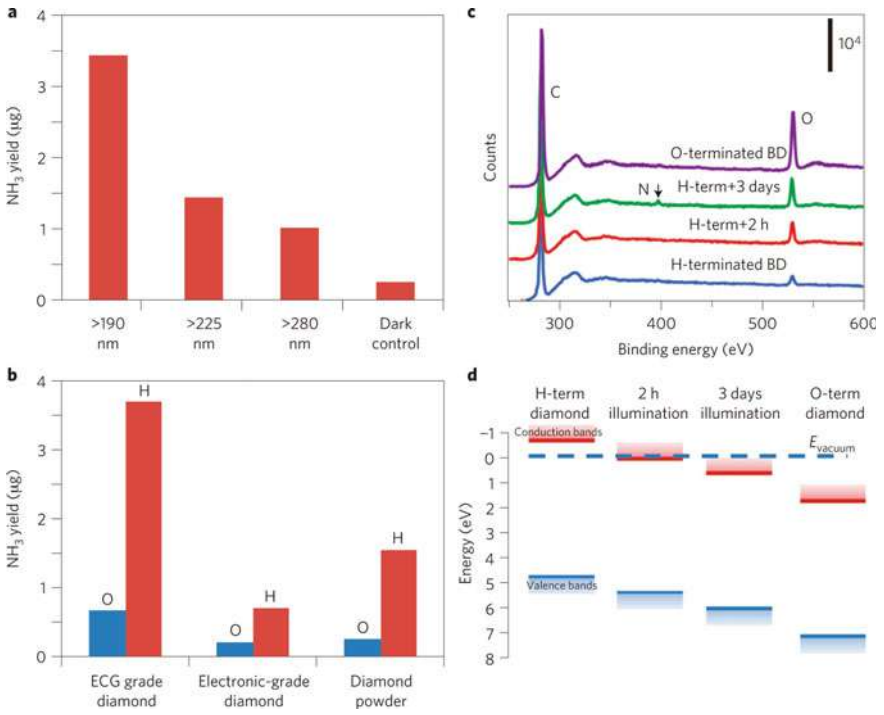

Fig. 8 The influence of excitation wavelength and surface termination on N_2 photoreduction activity. **a** Influence of illumination wavelength. Ammonia yield from boron-doped ECG diamond in the H-cell when illuminated for 1 h, using absorptive filters to limit the range of incident radiation. **b** Comparison of NH_3 yield from H-terminated and O-terminated diamond samples, measured after 2 h illumination. The ECG-grade sample was measured in the two-compartment cell geometry; others were in the single-cell geometry. **c** Comparison of X-ray photoelectron spectra of H-terminated and O-terminated BDD illuminated for 2 h and for 3 days. **d** Position of valence band and conduction bands of ECG diamond as determined by ultraviolet photoemission spectroscopy measurements, showing transition from NEA to PEA. Reprinted from [7], Copyright 2013, with permission from Springer Nature

of general semiconductors. It is considered that the high reduction potential of BDD with NEA may cause one-electron reduction of CO_2. Hamers et al. performed CO_2 reduction using inexpensive commercial grade diamond [8]. Since solvated electrons are at -5.2 eV versus SHE, they can sufficiently cause one-electron reduction of CO_2. Actually, an experiment was performed using two-component cells using BDD. The gas phase after the experiment was measured by FTIR. As a result, no absorption other than CO_2 was observed in the absence of light irradiation and diamond, but CO was observed under the conditions of CO_2 with light irradiation and diamond. H_2 was not observed below the detection limit of 5 ppm. On the other hand, analysis by ion chromatography confirmed a very small amount of formate ion. That is, in this experiment, CO was produced with high selectivity of more than 95% by reduction of CO_2. Further, in order to promote the reduction reaction of CO_2, it is necessary to

https://www.twirpx.org & http://chemistry-chemists.com

proceed with the oxidation reaction by holes in the valence band. Since the valence band is + 0.3 V versus SHE, diamond oxidation ($C + H_2O \sim CO + 2H^+ + 2e^-$; E_{red} = 0.71 V at pH 3.2) cannot occur. Actually, as a result of the reduction experiment using [9] CO_2, the produced CO was [9] CO.

4 Effect of Modification of Diamond Surface on Reduction Reactions

Terashima et al. conducted to reduce CO_2 using Ag-loaded BDD (boron concentration: 1000 ppm) [10]. No clear cathodic peak was observed in the electrolyte saturated with nitrogen (Fig. 9). On the other hand, a strong cathodic peak at -1.1 V versus RHE was observed in the electrolyte saturated with CO_2. The cathodic peak appeared more strongly under the light irradiation. The products were identified after CO_2 reduction using Ag-supported BDD under light irradiation. As a result, CO production was hardly observed for BDD without supporting Ag, but the CO production increased as the Ag loading increased (Fig. 10). On the other hand, H_2 was also produced, but in a smaller amount than that of CO. Note that no product was observed in the electrolyte. The BDD used by Terashima et al. has a boron concentration of 1000 ppm, but they also prepared Ag-supported BDD with a boron concentration of 10,000 ppm and glassy carbon for comparison (Fig. 11). As a result of CO_2 reduction under light irradiation, 1000 ppm BDD loaded with Ag had a faradaic efficiency of 72.5 and 9.08% for CO and H_2 production, exhibiting high CO selectivity. On the other hand, when 10,000 ppm of BDD was used, the faradaic efficiency of CO was 36.8% and H_2 was 38.3%, showing production ratio was almost 1:1. Diamond has high physical and chemical stability, but since there are few active sites on the surface, the substrate is difficult to absorb, resulting in low reactivity. Thus, it is necessary to conduct experiments under high pressure, when reduced CO_2. Therefore, it can be said that using diamond supporting Ag is more suitable for CO_2 reduction under normal pressure. In addition, Ag strongly binds to CO_2 molecule, giving high selectivity.

As above, the Ag-modified BDD electrode photoelectrochemically reduced CO_2 under the irradiation condition of ultraviolet light (225 nm) to generate CO ($\eta >$ 70%). On the other hand, CO generation at this electrode can also be performed at a considerably negative potential (-1.1 V vs. RHE), which is similar to those of BDD electrode modified with Cu–SnO_x (-1.6 V vs. RHE), and Ag foil and particles (-0.8 – -1.2 V vs. RHE). A possible reason of this is recombination of photoexcited electrons and holes at the Ag-modified BDD electrode. In the Ag-modified BDD electrode, photoexcited electrons and holes are easily recombined, and a large negative overpotential was required to separate them and perform photoelectrochemical CO_2 reduction. Ag has been experimentally reported to be an electrocatalyst that preferentially produces CO by CO_2 reduction. However, if the photoexcited electrons cannot be easily transferred between the BDD surface and the Ag co-catalyst, the electrons and holes are not separated, and CO_2 is not photoelectrochemically

https://www.twirpx.org & http://chemistry-chemists.com

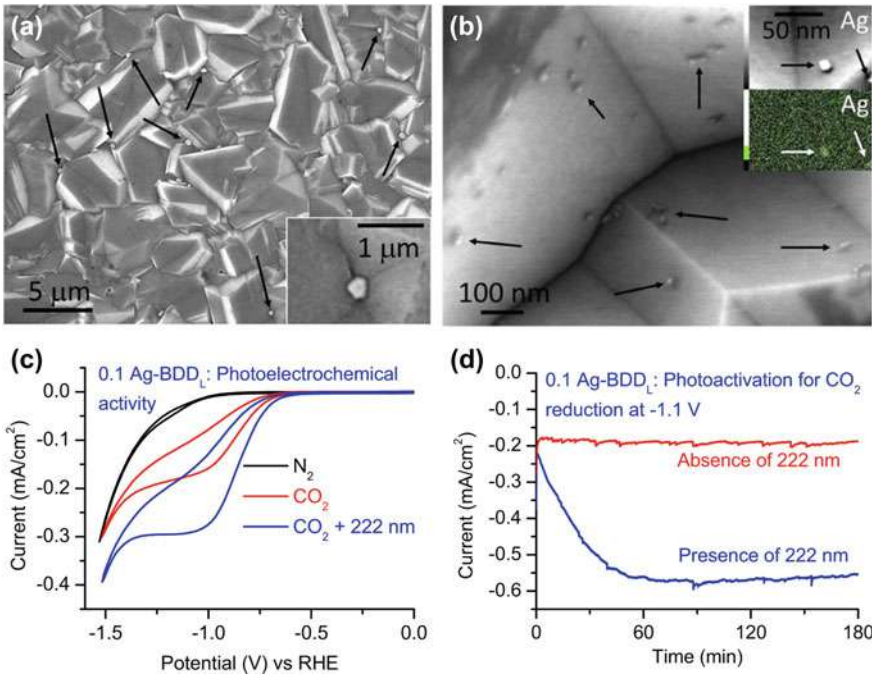

Fig. 9 Surface morphology and photoelectrochemical CO_2 reduction activity of Ag-BDD. **a** Low magnification FESEM image of 0.1 Ag-BDD_L (0.1 Ag indicates that the $AgNO_3$ concentration during deposition was 0.1 M; other parameters including potential and time were fixed at −0.5 V and 60 s, respectively), clearly indicating its smooth surface. Brighter Ag nanoparticles with a diameter of ~300 nm are indicated by arrows. **b** High-magnification FESEM image showing smaller Ag nanoparticles (~20 nm) as confirmed by elemental mapping (inset). **c** CVs of 0.1 Ag-BDD_L in 25 mM Na_2SO_4 aqueous electrolyte. The cathodic peak current at −1.1 V versus RHE under CO_2-saturated conditions indicates the cathodic reduction of CO_2 on the 0.1 Ag-BDD_L electrode. **d** Chronoamperometric current–time curves of the photocurrent generated by the 0.1 Ag-BDD_L electrode in the dark and under irradiation (222 nm). Photocurrent increased in the first hour and then became almost constant. Reprinted from [10], Copyright 2016, with permission from Springer Nature

reduced. In the previous study, BDD surface was observed with a scanning probe microscope to confirm that the conductivity of the BDD surface and the number of empty electron orbital increased with the increase of the C–H structure [9, 11, 12]. It was considered that the orbitals are related to the ease of electron movement on the BDD surface, and that the electrons easily move from the inside of the BDD to the surface by entering the empty orbital of the C–H structure.

In order to photoelectrocatalytically reduce CO_2 with the Ag-modified BDD electrode at a more positive potential, pre-treatment was performed before the Ag modification at the BDD surface to increase the C–H structure between BDD surface and Ag co-catalyst [13]. The dense C–H structure facilitates the transfer of electrons generated by photoexcitation between the BDD surface and the Ag co-catalyst and

https://www.twirpx.org & http://chemistry-chemists.com

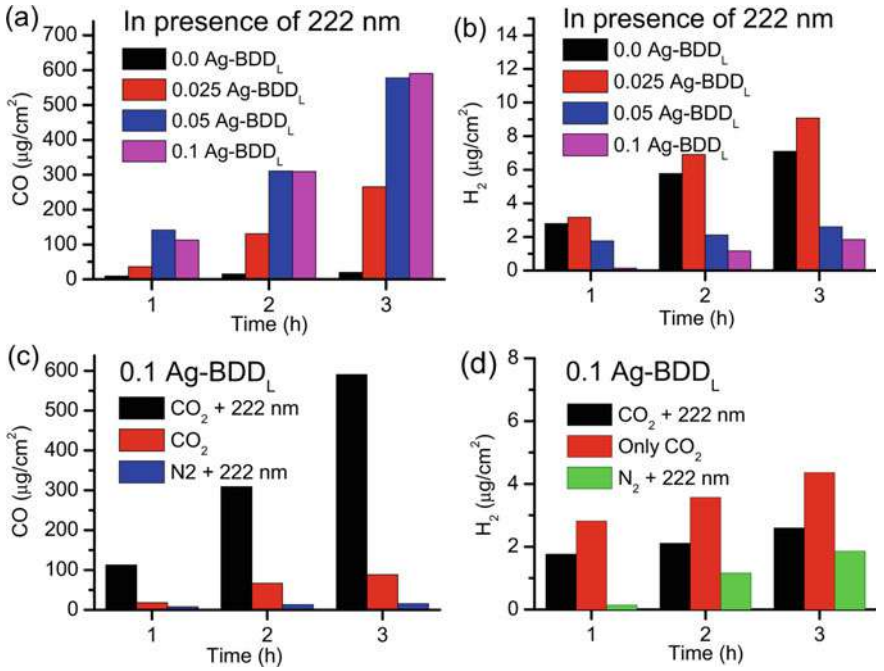

Fig. 10 CO_2 reduction product analysis. **a** Amount of CO produced during irradiation (222 nm) over different Ag-BDD_L electrodes in 25 mM Na_2SO_4 aqueous electrolyte at − 1.1 V versus RHE. At a particular duration, the amount of CO increases with the Ag concentration used during deposition on the BDD_L substrate. **b** Production of H_2 over the electrodes. At a particular irradiation time, the amount of H_2 decreased with increasing $AgNO_3$ concentration during electrode synthesis. **c** Photoelectrochemical effect of 0.1 Ag-BDD_L under different conditions in 25 mM Na_2SO_4 at − 1.1 V versus RHE. The amount of CO produced under irradiation (222 nm) is higher than that produced in the dark, revealing that the very high amount of CO produced originates from the photoelectrochemical effect of 0.1 Ag-BDD_L. Negligible CO was produced over 0.1 Ag- BDD_L under N_2-saturated conditions. **d** Amount of H_2 produced over the 0.1 Ag-BDD_L electrode under different conditions at −1.1 V, indicating that H_2 is mostly produced through electrochemical reactions. Reprinted from [10], Copyright 2016, with permission from Springer Nature

allows photoexcited electrons and holes to be separated at a lower overpotential. As a result, the Ag-modified BDD electrode with pre-treatment can photoelectrochemically reduce CO_2 at a more positive potential. Figure 12 shows the current–voltage curves of the Ag-modified BDD electrode with pre-treatment. Comparing the current–voltage curves of the Ag-modified BDD electrode in the dark and under UV irradiation, the cathodic current increased by the UV irradiation. This suggests that the photoexcited electrons generated by the irradiation of UV light promoted the reduction reaction at the Ag-modified BDD surface. Moreover, when the BDD electrode and the Ag-modified BDD electrode are compared under the same irradiation condition of UV light, the Ag-modified BDD electrode has a relatively large reduction current value. This indicates that the Ag co-catalyst on the BDD surface

https://www.twirpx.org & http://chemistry-chemists.com

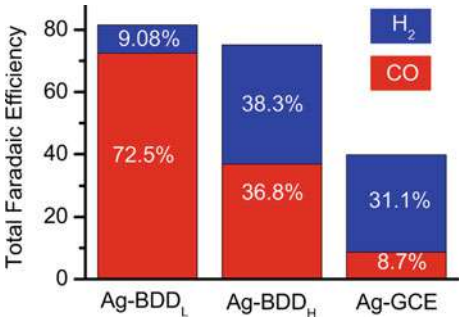

Fig. 11 Selectivity of different carbon electrodes. Ag was deposited on BDD_L, BDD_H, and GCE in 0.1 M $AgNO_3$ at −0.5 V for 60 s. Total Faradaic efficiency was measured after 3 h of photoelectrolysis at −1.1 V in 25 mM Na_2SO_4 under an excimer lamp (222 nm, 7 W). Reprinted from [10], Copyright 2016, with permission from Springer Nature

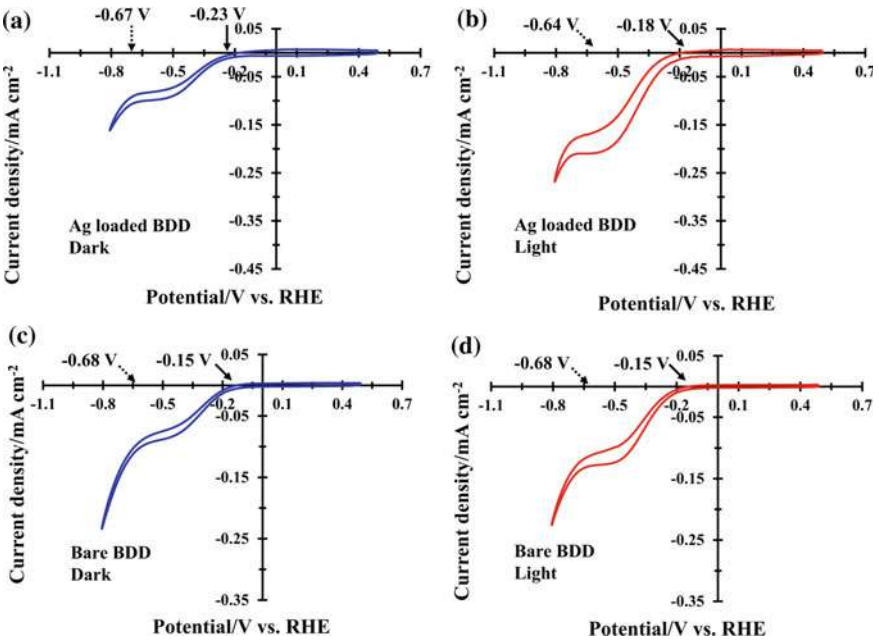

Fig. 12 Current–voltage curves of cyclic voltammetry swept at 0.05 V s^{-1} for the electrodes of **a**, **b** Ag-loaded BDD or **c**, **d** bare BDD in the present study under the conditions of dark (dark) or UV light irradiation (light), in which the curves were measured in the CO_2-purged 25 mM Na_2SO_4 solution. The apparent onset potentials for the cathodic currents were indicated for the electrodes with (solid line arrow) and without (broken line arrow) the electrochemical pre-treatment. Reprinted from [13], Copyright 2017, with permission from Springer

https://www.twirpx.org & http://chemistry-chemists.com

promotes the reduction reaction by photoexcited electrons in this electrolyte. Actually, the potential at which a reduction current is generated in this electrolyte was compared with and without pre-treatment of the BDD surface. As a result, a reduction current occurred at a more positive potential for the BDD surface with pre-treatment (0.18 V vs. RHE) than that without it (0.64 V vs. RHE). The reason why the Ag-modified BDD electrode with pre-treatment generated reduction current at a more positive electrode potential was not due to the effects of UV light irradiation or Ag co-catalyst modification, but due to the pre-treatment of the BDD surface.

Focusing on the current efficiencies of CO and H_2 generation of the Ag-modified BDD electrode, CO_2 can be reduced to CO to be preferentially generated ($\eta > 70\%$) under the irradiation of UV light, which is independent of pre-treatment. On the other hand, the electrode potential of the BDD with pre-treatment is more positive (0.61 V vs. RHE) than without it (1.1 V vs. RHE). Furthermore, even if CO_2 reduction was performed under the irradiation of UV light with pre-treated BDD electrode (without Ag modification), H_2 is perennially generated ($\eta = 37\%$) than CO ($\eta = 7\%$). Electrochemical pre-treatment increases the C–H structure that favors electron transfer on the BDD surface. As mentioned above, it is expected that the electrons can easily move from the inside of the BDD to the surface by entering the empty orbital of the C–H structure. The transfer of electrons from the BDD surface into the electrolyte was also promoted, and as a result, the electrochemical reduction reaction by photoexcited electrons at the BDD electrode began to occur at a more positive potential. On the other hand, it has been experimentally shown that CO_2 reduction on the BDD surface is not efficient for CO production. Therefore, CO could not be preferentially generated by reduction of CO_2 with the pre-treated BDD electrode even under UV irradiation.

When an Ag co-catalyst, which has been experimentally shown to be efficient for CO generation, is supported on a BDD electrode to form an Ag-modified BDD electrode, an effective site for CO generation is introduced on the BDD surface. When the C–H structure on the BDD surface is increased by pre-treatment, the C–H structure is densely present at the interface between the BDD surface and the Ag co-catalyst (Fig. 13). The photoexcited electrons generated in the BDD enter the empty electron orbital of the C–H structure and easily move to the BDD surface. The photoexcited electrons transferred to the BDD surface move to the Ag co-catalyst on the surface and reduce CO_2 in the electrolyte. Thus, the C–H structure facilitates the transfer of photoexcited electrons between the BDD surface and the Ag co-catalyst, so that photoexcited electrons and holes can be separated with a smaller overpotential. As a result, the pre-treatment and Ag-modified BDD surface show CO_2 reduction at more positive potential (0.61 V vs. RHE) than it without the pre-treatment (1.1 V vs. RHE), to generate CO.

Hydrogen-terminated diamond exhibits NEA. This is because there is a small positive charge on the H atom on the C-H surface and it has a surface dipole that is advantageous for electron emission. On the other hand, it is known that hydrogen termination gradually deteriorates the electron emission property due to oxidation. On the other hand, amino groups (primary and secondary amines) can be protonated, resulting in a positive charge depending on the surrounding pH, and can exist as

https://www.twirpx.org & http://chemistry-chemists.com

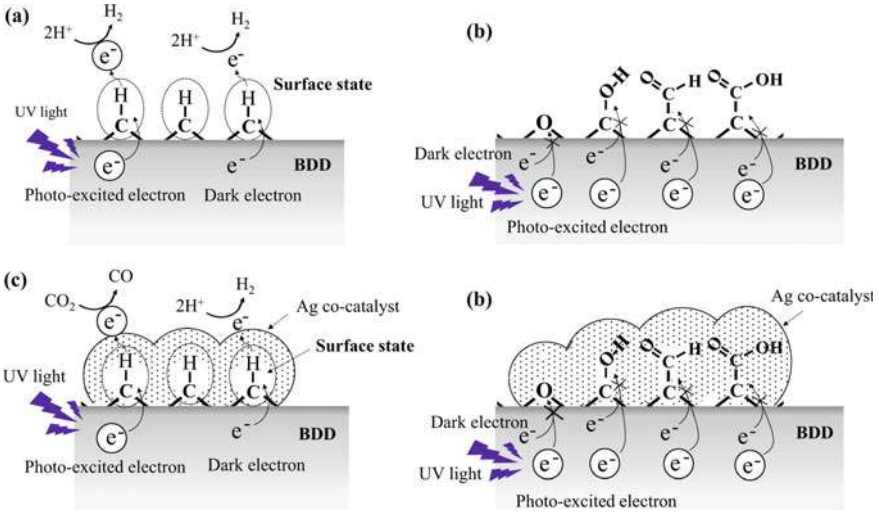

Fig. 13 Plausible mechanisms for the transfer of dark and photoexcited electrons in cathodic electrolysis on electrodes of **a**, **b** bare BDD or **c**, **d** Ag-loaded BDD in CO_2-purged solutions. The surfaces of BDD are assumed to be functionalized with **a**, **c** hydrogenated carbons or **b**, **d** oxygenated carbons. Reprinted from [13], Copyright 2017, with permission from Springer

quaternary cations on the diamond surface (C-NH_3^+, C_2-NH_2^+). In principle, protonated amino groups on the diamond surface are advantageous for electron emission. Hamers et al. fabricated NH_2-terminated diamond and measured the ultraviolet photoelectron spectroscopy (UPS) spectrum [14]. The amino group was protonated with HCl. Figure 14 shows the UPS spectra before and after protonation. In each case, a sharp peak appeared at around 17 eV. This is a characteristic of the NEA material and is attributed to the fact that electrons are excited, relaxed to the conduction band edge, and emitted electrons. For both samples, the intensity is similar at 5–10 eV, but the binding energy at 17 eV is clearly higher in the HCl-treated sample. Next, the surface photovoltage measurements were performed to measure the amount and polarity of excess charges existing on the surface. Figure 15 is a plot of surface charge versus incident photon energy. For hydrogen-terminated diamond, no peak was observed at <5.4 eV, but a negative surface charge was observed at higher photon energy. On the other hand, the amino-terminated diamond treated with HCl showed a large negative surface charge. This is due to the positive surface charge generated by protonation of the amino group, which increased the band-bending downward. Figure 16 shows the yield of ammonia production by nitrogen reduction. Amino group diamond treated with hydrochloric acid showed higher ammonia yield than hydrogen-terminated diamond. It is considered that this is because the surface of the protonated amino group diamond has an advantageous structure for NEA and an advantageous reaction for nitrogen reduction.

The electron emission of hydrogen-terminated diamond is based on the surface dipole. In contrast, the electron emission of amino-terminated diamond is based on a

https://www.twirpx.org & http://chemistry-chemists.com

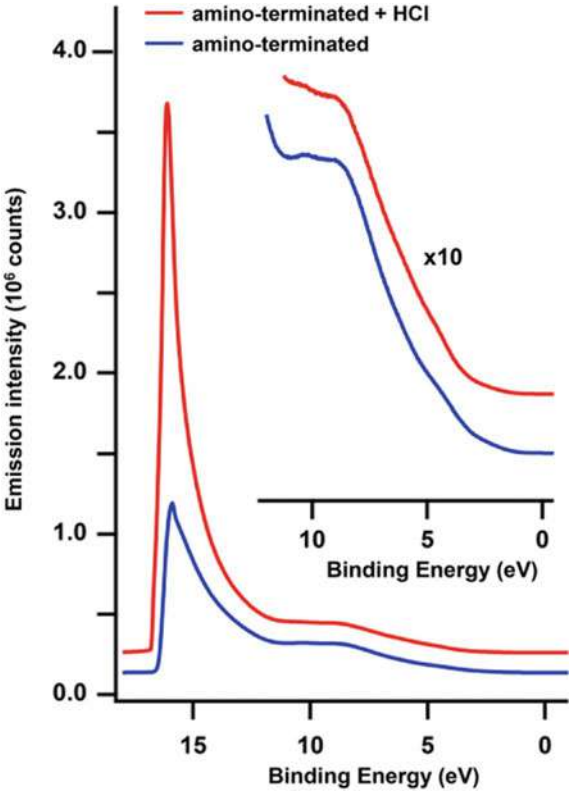

Fig. 14 Ultraviolet photoemission spectra from amino-terminated diamond before and after brief immersion in HCl. The inset shows the same data magnified 10 ×. Reprinted from [14], Copyright 2016, with permission from Elsevier

static positive charge. The fixed charges have stronger electrostatic interactions than the dipole. Therefore, the amino group termination is more advantageous in electron emission and chemically stable than the hydrogen termination.

5 Hybridization of Diamond and Nanomaterials

Diamond is an interesting material showing NEA. On the other hand, since diamond is an indirect band gap semiconductor, its absorption coefficient is small. Therefore, as one means for improving the NEA of diamond, it is considered to improve the absorption on the diamond surface. In recent studies, it has been known that small metal nanoparticles enhance photochemical reaction by Raman scattering and plasmon resonance. Hamers et al. fabricated a material with a sandwich structure in which Ag particles were deposited between polycrystalline diamonds and investigated the

https://www.twirpx.org & http://chemistry-chemists.com

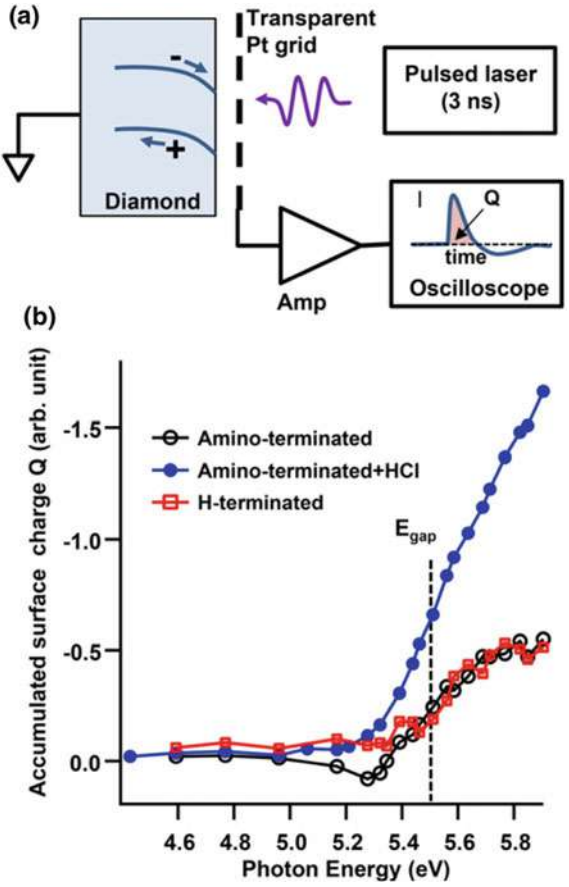

Fig. 15 Surface photovoltage measurements. **a** Schematic of apparatus; **b** plots of photo-initiated charge separation (Q) as a function of UV photon energy from amino-terminated B-doped diamond before and after acidification, measured at UV pulse energy of 0.1 mJ. The dashed line shows the 5.5 eV bandgap energy of diamond. Reprinted from [14], Copyright 2016, with permission from Elsevier

effect of nitrogen reduction on ammonia production [15]. Figure 17 shows how to make a diamond-Ag-diamond ("D-Ag-D") sandwich structure. First, a diamond thin film was deposited on a silicon substrate by microwave plasma-assisted chemical vapor deposition. Next, the diamond thin film was transferred to an electron beam metal evaporator and loaded with 100 nm of Ag. Then, the diamond thin film was deposited again. Diffused reflectance spectra were measured to investigate the optical properties of the prepared D-Ag-D. A new absorption was observed around 320 nm in D-Ag-D, as compared with the case where only the diamond thin film was deposited on the silicon substrate. This comes from the plasmon of buried Ag. In addition, the large absorption of D-Ag-D over the entire wavelength range compared to the control is considered to be partly due to scattering caused by the buried Ag nanoparticles.

Figure 18 is a comparison of ammonia production by nitrogen reduction in D-Ag-D and control. The yield of ammonia formation was higher in D-Ag-D than in diamond alone. Figure 19 shows a diagram of electron transfer in the D-Ag-D structure. When D-Ag-D is irradiated with light, electron emission proceeds through three

https://www.twirpx.org & http://chemistry-chemists.com

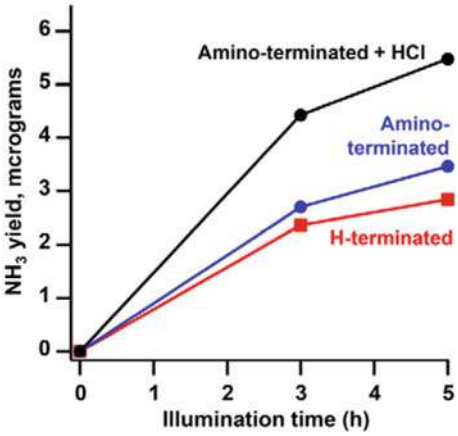

Fig. 16 Ammonia yield results for H-terminated and for amino-terminated diamond before and after exposure to HCl. Reprinted from [14], Copyright 2016, with permission from Elsevier

passes. The first is derived from the excitation from the valence band to the conduction band of diamond. At this time, Ag particles have a function of enhancing optical scattering. The second is due to electron excitation from Ag, where the excited electrons are injected into the conduction band of diamond and then released into water. The third is the defect-associated pathway, which has absorption at 340–360 nm, although it also overlaps with absorption by Ag plasmon resonance. However, from the comparison of the yields of ammonia generation by nitrogen reduction, when the wavelength larger than 280 nm is used, it is difficult to generate ammonia, so the 3rd passway does not have much influence.

6 Conclusion

In this chapter, we described reduction reactions using diamond as a photoelectrochemical and photocatalytic material under light irradiation. NEA is very interesting property of diamond, which allows unique reduction reactions such as nitrogen and CO_2 reductions to produce useful chemicals. Furthermore, the NEA can be controlled by surface termination that opens a new direction of utilizing NEA for reduction reactions. Diamond showing NEA can contribute new and green chemistry utilizing ambient temperature and pressure.

https://www.twirpx.org & http://chemistry-chemists.com

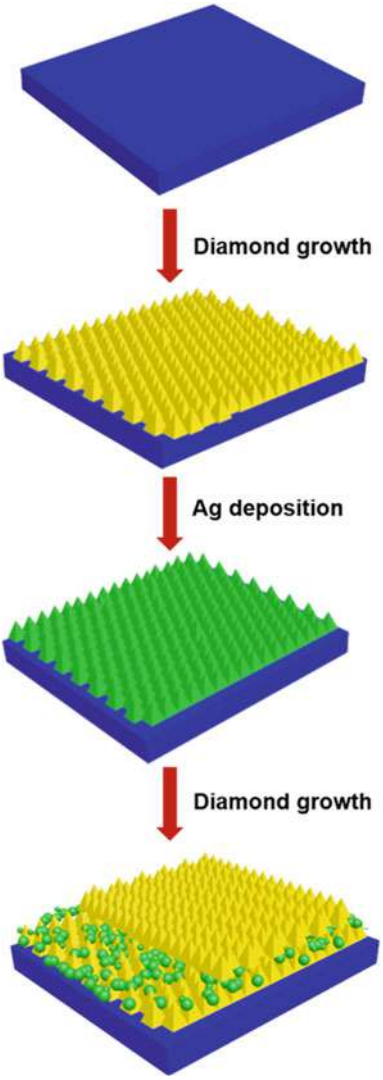

Fig. 17 Illustration of the growth mechanism of D−Ag−D plasmonic structure. After the first diamond growth, a thin Ag film is deposited; subsequent diamond growth forms Ag nanoparticles that are encapsulated by the growing diamond film. {Li, 2018 #6869} Reprinted from [15], Copyright 2018, with permission from American Chemical Society

https://www.twirpx.org & http://chemistry-chemists.com

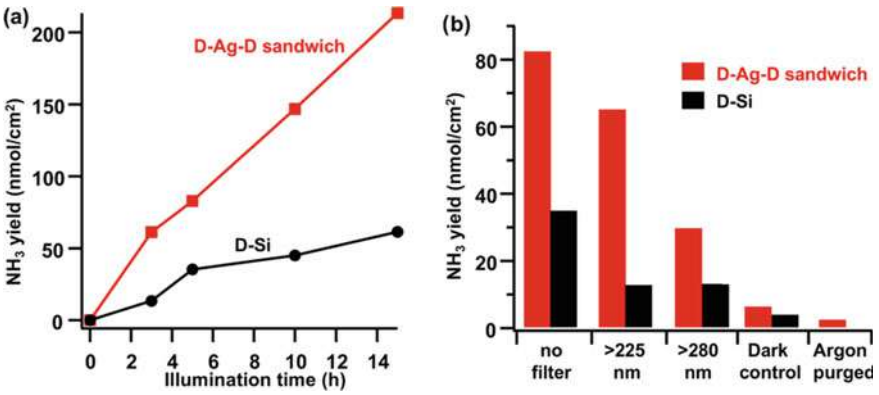

Fig. 18 **a** Photocatalytic ammonia yield from the D−Ag−D and D−Si samples for different illumination times. **b** Ammonia yield after 5 h illumination using selected wavelength regions. Reprinted from [15], Copyright 2018, with permission from American Chemical Society

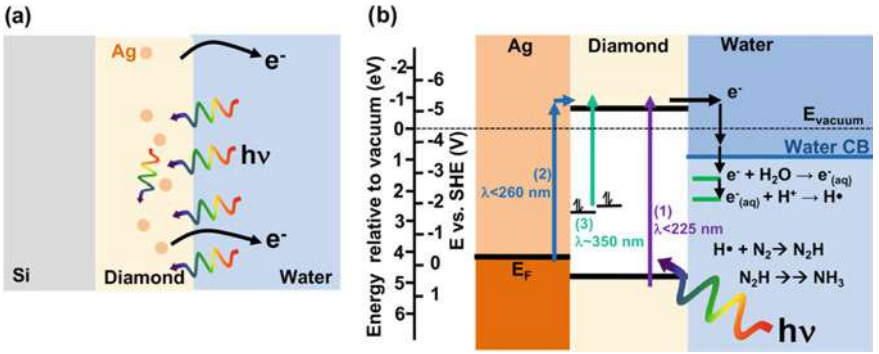

Fig. 19 Schematic illustration of the influence of Ag nanoparticles on diamond photocatalysis **a**, with Ag nanoparticles as scattering centers to enhance electron emission. **b** Illustration showing three pathways for the excitation to diamond's conduction band, and subsequent steps in the reaction to form NH_3. Reprinted from [15], Copyright 2018, with permission from American Chemical Society

References

1. Fujishima A, Einaga Y, Rao TN, Tryk DA (2005) Diamond electrochemistry. (BKC Inc and Elsevier)
2. Brillas E, Huitle CAM (2011) Synthetic diamond films: preparation, electrochemistry, characterization and applications (The Wiley Series on Electrocatalysis and Electrochemistry) (Wiley)
3. Pelskov YV, Sakharova AY, Krotova M, Bouilov L, Spitsyn B (1987) Photoelectrochemical properties of semiconductor diamond. J Electr Chem Interf Electroc 228:19–27
4. Patel K, Hashimoto K, Fujishima A (1992) Photoelectrochemical investigations on boron-doped chemically vapour-deposited diamond electrodes. J Photochem Photobiol, A 65:419–429

https://www.twirpx.org & http://chemistry-chemists.com

5. Boonma L, Yano T, Tryk D, Hashimoto K, Fujishima A (1997) Observation of photocurrent from band-to-band excitation of semiconducting p-type diamond thin film electrodes. J Electrochem Soc 144:L142
6. Himpsel FJ, Knapp JA, VanVechten JA, Eastman DE (1979) Quantum photoyield of diamond(111)—a stable negative-affinity emitter. Phys Rev B 20:624–627. https://doi.org/10.1103/PhysRevB.20.624
7. Zhu D, Zhang L, Ruther RE, Hamers RJ (2013) Photo-illuminated diamond as a solid-state source of solvated electrons in water for nitrogen reduction. Nat Mater 12:836–841
8. Zhang L, Zhu D, Nathanson GM, Hamers RJ (2014) Selective photoelectrochemical reduction of aqueous CO(2) to CO by solvated electrons. Angew Chem 53:9746–9750. https://doi.org/10.1002/anie.201404328
9. Busmann HG, Hertel IV (1998) Vapour grown polycrystalline diamond films: microscopic, mesoscopic and atomic surface structures. Carbon 36:391–406. https://doi.org/10.1016/S0008-6223(97)00199-1
10. Roy N et al (2016) Boron-doped diamond semiconductor electrodes: efficient photoelectrochemical CO_2 reduction through surface. Sci Rep 11:9. https://doi.org/10.1038/srep38010
11. Liu FB, Wang JD, Liu B, Li XM, Chen DR (2007) Effect of electronic structures on electrochemical behaviors of surface-terminated boron-doped diamond film electrodes. Diam Relat Mater 16:454–460. https://doi.org/10.1016/j.diamond.2006.08.016
12. Kawarada H, Sasaki H, Sato A (1995) Scanning-tunneling-microscope observation of the homoepitaxial diamond (001) 2\ifmmode\times\else\texttimes\fi{}1 reconstruction observed under atmospheric pressure. Phys Rev B 52:11351–11358. https://doi.org/10.1103/PhysRevB.52.11351
13. Nakabayashi Y, Hirano Y, Sakurai Y, Okazaki A, Kuriyama H, Roy N, Suzuki N, Nakata K, Katsumata KI, Fujishima A, Terashima C (2018) Positive shift in the potential of photoelectrochemical CO_2 reduction to CO on Ag-loaded boron-doped diamond electrode by an electrochemical pre-treatment. J Appl Electrochem 48:61–73. https://doi.org/10.1007/s10800-017-1132-8
14. Zhu D, Bandy JA, Li S, Hamers RJ (2016) Amino-terminated diamond surfaces: photoelectron emission and photocatalytic properties. Surf Sci 650:295–301. https://doi.org/10.1016/j.susc.2016.01.003
15. Li S, Bandy JA, Hamers RJ (2018) Enhanced photocatalytic activity of diamond thin films using embedded Ag nanoparticles. ACS Appl Mater Interfaces 10:5395–5403. https://doi.org/10.1021/acsami.7b13821
16. Bauer N (1960) Theoretical pathways for the reduction of N2 molecules in aqueous media: thermodynamics of N2Hn1. J Phys Chem 64:833–837. https://doi.org/10.1021/j100836a001

https://www.twirpx.org & http://chemistry-chemists.com

Electrochemical CO_2 Reduction

Mai Tomisaki and Yasuaki Einaga

Abstract BDD electrode was utilized as the cathode for the electrochemical CO_2 reduction due to its high hydrogen overpotential and high stability. Electroreduction of CO_2 is one of the ways to convert CO_2 into useful compounds which can be used in industrial fields and can be used as fuels. The efficiency or selectivity for the production of CO_2 reduction products can be affected by electrode materials and electrolysis conditions. BDD electrode is inert, so formic acid production was predominant. However, we could also produce various kinds of products from CO_2 by optimizing the electrode itself or electrolysis conditions. Many kinds of BDD electrodes were used such as BDD electrodes with various boron doping level, BDD electrodes with sp^2 carbon impurities and BDD electrodes modified with metal particles electrochemically. Electrolysis conditions were also optimized such as the applied potential, applied current, catholyte and anolyte. In this chapter, the electrochemical CO_2 reduction using BDD electrodes or using metal-modified BDD electrodes was described.

Keywords Boron-doped diamond · Carbon dioxide · Infrared spectroscopy · Electrochemical CO_2 reduction · Metal-modified electrode

1 Introduction

The electrochemical CO_2 reduction is one of the ways to convert CO_2, which is an abundant source of carbon, into valuable products like alcohol, hydrocarbons, formic acid or carbon monoxide [1, 2]. There are some advantages to utilize CO_2 electrochemically. It can be performed under room temperature and ordinary pressure. The reaction can be controlled by optimizing the applied potential and current. It is relatively easy to scale up the reaction. There are some requirements for CO_2 reduction taken place in aqueous solution. They are the efficient and selective production of reduction products, the decrease of overpotential for CO_2 reduction reaction,

M. Tomisaki · Y. Einaga (✉)
Faculty of Science and Technology, Department of Chemistry, Keio University, 3-14-1 Hiyoshi, Yokohama 223-8522, Japan
e-mail: einaga@chem.keio.ac.jp

© Springer Nature Singapore Pte Ltd. 2022

Y. Einaga (ed.), *Diamond Electrodes*,
https://doi.org/10.1007/978-981-16-7834-9_10

https://www.twirpx.org & http://chemistry-chemists.com

high overpotential for hydrogen evolution reaction which is a competing reaction in CO_2 reduction reaction and a high durability to withstand a reaction for a long time [1, 3, 4].

BDD electrode can be a candidate for the working electrode used in CO_2 reduction for its great electrochemical properties [5]. BDD has a wide potential window in an aqueous solution, so a hydrogen evolution reaction can be restrained. BDD also has a high chemical and physical stability the electrochemical properties of BDD electrode can be changed by the boron doping level, the presence of sp^2 carbon impurities, and the surface chemical species [5–8], so the selective production of various products or the decrease of overpotential for CO_2 reduction can be achieved by optimizing these conditions. BDD has been used as the working electrode of CO_2 reduction so far, and several reduction products have been produced. In many cases, BDD electrodes showed a great durability for the electrolysis [9–12]. Each research is explained from the next section.

2 CO_2 Reduction Using Bare-BDD Electrodes

First, bare-BDD electrodes which are not modified with any metal microparticles or any organic compounds were used as the working electrode. Formic acid, carbon monoxide, methanol and formaldehyde were produced from CO_2 reduction using bare-BDD.

2.1 Formic Acid Production

Formic acid was produced efficiently when relatively high current (-2.0 mA cm^{-2}) was applied. The flow rate of electrolyte, applied current density, boron concentration of BDD electrodes, sp^2 carbon impurity concentration and electrolytes were varied and studied each effect on CO_2 reduction using BDD electrodes.

Each electrolysis was conducted by using a two-compartment flow cell separated by a Nafion membrane [9] (Fig. 1). 0.1% BDD whose boron-to-carbon ratio in the feed gases was 1000 ppm (0.1%) was used as the working electrode. Pt plate and Ag/AgCl were used as the counter and reference electrodes, respectively. The Faradaic efficiency was calculated by the following equation:

$$\text{Faradaic efficiency } (\%) = nFc/Q \times 100$$

where n is the number of electrons used to produce the certain product from CO_2 (e.g. $n = 2$ to produce formic acid from CO_2), F is the Faraday's constant (96,485 C mol^{-1}), c is the number of moles for the certain product and Q is all the charge passed.

https://www.twirpx.org & http://chemistry-chemists.com

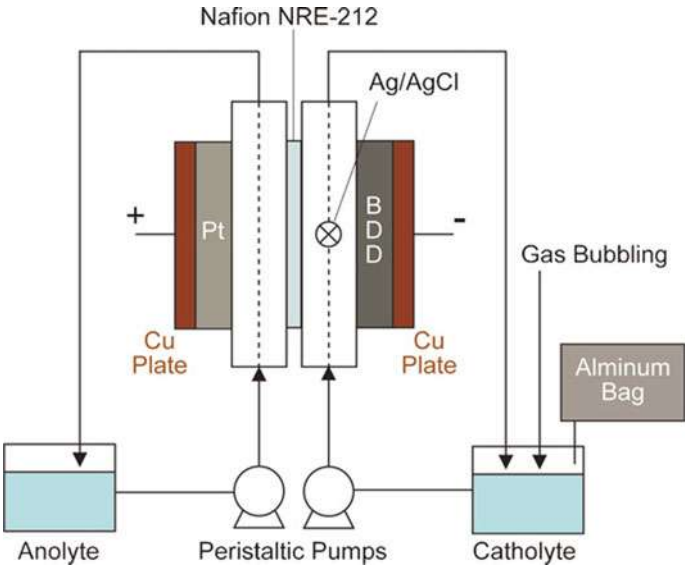

Fig. 1 Schematic diagram of a two-compartment flow cell separated with a Nafion membrane

First, the flow rate of electrolyte was varied from 20 mL min^{-1} to 500 mL min^{-1} and the electrolysis was conducted at -2.0 mA cm^{-2} for 1 h in KCl aqueous solution. Formic acid was mainly produced, and a small amount of carbon monoxide and hydrogen were obtained (Table 1). By using the electrodes on which the intermediate of CO_2 reduction reaction ($CO_2^{\bullet-}$ intermediates) is hardly adsorb, formic acid can be produced easily [2, 13]. As the surface of BDD electrode is chemically inert [5], it is supposed that $CO_2^{\bullet-}$ intermediates might hardly adsorb on BDD surface and formic acid production can be easy to undergo. The Faradaic efficiency for formic acid production increased as a flow rate of electrolyte increased, and the maximum Faradaic efficiency (94.7%) was observed at a flow rate of 200 mL min^{-1}. The

Table 1 The production rate of formic acid and the Faradaic efficiencies for the production of formic acid, carbon monoxide, and hydrogen by the electrochemical reduction of CO_2 with a flow cell using 0.1% BDD electrode at -2.0 mA cm^{-2} in KCl aqueous solution with various flow rates of the electrolyte

Flow rate [mL min^{-1}]	Production rate of HCOOH [μmol m^{-2} s^{-1}]	Faradaic efficiency [%]			
		HCOOH	CO	H_2	Total
20	36.6 ± 9.8	35.4 ± 9.4	0.4 ± 0.1	40.8 ± 9.6	76.6 ± 5.1
50	87.7 ± 2.0	84.7 ± 2.0	0.9 ± 0.6	8.6 ± 2.5	94.2 ± 0.7
100	94.3 ± 0.8	91.1 ± 0.7	0.5 ± 0.4	3.6 ± 1.3	95.2 ± 0.9
200	97.9 ± 2.3	94.7 ± 2.3	0.6 ± 0.5	4.1 ± 1.9	99.4 ± 0.6
500	91.4 ± 1.9	88.4 ± 1.8	2.7 ± 2.6	8.1 ± 3.4	99.2 ± 0.8

https://www.twirpx.org & http://chemistry-chemists.com

fresh CO_2 was supplied more frequently to the surface of the electrode as the flow rate of electrolyte increased, so the Faradaic efficiency for producing formic acid increased. When the flow rate was too fast, the electron transfer from BDD electrode to CO_2 was restrained and formic acid production decreased. Next, the applied current density was varied from -2.0 mA cm^{-2} to -20 mA cm^{-2}. The Faradaic efficiency of formic acid production decreased as the applied current density was increased. However, the production rate of formic acid increased and reached the maximum rate of 473 μmol m^{-2} s^{-1}.

It is known that the electrochemical properties of BDD can be changed by the boron doping level and the presence or absence of sp^2 carbon impurities [6, 7], so we studied the effect of them to the electrochemical CO_2 reduction [14, 15]. By using BDD electrodes whose boron concentration is 0.01, 0.1, 0.5, 1 and 2% as the working electrode, CO_2 reduction was conducted at -2.0 mA cm^{-2} for 1 h in KCl aqueous solution. The applied potential shifted to more positive potential with increasing the boron concentration of BDD electrodes. Formic acid was produced as a main product and a small amount of carbon monoxide and hydrogen production were also observed (Fig. 2). The Faradaic efficiency for the production of formic acid became the maximum when using 0.1% BDD electrode as a cathode, and it decreased as the boron concentration of BDD electrodes became high due to the high hydrogen production caused from their narrow potential window [6]. On the other hand, the Faradaic efficiency for the production of carbon monoxide slightly increased as the boron concentration of BDD electrodes was increased. Carbon monoxide production is promoted by using the electrodes on which $CO_2^{\bullet-}$ intermediates adsorb [2, 13]. It is assumed that on the high boron content BDD electrodes $CO_2^{\bullet-}$ intermediates can adsorb more easily than the low boron content one. Moreover, BDD electrodes with various sp^2 existence level were used as the cathode. As the sp^2 existence was increased, the Faradaic efficiency for the production of formic acid decreased and that for the production of hydrogen increased (Fig. 3). More negative potential was applied during CO_2 reduction at -2.0 mA cm^{-2} as sp^2 existence was increased. In addition,

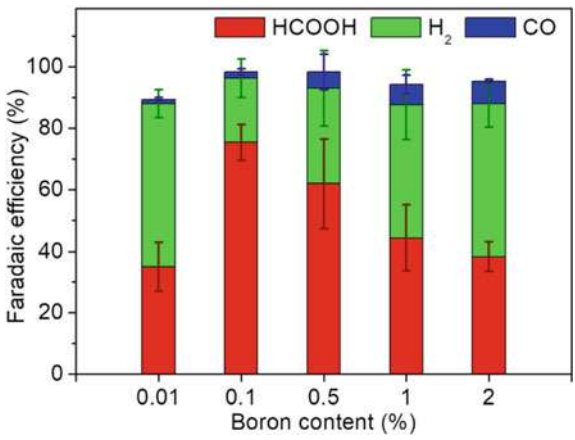

Fig. 2 Faradaic efficiencies for the production of formic acid (red), hydrogen (green), and carbon monoxide (blue) by the electrochemical reduction of CO_2 with a flow cell using BDD electrodes with various boron doping level at -2.0 mA cm^{-2} in KCl aqueous solution

https://www.twirpx.org & http://chemistry-chemists.com

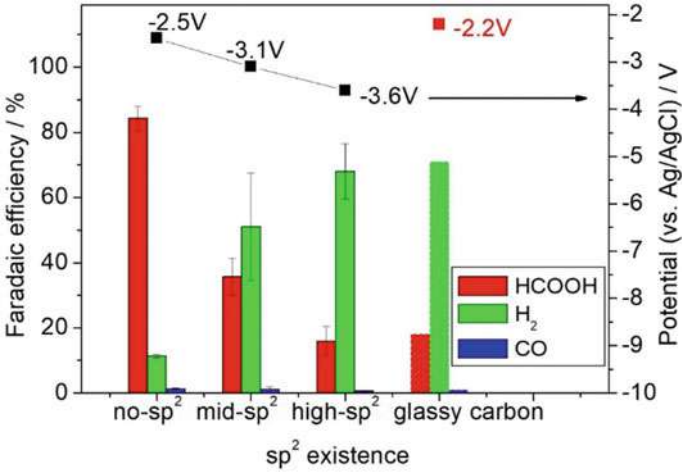

Fig. 3 Faradaic efficiencies for the production of formic acid (red), hydrogen (green), and carbon monoxide (blue) and the observed potential by the electrochemical reduction of CO_2 with a flow cell using 0.1% BDD electrodes with various sp^2 existence level or glassy carbon electrode at -2.0 mA cm^{-2} in KCl aqueous solution

carbon monoxide production was slightly promoted by using BDD electrodes with sp^2 species.

Furthermore, the products by CO_2 reduction can be affected by the electrolyte [1, 2, 13, 16]. We studied how the electrolyte can affect the efficiency or the selectivity of the products by CO_2 reduction reaction [17]. First, the effect of cations was investigated. Electrochemical CO_2 reduction was conducted in the catholytes containing alkali metal cations and halide anions (MX: M = Li, Na, K, Rb, and Cs; X = Cl, Br, and I). Other electrolysis conditions were same as written above. The main reduction product was formic acid. Carbon monoxide and hydrogen were also obtained (Fig. 4a). When K^+, Rb^+ and Cs^+ were contained, the Faradaic efficiency for formic acid production was high and that for hydrogen production was low. Meanwhile, when Li^+ and Na^+ were contained, opposite tendency was observed. This is due to the buffering effect of hydrated alkali metal ions [16]. During the electrolysis, hydrogen ions are consumed by CO_2 reduction reaction and hydrogen evolution reaction, so pH near the cathode increases. Hydrated cations can emit oxonium ions to the electrolyte and this reaction is promoted more when K^+, Rb^+ or Cs^+ are used as cations. In the electrolytes containing these cations, increase of pH near the cathode was suppressed, so the concentration of molecular CO_2, which was thought to be electrochemically reduced in CO_2 reduction reaction [16], was kept high [18] leading to an efficient formic acid production. Next, the effect of anions was investigated. Electrolysis was conducted using the electrolytes whose cation was K^+ and anions were NO_3^-, SO_4^{2-}, Cl^-, Br^-, I^- and ClO_4^- (Fig. 4b). In the electrolyte containing NO_3^-, neither CO_2 reduction products nor hydrogen were obtained. This is because electrons were consumed by NO_3^- reduction reaction [19, 20]. When SO_4^{2-} or halide

https://www.twirpx.org & http://chemistry-chemists.com

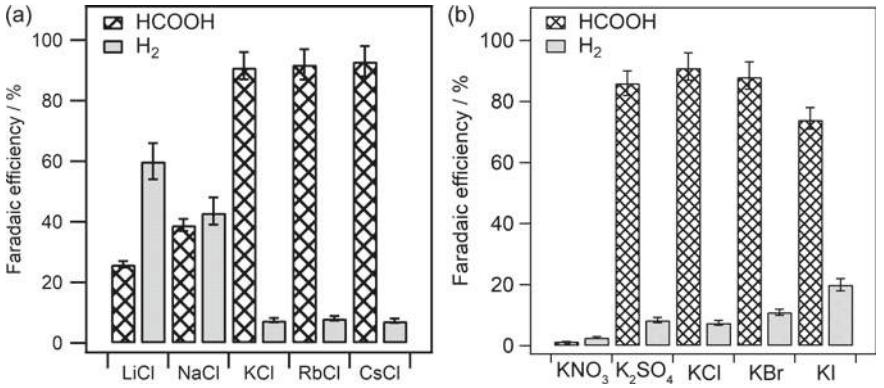

Fig. 4 Faradaic efficiencies for the production of formic acid (net pattern) and hydrogen (dot pattern) by the electrochemical reduction of CO_2 with a flow cell using 0.1% BDD electrodes at -2.0 mA cm^{-2} in **a** MCl and **b** KNO_3, K_2SO_4 and KX aqueous solutions (M = Li, Na, K, Rb, and Cs; X = Cl, Br, and I)

anions which are thought to be specifically adsorbed on electrodes were contained, formic acid was produced efficiently. These specifically adsorbed anions can restrict the movement of CO_2 to near the cathode, so the electron transfer from the cathode to CO_2 can be promoted [21]. On the other hand, when the electrolyte containing ClO_4^- was used, production of formic acid was suppressed but that of carbon monoxide increased slightly. The details are written in the next section.

Efficient and selective formic acid production was achieved in the electrochemical reduction of CO_2 on BDD electrodes. It was also revealed that boron concentration and sp^2 carbon impurities of BDD electrodes and electrolytes can affect the production.

2.2 *Carbon Monoxide Production*

Although small amount of carbon monoxide production has been reported in CO_2 reduction using bare-BDD electrodes [9, 10, 14, 22], by changing the electrolyte and optimizing the electrolysis conditions, we also achieved to produce carbon monoxide efficiently. In the previous section, carbon monoxide production increased when $KClO_4$ was used as the electrolyte. CO_2 reduction using $KClO_4$ as the electrolyte was investigated in detail to improve the Faradaic efficiency and the selectivity for producing carbon monoxide [23].

CO_2 reduction using 0.1% BDD in $KClO_4$ aqueous solution was conducted at various applied potential (-2.5 V ~ -2.0 V *vs.* Ag/AgCl). Carbon monoxide and formic acid were mainly obtained as CO_2 reduction products. The Faradaic efficiency of carbon monoxide production increased as the applied potential shifted to the positive potential and reached the maximum at -2.1 V (Fig. 5a). CO_2 reduction

https://www.twirpx.org & http://chemistry-chemists.com

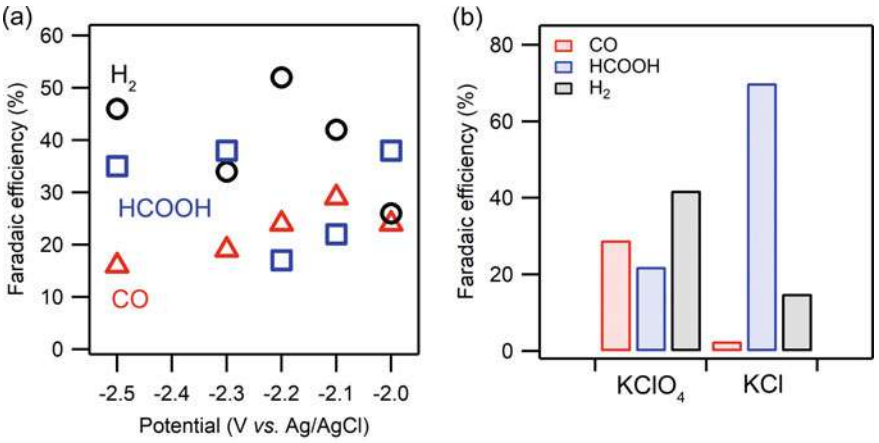

Fig. 5 **a** Faradaic efficiencies for the production of carbon monoxide (red triangles), formic acid (blue squares), and hydrogen (black circles) by the electrochemical reduction of CO_2 with a flow cell using 0.1% BDD electrodes in $KClO_4$ aqueous solution. **b** Comparison of the Faradaic efficiencies of reduction products between the electrochemical reduction of CO_2 with a flow cell using 0.1% BDD electrodes at −2.1 V (*vs.* Ag/AgCl) in $KClO_4$ and KCl aqueous solutions

at −2.1 V using KCl aqueous solution in which formic acid was produced efficiently in the previous section was also conducted and compared with the results taken in $KClO_4$ aqueous solution (Fig. 5b). When KCl was used as the electrolyte, formic acid was produced efficiently. It is supposed that in $KClO_4$ aqueous solution carbon monoxide production is promoted, but in KCl aqueous solution formic acid production is promoted. Carbon monoxide can be produced by using the electrodes which $CO_2^{\bullet-}$ intermediates can adsorb on, and formic acid can be produced by using the electrodes which $CO_2^{\bullet-}$ intermediates hardly adsorb on [2, 13]. It is assumed that when $KClO_4$ was used as the electrolyte, $CO_2^{\bullet-}$ intermediates can adsorb on the surface of BDD electrode, and when KCl was used as the electrolyte, $CO_2^{\bullet-}$ intermediates hardly adsorb on it.

To investigate the effect of the anions, attenuated total reflectance-infrared (ATR-IR) measurements using BDD film deposited onto a Si ATR-IR prism [24, 25] were conducted during electrolysis at −2.1 V (*vs.* Ag/AgCl) in $KClO_4$ and KCl aqueous solutions (Fig. 6). The peak which can be assigned to asymmetric OCO stretching was observed at around 1600 cm^{-1}. This peak suggests the presence of $CO_2^{\bullet-}$ intermediates. It was observed at 1634 cm^{-1} in $KClO_4$ aqueous solution, but in KCl aqueous solution, it was observed at 1616 cm^{-1}. Thus, the nature of the adsorption of $CO_2^{\bullet-}$ intermediates on the BDD electrodes is different in the two different solutions. BDD film was also deposited by using $^{13}CH_4$ as carbon source (^{13}C-BDD), and ATR-IR measurements were done by using ^{13}C-BDD film for the further study. The peak which is assigned to $CO_2^{\bullet-}$ intermediates was shifted to 1624 cm^{-1} in $KClO_4$ aqueous solution, but in KCl aqueous solution, no peak shift was observed. Only in $KClO_4$ aqueous solution, we observed the difference caused by an isotope labelling,

https://www.twirpx.org & http://chemistry-chemists.com

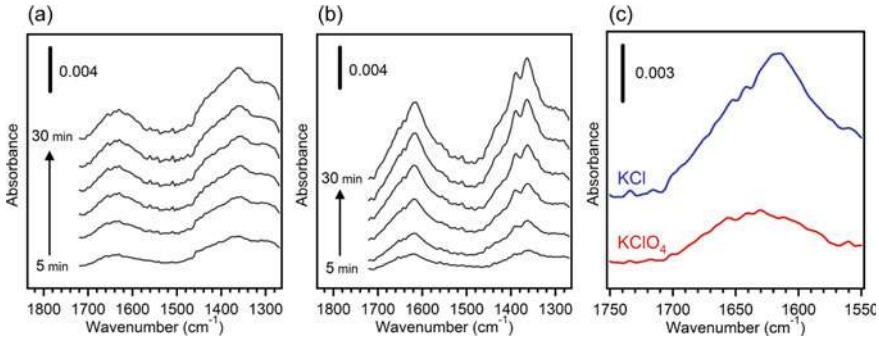

Fig. 6 Time-dependent ATR-IR spectra during the electrochemical reduction of CO_2 using BDD film deposited onto a Si ATR-IR prism at −2.1 V (*vs.* Ag/AgCl) in **a** $KClO_4$ and **b** KCl aqueous solutions. Each spectrum was taken every five minutes during the electrolysis. **c** Comparison of the spectra taken after 30 min of electrolysis in $KClO_4$ (red) and KCl (blue) aqueous solutions

so it is plausible that $CO_2^{\bullet-}$ intermediates adsorb on the surface of BDD in $KClO_4$ aqueous solution, but in case of KCl aqueous solution, many intermediates exist as free intermediates.

In addition, the boron concentration of BDD electrodes and a flow rate of electrolyte were varied to obtain good selectivity and efficiency for producing carbon monoxide. By increasing the boron concentration of BDD electrodes to 1% and using $KClO_4$ as the electrolyte, the Faradaic efficiency of carbon monoxide production increased and the selectivity to produce carbon monoxide also improved. It was reported that BDD electrodes which are highly doped with boron have more acceptor states and holes [26], so $CO_2^{\bullet-}$ intermediates can adsorb on the surface of BDD more easily. Furthermore, a flow rate of the electrolyte was varied from 100 mL min^{-1} to 500 mL min^{-1}. The Faradaic efficiency for producing carbon monoxide and formic acid increased and that for producing hydrogen dramatically decreased as the flow rate was increased. When the flow rate was high, fresh CO_2 was supplied more to the surface of cathode [9], and the removement of carbon monoxide which was produced on the cathode was also promoted.

By using $KClO_4$ as the electrolyte and high boron content BDD as the cathode, the Faradaic efficiency for producing carbon monoxide was reached to 68%.

2.3 Other C1 Products Production

In CO_2 reduction using BDD electrode, formic acid or carbon monoxide is easily produced. However, methanol and formaldehyde were also produced by reducing the applied potential or changing the solution.

An aqueous ammonia solution which is one of the strong CO_2 absorbers was used as the catholyte in CO_2 reduction with a batch cell using 1% BDD electrodes [10].

https://www.twirpx.org & http://chemistry-chemists.com

Table 2 The Faradaic efficiencies for the production of methanol, carbon monoxide, methane and hydrogen by the electrochemical reduction of CO_2 with a batch cell using 1% BDD electrodes at −1.5 V to −1.2 V (*vs.* Ag/AgCl) in an aqueous ammonia solution

Potential (V *vs.* Ag/AgCl)	Faradaic efficiency (%)			
	CH_3OH	CO	CH_4	H_2
–1.2	2.61	0	0.24	0
–1.3	24.3	0.05	0.13	19.7
–1.4	15.1	0.12	0.03	25.8
–1.5	2.02	0.20	0	57.2

Methanol was mainly produced and a small amount of methane and carbon monoxide were also obtained (Table 2). The Faradaic efficiency of methanol production was reached to 24.3% at −1.3 V (*vs.* Ag/AgCl). The Faradaic efficiencies for producing methane and carbon monoxide were quite small, so a selective methanol production was achieved which could not be achieved even using metal-modified BDD electrodes [27]. The pH of an aqueous ammonia solution saturated with CO_2 was neutral, so CO_2 bubbled into the solution exists as HCO_3^- in the solution [18]. Thus, it is assumed that HCO_3^- undergoes CO_2 reduction in this system. The electrochemical reduction of CO_2 in NH_4HCO_3 aqueous solution was also conducted without CO_2 bubbling to confirm that HCO_3^- is a reactant. The results showed that methanol was mainly produced.

CO_2 reduction with a batch cell using BDD electrodes in a methanol solution containing tetrabutylammonium perchlorate as a supporting electrolyte was investigated at relatively positive potential (−1.9 V ~ −1.0 V *vs.* Ag/Ag^+) compared to that applied to produce formic acid [11]. In this condition, formaldehyde was mainly produced and formic acid was produced as a by-product (Fig. 7). The Faradaic efficiency of producing formaldehyde became the maximum (74%) at −1.7 V and that

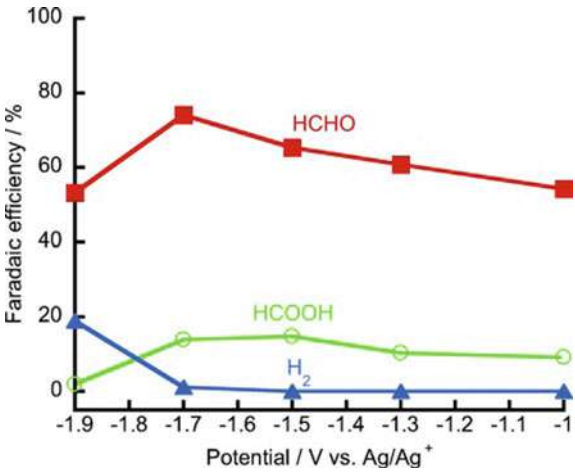

Fig. 7 Faradaic efficiencies for the production of formaldehyde (red squares), formic acid (green circles), and hydrogen (blue triangles) by the electrochemical reduction of CO_2 with a batch cell using 1% BDD electrodes in a methanol solution containing tetrabutylammonium perchlorate as a supporting electrolyte

https://www.twirpx.org & http://chemistry-chemists.com

of producing formic acid reached to 15% at −1.5 V. It is reported that the pH near the cathode becomes basic when more negative potential was applied, and Cannizzaro-type disproportionation reactions occur [28]. Formic acid and methanol are thought to be produced from formaldehyde by this reaction. It is likely that one of the reasons why formic acid was easily produced in the previous sections is that applying more negative potential during the electrolysis. Furthermore, the electrolysis using BDD electrodes for both the cathode and the anode was investigated in Na_2SO_4 aqueous solution, and the highest Faradaic efficiency for the production of formaldehyde (42%) was obtained at −1.2 V *vs.* Ag/AgCl [29].

By changing applied potential or the electrolyte, methanol and formaldehyde were also obtained from CO_2 electroreduction using bare-BDD electrodes.

3 CO_2 Reduction Using Metal-Modified BDD Electrodes

CO_2 reduction reaction using BDD electrodes occurs at more negative potential compared to using metal electrodes. It is also important to reduce the overpotential for CO_2 conversion [3]. By modifying metal particles on the surface of BDD electrodes, we attempt to reduce the overpotential and expect to get other reduction products.

3.1 Cu-Modified BDD Electrodes: C2 and C3 Species Production

Cu has a specific property for CO_2 reduction reaction as it is the only metal which can also produce C2 and C3 products. CO_2 reduction with a batch cell using Cu-modified BDD (Cu-BDD) electrodes was investigated [30]. Cu-BDD electrodes were prepared by chronoamperometry at −0.6 V (*vs.* Ag/AgCl) in H_2SO_4 aqueous solution containing $CuSO_4$ for 50 s (Cu-BDD-50), 100 s (Cu-BDD-100), and 300 s (Cu-BDD-300). The average size of Cu particles on each Cu-BDD electrode was around 50–85 nm (Fig. 8a). Cu-BDD and Pt mesh were used as the cathode and the anode, respectively. KCl aqueous solution saturated with CO_2 was used as the electrolyte. Although carbon monoxide was mainly produced in the previous research [31], ethanol was mainly produced, and acetaldehyde and acetone were also obtained (Fig. 8b). The Faradaic efficiency for producing ethanol was highest when using Cu-BDD-100 as the cathode. When Cu-BDD-50 was used, the amount of Cu particles was not enough to undergo efficient CO_2 reduction reaction. In case of Cu-BDD-300, the production of CO_2 reduction products decreased because of the instability of Cu particles. It is assumed that hydrogen evolution reaction was promoted due to the narrower potential window of highly metal-modified BDD electrodes, and Cu particles were detached by abundant hydrogen evolution. Moreover, CO_2 reduction using Cu-BDD-100 was carried out at several potentials (−1.2 V ~ −0.8 V *vs.*

https://www.twirpx.org & http://chemistry-chemists.com

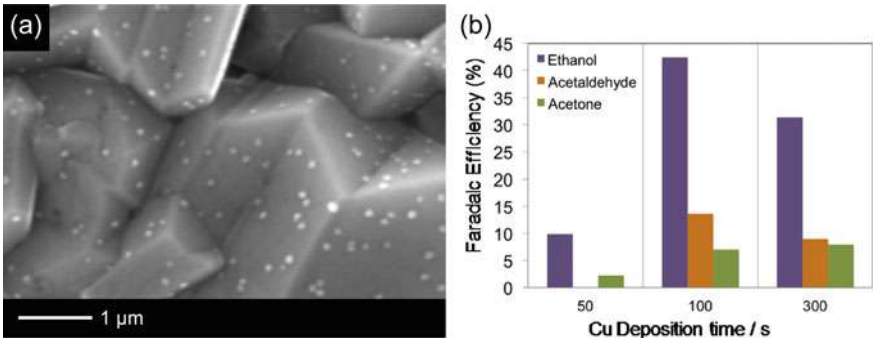

Fig. 8 **a** SEM images of Cu-BDD-100 electrode before the electrolysis. **b** The Faradaic efficiencies for the production of ethanol (purple), acetaldehyde (orange), and acetone (green) by the electrochemical reduction of CO_2 with a batch cell using Cu-BDD-50, Cu-BDD-100, and Cu-BDD-300 electrodes at −1.0 V (*vs.* Ag/AgCl) in KCl aqueous solution

Ag/AgCl). The Faradaic efficiency for the production of ethanol was highest at −1.0 V. At more negative potential than −1.0 V, the Faradaic efficiency for producing ethanol decreased, which is due to the detachment of Cu particles by hydrogen evolution reaction. At more positive potential than −1.0 V, Cu particles on BDD electrodes seemed to be stable after the electrolysis. It is supposed that at −1.0 V or at more positive potential than −1.0 V, hydrogen evolution reaction was suppressed and it is favourable to undergo C–C coupling reactions [32] which depend on the amount of carbon monoxide adsorbed to the surface of the cathode.

CO_2 reduction using Cu-BDD electrodes proceeded at low potential (−1.0 V), which bare-BDD electrodes cannot undergo efficient electrolysis. Using Cu-BDD as the cathode, it has advantages for lowering the overpotential for CO_2 reduction reaction and producing C2 and C3 species from CO_2.

3.2 Pd-Modified, Ag-Modified, and Cu-SnO_x-Modified BDD Electrodes: Carbon Monoxide Production

BDD electrodes modified with Pd [33, 34], Ag [22], and Cu-SnO_x [35] were also used in CO_2 reduction. Pd-modified BDD (PdBDD) electrodes were prepared by chronoamperometry at −0.15 V (*vs.* Ag/AgCl) in HCl aqueous solution containing $PdCl_2$ for 30 s (PdBDD30), 100 s (PdBDD100), 300 s (PdBDD300), 500 s (PdBDD500), and 1000 s (PdBDD1000). The average size of Pd particles on PdBDD30, PdBDD100, and PdBDD300 electrodes was around 50 nm, and it was around 160 nm on PdBDD500 and PdBDD1000 electrodes. PdBDD and Pt mesh were used as the cathode and the anode, respectively. NaCl aqueous solution saturated with CO_2 was used as the electrolyte. Carbon monoxide was mainly produced, and formic acid was also obtained (Fig. 9). The Faradaic efficiency for producing

https://www.twirpx.org & http://chemistry-chemists.com

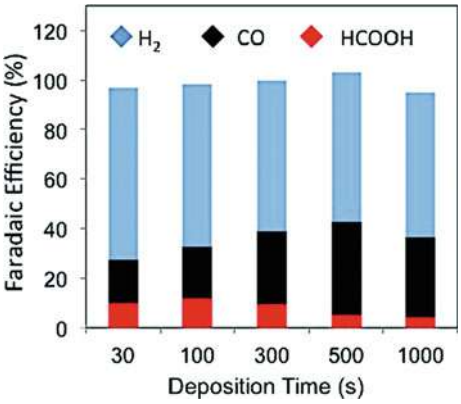

Fig. 9 Faradaic efficiencies for the production of hydrogen (blue), carbon monoxide (black) and formic acid (red) by the electrochemical reduction of CO_2 with a batch cell using PdBDD30, PdBDD100, PdBDD300, PdBDD500 and PdBDD1000 electrodes at −1.5 V (*vs.* Ag/AgCl) in NaCl aqueous solution

carbon monoxide increased as the amount of Pd particles modified on BDD electrodes was increased, but it decreased slightly with PdBDD1000. In addition, the optimum applied potential was studied at −1.9 V ~ −1.4 V (*vs.* Ag/AgCl). The highest Faradaic efficiency for the production of carbon monoxide (53.3%) was observed at −1.6 V using PdBDD300 as the cathode. For the further study, PdBDD300 was used as the cathode. The effect of electrolyte concentration was then investigated using NaCl aqueous solution whose concentration was 0.1, 0.3, 0.5, and 1.0 mol L^{-1}. Both the Faradaic efficiency and the partial current density for the production of CO_2 reduction products tended to increase as the concentration of electrolyte was increased for the higher ionic conductivity. Furthermore, other cations (K^+, Rb^+, and Cs^+) were used. The Faradaic efficiency for the production of carbon monoxide in KCl and CsCl aqueous solutions showed the similar trend observed in NaCl aqueous solution that is the Faradaic efficiency increased as the electrolyte concentration was increased. However, in RbCl aqueous solution, formic acid was a main product. In our previous research of CO_2 reduction using bare-BDD electrodes, the maximum production of formic acid was also achieved when Rb^+ was used as a cation of the catholyte [17, 36]. Moreover, the effect of anions was investigated in NaCl, Na_2SO_4, Na_2CO_3 , and $NaClO_4$ aqueous solutions. In NaCl and $NaClO_4$ aqueous solutions, carbon monoxide was well produced, but in Na_2CO_3 aqueous solution hydrogen evolution reaction was dominant. The pH of Na_2CO_3 aqueous solution saturated with CO_2 is neutral, so the concentration of CO_2 molecules is low and that of HCO_3^- is high, leading to the suppression of CO_2 reduction reaction.

Ag-modified BDD electrodes were prepared in a two-electrode system at 10 V (*vs.* Pt counter electrode) in $AgNO_3$ aqueous solution. CO_2 reduction using Ag-modified BDD was performed in K_2SO_4 and $KHCO_3$ aqueous solutions saturated with CO_2, and carbon monoxide production was promoted and the overpotential for CO_2 reduction was also decreased.

Cu-SnO_x-modified BDD electrodes were prepared by cyclic voltammetry (0 V ~ −1.0 V *vs.* Ag/AgCl) in $NaNO_3$ aqueous solution containing $CuSO_4$ and $SnCl_2$. The average size of Cu-SnO_x hybrid particles on BDD electrodes was 50–100 nm.

https://www.twirpx.org & http://chemistry-chemists.com

Cu-SnO_x-modified BDD and Pt net were used as the cathode and the anode, respectively. Na_2SO_4 aqueous solution saturated with CO_2 was used as the electrolyte. Carbon monoxide, formic acid, and methane were produced. At less negative potential (−1.8 V ~ −1.5 V *vs.* Ag/AgCl), carbon monoxide was mainly produced, but as the applied potential shifted to the more negative potential (−2.0 V ~ −1.9 V *vs.* Ag/AgCl), formic acid was mainly produced and methane production was also promoted. The Faradaic efficiency for the production of carbon monoxide reached to 82.5% at −1.6 V, and that for the production of formic acid reached to 46.6% at −2.0 V. It is assumed that this high activity of Cu-SnO_x modified BDD electrodes is due to the cooperative effects of Cu-SnO_x hybrid particles. The active sites through Cu doping and presence of oxides might stabilize $CO_2^{\bullet-}$ intermediates.

We could obtain carbon monoxide from the electrochemical CO_2 reduction using BDD electrodes modified with Pd, Ag, and Cu-SnO_x at relatively positive potential compared to the electrolysis using bare-BDD electrodes.

3.3 *CeO_2-Modified and IrO_2-Modified BDD Electrodes: Formic Acid Production*

BDD electrodes modified with CeO_2 [37] and IrO_2 [38] were also used in CO_2 reduction. CeO_2-modified BDD electrodes were prepared by chronoamperometry in $NaNO_3$ solution containing $Ce(NO_3)_3$. CO_2 reduction using CeO_2-modified BDD was carried out in $KHCO_3$ buffer solution or phosphate buffer solution. Formic acid was mainly produced and formaldehyde was also obtained (Fig. 10). The highest Faradaic efficiency for the production of formic acid (46%) was observed at quite low

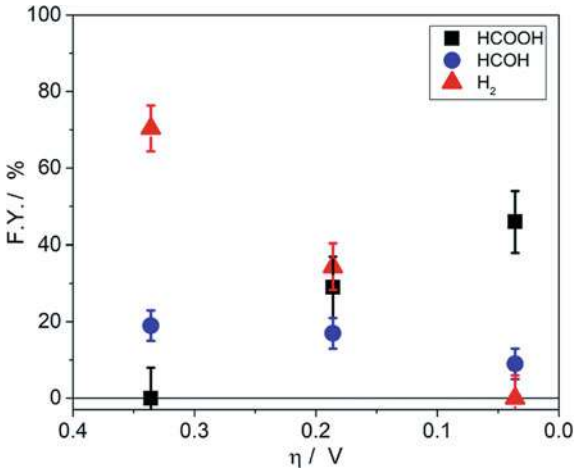

Fig. 10 Relationship between overpotential and the Faradaic efficiencies for the production of formic acid (black squares), formaldehyde (blue circles), and hydrogen (red triangles) in the electrochemical reduction of CO_2 using CeO_2-modified BDD electrodes

https://www.twirpx.org & http://chemistry-chemists.com

overpotential ($\phi \sim 40$ mV). Ceria seemed to act as a co-catalyst and adsorbed the reactants, so CO_2 reduction was promoted, leading to the decrease of the overpotential. Overpotential was calculated by the following equation:

Overpotential (ϕ) = $E_{vs.\ SHE} - E_{Eq\ (CO_2/HCOOH)}$

$E_{Eq\ (CO_2/HCOOH)} = -0.418$ V (at pH = 6.8).

IrO_2-modified BDD electrodes were prepared by cyclic voltammetry (+0.2 V ~ + 1.2 V *vs.* Ag/AgCl) in KNO_3 solution containing Na_2IrCl_6 whose pH was fixed at 10.5. CO_2 reduction using IrO_2-modified BDD was conducted in NaCl solution. Formic acid and carbon monoxide were produced at more positive potential than the electrolysis using bare-BDD electrodes. The Faradaic efficiency of producing formic acid could reach to 51.98% at −1.7 V (*vs.* Ag/AgCl).

In both cases, formic acid was produced at more positive potential than the previous electrolysis which was written in Sect. 2.1.

4 Conclusions

The electrochemical CO_2 reduction using bare-BDD and metal-modified BDD electrodes was investigated. We could obtain various CO_2 reduction products such as formic acid, carbon monoxide, methanol, formaldehyde, ethanol, acetaldehyde, and acetone by modifying the BDD electrodes, and using various electrolytes and applied potential. BDD electrode which is inert tends to produce formic acid efficiently. However, it is of great interest to produce several products by optimizing the electrolysis conditions. In most cases using bare-BDD electrodes, high durability was confirmed. In contrast, the electrolysis using metal-modified BDD electrodes showed some problems for the stability of metal-modified BDD electrodes. However, metal-modified BDD electrodes showed a decrease of the overpotential for CO_2 reduction reaction, and this is one of the things which CO_2 reduction using bare-BDD electrodes should achieve. Various products including C2 and C3 species can be produced more efficiently and selectively from the electroreduction of CO_2 using highly stable BDD electrodes in the future.

References

1. Hori Y (2008) Electrochemical CO_2 reduction on metal electrodes. Springer, New York, pp 89–189
2. Zhu DD, Liu JL, Qiao SZ (2016) Recent advances in inorganic heterogeneous electrocatalysts for reduction of carbon dioxide. Adv Mater 28:3423–3452
3. Ganesh I (2016) Electrochemical conversion of carbon dioxide into renewable fuel chemicals—the role of nanomaterials and the commercialization. Renew Sustain Energy Rev 59:1269–1297
4. Anawati, Frankel GS, Agarwal A, Sridhar N (2014) Degradation and deactivation of Sn catalyst used for CO_2 reduction as function of overpotential. Electrochim Acta 133:188–196

https://www.twirpx.org & http://chemistry-chemists.com

5. Yang N, Yu S, Macpherson JV, Einaga Y, Zhao H, Zhao G, Swain GM, Jiang X (2019) Conductive diamond: synthesis, properties, and electrochemical applications. Chem Soc Rev 48:157–204
6. Watanabe T, Honda Y, Kanda K, Einaga Y (2014) Tailored design of boron-doped diamond electrodes for various electrochemical applications with boron-doping level and sp^2-bonded carbon impurities. Phys Status Solidi A 211:2709–2717
7. Garcia-Segura S, Vieira dos Santos E, Martínez-Huitle CA (2015) Role of sp^3/sp^2 ratio on the electrocatalytic properties of boron-doped diamond electrodes: a mini review. Electrochem Commun 59:52–55
8. Szunerits S, Boukherroub R (2008) Different strategies for functionalization of diamond surfaces. J Solid State Electrochem 12:1205–1218
9. Natsui K, Iwakawa H, Ikemiya N, Nakata K, Einaga Y (2018) Stable and highly efficient electrochemical production of formic acid from carbon dioxide using diamond electrodes. Angew Chem Int Ed 57:2639–2643
10. Jiwanti PK, Natsui K, Nakata K, Einaga Y (2016) Selective production of methanol by the electrochemical reduction of CO_2 on boron-doped diamond electrodes in aqueous ammonia solution. RSC Adv 6:102214–102217
11. Nakata K, Ozaki T, Terashima C, Fujishima A, Einaga Y (2014) High-yield electrochemical production of formaldehyde from CO_2 and seawater. Angew Chem Int Ed 53:871–874
12. Ikemiya N, Natsui K, Nakata K, Einaga Y (2018) Long-term continuous conversion of CO_2 to formic acid using boron-doped diamond electrodes. ACS Sustain Chem Eng 6:8108–8112
13. Jones J-P, Prakash GKS, Olah GA (2014) Electrochemical CO_2 reduction: recent advances and current trends. Isr J Chem 54:1451–1466
14. Xu J, Natsui K, Naoi S, Nakata K, Einaga Y (2018) Effect of doping level on the electrochemical reduction of CO_2 on boron-doped diamond electrodes. Diamond Relat Mater 86:167–172
15. Xu J, Einaga Y (2020) Effect of sp^2 species in a boron-doped diamond electrode on the electrochemical reduction of CO_2. Electrochem Commun 115:106731
16. Singh MR, Kwon Y, Lum Y, Ager JW, III, Bell AT (2016) Hydrolysis of electrolyte cations enhances the electrochemical reduction of CO_2 over Ag and Cu. J Am Chem Soc 138:13006−13012
17. Tomisaki M, Natsui K, Ikemiya N, Nakata K, Einaga Y (2018) Influence of electrolyte on the electrochemical reduction of carbon dioxide using boron-doped diamond electrodes. Chem Select 3:10209–10213
18. Zhong H, Fujii K, Nakano Y, Jin F (2015) Effect of CO_2 bubbling into aqueous solutions used for electrochemical reduction of CO_2 for energy conversion and storage. J Phys Chem C 119:55–61
19. Reuben C, Galun E, Cohen H, Tenne R, Kalish R, Muraki Y, Hashimoto K, Fujishima A, Butler JM, Lévy-Clément C (1995) Efficient reduction of nitrite and nitrate to ammonia using thin-film B-doped diamond electrodes. J Electroanal Chem 396:233–239
20. Kuang P, Natsui K, Feng C, Einaga Y (2020) Electrochemical reduction of nitrate on boron-doped diamond electrodes: effects of surface termination and boron-doping level. Chemosphere 251:126364
21. Ogura K, Ferrell JR III, Cugini AV, Smotkin ES, Salazar-Villalpando MD (2010) CO_2 attraction by specifically adsorbed anions and subsequent accelerated electrochemical reduction. Electrochim Acta 56:381–386
22. Romero Cuellar NS, Wiesner-Fleischer K, Hinrichsen O, Fleischer M (2018) Electrochemical reduction of CO_2 in water-based electrolytes $KHCO_3$ and K_2SO_4 using boron doped diamond electrodes. Chem Select 3:3591–3595
23. Tomisaki M, Kasahara S, Natsui K, Ikemiya N, Einaga Y (2019) Switchable product selectivity in the electrochemical reduction of carbon dioxide using boron-doped diamond electrodes. J Am Chem Soc 141:7414–7420
24. Kasahara S, Ogose T, Ikemiya N, Yamamoto T, Natsui K, Yokota Y, Wong RA, Iizuka S, Hoshi N, Tateyama Y, Kim Y, Nakamura M, Einaga Y (2019) In Situ spectroscopic study on the surface hydroxylation of diamond electrodes. Anal Chem 91:4980–4986

https://www.twirpx.org & http://chemistry-chemists.com

25. Kamoshida N, Kasahara S, Ikemiya N, Hoshi N, Nakamura M, Einaga Y (2019) In Situ ATR-IR study of $Fe(CN)_6^{3-}$/$Fe(CN)_6^{4-}$ redox system on boron-doped diamond electrode. Diamond Relat Mater 93:50–53
26. Futera Z, Watanabe T, Einaga Y, Tateyama Y (2014) First principles calculation study on surfaces and water interfaces of boron-doped diamond. J Phys Chem C 118:22040–22052
27. Spataru N, Tokuhiro K, Terashima C, Rao TN, Fujishima A (2003) Electrochemical reduction of carbon dioxide at ruthenium dioxide deposited on boron-doped diamond. J Appl Electrochem 33:1205–1210
28. Birdja YY, Koper MT (2017) The importance of cannizzaro-type reactions during electrocatalytic reduction of carbon dioxide. J Am Chem Soc 139:2030–2034
29. Luo D, Liu S, Nakata K, Fujishima A (2019) Electrochemical reduction of CO_2 and degradation of KHP on boron-doped diamond electrodes in a simultaneous and enhanced process. Chin Chem Lett 30:509–512
30. Jiwanti PK, Natsui K, Nakata K, Einaga Y (2018) The electrochemical production of C2 /C3 species from carbon dioxide on copper-modified boron-doped diamond electrodes. Electrochim Acta 266:414–419
31. Roy N, Shibano Y, Terashima C, Katsumata K-I, Nakata K, Kondo T, Yuasa M, Fujishima A (2016) Ionic-liquid-assisted selective and controlled electrochemical CO_2 reduction at Cu-modified boron-doped diamond electrode. Chem Electro Chem 3:1044–1047
32. Gattrell M, Gupta N, Co A (2006) A review of the aqueous electrochemical reduction of CO_2 to hydrocarbons at copper. J Electroanal Chem 594:1–19
33. Jiwanti PK, Einaga Y (2019) Electrochemical reduction of CO_2 using palladium modified boron-doped diamond electrodes: enhancing the production of CO. Phys Chem Chem Phys 21:15297–15301
34. Jiwanti PK, Einaga Y (2020) Further study of CO_2 electrochemical reduction on palladium modified BDD electrode: influence of electrolyte. Chem Asian J 15:910–914
35. Roy N, Suzuki N, Nakabayashi Y, Hirano Y, Ikari H, Katsumata K-I, Nakata K, Fujishima A, Terashima C (2018) Facile deposition of Cu−SnOx hybrid nanostructures on lightly boron-doped diamond electrodes for CO_2 reduction. ChemElectroChem 5:2542–2550
36. Ikemiya N, Natsui K, Nakata K, Einaga Y (2017) Effect of alkali-metal cations on the electrochemical reduction of carbon dioxide to formic acid using boron-doped diamond electrodes. RSC Adv 7:22510–22514
37. Verlato E, Barison S, Einaga Y, Fasolin S, Musiani M, Nasi L, Natsui K, Paolucci F, Valenti G (2019) CO_2 reduction to formic acid at low overpotential on BDD electrodes modified with nanostructured CeO_2. J Mater Chem A 7:17896–17905
38. Jiwanti PK, Ichzan AM, Dewandaru RKP, Atriardi SR, Einaga Y, Ivandini TA (2020) Improving the CO_2 electrochemical reduction to formic acid using iridium-oxide-modified boron-doped diamond electrodes. Diamond Relat Mater 106:107874

https://www.twirpx.org & http://chemistry-chemists.com

Electro-Organic Synthesis

Takashi Yamamoto and Tsuyoshi Saitoh

Abstract In this chapter, we describe electro-organic synthesis using a boron-doped diamond (BDD) electrode. First, a brief introduction about electro-organic synthesis is provided. This section begins with an explanation of a basic concept in electro-organic synthesis, followed by an introduction of the important milestones. Second, we focus on the electrochemical molecular conversions where the BDD electrodes play a significant role. This section begins with a review of electrochemical properties of BDD, followed by an introduction of reported examples such as anodic methoxylation and dehydrogenative anodic C−C coupling reactions. Third, we describe our approaches toward natural product synthesis via electro-organic synthesis using a BDD electrode: (1) anodic oxidation of the phenol compound possessing a phenylpropanoid framework and (2) cathodic reduction of aromatic carbonyl compounds.

Keywords Electro-organic synthesis · Boron-doped diamond · Anodic oxidation · Cathodic reduction

1 Introduction

Electro-organic synthesis refers to an organic synthetic method combined with electrochemistry [1, 2]. A striking feature in electro-organic synthesis is the use of electricity as a reagent, which allows to replace conventional oxidizing and reducing agents and reduce the reagent waste to a minimum. Obviously, as this characteristic matches well with the increasing demands to realize sustainable society, the field of electrosynthesis has experienced a renaissance [3, 4]. Although the application of electricity to organic synthesis offers a new perspective, some researchers might be

T. Yamamoto (✉)
Department of Chemistry, Keio University, 3-14-1 Hiyoshi, Yokohama 223-8522, Japan
e-mail: takyama@chem.keio.ac.jp

T. Saitoh
International Institute for Integrative Sleep Medicine (WPI-IIIS), University of Tsukuba, Tennodai 1-1-1, Tsukuba, Ibaraki 305-8575, Japan

© Springer Nature Singapore Pte Ltd. 2022

Y. Einaga (ed.), *Diamond Electrodes*,
https://doi.org/10.1007/978-981-16-7834-9_11

https://www.twirpx.org & http://chemistry-chemists.com

passive to take advantage of such opportunities. However, thanks to the renaissance, a wide variety of literatures including review articles is now available, providing the concept, experimental setup and others [5, 6].

Figure 1 is adapted from the perspective article by Waldvogel et al., summarizing modes of operation for electro-organic synthesis and electrochemical facts [7]. As reactions occur at the anode (oxidation) and/or cathode (reduction), electrode materials are a significant parameter for electro-organic conversion. An electrolyte system consists of a chemically (or electrochemically) inert solvent and supporting electrolyte to ensure electrical conductivity. Particularly, the supporting electrolyte contributes to the formation of an electrochemical double layer at the electrode surface where highly active species such as radical cations and anions are accumulated. Besides, applied charge and current density (or potential) influence on the process: The former corresponds to the number of equivalents of reagent, and the latter controls the electrode reactions.

Figure 2 is adapted from the review article by Baran et al., summarizing the selected milestones in electro-organic chemistry [3]. Inspired by the invention of Volta Pile (1800) that allows the movement of electrons through a circuit [8], Faraday's pioneering efforts (1830s) triggered the utilization of the electric current for organic reactions [9]. Particularly, Faraday's electrolysis of acetic acid is the first preparative organic electrochemical experiment that leads to the invention of the Kolbe electrolysis (1847), in which anodic oxidation of carboxylic acids provides a convenient means for alkyl radicals [10]. On the other hand, Schoebein's dehalogenation of trichloromethanesulfonic acid is the first cathodic reduction of an organic compound (1845) [11]. Scalability of electro-organic synthesis was demonstrated by Simons fluorination process (1949) [12] and Monsanto adiponitrile process (1960s)

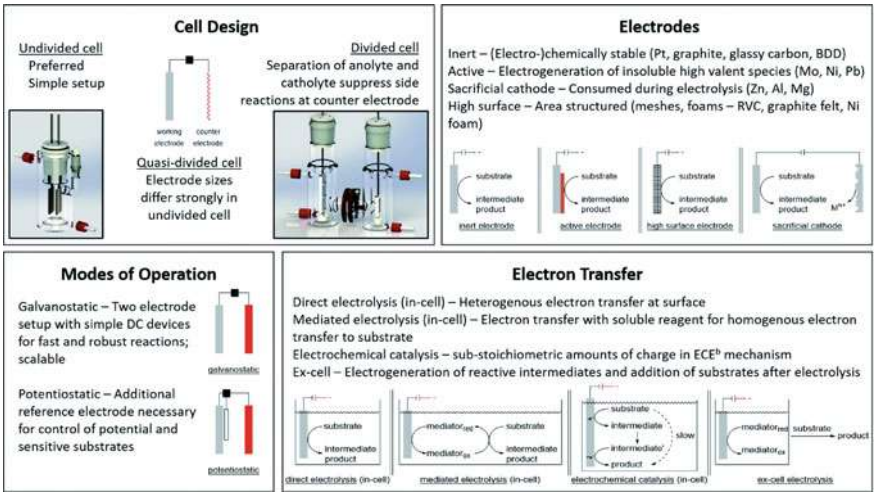

Fig. 1 Modes of operation for electro-organic synthesis and electrochemical facts. Adapted with permission from *Chem. Sci.* **2020**, *11*, 12,386–12,400. Copyright (2020) Royal Society of Chemistry

https://www.twirpx.org & http://chemistry-chemists.com

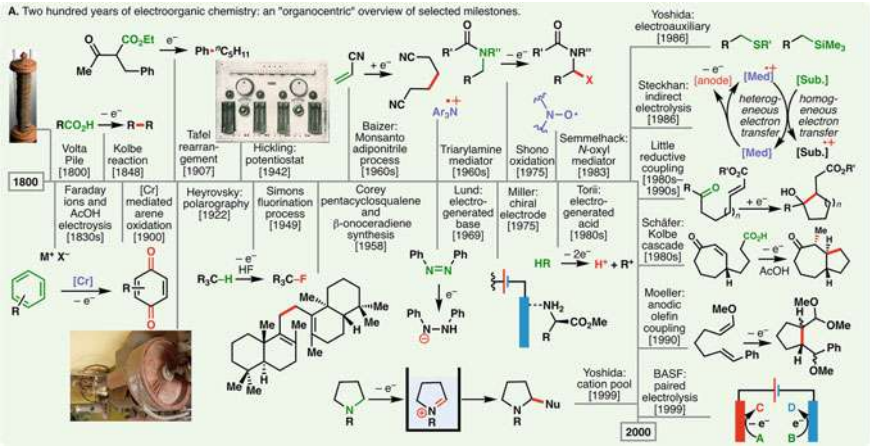

Fig. 2 Two hundred years of electro-organic chemistry: an "organocentric" view of selected milestones. Adapted with permission from *Chem. Rev.* **2017**, *117*, 13,230−13,319. Copyright (2017) American Chemical Society

[13]. In terms of stabilization of an electrogenerated intermediate, indirect electrolysis using redox mediators has been developed such as triarylamine (1970s) [14] and nitroxyl radical (1980s) [15].

Other notable achievements are summarized as follows. Shono oxidation (1975) allowed the α-functionalization of alkyl amides [16]. Yoshida et al. introduced the concept of electroauxiliary (1986), allowing controls over regio- and chemoselectivities [17]. Little et al. established the cathodic reduction methodology (1980−1990s) as a robust means to accomplish ring-forming reactions without utilizing sensitive single-electron metal reductants [18]. Moeller's anodic olefin coupling (1990) provided fundamental insights on the polarity of radical cations [19]. BASF utilized paired electrolysis, highlighting the possibility of boosting the energy efficiency of electro-organic synthesis in an industrial setup [20]. Yoshida's concept of cation pool (1999) enabled the accumulation of reactive cations that can engage various nucleophilic species in further functionalization [21].

2 Electro-Organic Synthesis Using a Boron-Doped Diamond (BDD) Electrodes

This section introduces the electrochemical molecular conversions where the BDD electrodes play a significant role. As the electrochemical properties of BDD can be found in the review articles [22], the attractive properties are briefly described from the perspective of electro-organic synthesis. BDD is chemically inert and does not swell in electrolyte solution. Moreover, BDD exhibits high chemical stability even

https://www.twirpx.org & http://chemistry-chemists.com

in harsh conditions, at high current densities and potentials. As the electrochemical properties, BDD exhibits a wide electrochemical potential window, weak molecular adsorption, and microstructural stability. Especially, the ability to generate alkoxyl or hydroxyl radicals easily is attractive [23].

2.1 Anodic Methoxylation

Comninellis is the pioneer about electro-organic synthesis using BDD electrodes. In 2004, anodic methoxylation of 4-*tert*-butyltoluene has been reported [24]. A twofold two-electron oxidation yielded 4-*tert*-butylbenzaldehyde dimethyl acetal, which can be considered as protected aldehyde (Fig. 3a). Hydrolysis provides corresponding aldehyde and hydrolyzed methanol can be recovered. In 2006, anodic methoxylation of dimethoxymethane to trimethylorthoformate has been reported (Fig. 3b) [25]. Trimethylorthoformate is a widely used reagent as a formic acid equivalent exhibiting a strong dehydrating characteristic. Later, such anodic methoxylation has also been reported by Suryanarayanan et al. in 2013, in which 2-oxazolidinone was methoxylated in a regioselective manner (Fig. 3c) [26].

Comninellis et al. have also reported the bond cleavage reactions and subsequent methoxylation. Anodic oxidation of 1,2-bis(4-*tert*-butylphenyl)ethane led to C − C bond cleavage and the subsequent methoxylation yielded the methoxylated compounds (Fig. 4a) [27]. In addition, phenanthrene was cleaved to yield the corresponding acetal (Fig. 4a) [28].

2.2 Dehydrogenative Anodic C−C Coupling Reactions

Coupling reactions of aryls are significantly important in modern organic chemistry [29]. This molecular transformation is essential for synthesizing complex and nonsymmetric structures, which contributes to a wide variety of research fields ranging from material science [30] and natural product synthesis [31]. Generically, such coupling reactions require a leaving functionality and a transition metal catalyst. On the other hand, as described in introduction, the most striking advantage of electro-organic synthesis is the reduction or avoidance of reagent waste. Furthermore, electrochemistry enables a mild and easy procedure to generate radical intermediates from substrates in addition to typical oxidative or reductive transformations. Based on these advantages, Waldvogel et al. developed a large number of anodic coupling reactions that offers a new sustainable method to obtain biaryl compounds [32].

The first example was the anodic homo-coupling of 2,4-dimethylphenol (Fig. 5a) [33]. Using BDD as an anode enabled the controlled conversion with almost no over-oxidation or mineralization, leading to high selectivity and yield of the corresponding biphenol. In 2009, Waldvogel et al. have reported *ortho*-selective phenol coupling reactions using fluorinated alcohols as solvent (Fig. 5b) [34]. Among the

https://www.twirpx.org & http://chemistry-chemists.com

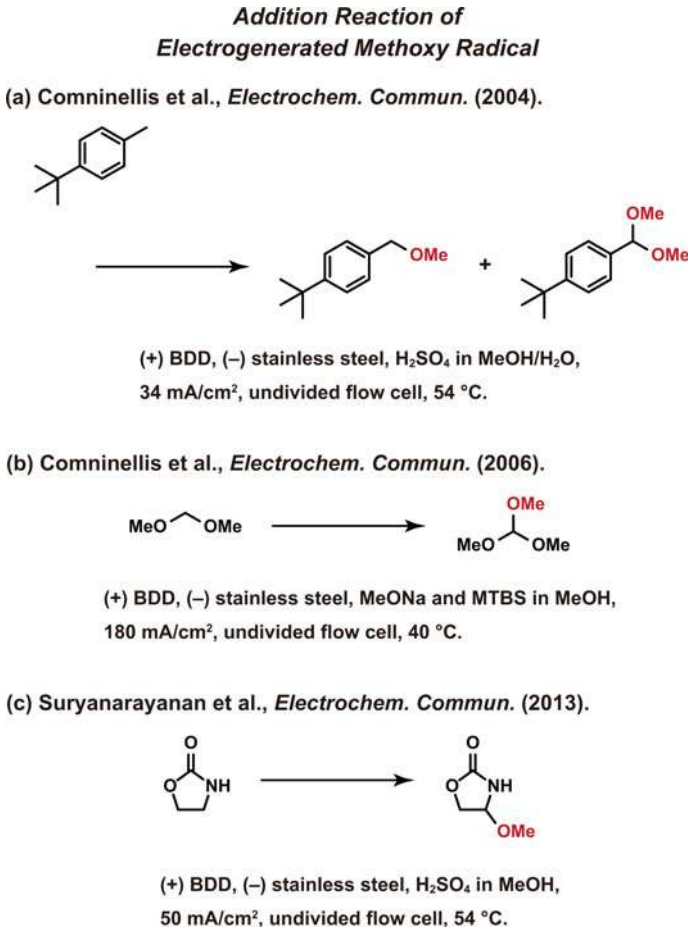

Fig. 3 Addition reactions of electrogenerated methoxy radicals. **a** Anodic methoxylation of 4-*tert*-butyltoluene [24]. **b** Anodic methoxylation of dimethoxymethane [25]. MTBS denotes *N*-methyl-*N*,*N*,*N*-tributylammonium methylsulfate. **c** Anodic methoxylation of 2-oxazolidinone [26]

examined fluorinated alcohols, 1,1,1,3,3,3-hexafluoroisopropanol (HFIP) was found to be a major effect on the lifetime of phenoxyl radicals, due to the ability to act as a strong hydrogen bonding donor. It should be noted that HFIP is electrochemically inert and offers, especially in combination with BDD electrodes, the largest known electrochemical potential window [35]. Recently, the *para*-selective coupling reactions (Fig. 5c) [36] and coupling reactions of phenols bearing electron-withdrawing groups (Fig. 5d) [37] have been reported.

In 2010, Waldvogel et al. have reported the first example of the anodic phenol – arene cross-coupling reactions in BDD/HFIP system (Fig. 6a) [38]. Afterward, cyclic voltammetry measurements revealed the role of protic additives such as water and methanol, in which an oxidation potential of substrates can be controlled within

https://www.twirpx.org & http://chemistry-chemists.com

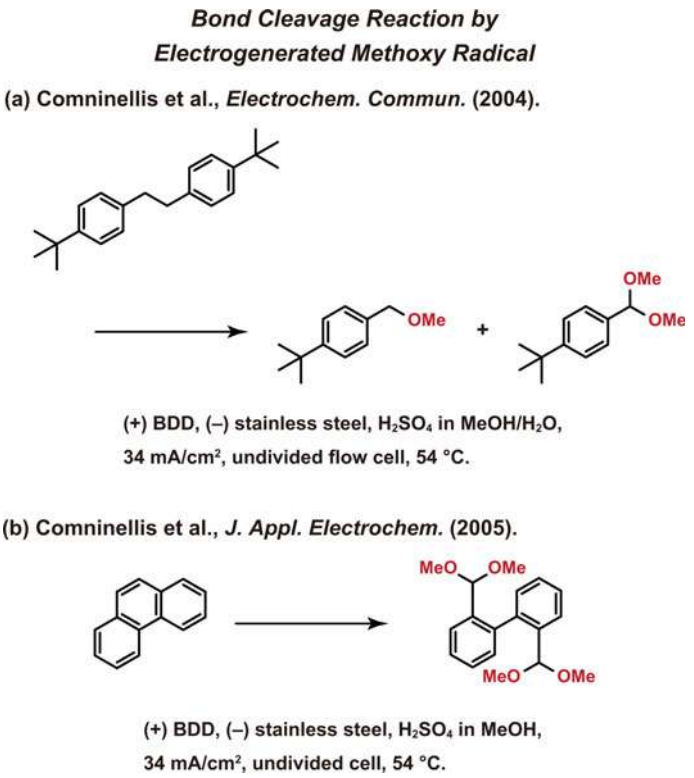

Fig. 4 Bond cleavage reactions by electrogenerated methoxy radicals. **a** Anodic cleavage and methoxylation reactions of 1,2-bis(4-*tert*-butylphenyl)ethane [27]. **b** Anodic cleavage and methoxylation reactions of phenanthrene [28]

a given range and therefore define the predominantly oxidized species [39]. HFIP is capable of a unique decoupling of nucleophilicity and oxidation potential of the substrates due to a tight solvation sphere (Fig. 7) [40, 41]. Based on these features, the anodic phenol – phenol cross-coupling reactions to yield nonsymmetrical 2,2'-biphenols have been reported (Fig. 6b) [42]. Installing a protective group to phenol with the higher oxidation potential enabled high-yield synthesis of the nonsymmetric 2,2'-biphenols and the of extremely electron-rich phenols (Fig. 6c) [43]. Recently, the anodic cross-coupling reactions of thiophenes/benzo[b]thiophenes with phenols have been also reported (Fig. 6d) [44].

Figure 8 shows the mechanistic rationale for an anodic cross-coupling reaction of phenol with arene. A selective oxidation of phenol (**A**) exhibiting the lower oxidation potential resulted in generating a strongly acidic radical cation. This radical cation loses a proton immediately and is converted to the phenoxyl radical (**I**) that is stabilized over resonance structures. Subsequently, the radical is attacked nucleophilically

https://www.twirpx.org & http://chemistry-chemists.com

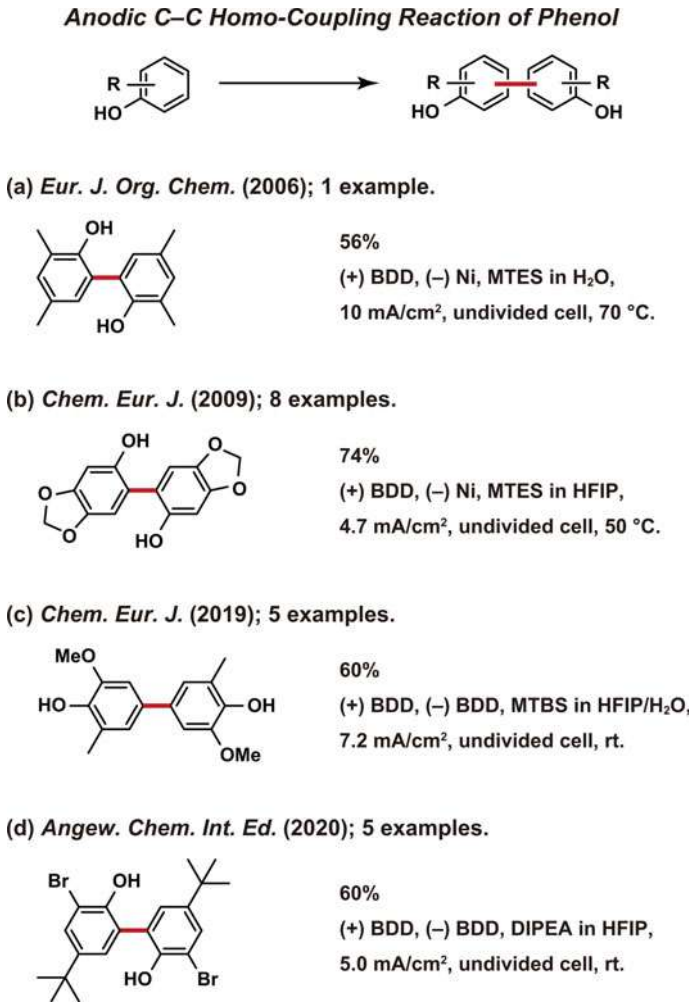

Fig. 5 Anodic C−C homo-coupling reactions of phenols. **a** An *ortho*-coupling reaction [33]. MTES denotes *N*-methyl-*N*,*N*,*N*-triethylammonium methylsulfate. **b** *ortho*-selective coupling reactions [34]. **c** Selective formation of 4,4'-biphenol [36]. **d** Coupling reactions of phenols bearing electron-withdrawing groups [37]. DIPEA denotes diisopropylethylamine

by arene (**B**) exhibiting the higher oxidation potential. The resulting radical intermediate (**II**) is rearomatized, and the loss of an electron and proton leads to the cross-coupling product (**AB**).

The above concept was extended to the electrochemical synthesis of teraryls. A twofold anodic cross-coupling of biaryls with an phenol species led to symmetrical and nonsymmetrical *meta*-terphenyl-2,2"-diols (Fig. 9a) [45, 46]. Similarly,

https://www.twirpx.org & http://chemistry-chemists.com

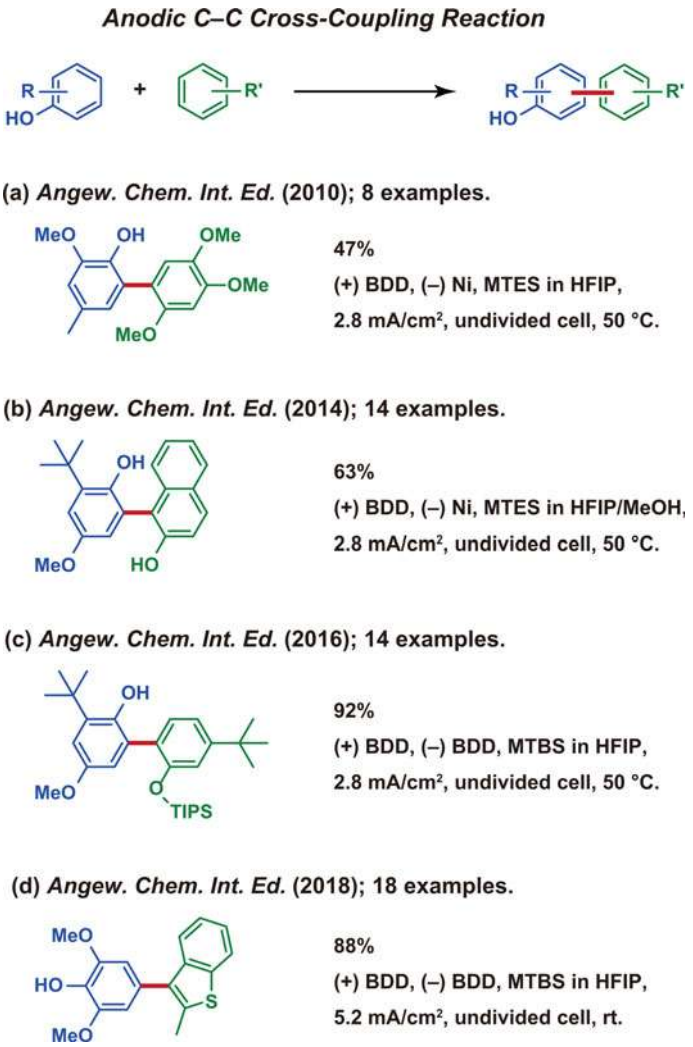

Fig. 6 Anodic C−C cross-coupling reactions to biaryl. **a** Phenol−arene coupling reactions [38]. **b** Phenol−phenol (napthol) coupling reactions [42]. **c** Phenol−protected phenol coupling reactions [43]. **d** Phenol−thiophene coupling reactions [44]

2,5-bis(2-hydroxyphenyl)thiophenes have been obtained by a twofold anodic cross-coupling of phenol with an thiophene species (Fig. 9b) [47]. Other examples reported by Waldvogel et al. can be found in their review articles [32, 48].

https://www.twirpx.org & http://chemistry-chemists.com

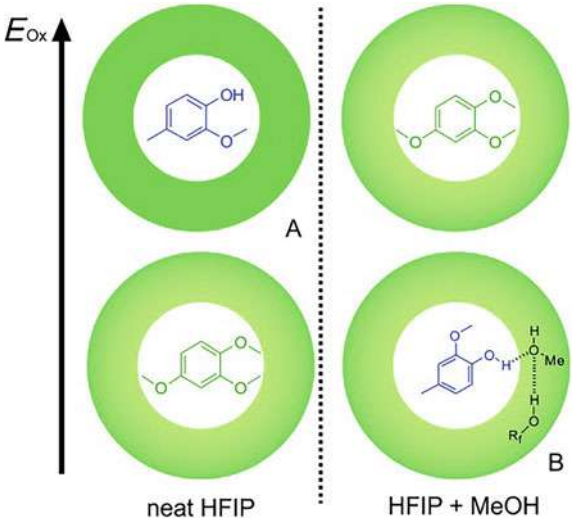

Fig. 7 Decoupling of the nucleophilicity and oxidation potential of the substrates due to a tight solvation sphere of HFIP. Adapted with permission from *Chem. Eur. J.* **2015**, *21*, 12,321−12,325. Copyright (2015) Wiley–VCH

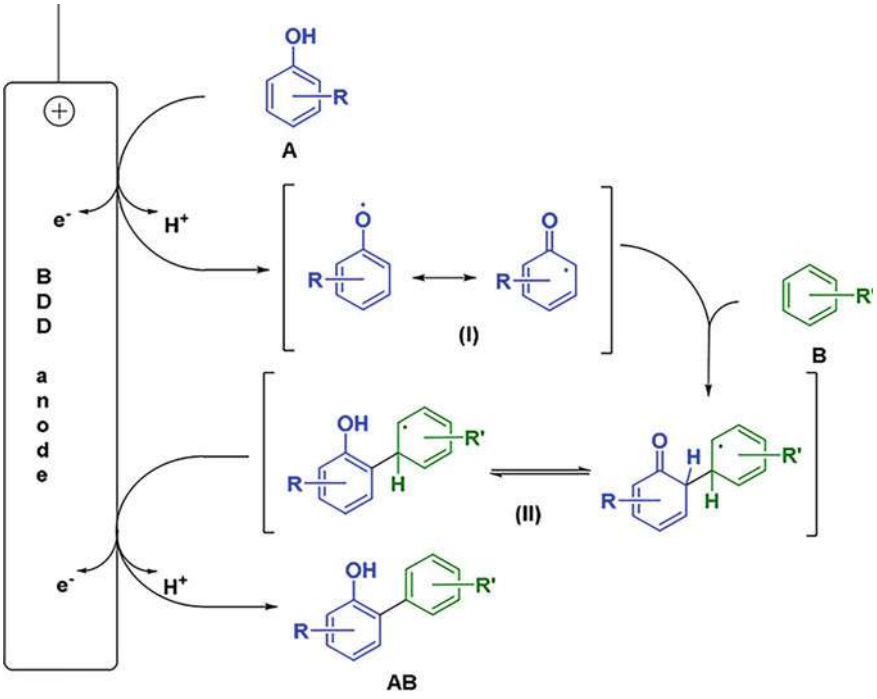

Fig. 8 Mechanistic rationale for an anodic cross-coupling reaction of phenol with arene. Adapted with permission from *ChemElectroChem* **2019**, *6*, 1649 − 1660. Copyright (2019) Wiley–VCH

https://www.twirpx.org & http://chemistry-chemists.com

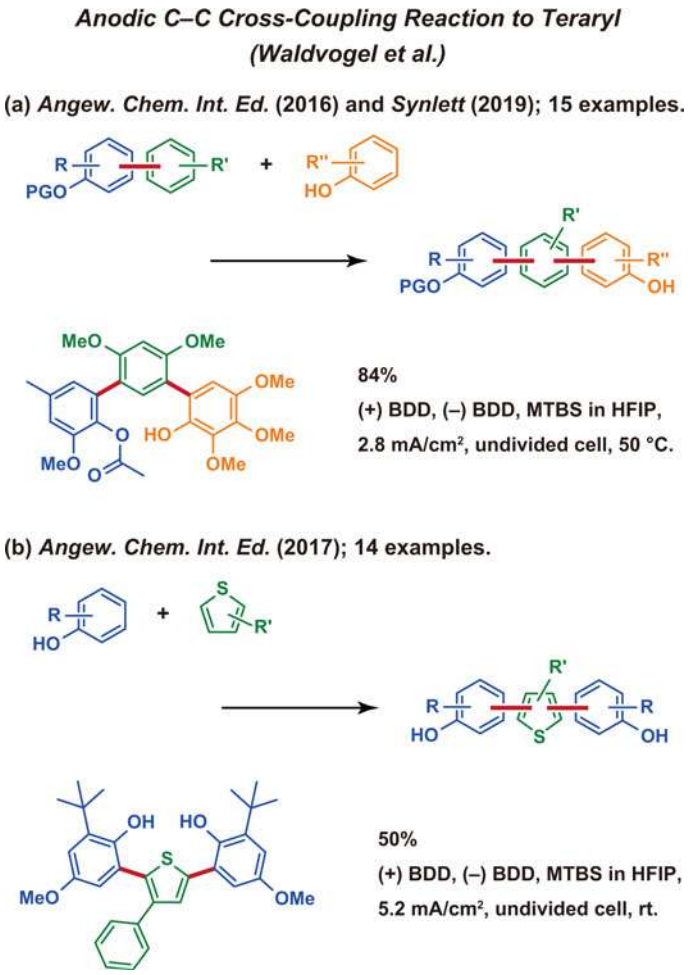

Fig. 9 Anodic C−C cross-coupling reactions to teraryl. **a** Biphenol−phenol coupling reactions [45, 46]. **b** Phenol−thiophene coupling reactions [47]

3 Electro-Organic Synthesis Using BDD Electrodes Toward Natural Product Synthesis

Obviously, natural products are an important class of materials for our life because a wide variety of natural products and their synthetic derivatives have been used as a drug for a wide variety of diseases [49]. In nature, natural products are synthesized through an enzyme-catalyzed multi-step reaction, called biosynthesis. Therefore, it would be straightforward to synthesize natural products by mimicking the biosynthesis. Among a numerous number of enzymes involved in the biosynthesis, we have

https://www.twirpx.org & http://chemistry-chemists.com

focused on the oxidative enzymes because the reaction conducted by such enzymes could be replaced with electro-organic chemistry.

3.1 Anodic Oxidation of Phenol Compound

The beginning of the electrochemical natural product synthesis using BDD electrodes started in 2012 reporting the anodic oxidation of isoeugenol in methanol [50], aiming at the synthesis of the benzofuran-type neolignan, licarin A. Previously, the anodic oxidation of isoeugenol using a Pt anode provided licarin A in the isolated yield of 29% [51], which would be a benchmark for the performance of a BDD electrode.

Prior to the anodic oxidation of isoeugenol in BDD/methanol system, we carried out electron spin resonance (ESR) measurements to confirm the generation of methoxy radicals (Fig. 10, top). Anodic oxidation of methanol solution containing the radical trapping agent (5,5-dimethyl-1-pyrroline-*N*-oxide (DMPO)) were performed under constant potential condition (1.06 V *vs.* saturated calomel electrode (SCE)). The obtained ESR signals and the magnetic field value anticipated for nitroxyl radicals generated by reaction of DMPO with methoxy radicals [52]. Clearly, the intensities of the ESR signals varied with the anode used and followed the order of boron-doped diamond (BDD) > Pt > glassy carbon. Therefore, methoxy radicals generated efficiently by the anodic oxidation of methanol using the BDD anode. It should be emphasized that this observation is the first experimental evidence of the electrogenerated methoxy radical in BDD/methanol system.

Based on this finding, the anodic oxidation of isoeugenol was performed in BDD/methanol system. As a result, licarin A and dimethoxylated phenol were obtained in 40 and 16% yield, respectively, which suggests that the electrogenerated methoxy radicals participated in the mechanism of molecular conversions. Please note that this rationale is supported by the investigations of reaction conditions such as electrode materials, applied potential, and solvent. Subsequently, we conducted the anodic oxidation in a flow cell system, aiming at the improvement of current efficiency and avoidance of secondary oxidation reactions. Moreover, we expected that the highly concentrated methoxy radicals at the anode would facilitate an efficient one-electron oxidation process. Investigations of current density and flow rate gave the optimized condition, providing dimethoxylated phenol in 90% yield. This observation suggests that the radical intermediate generated by sequential one-electron oxidation and deprotonation reacts rapidly with methoxy radicals.

As described in Sect. 10.2.2, the combination of BDD electrodes and HFIP solvent is a particularly powerful electrolytic system. BDD allows clean electrode reactions leading to a far superior anode material even at much more positive potentials [53]. In addition, the outstanding feature of HFIP lies in the solvent effect enabling highly selective electro-conversions [40]. Based on these advantages, we expected a unique anodic conversion of isoeugenol in the BDD/HFIP system [54].

The anodic oxidation under constant current conditions resulted in complete consumption of isoeugenol and a sole peak corresponding to a coupling product was

https://www.twirpx.org & http://chemistry-chemists.com

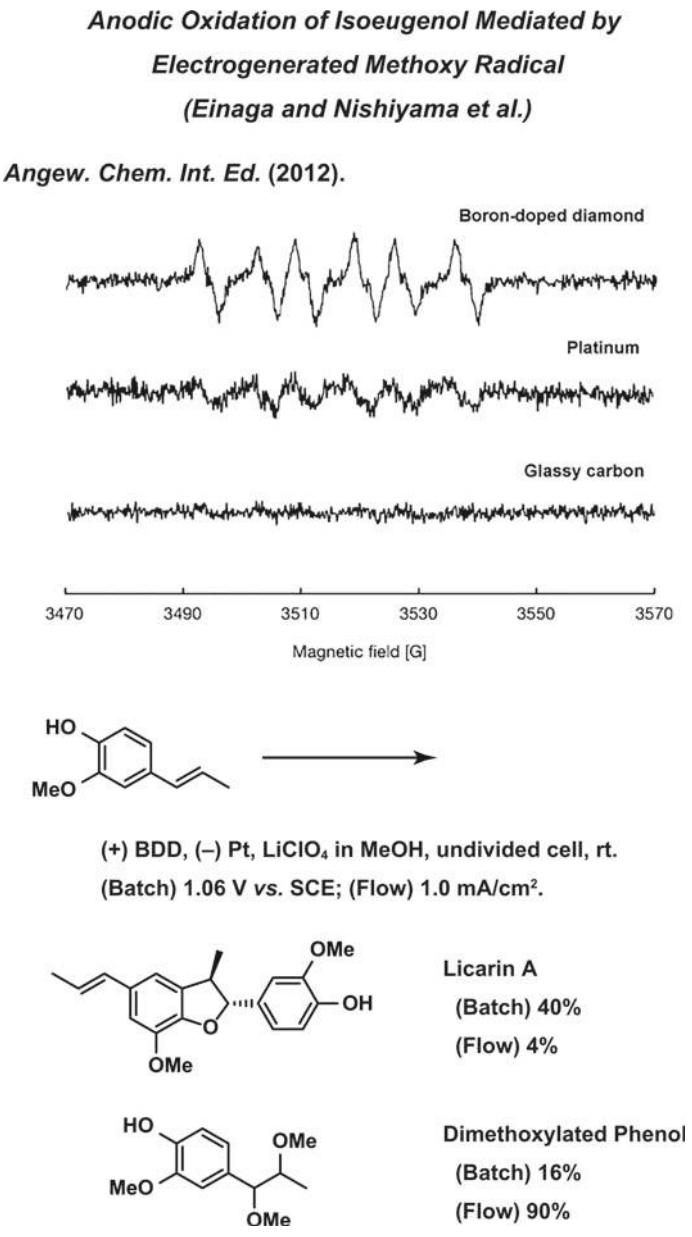

Fig. 10 Anodic oxidation of isoeugenol in MeOH [50]. The top graph shows the ESR spectra of the electrogenerated methoxy radicals. Adapted with permission from *Angew. Chem. Int. Ed.* **2012**, *51*, 5443−5446. Copyright (2012) Wiley–VCH

https://www.twirpx.org & http://chemistry-chemists.com

found in the gas chromatography–mass spectrometry (GC–MS) analysis, even upon applying a low current density. Presumably, in keeping with the seminal findings of Chiba et al. [55], the anodic oxidation of electron-rich substrates proceeded via the radical cation chain reaction, where a catalytic amount of electricity was sufficient to complete the conversion. Furthermore, investigations with varying the amount of charge revealed that isoeugenol was completely consumed even upon applying a small amount of charge. As different solvents such as acetonitrile or dichloromethane did not work well, the unique ability of HFIP to stabilize radical species is crucial for the anodic conversion. Upon isolation of the product, we could unequivocally assign the molecular structure of the coupling product as α-diisoeugenol, which was identical regardless of the electrolytic conditions.

Figure 11 (bottom) displays a mechanistic rationale for the stereoselective and electrocatalytic conversion. In the initial step, isoeugenol is anodically oxidized at the BDD electrode to generate the corresponding radical species, followed by the loss

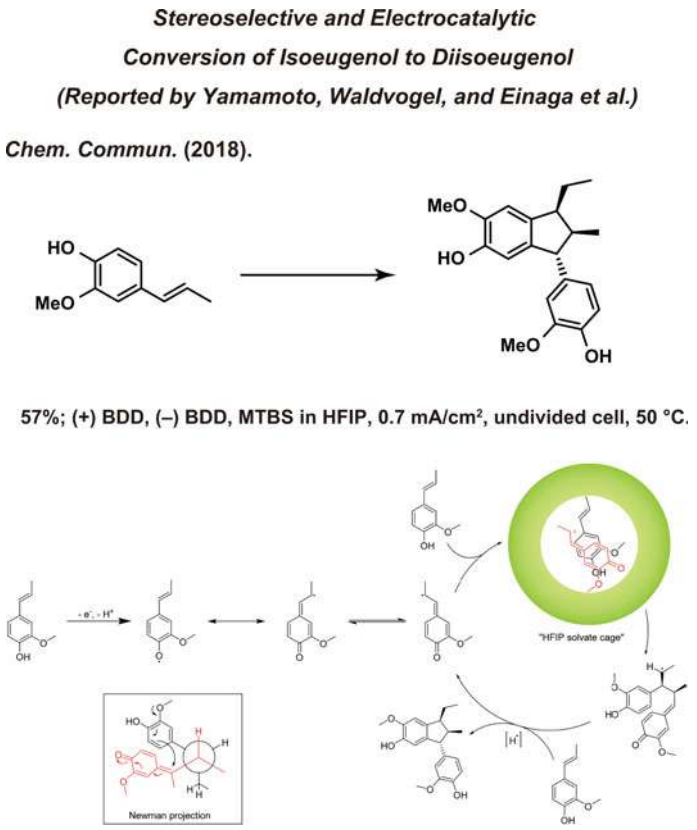

Fig. 11 Anodic oxidation of isoeugenol in HFIP [54]. The bottom illustration shows the postulated electrocatalytic cycle of the anodic conversion. Adapted with permission from *Chem. Commun.* **2018**, *54*, 2771−2773. Copyright (2018) Royal Society of Chemistry

https://www.twirpx.org & http://chemistry-chemists.com

of a proton. This radical species can be solvated by HFIP and trapped by an another isoeugenol molecule to afford the intermediate species. In the solvate structure, the dispersion interaction and the solvation result in a specific molecular orientation, probably due to an aromatic donor−acceptor interaction, leading to unusual addition onto the exocyclic C−C double bond. The generated carbon-centered radical undergoes a hydrogen atom transfer to maintain the radical chain reaction. A cyclization reaction followed by an aromatization reaction afford α-diisoeugenol. The first C−C bond formation (addition step) is crucial to control the stereochemistry, in which the orthogonal approach would be favored due to the aromatic donor−acceptor interaction. Here, the roles of HFIP are rationalized as follows. First, HFIP strongly enhances the stability of the radical species and suppresses the carbonization of isoeugenol, due to its non-nucleophilic and protic nature [56]. Second, HFIP forms a unique hydrogen bonding network, where the fluorine atoms are excluded and cluster together [41]. Overall, confinement of the radical species in the HFIP solvate cage is supposed to induce the specific molecular orientation that is favorable for the stereoselective conversion in α-configuration.

3.2 Cathodic Reduction of Aromatic Carbonyl Compounds

While anodic oxidation reactions have been extensively investigated with a wide variety of substrates, cathodic reduction reactions are rare. Generically, in protic media, a high overpotential for hydrogen evolution is required for cathode materials, in which a substrate itself should be reduced preferentially. Although heavy metals such as cadmium, mercury, and lead satisfy the requirements, such metals are highly toxic and have a high environmental load. Carbon-based electrodes exhibit a lower overpotential for hydrogen revolution than heavy metals. With this regard, BDD electrodes would be beneficial for cathodic reduction, and therefore offer a new perspective in electro-organic synthesis.

First, we performed the cathodic reduction of methyl cinnamate (Fig. 12a) [57], aiming at the synthesis of lignans and/or neolignans possessing two phenlypropane (C_6-C_3) fragments that exhibit interesting biological activities [58].

In the cathodic reduction under constant current conditions, solvents played a significant role in the desired coupling reaction. Particularly, acetonitrile containing phosphate-buffer (PB) was the optimized solvent that afford the coupling product in 85% yield (racemate/meso = 74:26). The obtained molecule was submitted to the chemical conversion and could be derivatized into the new neolignan-type compounds.

Second, we investigated the reductive coupling of carbonyl compounds to 1,2-diol, so-called pinacol coupling (Fig. 12b) [59]. This is because the pinacol coupling reaction is still a powerful tool for organic chemists as can be found in total synthesis of taxol [60]. Moreover, electro-organic synthesis helps to avoid using a stoichiometric or even more amounts of reducing reagents to generate a radical intermediate. We chose acetophenone as the substrate, and optimization of reaction conditions

https://www.twirpx.org & http://chemistry-chemists.com

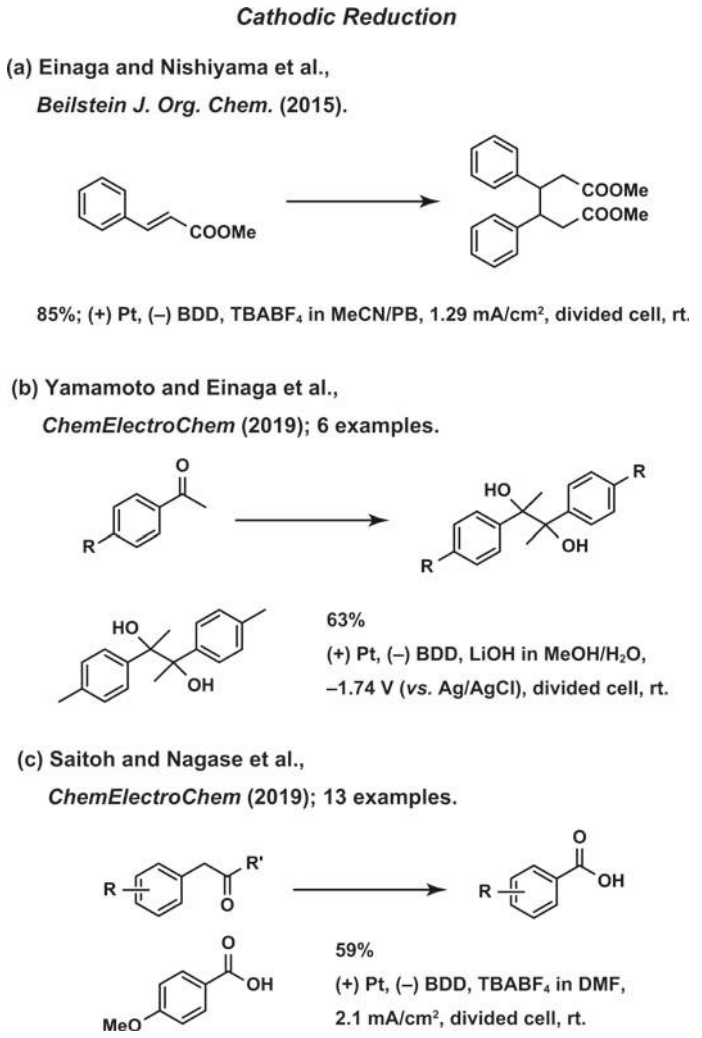

Fig. 12 Cathodic conversions of aromatic carbonyl compounds. **a** A reductive coupling reaction [57]. $TBABF_4$ denotes tetrabutylammonium tetrafluoroborate. **b** Pinacol coupling reactions [59]. **c** Acyl-carbon bond cleavage reactions [61]

such as supporting electrolyte and solvent revealed that lithium ions increased a reactivity of the radical intermediate and water apparently influenced on the electrochemical potential of one-electron reduction. Overall, the reaction was relatively tolerant to *para*-substituted acetophenone derivatives and afforded the corresponding pinacol-type compounds with good conversion yields.

During the investigation of the electrochemical pinacol coupling reaction, we unexpectedly discovered a cleavage of the acyl-carbon bond in a phenylacetone

https://www.twirpx.org & http://chemistry-chemists.com

derivative to give a benzoic acid derivative (Fig. 12c) [61]. Since the conversion of ketone into acid requires transition metal catalysts and/or chemical oxidants [62], this finding demonstrates a metal-, oxidant-, and acid/base-free molecular conversion. Optimization of reaction conditions clearly highlighted the importance of molecular oxygen in the electrolyte. Cyclic voltammetry and UV–vis absorption spectroscopy revealed that a superoxide anion (SOA) was generated by reduction of dissolved molecular oxygen, which mediate the oxidative cleavage of the acyl-carbon bond in the phenylacetone derivative. The electrogenerated superoxide anion does not cause undesired side reactions such as the oxidation of amine and aryl moieties. Notably, molecular transformations accompanied by bond cleavage are useful for the modification and derivatization of biologically important substances [63].

4 Conclusion

In this chapter, we described the electro-organic synthesis utilizing boron-doped diamond (BDD) electrodes. The outstanding electrochemical properties of BDD play a significant role in both anodic and cathodic molecular conversion. The strong ability to generate alkoxyl radicals contributes to the anodic methoxylation that is obviously unique to BDD. Combination of BDD and 1,1,1,3,3,3-hexafluoroisopropanol (HFIP) enables the dehydrogenative anodic C−C coupling reactions: (1) position selective homo-coupling reactions of phenol, (2) selective cross-coupling reactions of phenol−arene, phenol−phenol, and phenol−thiophene, and (3) cross-coupling reactions of phenol to afford teraryls. Electro-organic synthesis of natural products is also demonstrated: (1) the electrogenerated methoxy radicals-mediated coupling reaction to give licarin A, (2) the cathodic coupling reaction to afford the precursor of the neolignane-type compound, and (3) the stereoselective and electrocatalytic synthesis of α-diisoeugenol driven by the solvate interaction. The clever use of BDD electrodes does lead to develop a unique molecular conversion, which contributes to a future sustainable society.

References

1. Fuchigami T, Atobe M, Inagi S (eds) (2015) Fundamentals and applications of organic electrochemistry: synthesis, materials, devices. John Wiley & Sons, Chichester
2. Hammerich O, Speiser B (eds) (2016) Organic electrochemistry, fifth edition: revised and expanded. CRC Press, Boca Raton
3. Yan M, Kawamata Y, Baran PS (2017) Synthetic organic electrochemical methods since 2000: on the verge of a renaissance. Chem Rev 117:13230–13319
4. Wiebe A, Gieshoff T, Mohle S, Rodrigo E, Zirbes M, Waldvogel SR (2018) Electrifying organic synthesis. Angew Chem Int Ed 57:5594–5619
5. Little RD, Moeller KD (eds) (2018) Electrochemistry: technology, synthesis, energy, and materials. Chem Rev 118(9)
6. Francke R, Little RD, Inagi S (eds) (2019) Organic electrosynthesis. ChemElectroChem 6(16)

https://www.twirpx.org & http://chemistry-chemists.com

7. Pollok D, Waldvogel SR (2020) Electro-organic synthesis—a 21st century technique. Chem Sci 11:12386–12400
8. Volta AGA (1800) Nat Phiols Chem Arts 4:179–187
9. Faraday M (1834) Ann Phys Leipzig 47:438
10. Kolbe H (1847) Beobachtungen über die oxydirende Wirkung des Sauerstoffs, wenn derselbe mit Hülfe einer elektrischen Säule entwickelt wird. J Prakt Chem 41:137–139
11. Schönbein CF (1845) Liebigs Ann Chem 54:164
12. Simons JH (1949) Production of fluorocarbons I. the generalized procedure and its use with nitrogen compounds. J Electrochem Soc 95:47–52
13. Beizer MM (1980) ChemTech 10:161
14. Seo ET, Nelson RF, Fritsch JM, Marcoux LS, Leedy DW, Adams RN (1966) Anodic oxidation pathways of aromatic amines. electrochemical and electron paramagnetic resonance studies. J Am Chem Soc 88:3498–3503
15. Semmelhack MF, Chou CS, Cortes DA (1983) Nitroxyl-mediated electrooxidation of alcohols to aldehydes and ketones. J Am Chem Soc 105:4492–4494
16. Shono T, Hamaguchi H, Matsumura Y (1975) Electroorganic chemistry. XX. anodic oxidation of carbamates. J Am Chem Soc 97:4264–4268
17. Yoshida J, Mirata T, Isoe S (1986) Electrochemical oxidation of organosilicon compounds I. oxidative cleavage of carbon-silicon bond in allylsilanes and benzylsilanes. Tetrahedron Lett 27:3373–3376
18. Little RD, Schwaebe MK (1997) Reductive cyclizations at the cathode. Top Curr Chem 185:1–48
19. Moeller KD (2000) Synthetic applications of anodic electrochemistry. Tetrahedron 56:9527–9554
20. Paddon CA, Atobe M, Fuchigami T, He P, Watts P, Haswell SJ, Pritchard GJ, Bull SD, Marken F (2006) Towards paired and coupled electrode reactions for clean organic microreactor electrosyntheses. J A Electrochem 36:617–634
21. Yoshida JI, Suga S, Suzuki S, Kinomura N, Yamamoto A, Fujiwara K (1999) Direct oxidative carbon−carbon bond formation using the “cation pool” method. 1. generation of iminium cation pools and their reaction with carbon nucleophiles. J Am Chem Soc 121:9546–9549
22. Yang N, Yu S, Macpherson JV, Einaga Y, Zhao H, Zhao G, Swain GM, Jiang X (2019) Conductive diamond: synthesis, properties, and electrochemical applications. Chem Soc Rev 48:157–204
23. Griesbach U, Malkowsky IM, Waldvogel SR (2008) Green electroorganic synthesis using BDD electrodes. In: Comninellis C, Chen G (eds) Electrochemistry for the environment. Springer, Berlin, pp 125–141
24. Zollinger D, Griesbach U, Pütter H, Comninellis C (2004) Methoxylation of p-tert-butyltoluene on boron-doped diamond electrodes. Electrochem Commun 6:600–604
25. Fardel R, Griesbach U, Pütter H, Comninellis C (2005) Electrosynthesis of trimethylorthoformate on BDD electrodes. J Appl Electrochem 36:249–253
26. Saravanan KR, Selvamani V, Kulangiappar K, Velayutham D, Suryanarayanan V (2013) Regioselective anodic α-methoxylation of 2-oxazolidinone on boron doped diamond in acidic methanol medium. Electrochem Commun 28:31–33
27. Zollinger D, Griesbach U, Pütter H, Comninellis C (2004) Electrochemical cleavage of 1,2-diphenylethanes at boron-doped diamond electrodes. Electrochem Commun 6:605–608
28. Griesbach U, Zollinger D, Pütter H, Comninellis C (2005) Evaluation of boron doped diamond electrodes for organic electrosynthesis on a preparative scale. J Appl Electrochem 35:1265–1270
29. Nicolaou KC, Bulger PG, Sarlah D (2005) Palladium-catalyzed cross-coupling reactions in total synthesis. Angew Chem Int Ed 44:4442–4489
30. Franke R, Selent D, Borner A (2012) Applied hydroformylation. Chem Rev 112:5675–5732
31. von Nussbaum F, Brands M, Hinzen B, Weigand S, Habich D (2006) Antibacterial natural products in medicinal chemistry–exodus or revival? Angew Chem Int Ed 45:5072–5129

https://www.twirpx.org & http://chemistry-chemists.com

32. Waldvogel SR, Lips S, Selt M, Riehl B, Kampf CJ (2018) Electrochemical arylation reaction. Chem Rev 118:6706–6765
33. Malkowsky IM, Griesbach U, Pütter H, Waldvogel SR (2006) Unexpected highly chemoselective anodic ortho-coupling reaction of 2,4-dimethylphenol on boron-doped diamond electrodes. Eur J Org Chem 4569−4572
34. Kirste A, Nieger M, Malkowsky IM, Stecker F, Fischer A, Waldvogel SR (2009) ortho-Selective phenol-coupling reaction by anodic treatment on boron-doped diamond electrode using fluorinated alcohols. Chem Eur J 15:2273–2277
35. Francke R, Cericola D, Kötz R, Weingarth D, Waldvogel SR (2012) Novel electrolytes for electrochemical double layer capacitors based on 1,1,1,3,3,3-hexafluoropropan-2-ol. Electrochim Acta 62:372–380
36. Dahms B, Kohlpaintner PJ, Wiebe A, Breinbauer R, Schollmeyer D, Waldvogel SR (2019) Selective formation of 4,4'-biphenols by anodic dehydrogenative cross- and homo-coupling reaction. Chem Eur J 25:2713–2716
37. Rockl JL, Schollmeyer D, Franke R, Waldvogel SR (2020) Dehydrogenative anodic C−C coupling of phenols bearing electron-withdrawing groups. Angew Chem Int Ed 59:315–319
38. Kirste A, Schnakenburg G, Stecker F, Fischer A, Waldvogel SR (2010) Anodic phenol-arene cross-coupling reaction on boron-doped diamond electrodes. Angew Chem Int Ed 49:971–975
39. Kirste A, Elsler B, Schnakenburg G, Waldvogel SR (2012) Efficient anodic and direct phenol-arene C, C cross-coupling: the benign role of water or methanol. J Am Chem Soc 134:3571–3576
40. Elsler B, Wiebe A, Schollmeyer D, Dyballa KM, Franke R, Waldvogel SR (2015) Source of selectivity in oxidative cross-coupling of aryls by solvent effect of 1,1,1,3,3,3-hexafluoropropan-2-ol. Chem Eur J 21:12321–12325
41. Hollóczki O, Berkessel A, Mars J, Mezger M, Wiebe A, Waldvogel SR, Kirchner B (2017) The catalytic effect of fluoroalcohol mixtures depends on domain formation. ACS Catal 7:1846–1852
42. Elsler B, Schollmeyer D, Dyballa KM, Franke R, Waldvogel SR (2014) Metal- and reagent-free highly selective anodic cross-coupling reaction of phenols. Angew Chem Int Ed 53:5210–5213
43. Wiebe A, Schollmeyer D, Dyballa KM, Franke R, Waldvogel SR (2016) Selective synthesis of partially protected nonsymmetric biphenols by reagent- and metal-free anodic cross-coupling reaction. Angew Chem Int Ed 55:11801–11805
44. Lips S, Schollmeyer D, Franke R, Waldvogel SR (2018) Regioselective metal- and reagent-free arylation of benzothiophenes by dehydrogenative electrosynthesis. Angew Chem Int Ed 57:13325–13329
45. Lips S, Wiebe A, Elsler B, Schollmeyer D, Dyballa KM, Franke R, Waldvogel SR (2016) Synthesis of meta-terphenyl-2,2''-diols by anodic C−C cross-coupling reactions. Angew Chem Int Ed 55:10872–10876
46. Lips S, Franke R, Waldvogel SR (2019) Electrochemical synthesis of 2-hydroxy-para-terphenyls by dehydrogenative anodic C-C cross-coupling reaction. Synlett 30:1174–1177
47. Wiebe A, Lips S, Schollmeyer D, Franke R, Waldvogel SR (2017) Single and twofold metal- and reagent-free anodic C−C cross-coupling of phenols with thiophenes. Angew Chem Int Ed 56:14727–14731
48. Lips S, Waldvogel SR (2019) Use of boron-doped diamond electrodes in electro-organic synthesis. ChemElectroChem 6:1649–1660
49. Newman DJ, Cragg GM (2016) Natural products as sources of new drugs from 1981 to 2014. J Nat Prod 79:629–661
50. Sumi T, Saitoh T, Natsui K, Yamamoto T, Atobe M, Einaga Y, Nishiyama S (2012) Anodic oxidation on a boron-doped diamond electrode mediated by methoxy radicals. Angew Chem Int Ed 51:5443–5446
51. Nishiyama A, Eto H, Terada Y, Iguchi M, Yamamura S (1983) Anodic oxidation of some propenylphenols: synthesis of physiologically active neolignans. Chem Pharm Bull 31:2834–2844

https://www.twirpx.org & http://chemistry-chemists.com

52. Janzen EG, Liu JIP (1973) Radical addition reactions of 5,5-dimethyl-1-pyrroline-1-oxide. ESR spin trapping with a cyclic nitrone. J Magn Reson 9:510–512
53. Wiebe A, Riehl B, Lips S, Franke R, Waldvogel SR (2017) Unexpected high robustness of electrochemical cross-coupling for a broad range of current density. Sci Adv 3:eaao3920
54. Yamamoto T, Riehl B, Naba K, Nakahara K, Wiebe A, Saitoh T, Waldvogel SR, Einaga Y (2018) A solvent-directed stereoselective and electrocatalytic synthesis of diisoeugenol. Chem Commun 54:2771–2773
55. Okada Y, Yamaguchi Y, Ozaki A, Chiba K (2016) Aromatic "Redox Tag"-assisted Diels-Alder reactions by electrocatalysis. Chem Sci 7:6387–6393
56. Eberson L, Michael MP, Persson O (1995) Detection and reactions of radical cations generated by photolysis of aromatic compounds with tetranitromethane in 1,1,1,3,3,3-hexafluoro-2-propanol at room temperature. Angew Chem Int Ed 34:2268–2269
57. Kojima T, Obata R, Saito T, Einaga Y, Nishiyama S (2015) Cathodic reductive coupling of methyl cinnamate on boron-doped diamond electrodes and synthesis of new neolignan-type products. Beilstein J Org Chem 11:200–203
58. Apers S, Vlietinck A, Pieters L (2003) Lignans and neolignans as lead compounds. Phytochem Rev 2:201–217
59. Nakahara K, Naba K, Saitoh T, Sugai T, Obata R, Nishiyama S, Einaga Y, Yamamoto T (2019) Electrochemical pinacol coupling of acetophenone using boron-doped diamond electrode. ChemElectroChem 6:4153–4157
60. Mukaiyama T, Shiina I, Iwadare H, Saitoh M, Nishimura T, Ohkawa N, Sakoh H, Nishimura K, Tani Y, Hasegawa M, Yamada K, Saitoh K (1999) Asymmetric total synthesis of taxol. Chem Eur J 5:121–161
61. Zhang Y, Sugai T, Yamamoto T, Yamamoto N, Kutsumura N, Einaga Y, Nishiyama S, Saitoh T, Nagase H (2019) Oxidative cleavage of the acyl-carbon bond in phenylacetone with electrogenerated superoxide anions. ChemElectroChem 6:4194–4198
62. Paria S, Halder P, Paine TK (2012) Oxidative carbon-carbon bond cleavage of a α-hydroxy ketone by a functional model of 2,4'-dihydroxyacetophenone dioxygenase. Angew Chem Int Ed 51:6195–6199
63. Crane EA, Gademann K (2016) Capturing biological activity in natural product fragments by chemical synthesis. Angew Chem Int Ed 55:3882–3902

https://www.twirpx.org & http://chemistry-chemists.com

Industrial Application of Electrochemical Chlorine Sensor

Yasuaki Einaga

Abstract Monitoring free chlorine concentration is an important issue in various situations. Residual chlorine that does not react with organic compounds, and metals dissolve in water to produce HClO (hypochlorous acid) and ClO- (hypochlorite ion). In 2008, we reported that free chlorine, which has a strong disinfecting effect, can be monitored with high sensitivity using a boron-doped diamond (BDD) electrode. However, the problem of pH fluctuation of the solution and the detailed mechanism of redox have not been completely clarified. Then, in 2016, the electrochemical redox mechanism of this free chlorine was carefully studied. Based on these results, we designed a new system using BDD electrodes that can monitor the free chlorine concentration in real time.

1 Introduction

Free chlorine, which is defined as the concentration of dissolved gas (Cl_2), hypochlorous acid (HClO), and hypochlorite (ClO-) have been widely utilized as a disinfecting agent in various fields such as in clinical practice, the food industry, and drinking water treatment. Therefore, it is necessary to monitor and control the free chlorine concentration for public health maintenance.

The general detection methods for free chlorine include the colorimetric method such as DPD (N,N-diethyl-p-phenylenediamine) method, the amperometric titration method, and iodometry [1–3]. However, these methods are unsuitable for continuous on-line monitoring because they each have a number of disadvantages, such as the requirement for many types of reagent that may produce greater toxicity, a high detection limit, and the difficulty of operation. As one of the methods, electrochemical techniques can be used for real-time monitoring of the free chlorine concentration [4–8]. Indeed, free residual chlorine sensors based on electrochemical reduction with platinum or gold electrodes are commercially available from many companies. However, the conditions under which systems with these sensors can

Y. Einaga (✉)
Department of Chemistry, Keio University, 3-14-1 Hiyoshi, Yokohama 223-8522, Japan
e-mail: einaga@chem.keio.ac.jp

© Springer Nature Singapore Pte Ltd. 2022

Y. Einaga (ed.), *Diamond Electrodes*,
https://doi.org/10.1007/978-981-16-7834-9_12

https://www.twirpx.org & http://chemistry-chemists.com

be operated are constrained, since they require skillful operators and frequent calibration to make reliable measurements because the electrochemical reaction of free chlorine is affected by various factors such as pH, surface fouling, and dissolved oxygen [9]. Consequently, a more reliable and versatile system are needed for the continuous monitoring of free chlorine.

Here in this chapter, the development on chlorine detection by BDD electrodes is introduced.

2 Oxidation Reaction of Free Chlorine (2008)

In 2008, we have reported the quantitative determination of free chlorine based on its oxidation. NaClO solutions were used for the experiment of free chlorine detection [10]. Cyclic voltammograms for various concentrations of NaClO in a 0.1 M $NaClO_4$ obtained at a scan rate of 100 mV s^{-1} using BDD electrode were shown (Fig. 1). An irreversible oxidation peak was observed at ~ 1.4 V (vs. Ag/AgCl). The oxidation reaction is due to the oxidation of ClO^- as follows.

$$6ClO^- + 3H_2O \prime \quad 2ClO_3^- + 4Cl^- + 6H^+ + 3/2O_2 + 6e^- \; E_0 = 1.316\ \text{V} \tag{1}$$

The inset in Fig. 1a shows a plot of the oxidation peak current versus the free chlorine concentration. A linear calibration curve was obtained in the concentration range of 20–100 mg Cl L^{-1}, indicating that determination of free chlorine can be possible at BDD electrodes. This sensitivity (slope: 0.744 A cm^{-2} mg^{-1} L) was more than 3 times higher than those at conventional electrodes, [11, 12] suggesting the superiority of using BDD for chlorine oxidation. The background current of 3 μA cm^{-2} was obtained very small in comparison with that at Pt electrode in the same condition (115 μA cm^{-2}). It is known that BDD electrodes have a small background current due to the inert surface [13]. The small background current can give rise to a very low detection limit due to the decrease in the noise. Furthermore, excellent stability is shown with a relative standard deviation (RSD) of 2.56% for 10 repetitive voltammograms (Fig. 1b).

Then, flow injection analysis (FIA) with amperometric measurement was applied to estimate the low limit of detection (LOD). A solution of 0.1 M phosphate buffer solution (PBS) with pH = 8 was used for the mobile phase. A hydrodynamic voltammogram in the range of potential from 0.9 to 1.5 V versus Ag/AgCl was obtained to optimize the experimental conditions. A potential of 1.1 V versus Ag/AgCl was fixed for the FIA. Figure 2 shows FIA measurements for a series of 20 μl injections in various concentrations of free chlorine. The stability was confirmed by 5 repeated injections for each concentration of free chlorine. The amperometric calibration curve obtained from the responses is linear over the range from 0.1 to 2.0 mg Cl L^{-1} (n = 5) with a correlation coefficient of 0.96. The background current was ~ 0.1 nA. A LOD of 0.0083 mg Cl L^{-1} (8.3 ppb) was estimated (S/N = 3), suggesting

https://www.twirpx.org & http://chemistry-chemists.com

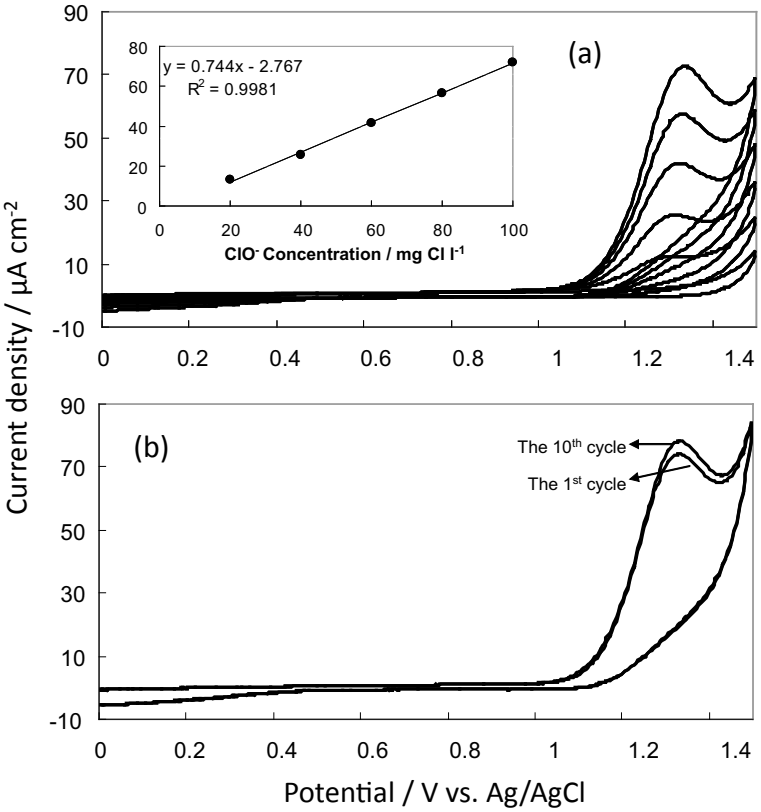

Fig. 1 Cyclic voltammograms of a 0.1 M $NaClO_4$ solution **a** in the presence of various concentrations of free chlorine (2–100 mg Cl L^{-1}) and **b** for 10 repetitive scans of 50 mg Cl L^{-1} using an as-deposited BDD electrode. Linear calibration plots are shown in the inset. Reprinted from [10], Copyright 2008, with permission from Elsevier

that this method can be adapted for application in a monitoring instrument for high free chlorine concentrations in disinfection, bleaching, and various manufacturing processes and low concentration in drinking water.

3 Reduction Behavior of Free Chlorine

In order to apply to practical application, not only the concentration of ClO^- but also that of HClO should be monitored, because the equilibrium distribution of the free chlorine species, HClO and ClO-, depends on the pH of the solution.

$$HClO \rightleftarrows ClO- + H^+ \qquad pKa = 7.53 \tag{2}$$

https://www.twirpx.org & http://chemistry-chemists.com

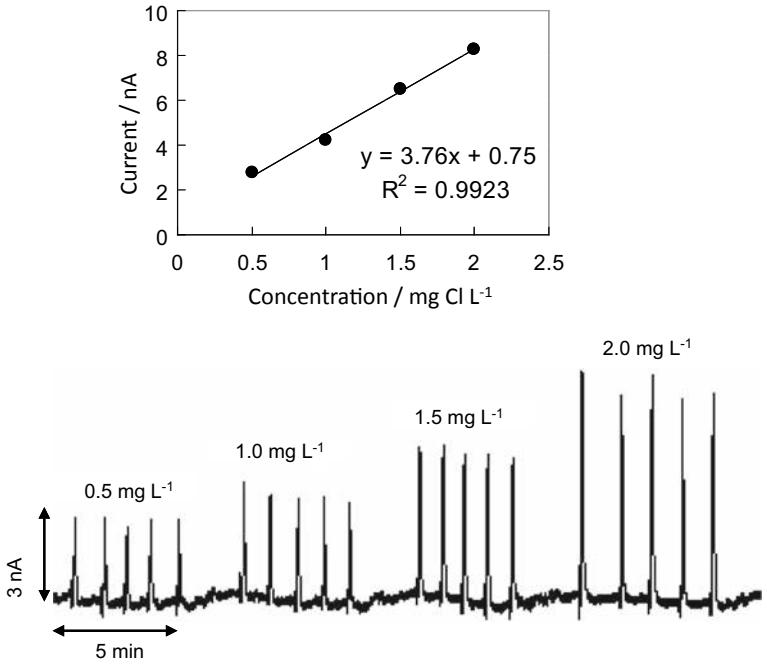

Fig. 2 Flow injection analysis plots of free chlorine for various concentrations between 0.1 to 2.0 mg Cl L^{-1} obtained with a BDD electrode at an applied potential of 1.1 V versus Ag/AgCl. The mobile phase was 0.1 M PBS (pH 8), and the flow rate was 1 mL min^{-1}. The inset shows the linear calibration plot. Reprinted from [10], Copyright 2008, with permission from Elsevier

HClO can be deprotonated to form ClO- at higher pH. This equilibrium distribution of HClO and ClO- is practically important for free chlorine sensing because the pH of tap water is usually controlled to be neutral over a range (from 5 to 9).

Here, the electrochemical reduction behavior of ClO- and HClO at BDD electrodes is studied [14].

Figure 3a shows linear sweep voltammograms (LSVs) of 1.4 mM free chlorine in 0.1 M $NaClO_4$ with different pH from 5 to 9 using a BDD electrode. For the LSVs in the presence of free chlorine, the BDD exhibits two reduction waves at around -0.4 and -1.3 V (vs. Ag/AgCl). The first peak at -0.4 V (vs. Ag/AgCl) is assigned to the reduction of HClO.

$$HClO + e^- \rightleftharpoons HClO^-_{(ads)} \quad (3)$$

As for the first reduction wave, the peak current decreases with increasing pH and almost disappears at pH 9. Figure 3b shows the pH dependence of the peak current at the potential at which the peak or minimum |dI/dV| in the first wave occurs. The ratio of HClO to total free chlorine, which can be determined from pKa, is also displayed in Fig. 3b. The trend is consistent with the equilibrium distribution shown in Eq. (2).

https://www.twirpx.org & http://chemistry-chemists.com

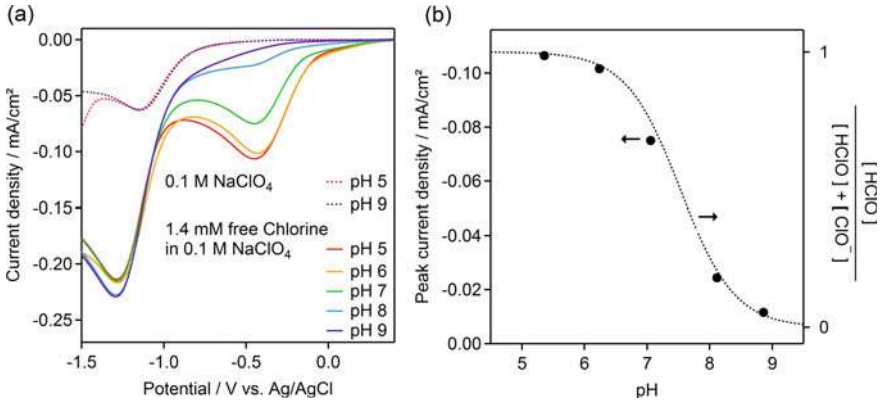

Fig. 3 **a** LSVs for 1.4 mM free chlorine in 0.1 M $NaClO_4$ with different pH and the LSVs in the absence of free chlorine in 0.1 M $NaClO_4$ at a scan rate of 20 mV/s using a BDD electrode. **b** The pH dependence of peak current in the first reduction waves of the LSVs and the ratio of HClO to HClO plus ClO^- in equilibrium. Reprinted from [14], Copyright 2016, with permission from Elsevier

As for the second reduction wave (at -1.3 V (vs. Ag/AgCl), on the other hand, the wave seems to be independent of pH (Fig. 3a). Therefore, ClO- can also be reduced in the second reduction wave although the potential significantly overlaps with the oxygen reduction reaction (ORR), which is observed in the absence of free chlorine. In order to understand the mechanisms for the second wave, peak currents at -1.3 V (vs. Ag/AgCl) and -0.4 V were carefully monitored in both pH = 6 and pH = 8–9. Figure 4 shows the free chlorine concentration dependences of LSVs obtained in non-degassed 0.1 M $NaClO_4$ around pH 6 (Fig. 4a) and pH 8–9 (Fig. 4b), and therefore, most of the free chlorines are HClO (pH = 6) and ClO- (pH = 8–9). In Fig. 4a, the peak current in the first wave increases in proportion to the concentration of HClO. In contrast, a small current in the first wave can be seen in Fig. 4b due to the low fraction of HClO. On the other hand, the current in the second wave increases, dependent on the concentration of both species. Interestingly, the slope value of peak current-concentration curve of ClO- is approximately two times the one of first wave for HClO (Fig. 4c) while it is known that two electrons are involved in electrochemical reduction of both species [15]. It indicates that two electrons are involved in the second wave for reduction of ClO-, and one electron is involved in the first wave for HClO reduction. In addition, the second wave for HClO reduction also implies two electron reduction mechanism as well as ClO- because of higher slope value than first wave.

https://www.twirpx.org & http://chemistry-chemists.com

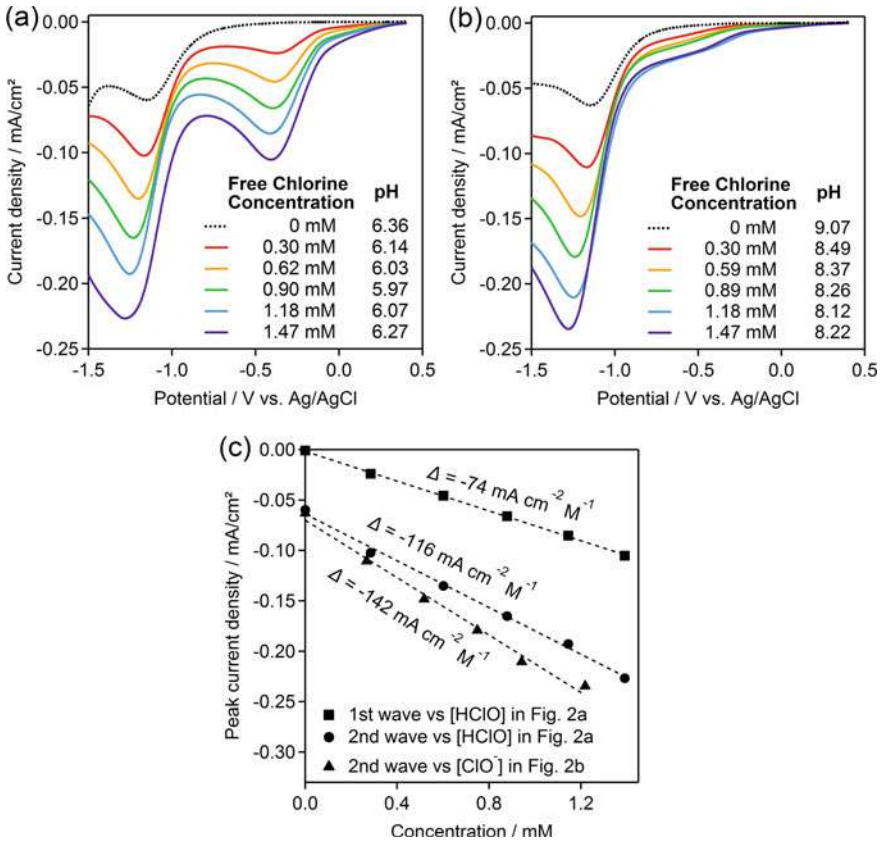

Fig. 4 LSVs for different concentration of free chlorine in 0.1 M $NaClO_4$ with pH **a** around pH 6 and **b** pH 8–9 at scan rates of 20 mV/s using a BDD electrode. **c** Their peak current values versus concentration of HClO or ClO^-. Reprinted from [14], Copyright 2016, with permission from Elsevier

4 For Practical Application of Chlorine Sensor

4.1 Concentration of Free Chlorine: Sum of Current Values (Oxidation and Reduction)

Based on the results on oxidation and reduction of free chlorine (shown in 11–2 and 11–3), it is possible to estimate the total free chlorine concentration that does not depend on the pH (Fig. 5). Furthermore, the pH of the solution can be measured by calculating the abundance ratio.

https://www.twirpx.org & http://chemistry-chemists.com

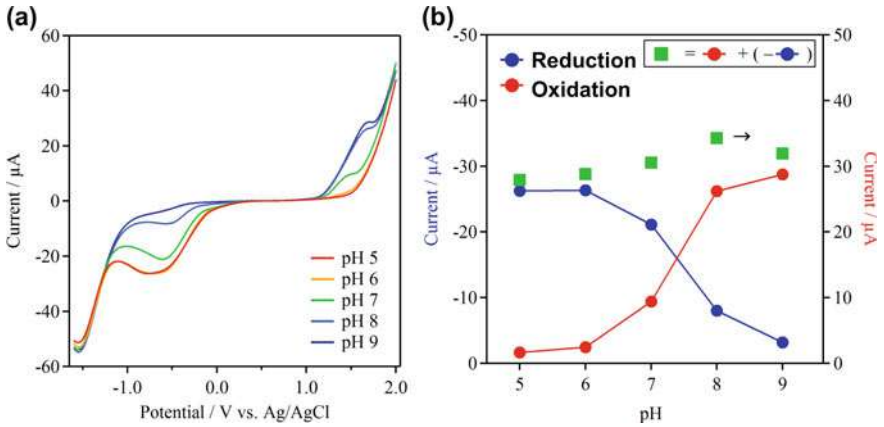

Fig. 5 **a** Cyclic voltammograms for 100 ppm NaClO in 0.1 M $NaClO_4$ with different pH using BDD electrode. **b** The pH dependence of peak current at -0.4 V (vs. Ag/AgCl) (blue), at +1.6 V ((vs. Ag/AgCl) (red), and the sum of both current values (green)

4.2 Design of Prototype for Practical Sensor

We have developed a prototype for free chlorine sensor based on the results shown in this chapter. Figure 6 is an external view of the designed prototype sensor. The electrode had a three-electrode configuration of a working electrode, a counter electrode,

Fig. 6 Designed prototype sensor

https://www.twirpx.org & http://chemistry-chemists.com

Fig. 7 Commercial product for free chlorine sensor produced by HORIBA Advanced Techno, Co., Ltd

and a reference electrode, and a BDD electrode was used as the working electrode and the counter electrode. A silver rod is used as the reference electrode.

In October 2017, apparatus for producing hypochlorous acid water was established as "JIS (Japanese Industrial Standard) B 8701" [16]. Then, HORIBA Advanced Techno, Co., Ltd. prepared the commercial product for free chlorine sensor by modifying our first prototype (Fig. 7). This example can open the future potential of BDD electrochemical sensors.

References

1. Icardo MC, Mateo JVG, Catayud JM (2001) o-Dianisidine: a new reagent for selective spectrophotometric, flow injection determination of chlorine. Analyst 126:2087–2092
2. APHA, AWWA, WCCF (1992) Standard Method for the Examination of Water and Wastewater, 18th ed.
3. White GC (1986) Handbook of chlorination, 2nd edn. Van Nostrand, Reinhold, New York
4. Ibl N, Landolt D (1968) On the mechanism of anodic chlorate formation in dilute NaCl solutions. J Electrochem Soc 115:713–717
5. Djordjević AB, Nikolić BZ, Kadija IV, Despić AR, Jakšić MM (1973) Kinetics and mechanism of electrochemical oxidation of hypochlorite ions. Electrochim Acta 18:465–469

https://www.twirpx.org & http://chemistry-chemists.com

6. Tasaka A, Tojo T (1985) Anodic oxidation mechanism of hypochlorite ion on platinum electrode in alkaline solution. J Electrochem Soc 132:1855–1859
7. Czarnetzki L, Janssen LJJ (1988) Electrochemical oxidation of hypochlorite at platinum anodes. Electrochim Acta 33:561–566
8. Qin Y, Kwon HJ, Howlader MMR, Deen MJ (2015) Microfabricated electrochemical pH and free chlorine sensors for water quality monitoring: recent advances and research challenges. RSC Adv 5:69086–69109
9. Badalyan A, Buff J, Holmes M, Chow CWK, Vitanage D (2009) On-line free-chlorine/total-chlorine monitors' evaluation—a step towards a correct choice of residual disinfectant monitor. J Water Supply Res Technol 58:181
10. Murata M, Ivandini TA, Shibata M, Nomura S, Fujishima A, Einaga Y (2008) Electrochemical detection of free chlorine at highly boron-doped diamond electrodes. J Electroanal Chem 612:29–36
11. Kodera F, Ueda M, Yamada A (2005) Detection of hypochlorous acid using reduction wave during anodic cyclic voltammetry. Jpn J Appl Phys 44:L718–L719
12. Kodera F, Kishioka S, Ueda M, Yamada A (2004) Electrochemical detection of free chlorine using anodic current. Jpn J Appl Phys 43:L913–L914
13. Einaga Y (2010) Diamond electrodes for electrochemical analysis. J Appl Electrochem 40:1807–1816
14. Watanabe T, Akai K, Einaga Y (2016) The reduction behavior of free chlorine at boron-doped diamond electrodes. Electrochem Commun 70:18–22
15. Schwarzer O, Landsberg R (1968) Zur Reduktion der Hypochlorsäure und ihres Anions an Platin-Elektroden. J Electroanal Chem Interf Electrochem 19:391–404
16. JIS (Japanese Industrial Standard) (Japanese site). https://www.kikakurui.com/b8/B8701-2017-01.html

https://www.twirpx.org & http://chemistry-chemists.com

Modified Boron-Doped Diamond Electrodes for Sensors and Electroanalysis

Prastika K. Jiwanti, Shafrizal R. Atriardi, Yulia M. T. A. Putri, Tribidasari A. Ivandini, and Yasuaki Einaga

Abstract Boron-doped diamond (BDD) has been established as a superior electrode among other conventional solid electrodes due to its unique properties, such as very low background current, wide potential window, and high physical and chemical stability. However, in compare to metal electrodes, BDD has much lower kinetic activity in some important chemical reactions, which causes limitation for sensor and biosensor applications. Modification of BDD surface with redox-active particles/compounds was reported to facilitate electron transfer between the BDD substrate and analytes with a significant reduction in activation overpotential; therefore, the catalytic activity and sensitivity are improved. In addition, the modification can increase the selectivity in some reactions. On the other hand, to have a stable modified surface of BDD electrode is not easy, since the main composition of BDD is carbon atoms with sp^3 configuration, which is very compact and stable, and actually one of the advance characteristics of BDD electrodes. However, the stability of the BDD surface causes the modified surface to be easily detached or dissolved after several usages. In this chapter, preparations and applications of the modified BDD for electrochemical sensors and biosensors are described and compared.

Keywords Surface modification · Physical · Electrochemical · Photochemical · Sensors · Biosensors

P. K. Jiwanti
Nanotechnology Engineering, School of Advanced Technology and Multidisciplinary, Airlangga University, Surabaya 60115, Indonesia

S. R. Atriardi · Y. M. T. A. Putri · T. A. Ivandini (✉)
Faculty of Mathematics and Science, Department of Chemistry, University of Indonesia, Kampus UI Depok, Jakarta 16-424, Indonesia
e-mail: ivandini.tri@sci.ui.ac.id

Y. Einaga
Faculty of Science and Technology, Department of Chemistry, Keio University, 3-14-1 Hiyoshi, Yokohama 223-8522, Japan
e-mail: einaga@keio.ac.jp

© Springer Nature Singapore Pte Ltd. 2022

Y. Einaga (ed.), *Diamond Electrodes*,
https://doi.org/10.1007/978-981-16-7834-9_13

https://www.twirpx.org & http://chemistry-chemists.com

1 Introduction

Boron-doped diamond (BDD) electrodes have been widely studied because of its excellent properties. BDD electrodes provide excellent physical and chemical stability, which is the intrinsic property of diamond substrate due to its sp^3 configuration [1–7]. Low background currents and wide potential windows are also generally observed as the results of the less adsorption process on the BDD surface [1–7]. In addition to that high stability of BDD provides a high biocompatibility for bioapplications [8, 9]. These unique properties established BDD as the superior electrode among other conventional metal and carbon-based electrodes for many applications, including sensors and biosensors, [10–12] electroanalysis, [13, 14] electrocatalytic, and electrosynthesis, [15–22] as well as energy conversion and energy storages [23, 24]. There have been also several reviews related to the study of BDD electrode including its applications [25–31].

However, BDD is mainly composed of carbon atoms. Therefore, like other carbon-based electrodes, its low kinetic activity is often found in some chemical reactions [8, 14, 32–34]. For example, BDD is not electroactive in reduction reactions of oxygen and peroxide as well as in oxidation of glucose, [8, 35, 36] which are often utilized as the basic reactions to develop enzymatic sensors and biosensors [8, 37–39]. BDD is also found to be not electroactive for oxidation and reduction of arsenic [40, 41]. Modification with redox-active particles/compounds was reported to improve the electrochemical activity of BDD surface by facilitating the electron transfer between the BDD substrate and the analytes [8, 14, 35, 36, 40]. Furthermore, modification of the BDD surface with metals is the most popular and has been used for many electroanalysis and electrocatalytic applications [8, 14, 35, 36, 40]. In addition to the increase of catalytic activity of the BDD surface, modification with metal particles also increases the ratio of signal to noise because the deposited metal on the BDD surface acts as a microelectrode array, which can promote higher sensitivity to the analytes with low background current and low current noises [8, 14, 35, 36, 40]. Modification can also increase selectivity of the reaction [8, 14, 35, 36, 40]. In particular condition, a specific metal catalyst could be not only sensitive to detect the analytes that is not observed by the unmodified BDD electrode, but also can detect the analytes with better limit of detection (LOD) than its related metal bulk electrode [8, 14, 35, 36, 40]. Ni and Cu particles are often modified on surface of BDD electrode for glucose sensors as BDD is inactive for the oxidations of glucose and other carbohydrates, [36, 42, 43] while Pt and Au are often utilized in oxygen and peroxide sensors as well as biosensors [8, 35].

On the other hand, to modify the BDD surface is not very easy due to the sp^3 configuration of the BDD surface, which limits the adsorption process as well as chemical bond formations on the BDD surface [4, 6]. Physical adsorption is considered as the simplest techniques to modify BDD. However, by using these techniques, a lack of chemical interaction between the modifying particles/compounds with the surface of BDD results in the detached/dissolution of the modified surface after several usages [14, 41]. Electrochemical techniques have a similar problem to the physical

https://www.twirpx.org & http://chemistry-chemists.com

adsorption. Moreover, it was reported that conductivity of the BDD surface is not homogeneous and affects the distribution of the modifying particles/compounds [44]. On the other hand, ion implantation technique was reported to immobilize the modifying particles/compounds into the subsurface of BDD; therefore, a better stability of the modified surface could be achieved. However, special instrumentations with many procedural steps as well as the skillful technicians to conduct the procedures are necessary, causes this technique to be less practicable [35, 42]. Furthermore, modification with photochemical technique was reported to provide active sites for better attachment of the modifying particles/compounds, and good stability of the modifying particles/metals was achieved [8, 9, 45].

In this chapter, preparation of modified BDD electrode for sensor and biosensor applications is discussed and compared thoroughly.

2 Physical Adsorption

A simple deposition method with less time-consuming and the requirement of many preparation steps, but stable enough to be used in many applications is desired by many researchers. The physical adsorption technique is the simplest one. The deposition is often carried out by painting or dropping the prepared solution onto the surface of BDD electrode, or by immersing a piece of BDD electrode into the prepared solution of the modifying compounds or their precursors. Uchikado et al. (2001) have reported the modification of BDD surface by dropping nickel and copper ion solutions onto the BDD surface and dried [36]. Applications of these electrodes for glucose detections showed good limits of detection with stable responses for around one week by using flow injection analysis.

The sol–gel reaction on the surface of BDD was also reported to be able to modify the stainless steel substrate by metal oxide particles [46]. Salazar-Banda et al. (2005) have applied this method to modify BDD surface with platinum oxide particles in combination with cathodic pre-treatment on BDD surface and Nafion® coating after the deposition to inhibit the detachment of the deposited metal particles [47]. They reported that the increase of stability for electrochemical applications in acid medium, in which the modified particles can be retained 91.6%, after 1000 voltammetric cycles performed [47]. This method was claimed to be easy and cheap. Similar method was then used for deposition of other metal particles, including Pb, Ru, and Ir as shown in AFM images in Fig. 1 [48, 49].

However, in fact, without any chemical bond or absorption force between metal particles as well as Nafion® with the compact sp^3 surface of BDD, the interactions between them are also weak, resulted in the instability of the modifying particles/films. This adsorption method might be more suitable for porous materials, such as graphite, which can absorb and trap the modifying particles/compounds inside the porous.

https://www.twirpx.org & http://chemistry-chemists.com

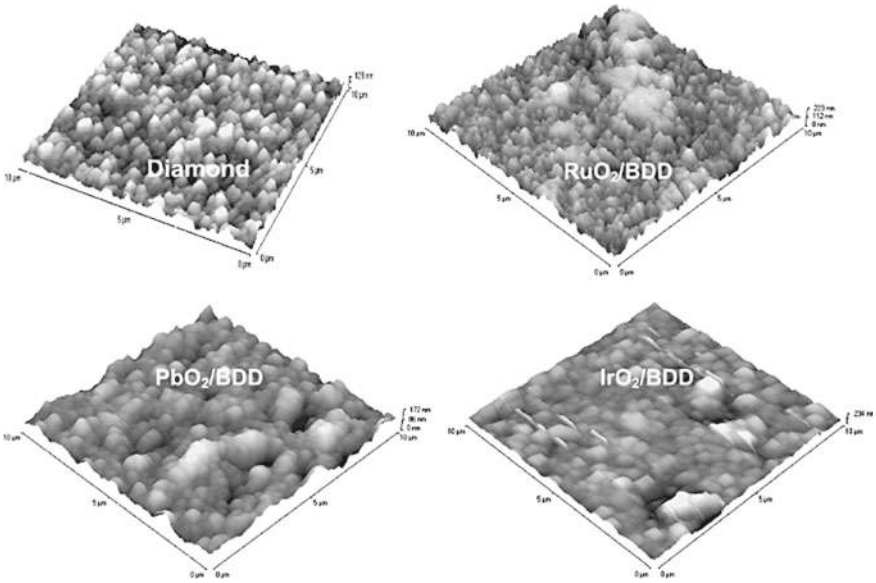

Fig. 1 Deposited metal oxide particles of RuO_2, PbO_2, and IrO_2 on surface of BDD electrode, studied by AFM technique. Reprinted with permission from [48]

3 Electrochemical Deposition

Electrochemical deposition method is considered as a better technique than physical adsorption process. This method has been widely used to modify the surface of BDD electrode due to its simplicity and reproducibility. This method is also controllable, in which the process could be performed by maintaining the applied potentials or currents. In addition, this method is also convenient as the process is possible to be carried out at room temperature without any requirement of expensive instrumentations. Numerous reports about electrodeposition techniques have been published for wide-range electrochemical applications [50–52]. Electrochemical deposition method is generally carried out in a cell containing of three electrodes and an electrolyte. Amperometry is a common technique used to deposit the metal particles although the use of cyclic voltammetry (CV) technique was also reported. These techniques are basically performed by reduction reactions of metal ions to be metal particles at the surface of the working electrodes, in this case the BDD electrode.

Amperometric technique is carried out by applying a constant potential at or higher than the reduction potential or the related metal ions. This process supplies electrons to the working electrode; therefore, the negative charges at the working electrode will attract the positive charges of metal ions to its surface, followed by electron transfer from electrode to the metal ions. On the other hand, supplying electrons process involves the conductivity of the working electrode, in which reduction process is easier to be performed on the surface with higher conductivity. Meanwhile, the

https://www.twirpx.org & http://chemistry-chemists.com

conductivity of the polycrystalline of the BDD films is quite heterogeneous; the nonuniform doping of boron in diamond crystals causes surface conductivity to be inhomogeneous [44]. As a result, the dispersion and the size of metal deposits depend on the diamond microcrystals on the surface. The difference of conductivity was observed at different crystal facets [53] and in the crystal boundary of BDD polycrystalline, which generally containing some amount of sp^2 graphite fraction with higher conductivity than BDD crystal [44].

Moreover, the polycrystalline BDD is synthesized by using chemical vapor deposition technique in a hydrogen atmosphere; therefore, the surface of as-deposited polycrystalline BDD films is initially terminated by hydrogen functional sites [54]. The roughness of the as-deposited BDD surface was also generally very high due to very small BDD crystals deposited on the surface. These two reasons make the as-deposited BDD has hydrophobic properties, which inhibits the interaction of the metal ions to the surface of BDD electrodes [55].

To increase the affinity of the metal ions toward the BDD surface, hydrogen-terminated BDD (H-terminated BDD) can be oxidized to create oxygen-terminated surface (O-terminated BDD). As it is well known, oxygen has higher affinity to metal ions than hydrogen. Various methods to change H-terminated to O-terminated BDD have been reported, including anodic treatment at high positive potential, [5] treatment in oxygen plasma, [57] boiling in strong acid, [58] or long-term exposure to air [55]. These methods generally oxidize the surface of diamond. As the results, oxidizing the surface is reported not only to change the oxygen to carbon ratio (O/C ratio) but also increase the hydrophilic properties of the BDD surface as well as clean sp^2 fractions from the electrode [45, 55]. Therefore, the increasing coverage of metal particles was observed. X-ray photoelectron spectroscopic (XPS) measurements observed that the O/C ratio of the BDD surface could be increased from around 0.03 to around 0.3 after oxidation process, [54, 56] while the deconvolution of the XPS spectra indicated that C-O, C = O, and C–O–C bonds were formed after the oxidation process [53]. Other advantages of O-BDD than H-BDD have been discussed in another chapter [59–61]. Furthermore, O-BDD can be converted back to H-BDD by hydrogen-flame, hydrogen-plasma treatment, and by reduction reactions at a very negative potential [62–64].

Beside the amperometric technique, CV technique can deposit particles on the BDD surface with smaller particles sizes and better distributions than amperometry as this technique is carried out by potential scanning from negative to positive potential, and vice versa, for several cycles. Therefore, the unstable particles were expected to be removed, leaving the stable particles on the surface only. However, it is necessary to carefully consider the potential range to suppress the metal lost caused by hydrogen evolution or metal oxidation. Rismetov et al. [65] have reported that by applying various number of scan cycles (20, 40, and 80 cycles) at a potential range of -0.5 V to + 0.8 V, Pt particles could be deposited at around 330–722 particles/100 μm^2 surface area with particle size around 30–122 nm (Fig. 2). The increase of the deposited metal particles was observed with the number of voltammetric cycles.

https://www.twirpx.org & http://chemistry-chemists.com

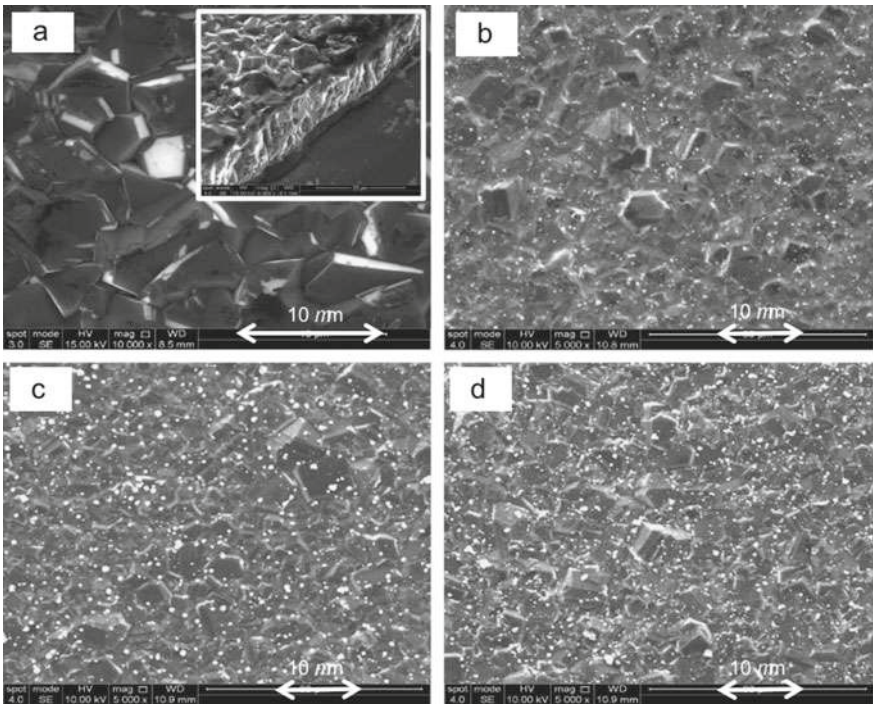

Fig. 2 SEM image of the unmodified BDD electrode (**a**) and Pt-modified BDD electrode prepared by CV method with 20 (**b**), 40 (**c**), and 80 (**d**) number of scan cycles. Reprinted from [65] copyright 2014, with permission from Elsevier

In order to increase the stability of the deposited metal on the BDD surface, combination method with electrochemical deposition method was also reported. Sphilevaya et al. combine the electrochemical deposition method of Pt with annealing in hydrogen and oxygen plasma [66]. Combining amperometry with physical adsorption method was also reported [67]. Gao et al. deposited Pt, Ni, Au, and Cu nanoparticles on the BDD surface by dropping the related metal ions solution on the BDD surface followed by reduction reaction using $NaBH_4$ to form the metal seeds [67]. Then, applying the potential step application (amperometry) at -1.2 V was performed. The metal seeds will act as the active site of BDD surface for the deposition process. Afterward, annealing at high temperature (700 °C) and activation method were applied. The modified BDD provided a very stable particles attached on the surface of BDD. A test conducted using ultrasound removal at 130 W demonstrated that less than 1% of metal particles with annealing was removed compared to 35% of metal particles removal from the electrode without annealing (Fig. 3). Besides, Gao et al. suggested that H-terminated BDD is more favorable for the seeding technique than O-terminated BDD due to stronger adsorption of $NaBH_4$ on H-terminated BDD. This method was then also applied to prepare Pt-modified BDD and Ir-modified BDD for hemoglobin-based acrylamide and arsenic sensors, respectively [68, 69].

https://www.twirpx.org & http://chemistry-chemists.com

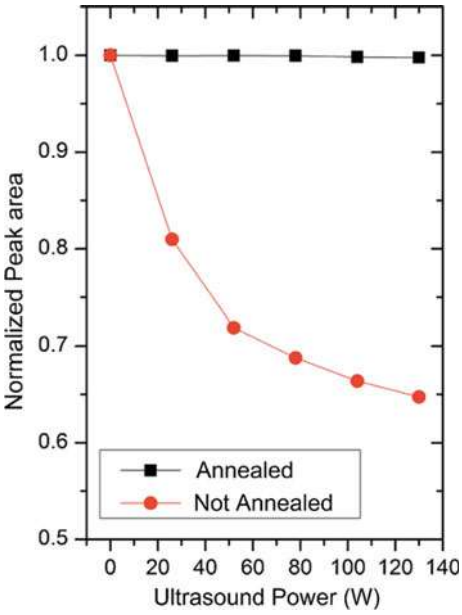

Fig. 3 Stability check of deposited metal particles with and without annealing treatment. The electrode was Pt particles modified on BDD. The ultrasound power was 130 h. Reprinted from [67] Copyright 2013, with permission from Elsevier

Stability check of deposited metal particles with and without annealing treatment. The electrode was Pt particles modified on BDD. The ultrasound power was 130 h. Reprinted from [67]. Copyright 2013, with permission from Elsevier

The deposition of two or more metal particles can also be performed with amperometric technique by applying the highest reduction potential of the related metals ions [70]. However, the reduction potential of each metal could be very different, thus allowing one metal to be deposited more than the others. To overcome this problem, applying a combination of two potentiostatic methods in a row was reported [71, 72]. Mavrokefalos et. al. reported the deposition of bimetallic Pd-Sn through two steps [71]. The first step was to deposit Pd particles on the surface BDD electrode by using amperometry at potential -0.15 V. Then, Sn was deposited on the modified Pd-BDD surface by applying LSV at potential range of -0.6 V to + 0.0 V at 0.01 V/s for one cycle. Sn particles were found to be deposited at both Pd metal site and BDD surface (Fig. 4). Similar method to deposit bimetal particles Pt-Cu was also reported [72].

Another reported combination method was recorded by using combination between amperometric step and physical adsorption to deposit bimetallic Pt-Ni and composite Pt–PrO_{2-x} at the BDD surface [73, 74]. The first step was to deposit Pt by using amperometry, then, followed by monodispersing of metal or metal oxide nanoparticles on the Pt-modified BDD surface due to the electrostatic interaction between the modified BDD surface and the nanoparticles. The bimetallic Pd-M nanoparticles showed higher mass activity than the similar systems from literature as well as stability when operated in alkaline media. However, to the best of our knowledge, there is no report of this preparation method was found in literatures for sensor applications. Table 1 shows a summary of the reported publications of

https://www.twirpx.org & http://chemistry-chemists.com

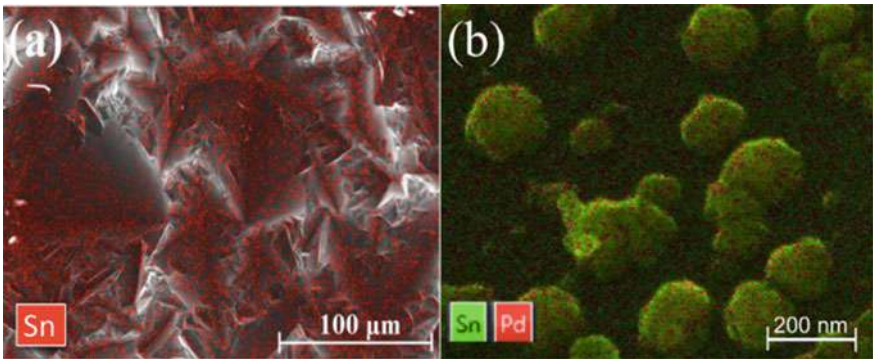

Fig. 4 SEM–EDX images of Sn (**a**) and Pd-Sn (**b**) deposited on surface of BDD electrode. Reprinted from [71] copyright 2017, with permission from Elsevier

Table 1 Recent updates of various metal depositions with different electrochemical method

Method	Metal	Parameters	Applications/Ref
CV	Ir	E = -0.2 V to + 1.2 V at scan rate 50 mV/s, 15 cycles	Arsen (III) sensor [40]
	Pt	E = -0.5 V to + 0.8 V at 100 mV/s, 80 cycles	Peroxide detection for melamine sensor [65]
Amperometric	Au	E = -0.2 V, 100 s	Neuraminidase sensors [75, 76]
	Au	E = -0.4 V, 30 s	Arsen(III) sensor and selenium sensors [77, 78]
	Pt-Au	E = -0.5 V, 180 s	Glucose detection [70]
	Ni	E = -1.3 V, 300 s under stirring	Glucose detection [43]
	Ni	E = -1.3 V, time deposition was varied	Primer alcohol detection [79]
	Ag	Deposition potential, time, and metal electrolyte concentration were varied	Peroxide detection for cholesterol sensor [37]
	Ag	E = -0.1 V, 100 s	Peroxide detection [80]
	Ag/graphene	E = -1.2 V, 30 s	Carbaryl and paraquat detection [81]
	Bi	E = -1.2 V, 120 s with stirring followed by a 15 s equilibration time without stirring	Cadminum and lead detection [82]
	Bi	E = -0.95 V, 45 s under string, at Nafion®-modified BDD	Caffeine and paracetamol [83]

https://www.twirpx.org & http://chemistry-chemists.com

electrochemical modification on BDD surface with various methods together with their applications for sensors.

4 Ion Implantation

Ion implantation is performed by acceleration of one element into the material to change the chemical, physical, and electrical properties of the material. Technology of ion implantation was developed from 1940s for nuclear research and isotope separation, but the major development was achieved in 1960s when ion implantation applied for semiconductor material [84]. Since then, many reports were using ion implantation technique to insert the impurities into the material. In 1989, Takeuchi et al. successfully implanted Mg^+ ion into GaAs [85]. Moreover, numerous articles [86–89] and reviews [84, 90–92] were also reported, whether implantation was performed for insulator, semiconductor, or metallic material.

Modification of BDD using ion implantation was firstly reported by Fujishima group to develop nickel implanted for glucose sensors, [93] and continued by Einaga group, who developed copper, iridium, and platinum-implanted BDD for arsenic and peroxide sensors, respectively [35, 41, 94]. Furthermore, in 2005–2006, publications about Ni implanted for glucose and tetracycline sensors and Au-implanted BDD electrodes for dopamine and uric acid sensors were also reported [95–97].

Applying high energy of ion implantation (around 400–800 keV) placed the metal to be buried at the subsurface of BDD. However, during the ion implantation process, the damages of some sp^3 bonds in diamond structure occurred due to ion the impacts to form broken sp^3 bonds in a transition stages between diamond and graphite. An annealing process was reported to recover the damaged diamond back to sp^3 structure by supplying sufficient energy to allow recombination of interstitials and vacancies to occur [41, 98]. Figure 5 shows the Raman spectra of the as-deposited BDD electrode, the BDD after ion implantation, and after annealing. A typical peak of sp^3 carbon at 1333 cm^{-1} was observed in all spectra. However, a peak at around 1500 cm^{-1} related to sp^2 carbon is shown at the spectra of BDD after ion implantation, while it is not observed at the spectra of as-deposited BDD. The annealing step relieved the strained diamond film as shown by the absence of the peak at around 1500 cm^{-1} in the spectrum after annealing.

However, a critical damage level in diamond needs to be considered as it is reported that the disrupted diamond structure below the level can be annealed back to diamond, while the damage densities beyond the level cannot be restored upon annealing but rather collapsed into graphite [98]. Accordingly, the implantation dose as well as the energy level have to be carefully calculated, resulted in limitation of the modification at the BDD surface.

The metal ion-implanted BDD electrode was developed from 2002 to 2011; since then, no further investigation was carried out. Ion implantation method requires ion bombardment with high power and special design instruments, which unfortunately

https://www.twirpx.org & http://chemistry-chemists.com

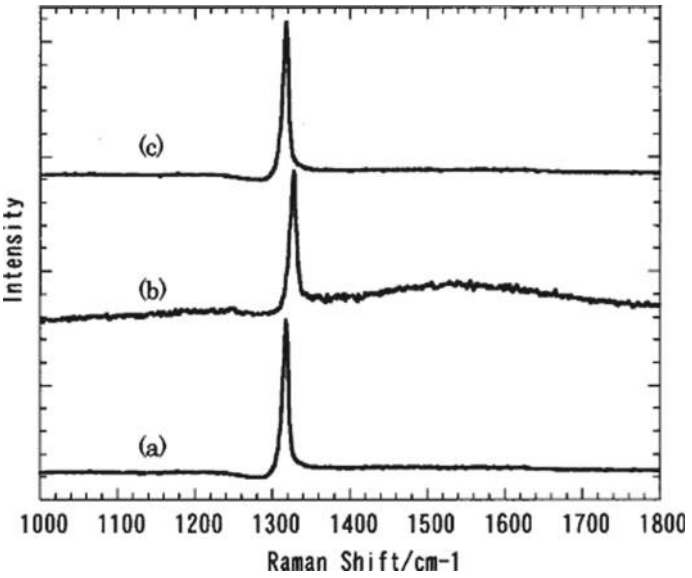

Fig. 5 Raman spectra of as-deposited BDD (**a**), ion implanted (**b**), and after annealing at 850 °C from 10 min (**c**). Reprinted from [93] with the permission of IOP Publishing

consumes a high-cost operation. The reports about ion implantation modification and its applications are summarized in Table 2.

Table 2 Ion implantation conditions of some ions to the surface of BDD electrode and its electroanalysis applications

Metal	Metal Ion implanted	Implanting dose	Energy (keV)	Annealing temperature and time	Application	Ref
Ni	Ni^{2+}	5×10^{14} cm^{-2}	750	850 °C, 10 min	Glucose and tetracycline sensor	[93–96]
Cu	Cu^{2+}	5×10^{14} cm^{-2}	750	850 °C, 10 min	Glucose oxidation	[94]
Pt	Pt^{2+}	5×10^{14} cm^{-2}	750	850 °C, 45 min	hydrogen peroxide sensor	[35]
Ir	Ir^{+}	5×10^{14} cm^{-2}	800	850 °C, 45 min	Arsenic (III) sensor	[94]
Au	14% Au^{+} 75% Au^{2+} 11% Au^{3+}	5×10^{17} ions.cm^{-2}	20	-	Dopamine oxidation	[75]

https://www.twirpx.org & http://chemistry-chemists.com

5 Photochemical Reaction

From the previous discussion, it is clear that pre-treatment of BDD surface before modification is necessary. So far, electrochemical treatments to clean the surface and to change the H-termination surface to be O-terminated one are the most favorable method. A remarkable result was reported in 2005 for a preparation of N-terminated BDD through photochemistry reaction between BDD surface and allylamine to modify BDD surface with gold nanoparticles [45]. It has been discovered that nitrogen-modified BDD has a better affinity for gold nanoparticles than the BDD modified with oxygen or hydrogen. Preparation of nitrogen-terminated BDD was performed by a photochemistry reaction under UV light irradiation (β = 254 nm) in concentrated allylamine. Then, the N-terminated BDD was immersed in colloidal nanoparticles to provide interaction with gold nanoparticles. XPS results indicated that the double bonds in the allylamine were destroyed to form new covalent bonds between the C ions in allylamine and the C ions in BDD. Figure 6 shows the comparison among the XPS spectrum of the surface of as-deposited BDD, the BDD surface after photochemistry reaction with allylamine, and after modification with gold nanoparticles [8]. It was concluded from the spectrum that new chemical bonds between N-terminated BDD and gold nanoparticles were formed.

This method was then applied to develop a biochemical oxygen demand sensors using gold nanoparticles-modified BDD electrodes [8, 9]. Furthermore, although the specific steps are required to prepare the modified BDD, a better stability than conventional electrochemical pre-treatment can be achieved.

6 Electroanalysis Applications

Numerous applications of the modified BDD electrode have been reported for sensor and biosensors. The use of metal-modified BDD electrode is growing year by year and has been used for various applications. In this section, the modified BDD electrodes for various applications are limited into metal modifications.

6.1 Electrochemical Sensors

High and specific catalytic activity of metals are very useful to develop sensors and biosensors. The metal-deposited on BDD surface not only increase the sensitivity but also provide better limits of detection than the related bulk metal due to its lower background current. A metal particle sometimes gives a very specific performance toward one compound that could not be shown by other metals. However, a compound could also be detected by different metals, for example, Cu, Au, and Pt could be used to develop an oxygen sensor. Nevertheless, each metal will promote different

https://www.twirpx.org & http://chemistry-chemists.com

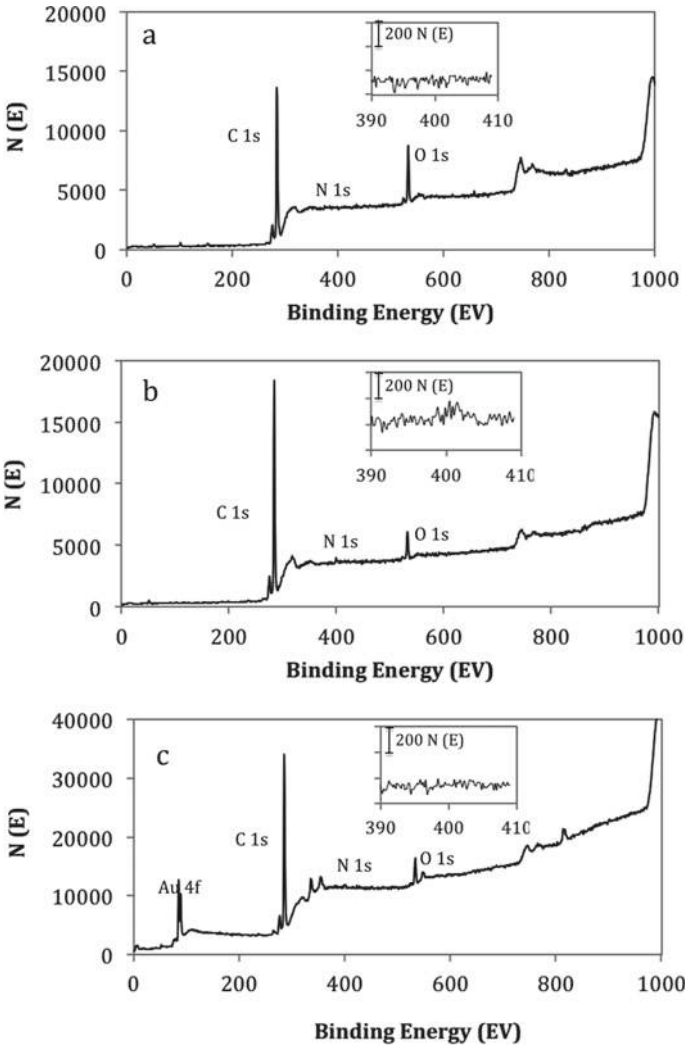

Fig. 6 XPS spectrum of **a** as deposited, **b** allylamine modified, and **c** gold-modified BDD. The insets show magnifications of the N 1 s peaks for each BDD. Reprinted with permission from [8] Copyright 2012 American Chemical Society

properties, due to the intrinsic properties mentioned above and also significance of the preparation process that could affect the particle size, surface morphology, and other behaviors. Table 3 summarizes some metal particles deposited on BDD surface for various sensor applications, such as sensor for gas, heavy metals, organic compound, and others.

https://www.twirpx.org & http://chemistry-chemists.com

Table 3 Various metal particle deposited on BDD surface for sensor applications

Metal	Sensor application/ref	Metal	Sensor applications/ref
Ag	Cholesterol [47]	Cu	Nitrate [103]
Ag	Hydrogen peroxide [80]	Cu-Au	Oxygen [104]
Ag	Carbaryl and paraquat [81]	Ir	Arsenic [40, 41]
Au	Arsine gas [77]	Ir	Hydrogen peroxide [35, 105]
Au	Neuraminidase [75, 76]	Ni	Glucose [43, 93, 106]
Au	Selenium (IV) and (VI) [14]	Ni	Methanol [107]
Au	BOD [8, 9]	Pt	Arsenite [108]
Au	Arsenic and Arsenate [96]	Pt	Neuraminidase [109]
Au	Melamine [97]	Pt	Hydrogen peroxide [65]
Au	Dopamine [98]	Pt	Oxygen [110]
Au	Proton [99]	Pt-Au	Glucose [37]
Au	17β-estradiol (aptasensor) [100]	Sb	Cd and Pb [82]
Au-Ni	Glucose [101]	Bi	Caffeine and paracetamol [83]
Au–Pd	Oxygen [102]	Cu	Glucose [111, 112]

6.1.1 Gold

Among many metals, gold is one of the metals that widely known to be employed especially for biochemical sensor and often be used as a marker detector. It has been reported that gold nanoparticles modified on interdigitated finger electrodes sensor could help to stabilize the immobilization of biomolecules; besides, it has a high surface-to-volume ratio, high surface energy, and could decrease the distance between protein and metal particles [113]. Not only for biochemical sensor, Au is employed for inorganic sensor, such as for heavy metal sensor, [14, 96] and also known to be very active for CO oxidation even at low temperature [114]. Wahyuni et al. (2015) reported the electrochemical sensor of neuraminidase (NA) through zanamivir detection as NA inhibitor [75, 76]. The detection was performed by the decrease of zanamivir redox currents at gold electrode in the presence of NA. This method was also successfully applied under the mucin interference. A comparable LODs of 0.25 mU could be achieved with and without mucin interference, showing an excellent sensor that could work under the presence of interference (Fig. 7). Similar

https://www.twirpx.org & http://chemistry-chemists.com

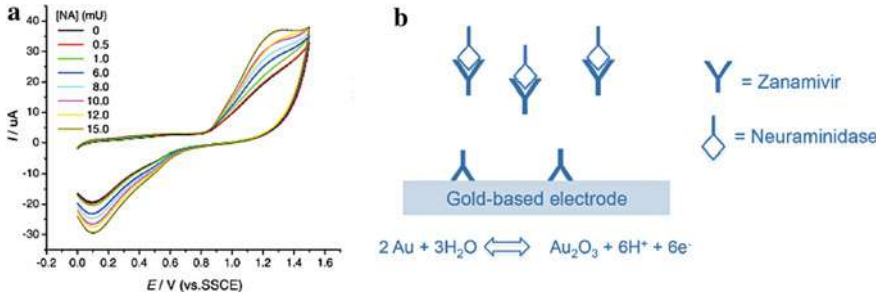

Fig. 7 **a** Cyclic voltammograms of 1.5×10^{-5} M zanamivir with different concentrations of NA in 0.1 M PBS (pH 5.5) containing 0.33 mg/mL of mucin bovine submaxillary glands type I-S M3895 and **b** The scheme of NA inhibition by zanamivir on gold-modified BDD electrode (**b**). Reprinted from [75] with the permission of Japan Electrochemical Society and from [76] copyright 2016, with the permission of Elsevier

method was also reported by using Pt-modified BDD electrode with a comparable result to the gold-modified one [109].

6.1.2 Platinum

Beside gold, platinum is also well-known sensor applications. Platinum has been deposited on BDD surface and applied for numerous applications such as sensor of hydrogen peroxide, oxygen, neuraminidase, as well as arsenite. Hutton et al. (2009) used Pt nanoparticles modified at polycrystalline BDD disk electrode to detect oxygen [110]. Excellent responses for both cyclic voltammetry and amperometric detection were reported as it is possible to detect dissolved oxygen lower than ~1 ppb under a wide range of pH solutions. Later, Rismetov et. al. (2014) reported the development of hydrogen peroxide sensor using Pt-modified BDD electrode to be applied in melamine strip tests. This sensor was developed by applying antibody of melamine as the sensing agent and horseradish peroxidase as the label of the antibody as shown in Fig. 8. A linear calibration curve ($R^2 = 0.99$) of the current responses in the melamine concentration range of 5–100 μg/ml could be achieved with LOD of 0.51 μg/ml [65].

6.1.3 Silver

Silver is also one of the popular metals used to be modified on BDD surface for sensor/biosensor applications. An example of the utilization of silver-modified BDD electrode was conducted by Nantaphol et al. (2015) to detect cholesterol with LOD of about 6.5 μM, showing a better performance compared with another metal or carbon-based material [47, 70]. Another report was the electrochemical sensor of

https://www.twirpx.org & http://chemistry-chemists.com

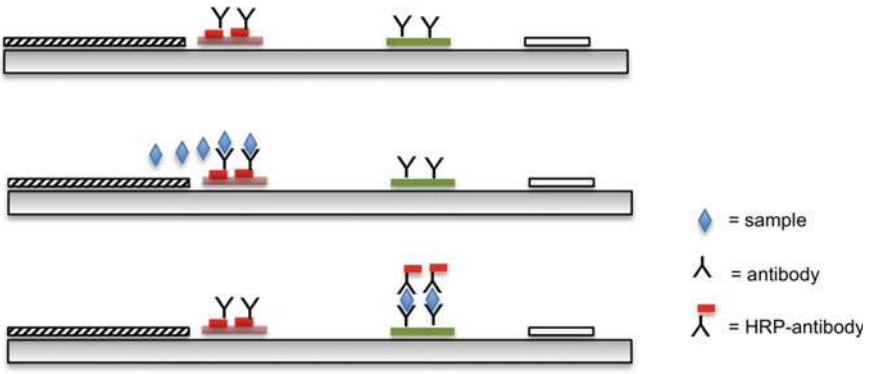

Fig. 8 Scheme of melamine strip test employing melamine antibody as the sensing agent, horseradish peroxidase as the antibody label, and Pt-BDD as the detector. Reprinted from [65] copyright 2014, with permission from Elsevier

hydrogen peroxide using silver nanoparticles modified at BDD and hemoglobin-silver nanoparticles modified BDD with LOD of 1.5 and 4.3 μM, respectively [80]. A strong synergic effect of silver particle and hemoglobin electrode was observed as silver enables the binding of hemoglobin to the electrode in an active form, leads to a significantly increase electrode response of H_2O_2. The utilization of silver along with graphene on BDD electrode was also reported for selective detection of carbaryl and paraquat from water using differential pulse voltammetry [81].

6.1.4 Copper

Copper is also known as one of metals that has a good catalytic activity in electrochemical applications. Welch et al. (2005) used copper nanoparticle that has been deposited onto BDD with in situ technique to detect nitrate, [103] while Sim et al. (2012) used $Cu(OH)_2$ nanoflower electrode covered at boron-doped nanocrystalline diamond layer to detect glucose [111]. They also reported the synergistic combination of $Cu(OH)_2$ nanoflowers and boron-doped nanocrystalline diamond provides both a significant increase to the electroactive surface area and efficiency of the direct electron transfer. Another glucose sensor developed by Mavrokefalos et al. (2015) reported the selectivity of the copper-modified BDD toward glucose in KOH [72].

6.1.5 Other Metals

Several examples of other metal-modified BDD electrodes were also reported in sensor applications. Toghill et al. in 2010 reported the determination of methanol using an electrolytically nickel microparticle-modified BDD [107]. This electrode was sensitive to methanol concentrations over a linear range for 0.5 to 500 mM,

https://www.twirpx.org & http://chemistry-chemists.com

with a limit of detection calculated as 0.28 mM and a sensitivity of 110 nA/mM of methanol. Besides, combination between nickel and gold on BDD electrode was studied by Zheng et al. in 2019 to detect glucose, resulted in good electrocatalytic performance with high sensitivity and stability [101].

Complexes compound with BDD can also be used to analyze some compounds. In 2014, Culkova et al. reported indirect voltmmetric sensing platforms for fluoride detection on BDD electrode mediated via $[FeF_6]^{3-}$ and $[CeF_6]^{2-}$ complexes formation [115]. The proposed procedure is based on the formation of electroinactive complexes $[FeF_6]^{3-}$ and $[CeF_6]^{2-}$. Meanwhile, bismuth-modified BDD has a good performance to be used in simultaneous and individual voltammetric assays of paracetamol and caffeine [83].In most cases, the obtained detection limits are lower or comparable to the ones obtained at other voltammetric sensors proposed for the simultaneous detection of paracetamol and caffeine. Other application reported by Sochr (2016) has employed the bismuth-modified BDD to determine the concentration of heavy metal cations (Zn^{2+}, Cd^{2+}, and Pb^{2+}) [116]. Later, Marton et al. also reported simultaneous determination of Zn, Cd, and Pb ions by using square wave anodic stripping voltammetry using bismuth-modified BDD [117].

Beside modification with bismuth, modification with antimony BDD also provided a good electrocatalytic activity to be used in electrochemical sensor of Cd(II) and Pb(II) [82]. An enhance of the electroanalytical ability of the BDD could be achieved by depositing a small amount of Sb as shown by a simultaneous detection of the Cd and Pb with two well-separated stripping peaks, in which it was not observed at the unmodified BDD.

In addition, noble metal such as palladium, iridium, rhodium, and ruthenium also has a good conductivity to be used in sensor application. However, cost issue and rarity are main disadvantages in using noble metal. Salimi et al. (2003) modified BDD electrodes with iridium and used it for the electrocatalytic oxidation of arsenic over a wide pH range [40]. In the same year, Terashima et al. modified BDD with iridium oxide (IrOx) and indicated that IrOx/BDD electrodes are appropriate for miniaturized sensor devices of H_2O_2 and pH sensors [105].

Combination between noble metals (bimetallics) has attracted many researchers. Luhur et al. (2018) used palladium nanoparticle to combine with gold in the form of core–shell nanoparticles to detect dissolved oxygen in water [102]. Previously, Belghiti et al. (2016) reported the detection of pesticides, including imidacloprid and paraoxon, in tap water using platinum and iridium nano-dots modified BDD, [118] while Zribi et al. (2019) reported the utilization of noble metal bimetallics such as Pt-Ir, Pt-Au, and Au-Ru in a broadly selective electrode array configuration to detect electroactive species in coffee samples [119].

7 Summary and Outlook

Modification of metal particles on the surface of BDD electrode has attracted significant attention to be employed for electroanalysis and electrocatalysis applications.

https://www.twirpx.org & http://chemistry-chemists.com

BDD electrode has been noted as an electrode which has low background current, that is, very beneficial for sensor application to suppress the signal-to-background, thus providing lower detection limit. On the other hand, BDD surface is less sensitive, in which, modifying BDD surface with metal particles will improve the catalytic, selectivity, and sensitivity of electrode.

As it is known that inert surface of BDD resulted less stability of the metal modification on BDD. Nevertheless, in most cases, avoiding the applications at extremely high potential can maintain the stability of deposited metal particles and thus maintain the analysis quality. Numerous studies have been reported to modify BDD surface with high stability, such as modification of physical or electrochemical deposition and also permanent modification by ion implantation. Among all techniques, ion implantation is the only technique that could produce a stable metal modification, despite of its high cost operation. As a result, physical or electrochemical modification is widely chosen due to its fast and simple procedure. Besides, high mechanical stability property of BDD electrode allows the repeated deposition without decreasing the performance of BDD electrode itself.

Finally, applications of various metal-modified BDD electrodes have been studied. Nonetheless, more exploration on various metal particles to be deposited on BDD surface still offers a big potential because each metal has specific properties. In addition, the unstable deposited metal particles on BDD surface remains a challenging issue. Annealing technique was proposed as one of the treatments to stabilize deposited metal particles; however, in actual practice, activation to the modified electrode is priorly required before the application. Thus, a new strategy of metal deposition technique is highly desired, with an easy and low-cost preparation.

Acknowledgements This work was partly funded by PUPT Kementerian Riset Dan Teknologi/Badan Riset Dan Inovasi Nasional Tahun Anggaran 2020. Contract No. NKB-330/UN2.RST/HKP.05.00/2020.

References

1. Pleskov YV (2002) Russ J Electrochem 38:1275–1291
2. Hupert M, Muck A, Wang J, Stotter J, Cvackova Z, Haymond S, Show Y, Swain GM (2003) Diam Relat Mater 12:1940–1949
3. Kraft A (2007) Int J Electrochem Sci 2:355–385
4. Macpherson JV (2015) Phys Chem Chem Phys 17:2935–2949
5. Xu J, Granger MC, Chen Q, Strojek JW, Lister TE, Swain GM (1997) Anal Chem 69
6. Yano T, Popa E, Tryk DA, Hashimoto K, Fujishima A (1999) J Electrochem Soc 146:1081–1087
7. Watanabe T, Honda Y, Kanda K, Einaga Y (2014) Phys Status Solidi Appl Mater Sci 211:2709–2717
8. Ivandini TA, Saepudin E, Wardah Harmesa H, Dewangga N, Einag Y (2012) Anal Chem 84:9825–9832
9. Ivandini TA, Harmesa E. Saepudin, Einaga Y (2015) Anal Sci 31:643–649
10. Su L, Qiu X, Guo L, Zhang F, Tung C (2004) Sens Actuat B Chem 99:499–504

https://www.twirpx.org & http://chemistry-chemists.com

11. Zhou Y, Zhi J (2009) Talanta 79:1189–1196
12. Mansano GR, Eisele APP, Dall'Antonia LH, Afonso S, Sartori ER (2015) J Electroanal Chem 738:188–194
13. Asai K, Ivandini TA, Falah MM, Einaga Y (2016) Electroanalysis 28:177–182
14. Ivandini TA, Einaga Y (2013) Electrocatal 4:367–374
15. Jiwanti PK, Natsui K, Nakata K, Einaga Y (2016) RSC Adv 6:102214–102217
16. Natsui K, Iwakawa H, Ikemiya N, Nakata K, Einaga Y (2018) Angew Chemie Int Ed 57:2639–2643
17. Muharam S, Jiwanti PK, Irkham, Gunlazuardi J, Einaga Y, Ivandini TA (2019) Diam Relat Mater 99:107464
18. Stolarczyk K, Nazaruk E, Rogalski J, Bilewicz R (2007) Electrochem commun 9:115–118
19. Cañizares P, Larrondo F, Lobato J, Rodrigo MA, Sáez C (2005) J Electrochem Soc 152:191–196
20. Shibano S, Ivandini TA, Terashima C, Nakata N, Einaga Y (2014) Chem Lett 43:1292–1293
21. Waldvogel SR, Lips S (2019) ChemElectroChem 6:1649–1660
22. Honda Y, Ivandini TA, Watanabe T, Murata K, Einaga Y (2013) Diam Relat Mater 40:7–11
23. Ullah M, Rana AM, Ahmed E, Raza R, Shah ZA, Ahmad EM (2017) J Ovonic Res 13:187–194
24. Yamamoto T, Riehl B, Naba K, Nakahara K, Wiebe A, Saitoh T, Waldvogel SR, Einaga Y (2018) Chem Commun 54:2771–2773
25. Eguiluz KIB, Peralta-Hernández JM, Hernández-Ramírez A, Guzmán-Mar JL, Hinojosa-Reyes L, Martínez-Huitle CA, Salazar-Banda GR (2012) Int J Electrochem 1–20
26. Baluchová S, Daňhel A, Dejmková H, Ostatná V, Fojta M, Schwarzová-Pecková K (2019) Anal Chim Acta 1077:30–66
27. Luong JHT, Male KB, Glennon JD (2009) Analyst 134:1965–1979
28. Cobb SJ, Ayres ZJ, Macpherson JV (2018) Annu Rev Anal Chem 11:463–484
29. Alfaro MAQ, Ferro S, Martínez-Huitle CA, Vong YM (2006) J Braz Chem Soc 17:227–236
30. Möhle S, Zirbes M, Rodrigo E, Gieshoff T, Wiebe A, Waldvogel SR (2018) Angew Chemie Int Ed 57:6018–6041
31. Waldvogel SR, Elsler B (2012) Electrochim Acta 82:434–443
32. Yuliarto B, Zulhendry DW, Septiani NLW, Irzaman Ferdiansjah, Fahmi Nugraha MZ (2019) Mater Sci Forum 947 MSF:35–39
33. Darmokoesoemo H, Habibulah MR, Harsini M, Kusuma HS (2016) J Mater Environ Sci 7:2731–2738
34. Kusuma HS, Sholihuddin RI, Harsini M, Darmokoesoemo H (2016) J Mater Environ Sci 7:1454–1460
35. Ivandini TA, Sato R, Makide Y, Fujishima A, Einaga Y (2004) Chem Lett 33:1330–1331
36. Uchikado R, Rao TN, Tryk DA, Fujishima A (2001) Chem Lett 2:144–145
37. Nantaphol S, Chailapakul O, Siangproh W (2015) Anal Chim Acta 891:136–143
38. Meier J, Hofferber E, Stapelton JA, Iverson NM (2019) Chemosensors 7:64
39. Yoo E-H, Lee S-Y (2010) Sensors 10:4558–4576
40. Salimi A, Hyde ME, Banks CE, Compton RG (2004) Analyst 29:9
41. Ivandini TA, Sato R, Makide Y, Fujishima A, Einaga Y (2006) Anal Chem 78:6291–6298
42. Gong Z, Hu N, Ye W, Zheng K, Li C, Ma L, Wei Q, Yu Z, Zhou K, Huang N, Lin C-T, Luo J (2019) J Electroanal Chem 841:135–141
43. Toghill KE, Xiao L, Phillips MA, Compton RG (2010) Sens Actuat B Chem 147:642–652
44. Yagi I, Ishida T, Uosaki K (2004) Electrochem Commun 6:773–779
45. Tian RH, Rao TN, Einaga Y, Zhi JF (2006) Chem Mater 18:939–945
46. Mattos-Costa FI, De Lima-Neto P, Machado SAS, Avaca LA (1998) Electrochim Acta 44
47. Salazar-Banda GR, Suffredini HB, Avaca LA (2005) J Braz Chem Soc 16:903–906
48. Suffredini HB, Salazar-banda GR, Tanimoto ST, Calegaro ML, Machado SAS, Avaca LA (2006) J Braz Chem Soc 17:257–264
49. Salazar-Banda GR, Suffredini HB, Calegaro ML, Tanimoto ST, Avaca LA (2006) J Power Sourc 162:9–20
50. Toghill KE, Compton RG (2010) Electroanalysis 22:1947–1956

https://www.twirpx.org & http://chemistry-chemists.com

51. Jiwanti PK, Aritonang R, Abdullah I, Einaga Y, Ivandini TA (2019) Makara J Sci 23:5
52. Sugitani A, Watanabe T, Ivandini TA, Iguchi T, Einaga Y (2013) Phys Chem Chem Phys 15:142–147
53. Ivandini TA, Watanabe T, Matsui T, Ootani Y, Iizuka S, Toyoshima R, Kodama H, Kondoh H, Tateyama Y, Einaga Y (2018) J Phys Chem C 123:5336–5344
54. Ivandini TA, Rao TN, Fujishima A, Einaga Y (2006) Anal Chem 78:3467–3471
55. Martin HB, Argoitia A, Landau U, Anderson AB, Angus JC (1996) J Electrochem Soc 143:L133-136
56. Notsu H, Yagi I, Tatsuma T, Tryk DA, Fujishima A (1999) Electrochem Solid-State Lett 2:522
57. Yagi I, Notsu H, Kondo T, Tryk DA, Fujishima A (1999) J Electroanal Chem 472:173
58. Hayashi K, Yamanaka S, Watanabe H, Sekiguchi T, Okushi H, Kajimura K (1997) J Appl Phys 81:744
59. Popa E, Notsu H, Miwa T, Tryk DA, Fujishima A (1999) Electrochem Solid State Lett 2:49–51
60. Popa E, Kubota Y, Tryk DA, Fujishima A (2002) Anal Chem 72:1724
61. Terashima C, Rao TN, Sarada BV, Tryk DA (2002) A Fujishima. Anal Chem 74:895
62. Lee J, Park S-M (2005) Anal Chim Acta 545:27
63. Granger MC, Swain GM (1999) J Electrochem Soc 146:4551
64. Vanhove E, de Sanoit J, Arnault J-C (2007) Phys Stat Solidi (A) Appl Mater Sci 204:2931−2939
65. Rismetov B, Ivandini TA, Saepudin E, Einaga Y (2014) Diam Relat Mater 48:88–95
66. Shpilevaya I, Smirnov W, Hirsz S, Yang N, Nebel CE, Foord JS (2014) RSC Adv 4:531–537
67. Gao F, Yang N, Nebel CE (2013) Electrochim Acta 112:493–499
68. Wulandari R, Ivandini, Irkham TA, Saepudin E, Einaga Y (2019) Sensors Mater 31:1105–1117
69. Agustiany T, Khalil M, Einaga Y, Jiwanti PK, Ivandini TA (2020) Mat Chem Phys 244:122723
70. Nantaphol S, Watanabe T, Nomura N, Siangproh W, Chailapakul O, Einaga Y (2017) Biosens Bioelectron 98:76–82
71. Mavrokefalos CK, Hasan M, Khunsin W, Schmidt M, Maier SA, Rohan JF, Compton RG, Foord JS (2017) Electrochim Acta 243:310–319
72. Mavrokefalos CK, Nelson GW, Poll CG, Compton RG, Foord JS (2015) Phys Status Solidi Appl Mater Sci 212:2559–2567
73. Mavrokefalos CK, Hasan M, Rohan JF, Foor JS (2017) ChemElectroChem 5:455−463
74. Chen L, Hu J, Foord JS (2017) Phys Status Solidi Appl Mater Sci 209:601–1820
75. Wahyuni WT, Ivandini TA, Jiwanti PK, Endang S, Gunlazuardi J, Einaga Y (2015) Electrochemistry 83:357–362
76. Wahyuni WT, Ivandini TA, Saepudin E, Einaga Y (2016) Anal Biochem 497:68–75
77. Ivandini TA, Yamada D, Watanabe T, Matsuura H, Nakano N, Fujishima A, Einaga Y (2010) J Electroanal Chem 645:58–63
78. Ivandini TA, Einaga Y (2013) Electrocatalysis 4:367–374
79. Stradiotto NR, Toghill KE, Xiao L, Moshar A, Compton RG (2009) Electroanalysis 21:2627–2633
80. Jiang L, Hu J, Foord JS (2015) Electrochim Acta 176:488–496
81. Pop A, Lung S, Orha C, Manea F (2018) Int J Electrochem Sci 13:2651–2660
82. Toghill KE, Xiao L, Wildgoose GG, Compton RG (2009) Electroanalysis 21:1113–1118
83. Sadok I, Tyszczuk-Rotko K, Nosal-Wiercińska A (2016) Sensors Actuators B Chem 235:263–272
84. Gardner PR (1987) Mater Des 8:210–219
85. Takeuchi Y, Makita Y, Mori M, Ohnishi N, Shibata H, Matsumori T (1989) Mater Res Soc 144:483–488
86. Mazzoldi P, Arnold GW, Battaglin G, Bertoncello R, Gonella F (1994) Nucl Inst Methods Phys Res B 91:478–492
87. Yamashita H, Honda M, Harada M, Ichihashi Y, Anpo M, Hirao T, Itoh N, Iwamoto N (1998) J Phys Chem B 102:10707–10711
88. Sealy BJ (1988) Int Mater Rev 33:38–52
89. Magruder RH, Haglund RF, Yang L, Wittig JE, Zuhr RA (1994) J Appl Phys 76:708–715

https://www.twirpx.org & http://chemistry-chemists.com

90. Teranishi N, Fuse G, Sugitani M (2018) Sensors (Switzerland) 18. https://doi.org/10.3390/s18072358
91. Picraux ST (1984) Annu Rev Mater Sci 14:335–372
92. Sugitani M (2014) Rev Sci Instrum 85:1–4
93. Ohnishi K, Einaga Y, Notsu H, Terashima C, Rao TN, Park SG, Fujishima A (2002) Electrochem Solid-State Lett 5:13–15
94. Ivandini TA, Sato R, Makide Y, Fujishima A, Einaga Y (2004) Diam Relat Mater 13:2003–2008
95. Treetepvijit S, Chuanuwatanakul S, Einaga Y, Sato R, Chailapakul O (2005) Anal Sci 21:531–535
96. Treetepvijit S, Preechaworapun A, Praphairaksit N, Chuanuwatanakul S, Einaga Y, Chailapakul O (2006) Talanta 68:1329–1335
97. Jiao J, Wang J, Chen Q, Hu J (2011) J Electrochem Soc 158:230–235
98. Kalish R, Reznik A, Nugent KW, Prawer S (1999) Nucl Inst Methods Phys Res B 148:626
99. Yamada D, Ivandini TA, Komatsu M, Fujishima A, Einaga Y (2008) J Electroanal Chem 615:145–153
100. Ivandini TA, Wicaksono WP, Saepudin E, Rismetov B, Einaga Y (2015) Talanta 134:136–143
101. Weng J, Xue J, Wang J, Ye JS, Cui H, Sheu FS, Zhang Q (2005) Adv Funct Mater 15:639–647
102. Song MJ, Lee SK, Lee JY, Kim JH, Lim DS (2012) J Electroanal Chem 677–680:139–144
103. Ke H, Liu M, Zhuang L, Li Z, Fan L, Zhao G (2014) Electrochim Acta 137:146–153
104. Zheng K, Longn H, Wei Q, Ma L, Qiao L, Li C, Meng L, Lin C-T, Jiang Y, Zhao T et al (2019) J Electrochem Soc 166:B373–B380
105. Luhur MSP, Ivandini TA, Khalil M (2018) AIP Conf Proc 2023. https://doi.org/10.1063/1.5064089
106. Welch CM, Hyde ME, Banks CE, Compton RG (2005) Anal Sci 21:1421–1430
107. Kurniawan AD, Saepudin E, Ivandini TA (2019) IOP Conf Ser Mater Sci Eng 496. https://doi.org/10.1088/1757-899X/496/1/012063
108. Terashima C, Rao TN, Sarada BV, Spataru N, Fujishima A (2003) J Electroanal Chem 544:65–74
109. Deng Z, Long H, Wei Q, Yu Z, Zhou B, Wang Y, Zhang L, Li S, Ma L, Xie Y et al (2017) Sensors Actuators B Chem 242:825–834
110. Toghill KE, Xiao L, Stradiotto NR, Compton RG (2010) Electroanalysis 22:491–500
111. Hrapovic S, Liu Y, Luong JHT (2007) Anal Chem 79:500–507
112. Ivandini TA, Ariani J, Jiwanti PK, Gunlazuardi J, Saepudin E, Einaga Y (2017) Makara J Sci 21:34–42
113. Hutton L, Newton ME, Unwin PR, Macpherson JV (2009) Anal Chem 81:1023–1032
114. Sim H, Kim JH, Lee SK, Song MJ, Yoon DH, Lim DS, Hong SI (2012) Thin Solid Films 520:7219–7223
115. Chiku M, Watanabe T, Einaga Y (2010) Diam Relat Mater 19:673–679
116. Altintas Z, Kallempudi SS, Gurbuz Y (2014) Talanta 118:270–276
117. Haruta M, Ueda A, Tsubota S, Torres Sanchez RM (1996) Catal Today 29:443–447
118. Culková E, Tomčík P, Švorc Ľ, Cinková K, Chomisteková Z, Durdiak J, Rievaj M, Bustin D (2014) Electrochim Acta 148:317–324
119. Sochr J, Machková M, Machyňák Ľ, Čacho F, Švorc Ľ (2016) Acta Chim Slovaca 9:28–35
120. Marton M, Michniak P, Behul M, Rehacek V, Vojs Stanova A, Redhammer R, Vojs M (2019) Vacuum 167:182–188
121. Belghiti DK, Zadeh-Habchi M, Scorsone E, Bergonzo P (2016) Procedia Eng 168:428–431
122. Zribi B, Dragoe D, Scorsone E (2019) Sensors Actuators B Chem 290:147–154

https://www.twirpx.org & http://chemistry-chemists.com

In Vivo Real-Time Measurement of Drugs

Genki Ogata, Seishiro Sawamura, Kai Asai, Hiroyuki Kusuhara, Yasuaki Einaga, and Hiroshi Hibino

Abstract Drugs play a key role in the treatment of patients with various diseases. A compound, when administered systemically, shows differential spatial and temporal distribution patterns not only in the body but also within each organ. In response to an increase or decrease in local concentrations in the organ, the activity of the cell population expressing the drug's target protein(s) changes over time. Therefore, real time, simultaneous detection of kinetics of the drug and its pharmacological effects in in vivo microenvironments is essential for evaluating the efficacy of medicines. Although such challenging dual-mode measurement has not yet been addressed by any conventional methods, it has been successfully achieved via a microsensing system that we recently developed. The system consists of two different sensors: a needle-type boron-doped diamond microelectrode for monitoring the drug and a glass microelectrode for tracking electrophysiological activity of the target cells. This state-of-the-art approach is applicable to various drugs in terms of "local" pharmacokinetic and pharmacodynamic assays in vivo and may contribute to the development of next-generation therapeutic interventions.

Keywords Pharmacokinetics · Pharmacodynamics · Needle-type boron-doped diamond microelectrode · Pharmacotherapy · Real-time measurement

G. Ogata · K. Asai · Y. Einaga
Department of Chemistry, Keio University, 3-14-1 Hiyoshi, Yokohama, Kanagawa 223-8522, Japan

S. Sawamura · H. Hibino (✉)
Division of Glocal Pharmacology, Department of Pharmacology, Graduate School of Medicine, Osaka University, 2-2 Yamadaoka, Suita, Osaka 565-0871, Japan
e-mail: hibino@pharma2.med.osaka-u.ac.jp

H. Kusuhara
Laboratory of Molecular Pharmacokinetics, Graduate School of Pharmaceutical Sciences, University of Tokyo, 7-3-1 Hongo, Bunkyo, Tokyo, Japan 113-0033

© Springer Nature Singapore Pte Ltd. 2022

Y. Einaga (ed.), *Diamond Electrodes*,
https://doi.org/10.1007/978-981-16-7834-9_14

https://www.twirpx.org & http://chemistry-chemists.com

1 Introduction

In humans, drugs that are administered via an oral, intravenous, intraperitoneal, intramuscular, or subcutaneous route enter the systemic circulation and are distributed to the majority of organs. An organ is made up of different cell population types, each of which can play distinct physiological roles. Most diseases are likely to be triggered by a disorder or pathological perturbation of a cell population that is small: sometimes less than 1 mm. Accordingly, it is crucial for pharmacological studies to analyze whether a drug reaches the target cell population in an organ and how the compound behaves in such a microenvironment over time [8, 18]. The other key issue is tracking the change in the target cell function. Such dual-mode measurement of "pharmacokinetics" and "pharmacodynamics" is necessary for further elucidation of the mechanisms underlying beneficial, adverse, and toxic effects of drugs. Addressing this challenging issue, in vivo requires a microsensing system that can measure multiple parameters for the drug in real time.

Representative methods currently available for determination of drug concentrations in vitro and/or in vivo are as follows: (1) high-performance liquid chromatography (HPLC), (2) liquid chromatography coupled with tandem mass spectrometry (LC–MS/MS), (3) positron emission tomography (PET), and (4) optical imaging techniques. LC–MS/MS and HPLC require collection of samples from body fluids, organs, or tissues, and therefore, they have relatively low temporal resolution for in vivo assays (Table 1). A combination of microdialysis with the abovementioned separation analytical methods should allow to continuously obtain the samples from environments of the target cell population, but the sampling period is usually limited to a few minutes [4]. Not only this issue but also relatively low spatial resolution seems to be the case for PET, which requires labeling of compounds with a positron-emitting isotope (Table 1) [6, 16]. Optical methods based on bioluminescence or fluorescence probes are capable of detecting compounds within an interval of a few seconds at a minimum, nevertheless, the spatial resolution is limited to several millimeters (Table 1) [6, 16]. Moreover, it is a hurdle to combine most of these conventional methodologies to biosensors engaged in longitudinal recording of the functionality of target cells.

Table 1 Comparison of conventional methods for analysis of pharmacokinetics

Measurement device	Time resolution	Spatial resolution	Quantitativity
LC-MS/MS • HPLC	>5 minutes	–	Quantitative
Microdialysis[a]	2–5 minutes	2–5 mm	Quantitative
PET	1–30 minutes	1–2 mm	Quantitative
Optical imaging	10 s to 1 minute	2–5 mm	Semiquantitative
BDD	~5 s	~500 μm	Semiquantitative[b]

[a]A method for collecting biological samples; the samples are analyzed by LC-MS/MS or HPLC. [b]Confirmed by LC-MS/MS. References: Massoud and Gambhir 2003; Dufort et al. 2010; Ogata et al. 2017

https://www.twirpx.org & http://chemistry-chemists.com

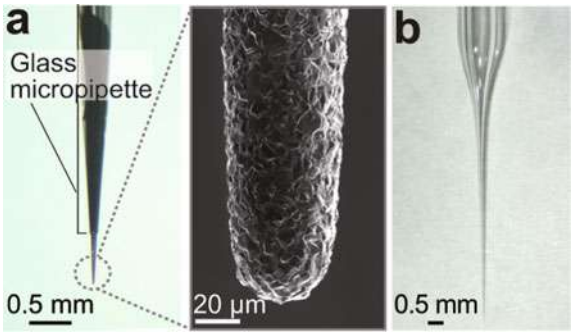

Fig. 1 A needle-type diamond microelectrode and a glass microelectrode. **a**. A needle-type boron-doped diamond (BDD) microelectrode. As shown in left panel, the BDD needle that was ~40 μm in diameter was encased with a prepulled glass capillary tube, such that the needle projected from the capillary tip. The tip of the BDD microelectrode is magnified by means of a scanning electron microscope and is displayed in the right-hand panel. **b.** A glass microelectrode. Adapted with permission from Springer Nature: Nature Biomedical Engineering [17], Copyright 2017

On the basis of this background, we recently described a drug-monitoring system [17] that involves two different sensors. One is a needle-type conductive boron-doped diamond (BDD) microelectrode with a tip diameter of 40 μm (Fig. 1a) [20], which can electrochemically detect drugs and their concentrations. In addition to a wide potential window for water stability, i.e., a property that may enable such assays for a number of drugs, the high speed of the response and longitudinal stability of the reaction are advantages of BDD microelectrodes for in vivo pharmacological studies [7, 10]. The other sensor is a classic glass microelectrode with a tip of a 1 μm diameter (Fig. 1b), which measures electrical activity: a key factor underlying cellular function. This advanced microsensing system can monitor local pharmacokinetics and pharmacodynamics of different drugs in live animals.

2 In Vivo Measurement of a Loop Diuretic in the Cochlea of the Inner Ear

In our previous study [17], we initially selected a loop diuretic, bumetanide, as a model drug for the microsensing system that we developed. This compound is used for a broad array of health problems including hypertension, edema, premenstrual syndrome, and disseminated cancer but causes hearing loss [13]. Dysfunction of the cochlea in the inner ear is at the root of this adverse effect, therefore, this organ in a guinea pig was examined by our analytical system.

Before the animal experiments, the electrochemical properties of bumetanide were evaluated in vitro with cyclic voltammetry by means of a needle-type BDD microelectrode. As compared to the effect of phosphate-buffered saline (PBS) without any chemical compound, in PBS containing bumetanide at 50 μM, an obvious anodic

https://www.twirpx.org & http://chemistry-chemists.com

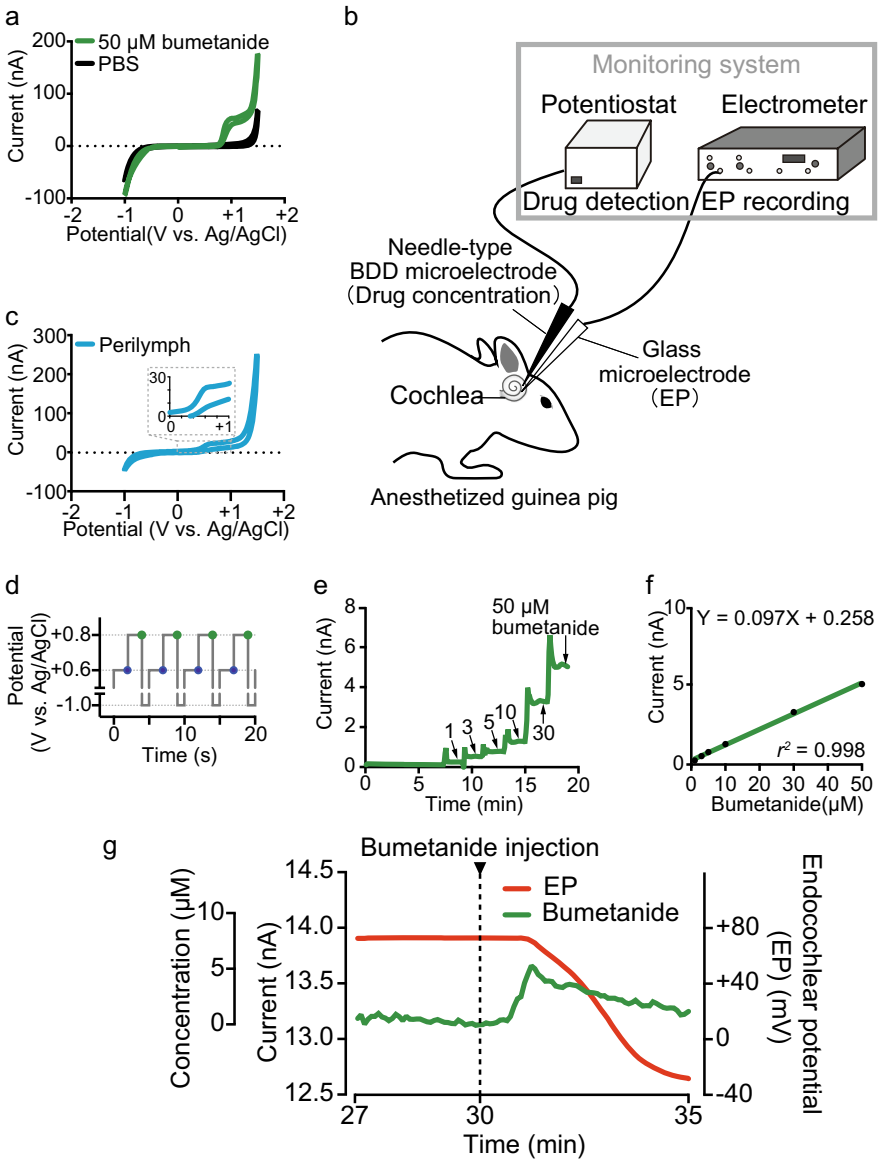

current was detected that began at 0.7 V (versus Ag/AgCl) and plateaued at 0.95 V (Fig. 2a).

The cochlea, which is the auditory peripheral organ that has snail-like structure and transduces mechanical energy of sounds into an electrical signal, is very small (approximately 3 mm in diameter), and the internal tissues and cells are encased

https://www.twirpx.org & http://chemistry-chemists.com

◀**Fig. 2** In vitro and in vivo detection of bumetanide. **a** An in vitro cyclic voltammogram of 50 μM bumetanide was dissolved in phosphate-buffered saline (PBS). The evoked current is shown in green. The black curve reflects the data on PBS alone. The voltage potential protocol was as follows: sweep rate, 100 mV s^{-1}; potential window, −1.0 to 1.5 V (versus Ag/AgCl); and initial potential, 0 V. **b** A schematic diagram of the in vivo experimental setup involving the cochlea of an anesthetized guinea pig. The tips of the needle-type BDD microelectrode and glass microelectrode were placed at close proximity. **c** A cyclic voltammogram of native perilymph of the cochlea (light blue curve). Scans were started from 0 V in the positive scan direction. The voltage potential was the same as that in **a**. **d.** The potential step protocol for in vivo measurement [0.6 V for 2 s, 0.8 V for 2 s, and −1.0 V for 1 s (versus Ag/AgCl)]. Bumetanide was analyzed in each potentials' combination through a difference in the current between 0.6 V (blue points) and a green point (0.8 V; "subtraction current;" see the text for details). **e** and **f**. Calibration of a needle-type BDD microelectrode. In **e**, bumetanide at 1–50 μM in PBS was assayed sequentially, whereas the potential step protocol presented in **d** was applied to the electrode continuously. The measured subtraction currents are shown in the panel. These data were employed to construct the calibration curve in **f**; the slope and coefficient of determination (r^2) of the regression line are indicated. **g.** In vivo measurement of the bumetanide response in the cochlea. Bumetanide at 30 mg kg^{-1} of body weight was injected intravenously at the time point indicated by the arrowhead. Displayed in the panel is the subtraction current detected by the BDD microelectrode in perilymph (green, sampling frequency: 5 Hz) and the endocochlear potential (EP) measured with the glass microelectrode (red, sampling frequency: 1 kHz). The concentration scale on the vertical axis is based on the calibration curve (**f**). Adapted with permission from Springer Nature: Nature Biomedical Engineering [17], Copyright 2017

by a bony wall. This organ has multiple chambers; one of them is filled with a unique extracellular fluid called "endolymph," which is always at +80 mV relative to perilymph, i.e., a regular extracellular fluid in different chambers [2, 3, 12]. The highly positive potential in endolymph is referred to as endocochlear potential (EP) and is crucial for high sensitivity of sensory hair cells. A reduction of the EP by a pharmacological or pathological perturbation results in hearing impairment. The microsensing system harbors a potentiostat for the needle-type BDD electrode and an electrometer for the glass electrode; the signals in these two modes are simultaneously monitored on a computer in real time (Fig. 2b). In the in vivo experiment, a live guinea pig was anesthetized, and both the needle-type diamond sensor and glass microelectrode were inserted into perilymph and endolymph, respectively, through a small hole made on the cochlear bony wall (Fig. 2b).

Next, native perilymph in the cochlea was examined in vivo by cyclic voltammetry using the BDD microelectrode. This experiment showed a considerable anodic current evoked at potentials from 0.3 to 1.5 V (versus Ag/AgCl; Fig. 2c). This background current may be caused by endogenous proteins and other factors in cochlear perilymph [19, 21], these factors can reduce the accuracy of drug measurements. Careful observation revealed that the anodic current was relatively stable at potentials between 0.6 and 0.8 V (versus Ag/AgCl; see the *inset* in Fig. 2c). On the basis of these observations, for in vivo measurements of bumetanide concentration, we designed a chronoamperometry protocol that clamped a potential at 0.6 V for 2 s, stepped to 0.8 V for 2 s, and then stepped to −1.0 V (versus Ag/AgCl) to remove any polymeric film that might form on the surface of the electrode (Fig. 2d). With this protocol, the difference in the currents evoked between 0.6 and 0.8 V (versus

https://www.twirpx.org & http://chemistry-chemists.com

Ag/AgCl), which is referred to as a "subtraction current," was subjected to extraction of bumetanide signals [17]. The subtraction currents were measured in vitro in PBS containing bumetanide at varying concentrations (Fig. 2e), and the results served as a calibration curve for in vivo experiments (Fig. 2f).

Under the arrangements mentioned above, the bumetanide concentration and the EP in the cochlea of the anesthetized live guinea pig were simultaneously measured by the needle-type BDD microelectrode and the glass microelectrode, respectively (Fig. 2g). Under control conditions, the EP was approximately + 70 mV: a hallmark of normal hearing. The bumetanide concentration began to increase 45 s after intravenous injection of the drug and then reached a peak of 5.3 μM in 30 s. The EP manifested completely different behavior. This potential started to decrease when the bumetanide concentration reached its maximum. Thereafter, the EP gradually changed and finally reached a negative value that mirrors the induction of severe hearing loss. These results indicate that the behavior of bumetanide was clearly different from the kinetics of the cochlear function.

In different guinea pigs, aliquots of perilymph were collected from the cochleae immediately after the in vivo measurements, and then, the samples' bumetanide concentrations were quantified by LC–MS/MS [17]. The results were in good agreement with the concentrations estimated by means of needle-type BDD microelectrodes. The limit of detection of these sensors was 0.4 μM, which falls into the range of clinically relevant concentrations, 0.5–4.0 μM [5, 9, 15].

3 In Vivo Measurement of an Antiepileptic in the Brain

We next applied our microsensing system to a different drug type, an antiepileptic [17]. Epilepsy, which is characterized by seizures, convulsions, and/or unconsciousness, is caused by hyperactivity of neurons in the brain. As the test drug, we chose lamotrigine, which blocks Na^+ channels. When this agent is administered to animals, neuronal activity in the brain is suppressed [14, 22].

During in vitro cyclic voltammetry with lamotrigine (10 μM) dissolved in PBS, the needle-type BDD microelectrode detected a significant cathodic current evoked at negative potentials of − 0.4 to − 1.0 V (versus Ag/AgCl; Fig. 3a). In accordance with this observation, we designed a chronoamperometry protocol that clamped a potential at 1.4 V for 1 s, stepped to − 0.6 V for 2 s, and then stepped to − 1 V (versus Ag/AgCl) for 1 s (Fig. 3b) [11, 17]. In this protocol, the current evoked at − 0.6 V was extracted for determination of lamotrigine concentrations. Then, lamotrigine at varying concentrations in PBS was analyzed via the BDD microelectrode (Fig. 3c), and the measurement results were used to obtain a calibration curve subjected to in vivo assays (Fig. 3d).

In an anesthetized rat, the needle-type BDD microelectrode for detection of lamotrigine and the glass microelectrode for the tracking of local field potentials that mirror neuronal activity was placed close to each other on the surface of the brain (Fig. 3e). After the drug was administered intravenously at 10 mg kg^{-1} of body weight, its

https://www.twirpx.org & http://chemistry-chemists.com

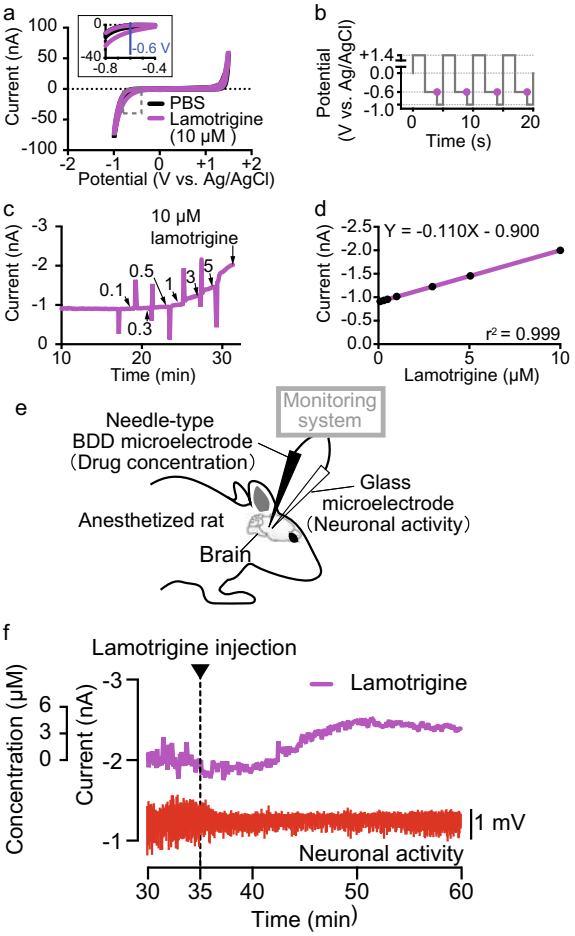

Fig. 3 In vitro and in vivo assays of lamotrigine. **a** The cyclic voltammogram of phosphate-buffered saline (PBS) either containing (magenta) or devoid of (black) lamotrigine (10 μM). The potential was provided from 0 toward 1.5 V and then was shifted to −1 V (versus Ag/AgCl) at a sweep rate of 100 mV s^{-1}. **b** The potential step protocol for lamotrigine detection in vivo. A potential step (1.4 V for 2 s, −0.6 V for 2 s, and −1.0 V for 1 s) was repeated multiple times for actual measurements. Lamotrigine was assayed via the current at the endpoints of −0.6 V steps. **c** and **d**. Calibration of lamotrigine with a needle-type BDD microelectrode in vitro. In **c**, the drug dissolved at 0.1–10 μM in PBS was sequentially analyzed with the microelectrode. The steady-state current for each lamotrigine concentration was analyzed in **d** to determine a current–concentration relation. In the panel, the slope and coefficient of determination (r^2) of the regression line are indicated. **e**. A schematic diagram of the in vivo experimental setup. Both the needle-type BDD microelectrode and glass microelectrode were inserted into the brain of an anesthetized rat. **f**. In vivo measurement of lamotrigine. The current at the endpoints of − 0.6 V (magenta) and local field potentials that represent neuronal activity (red) were simultaneously and continuously monitored by our microsensing system. Lamotrigine at 10 mg kg^{-1} was injected into the lateral tail vein at the time point indicated by the arrowhead. The concentration was estimated from the calibration curve (**d**). Adapted with permission from Springer Nature: Nature Biomedical Engineering [17], Copyright 2017

https://www.twirpx.org & http://chemistry-chemists.com

concentration gradually increased and reached a peak at 15 min (maximum concentration: 4.7 μM; Fig. 3f). These kinetics were slower than the behavior of bumetanide in the cochlea (see Fig. 2g). The amplitude of the local field potentials significantly diminished as soon as the lamotrigine concentration began to rise (Fig. 3f). This suppressive effect continued for some time.

4 Generality, Limitations, and Prospects of the Proposed Microsensing System

The microsensing system described here is effective at simultaneous tracking of the anticancer drug doxorubicin and the EP in the guinea pig cochlea (Table 2) [17]. Moreover, the results of in vitro experiments with BDD plate electrodes suggest that several types of antibiotics and antidepressants can be analyzed in vivo by this system (Table 2) [17]. As for limitations, the BDD electrodes do not respond to at least several agents such as acetazolamide, a phenobarbital sodium salt, a valproic acid sodium salt, and ouabain at pH 7.4 [17]. In general, an electrochemical method detects compounds with the help of redox currents evoked at particular potentials. This approach limits the selectivity of BDD microelectrodes. For example, if a drug and its metabolite(s) react at similar potentials, then separation of individual fractions may be difficult. This shortcoming can be overcome by modification of the surface of the diamond microelectrode. Indeed, a DNA aptamer that was designed to capture a specific compound type was immobilized on the BDD electrode surface, and this sensor could specifically detect an anticancer drug [1].

In conclusion, the "pharmacokinetics" and "pharmacodynamics" of drugs at local sites of the cochlea and brain are simultaneously and longitudinally measured at high temporal resolution by our in vivo microsensing system. It should be emphasized that the measurement of bumetanide concentration in the cochlea is semiquantitative. These issues have not been addressed by conventional approaches. It seems that the system can also be applied to organs other than the cochlea and brain. Further, improvement and application of the system may contribute to the development of drugs and therapeutic regimens that maximize the therapeutic index, to the design of strategies for drug repositioning, and to advances in personalized medicine.

https://www.twirpx.org & http://chemistry-chemists.com

Table 2 Examples of drugs detectable by the BDD plate electrode

Drug class	Chemical name	Concentration (μM)	Potential for reaction onset (V, vs Ag/AgCl)	Potential at peak current (V, vs Ag/AgCl)	Δ peak current[#] (μA)
Anticancer drug	Doxorubicin[a]	10	−0.30	−0.51	−55.91
Antidepressant	Nortriptyline	50	−0.30	−0.8	−6.24
			0.90	1.24	15.57
Antibiotics	Gentamicin	50	0.77	0.99	10.53
	Ceftriaxone	50	−0.48	−0.67	−5.50
			0.50, 0.99	0.92, 1.07	6.97, 13.24
	Teicoplanin	50	−0.55	−0.79	−5.00
			0.62	0.82	4.70

All the data were obtained by cyclic voltammetry [sweep rate, 100 mV s^{-1}; potential window, −1.0 to 1.5 V; and initial potential, 0 V (versus Ag/AgCl)]. [a]Doxorubicin was detected *in vivo* (Ogata et al. 2017.). The other drugs were confirmed by *in vitro* measurements. [#]A PBS-evoked background current was subtracted

References

1. Asai K, Yamamoto T, Nagashima S et al (2019) An electrochemical aptamer-based sensor prepared by utilizing the strong interaction between a DNA aptamer and diamond. Analyst 145:544–549. https://doi.org/10.1039/c9an01976f
2. Békésy GV (1952) DC resting potentials inside the cochlear partition. J Acoust Soc Am 24:72–76. https://doi.org/10.1121/1.1906851
3. Békésy GV (1952) Resting potentials inside the cochlear partition of the guinea pig. Nature 169:241–242. https://doi.org/10.1038/169241a0
4. Chaurasia CS, Müller M, Bashaw ED et al (2007) AAPS-FDA workshop white paper: microdialysis principles, application, and regulatory perspectives. J Clin Pharmacol 47:589–603. https://doi.org/10.1177/0091270006299091
5. Davies DL, Lant AF, Millard NR et al (1974) Renal action, therapeutic use, and pharmacokinetics of the diuretic bumetanide. Clin Pharmacol Ther 15:141–155. https://doi.org/10.1002/cpt1974152141
6. Dufort S, Sancey L, Wenk C et al (2010) Optical small animal imaging in the drug discovery process. Biochimica Et Biophysica Acta Bba—Biomembr 1798:2266–2273. https://doi.org/10.1016/j.bbamem.2010.03.016
7. Einaga Y, Kim G-S, Park S-G, Fujishima A (2001) A study of the crystalline growth of highly boron-doped CVD diamond: preparation of graded-morphology diamond thin films. Diam Relat Mater 10:306–311. https://doi.org/10.1016/s0925-9635(01)00375-2
8. Ferguson BS, Hoggarth DA, Maliniak D et al (2013) Real-Time, Aptamer-Based Tracking of Circulating Therapeutic Agents in Living Animals. Sci Transl Med 5:213ra165–213ra165. https://doi.org/10.1126/scitranslmed.3007095
9. Frelin C, Chassande O, Lazdunski M (1986) Biochemical characterization of the Na+/K+/Cl− co-transport in chick cardiac cells. Biochem Bioph Res Co 134:326–331. https://doi.org/10.1016/0006-291x(86)90566-8
10. Fujishima A, Einaga Y, Rao TN, Tryk DA (eds) (2005) Diamond electrochemistry, 1st edn. Elsevier Science

https://www.twirpx.org & http://chemistry-chemists.com

11. Hanawa A, Asai K, Ogata G et al (2018) Electrochemical measurement of lamotrigine using boron-doped diamond electrodes. Electrochim Acta 271:35–40. https://doi.org/10.1016/j.electacta.2018.03.112
12. Hibino H, Nin F, Tsuzuki C, Kurachi Y (2009) How is the highly positive endocochlear potential formed? The specific architecture of the stria vascularis and the roles of the ion-transport apparatus. Pflügers Archiv European J Physiology 459:521–533. https://doi.org/10.1007/s00424-009-0754-z
13. Higashiyama K, Takeuchi S, Azuma H et al (2003) Bumetanide-induced enlargement of the intercellular space in the stria vascularis critically depends on Na+ transport. Hearing Res 186:1–9. https://doi.org/10.1016/s0378-5955(03)00226-0
14. Hunt MJ, Garcia R, Large CH, Kasicki S (2008) Modulation of high-frequency oscillations associated with NMDA receptor hypofunction in the rodent nucleus accumbens by lamotrigine. Prog Neuro-psychopharmacology Biological Psychiatry 32:1312–1319. https://doi.org/10.1016/j.pnpbp.2008.04.009
15. Lopez-Samblas AM, Adams JA, Goldberg RN, Modi MW (1997) The pharmacokinetics of bumetanide in the newborn infant. Neonatology 72:265–272. https://doi.org/10.1159/000244492
16. Massoud TF, Gambhir SS (2003) Molecular imaging in living subjects: seeing fundamental biological processes in a new light. Gene Dev 17:545–580. https://doi.org/10.1101/gad.1047403
17. Ogata G, Ishii Y, Asai K et al (2017) A microsensing system for the *in vivo* real-time detection of local drug kinetics. Nat Biomed Eng 1:654–666. https://doi.org/10.1038/s41551-017-0118-5
18. Rizk M, Zou L, Savic R, Dooley K (2017) Importance of drug pharmacokinetics at the site of action. Clin Transl Sci 10:133–142. https://doi.org/10.1111/cts.12448
19. Spãtaru N, Sarada BV, Popa E et al (2001) Voltammetric determination of L-cysteine at conductive diamond electrodes. Anal Chem 73:514–519. https://doi.org/10.1021/ac000220v
20. Suzuki A, Ivandini TA, Yoshimi K et al (2007) Fabrication, characterization, and application of boron-doped diamond microelectrodes for *in vivo* dopamine detection. Anal Chem 79:8608–8615. https://doi.org/10.1021/ac071519h
21. Thalmann I, Comegys TH, Liu SZ et al (1992) Protein profiles of perilymph and endolymph of the guinea pig. Hearing Res 63:37–42. https://doi.org/10.1016/0378-5955(92)90071-t
22. Walker MC, Tong X, Perry H et al (2000) Comparison of serum, cerebrospinal fluid and brain extracellular fluid pharmacokinetics of lamotrigine. Brit J Pharmacol 130:242–248. https://doi.org/10.1038/sj.bjp.0703337

https://www.twirpx.org & http://chemistry-chemists.com

Influenza Virus

Teruhiko Matsubara and Toshinori Sato

Abstract The rapid diagnosis of patients in clinical practice is important for anti-influenza therapy. However, since the sensitivity of conventional rapid diagnostic test kits is low, false-negative results are often produced. Therefore, simple and convenient test kits with high sensitivity are needed in clinical practice. In this chapter, we describe the construction of a boron-doped diamond (BDD) electrode that terminates with a receptor (sialic acid-containing oligosaccharide chain)-mimicking peptide as well as its performance in the electrochemical detection of human and avian influenza viruses (IFVs).

Keywords Influenza virus · Boron-doped diamond electrode · Sialic acid-mimic peptide · Electrochemical impedance spectroscopy · Click chemistry

1 Introduction: Influenza

1.1 Influenza Virus

Influenza is an infectious disease caused by influenza A virus (IFV) and circulates every winter in the north hemisphere.[1, 2] The diameter of IFV is approximately 100 nm, and the structure of its envelope comprises two major antigenic proteins, hemagglutinin (HA) and neuraminidase (NA) (Fig. 1) [3]. Influenza subtypes are distinguished based on differences in the antigenicities of these proteins, and 18 HA and 11 NA types (such as H1N1 and H3N2) have been identified to date [1]. The notation of a virus strain involves the region initially isolated, the lineage number, and year of isolation (e.g., A/Puerto Rico/8/34 (H1N1)).

Recent studies reported that human infections with avian H5N1 and H7N9 viruses induced severe diseases with high mortality rates of 53.5% (483/903 cases) [4] and 33.8% (47/139 cases), [5] respectively. Therefore, the rapid detection of novel avian

T. Matsubara · T. Sato (✉)
Faculty of Science and Technology, Department of Biosciences and Informatics, Keio University, 3-14-1 Hiyoshi, Kohoku-ku, Yokohama 223-8522, Kanagawa, Japan
e-mail: sato@bio.keio.ac.jp

© Springer Nature Singapore Pte Ltd. 2022

Y. Einaga (ed.), *Diamond Electrodes*,
https://doi.org/10.1007/978-981-16-7834-9_15

https://www.twirpx.org & http://chemistry-chemists.com

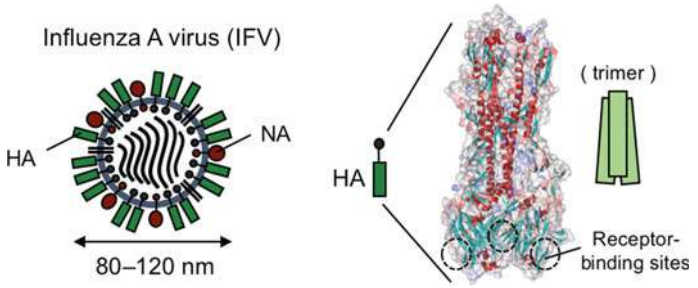

Fig. 1 Schematic diagram of influenza A virus. HA and NA are present on the surface envelope of the virus. Its diameter is approximately 100 nm. The HA trimer is shown (PDB entry ID: 1HGG)

viruses that may cause pandemics is crucial for preventing the circulation of avian virus infections in humans.

1.2 Anti-Influenza Therapy and Diagnosis

Influenza vaccination is the first strategy employed to prevent its transition to a more severe disease in high-risk groups, including infants, the elderly, and those with an underlying chronic condition. However, since the production of influenza vaccines is time-consuming, vaccines made from seasonal viruses are not capable of responding to outbreaks of new influenza strains.

The anti-influenza drugs, oseltamivir, and zanamivir were administered during the 2009 swine flu pandemic, and their efficacy was demonstrated. [6, 7] In the past two decades, several anti-influenza drugs that function as neuraminidase inhibitors (oseltamivir, zanamivir, peramivir, and laninamivir) have been developed [8]. A new type of anti-influenza drug, baloxavir marboxil, which inhibits the cap-dependent endonuclease of IFV, was recently released onto the market [9]. These anti-influenza drugs are established treatments in clinical practice.

Rapid IFV detection in specimens collected from patients with influenza-like symptoms in clinical practice is useful for subsequent treatment with anti-influenza drugs [10, 11]. Some anti-influenza drugs, such as neuraminidase inhibitors, including oseltamivir and zanamivir, are only effective up to 36 (or 48) hours after onset [8]. However, due to low sensitivity, the rapid diagnostic test (RDT) kits that are currently used do not detect IFV until approximately one day after onset. Furthermore, since these kits are based on immunochromatography, their sensitivity depends on the matching of antibodies in the kit to the antigenicity of IFV in the specimen. The polymerase chain reaction (PCR) method is highly sensitive, but requires 1–2 days to provide results, and its accuracy also depends on the skill of the operator [12]. Therefore, rapid and highly sensitive test kits that are easily available in clinical practice are needed.

https://www.twirpx.org & http://chemistry-chemists.com

2 Design of IFV-Binding Peptides

2.1 *Identification of Receptor-Mimicking Peptides by Phage Display Technology*

Antibodies are generally regarded as ideal candidate molecules for capturing a target virus and have been used in numerous biological experiments and detections. Their affinity is very high, and this specific feature is employed to confirm the presence of a target. However, the molecular mass of an antibody is approximately 150 kDa for IgG, and mass production is expensive and time-consuming. If other inexpensive materials, such as chemical receptors, exhibit affinity for targets, they may become a more desirable alternative to antibodies.

G. P. Smith, one of the winners of the Nobel prize in chemistry in 2018, proposed phage display technology to obtain target-binding peptides and proteins using affinity selection from random peptide/protein libraries [13]. We used this phage display system to identify pentadecapeptide sequences that are recognized by the receptor-binding site of HA instead of sialyloligosaccharide receptors (Fig. 2) [14–16]. One of the pentadecapeptides was matured using further randomization and biopanning processes, and the s2 peptide, ARLPRTMVHPKPAQP, was ultimately identified. The five N-terminal amino acids of s2, ARLPR, were employed for IFV detection in this chapter. This peptide is considered to mimic the sialic acid portion of sialyloligosaccharide, and a docking simulation of the s2 (1–5) peptide with the HA pocket supports this interaction (Fig. 3). This simulation suggests that the side chains of Ser136, Asn137, and Glu190 for HA form hydrogen bonding interactions with Leu3, Pro4, and Arg5 and these three residues in HA are involved in sialic acid recognition [14]. Furthermore, hydrophobic interactions of Leu194, Trp222, and Leu226 for HA with Ala1, Leu3, and Pro4 for the peptide were also suggested.

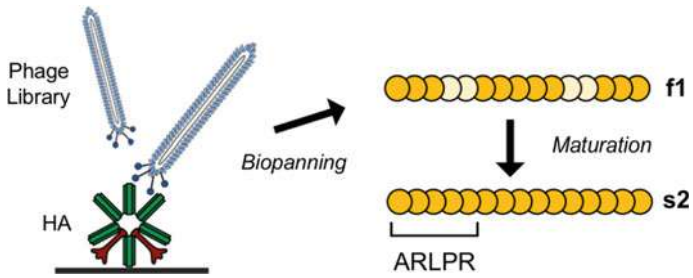

Fig. 2 Phage display selection (biopanning) for the identification of sialic acid-mimic peptides (f1 and s2). s2 (1–5) is the five N-terminal amino acids, ARLPR

https://www.twirpx.org & http://chemistry-chemists.com

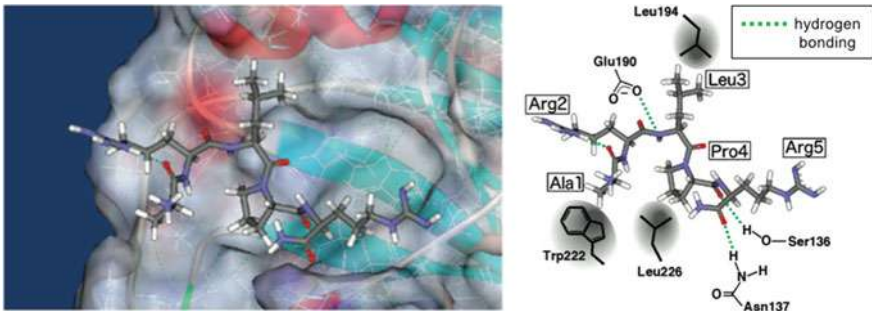

Fig. 3 Docking simulation between H3HA (PDB entry 1HGG) and the APRLR peptide. The suggested hydrogen bonds between HA and the peptide were drawn as green dotted lines. Hydrophobic interactions of Leu194, Trp222, and Leu226 for HA with Ala1, Leu3, and Pro4 for the peptide were also suggested. Adapted with permission from [14]. Copyright 2010 American Chemical Society

3 Preparation of a Peptide-Terminated BDD Electrode

3.1 Alkyne Termination on a BDD Electrode

The features of BDD electrodes include a wide potential window, low background current, chemical inertness, and mechanical durability [17, 18]. In recent years, electrochemical applications of conductive diamond electrodes have been reported for the detection of various biological materials. The weak adsorption of biomolecules is important in the development of biosensors.

In order to immobilize the peptide on BDD, the covalent modification of the carbon surface described by Leroux et al. was performed [19, 20]. The BDD surface was modified with the triisopropylsilyl-protected ethynyl aryl group (TIPS-Eth-Ar) by electroreduction (Fig. 4) [21, 22]. This reduction was confirmed by the presence of

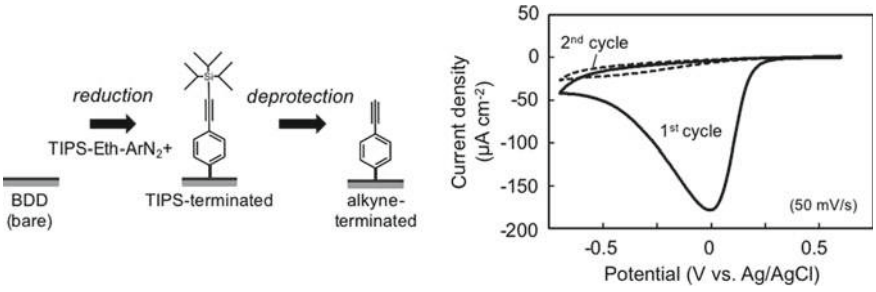

Fig. 4 Preparation of alkyne-terminated BDD. The immobilization of a TIPS-protected diazonium salt (TIPS-Eth-ArN_2^+) is shown using a voltammogram of the second cycle (*right*). Adapted with permission from [22]. Copyright 2020 American Chemical Society

https://www.twirpx.org & http://chemistry-chemists.com

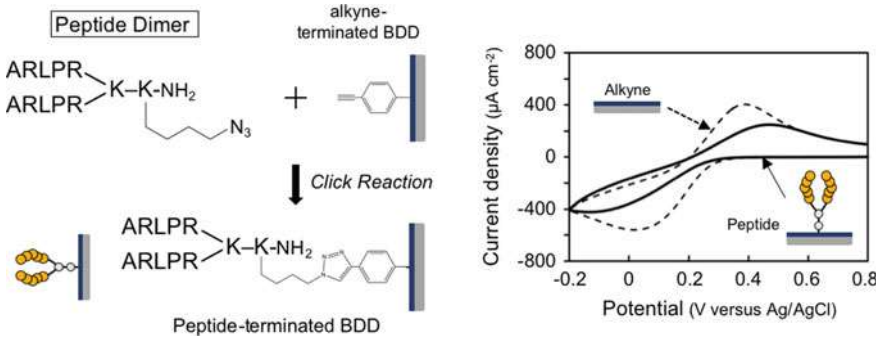

Fig. 5 Preparation of a peptide-terminated BDD electrode. Adapted with permission from [22]. Copyright 2020 American Chemical Society

a reduction peak at approximately 0 V in the first cycle of the cyclic voltammogram (CV). This peak disappeared in the second cycle due to the blockade of electric charge transfer between BDD and a bulky TIPS-Eth-Ar group. The TIPS group was then removed using tetrabutylammonium fluoride (TBAF), which exposed the ethynyl group (alkyne-terminated BDD).

3.2 Peptide Termination on a BDD Electrode

The alkyne-terminated electrode was incubated with an azide-containing peptide in the presence of Cu^{2+}, ascorbic acid, and a stabilizing ligand for the click reaction (Fig. 5) [23, 24]. The divalent peptide dendrimer (dimer) with a branched lysine (Lys) core was prepared for this immobilization [25]. Based on the CVs of $[Fe(CN)_6]^{3-/4-}$ using the peptide-terminated BDD electrode, the peak heights of the peptide-terminated BDD electrode decreased. In addition, peak potential separation between the oxidation and reduction reactions was greater than that of the alkyne-terminated BDD electrode. These results indicated the completion of peptide termination.

3.3 Estimation of Peptide Density on a BDD Electrode

To estimate peptide density immobilized on the BDD electrode, a ferrocene-containing peptide dimer was prepared and terminated (Fig. 6a) [26]. Since the ferrocenyl group was attached to the N terminus of the peptide dimer, the oxidation current of CV was integrated to estimate surface coverage. The amount of ferrocenyl peptide on the BDD electrode was estimated based on the area of the oxidation peak between + 0.21 and + 0.52 V. For example, when the surface coverage of the peptide

https://www.twirpx.org & http://chemistry-chemists.com

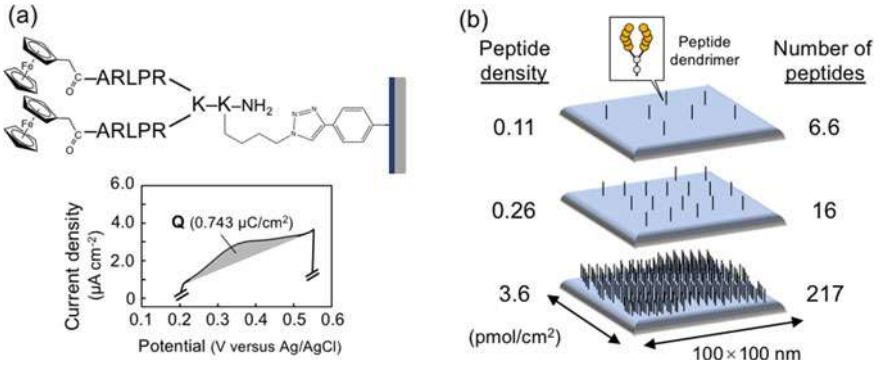

Fig. 6 Peptide density assessed using a ferrocene-linked peptide. **a** Cyclic voltammogram of a ferrocenyl peptide-terminated BDD electrode. The amount of ferrocenyl peptide immobilized on the electrode (3.85 pmol/cm^2) was estimated from the area of the oxidation peak (0.743 μC/cm^2) between +0.21 and +0.52 V. **b** BDD electrodes with various peptide densities (0.11–3.6 pmol/cm^2). The number of peptides was calculated to be 6.6–217 molecules in an area of 100 × 100 nm. Adapted with permission from [22]. Copyright 2020 American Chemical Society

immobilized on the BDD electrode was 3.6 pmol/cm^2, the density of the peptide was calculated as 217 molecules per 10,000 square nanometers (100 × 100 nm) (Fig. 6b).

The peptide-terminated BDD electrode with various densities was prepared by changing the conditions of the click reaction (Table 1). The peptide density termination depends on the peptide concentration and types of stabilizing ligand tris(benzyltriazolylmethyl)amine (TBTA) or water-soluble tris(3-hydroxypropyltriazolylmethyl)amine (THPTA). We obtained a peptide-terminated BDD electrode with a peptide density in the range of 0.11 to 5.6 pmol/cm^2.

Table 1 Various peptide densities and corresponding conditions for the click reaction. [a] The data are average values ± standard deviations (n = 3). Adapted with permission from [22]. Copyright 2020 American Chemical Society

Code	[Peptide dimer] (μM)	Ligand	Solvent	Peptide density (pmol/cm^2) [a]	Estimated peptides in a 100-nm square
TBTA-1	1	TBTA	50% MeOH	0.11 ± 0.01	6.6
TBTA-26	26	TBTA	50% MeOH	0.26 ± 0.01	16
TBTA-100	100	TBTA	50% MeOH	2.1 ± 0.6	127
THPTA-1	1	THPTA	Water	3.6 ± 0.4	217
THPTA-26	26	THPTA	Water	5.6 ± 0.1	337

https://www.twirpx.org & http://chemistry-chemists.com

4 Detection of IFVs with the Peptide-Terminated BDD Electrode

4.1 Human HA and IFV Detection with the Peptide Dimer-Terminated BDD Electrode

Prior to IFV detection, human HA was measured with the peptide dimer-terminated BDD electrode with a standard three-electrode configuration (Fig. 7a). The BDD surface was incubated with HA in PBS for 15 min, and electrochemical impedance spectroscopy (EIS) was performed using 5 mM $[Fe(CN)_6]^{3-/4-}$ in PBS as a redox probe. As the concentration of HA increased in the range of 5 to 375 nM, the diameter of the Nyquist plots became larger (Fig. 7b). Since the diameter of the semicircle in the Nyquist plots represents charge transfer resistance (R_{ct}) on the electrode surface, the HA-bound layer decreased charge transfer for the redox probe.

Human H1N1 influenza A virus (A/Puerto Rico/8/34) is one of the major seasonal H1 and H3 subtypes. H1N1 IFV-containing PBS (1–400 pfu in 50 μL) was incubated

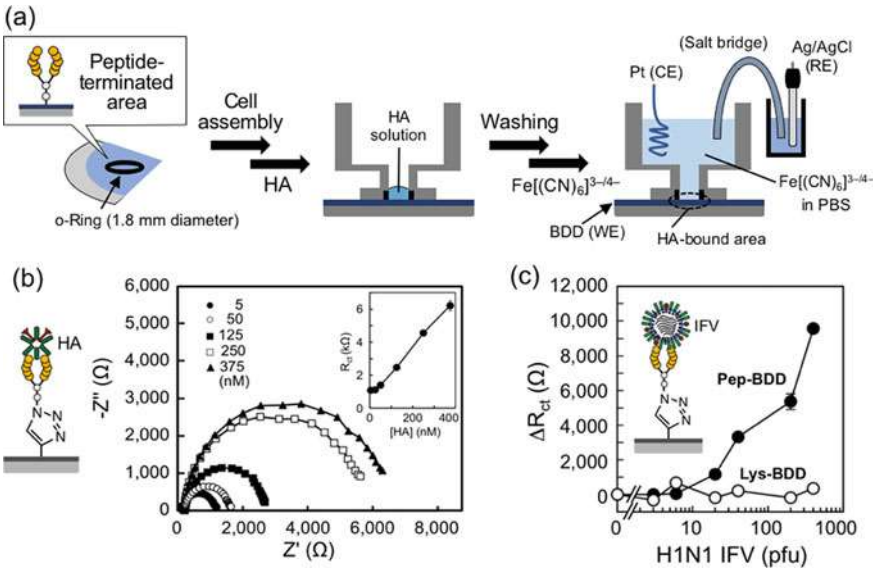

Fig. 7 Detection of HA and IFV using peptide dimer-terminated BDD electrodes. **a** Schematic representation of the measurement of H1 HA. The peptide dimer-terminated BDD electrode was assembled with electrochemical cell parts, and HA solution was incubated with the BDD surface. After washing, EIS was measured using $Fe[(CN)_6]^{3-/4-}$ in PBS. WE, working electrode; CE, counter electrode; RE, reference electrode. Adapted with permission from [22]. Copyright 2020 American Chemical Society. **b** Nyquist plots for HA measurements by EIS. The R_{ct} value was plotted as a function of HA concentrations (*inset*) [21]. **c** Dependence of changes in R_{ct} (ΔR_{ct}) on the number of H1N1 IFVs in PBS [21]. Pep-BDD, peptide-terminated BDD; Lys-BDD, Lys-terminated BDD. Data are average values ± standard deviations (n = 3)

https://www.twirpx.org & http://chemistry-chemists.com

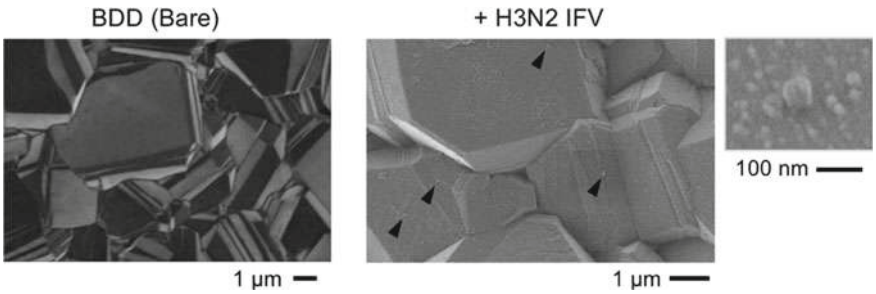

Fig. 8 Scanning electron micrographs of surfaces of a bare BDD and peptide dimer-terminated BDD (3.6 pmol/cm^2) after an IFV incubation (H3N2 IFV of 400 pfu). Arrowheads indicate IFV particles measuring approximately 100 nm in size. Adapted with permission from [22]. Copyright 2020 American Chemical Society

with the peptide dimer-terminated BDD electrode, and EIS was then performed. In comparisons with the results obtained using the Lys-terminated BDD electrode, the R_{ct} value of the Nyquist plots increased in the range of 20 to 400 pfu (Fig. 7c). The peptide dimer-terminated BDD electrode detected human H1N1 and H3N2 IFVs at 20–400 pfu. Since more than 1,000 pfu are required for detection with RDT kits, the performance of our peptide-terminated electrode was high for human IFV detection [10].

To confirm IFV binding on the BDD surface, scanning electron microscopy (SEM) of a surface of peptide-terminated BDD after the IFV incubation was performed. After the IFV incubation, particles of approximately 100 nm in size were observed on the surface of the electrode (Fig. 8). Small particles (approximately $10 - 20$ nm) may represent debris from viruses and/or other types of albumins.

4.2 Optimization of Peptide Termination: Peptide Density and Dendrimer Generations

To enhance the sensitivity of the electrode, several electrodes with different peptide densities of $0.11 - 5.6$ pmol/cm^2 were subjected to H1N1 IFV detection. Increases in the $\Delta R_{ct}/R_{ct0}$ value corresponding to the numbers of IFV were observed in all cases, but the nonspecific binding of IFV to the Lys-terminated electrode with peptide densities of 5.6 pmol/cm^2 was also observed (Fig. 9). The peptide-terminated BDD electrode with a peptide density of 3.6 pmol/cm^2 was selected for further investigations.

https://www.twirpx.org & http://chemistry-chemists.com

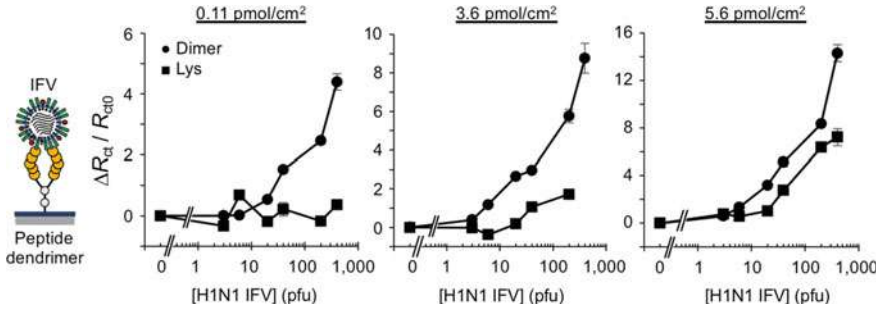

Fig. 9 IFV detection using peptide dimer-terminated BDD electrodes with three peptide densities. The IFV solution contained 0, 3, 6, 20, 40, 200, and 400 pfu in 50 μL PBS. Adapted with permission from [22]. Copyright 2020 American Chemical Society

4.3 Avian IFV Detection with the Peptide Tetramer-Terminated BDD Electrode

Avian H5N3 IFVs were not detected using the peptide dimer-terminated BDD electrode at a peptide density of 3.6 pmol/cm^2 (data not shown). Therefore, the peptide tetramer was designed and immobilized onto the BDD electrode at a density of 3.6 pmol/cm^2 (Fig. 10a). After an incubation with avian H5N3, H7N1, and H9N2 IFVs, the binding of IFV was detected by EIS. The $\Delta R_{ct}/R_{ct0}$ value was lower than that of human IFVs; however, more than 3 pfu avian IFVs were clearly detected (Fig. 10b). In addition, the tetramer-terminated BDD electrode showed excellent limit-of-detections (LODs) in the range of 0.13–6.7 pfu for avian IFV detection (Table 2). These results indicated that the peptide tetramer-terminated BDD electrode with a density of 3.6 pmol/cm^2 is applicable to the detection of both human and avian IFVs.

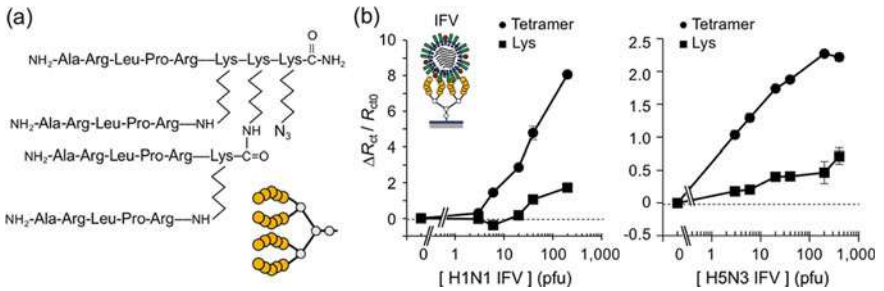

Fig. 10 Avian IFV detection using peptide tetramer-terminated BDD electrodes. **a** Chemical structure of the azide-containing peptide tetramer. **b** Avian IFV detection using peptide tetramer-terminated BDD electrodes. The peptide density of the peptide tetramer-terminated BDD was 3.6 pmol/cm^2. Adapted with permission from [22]. Copyright 2020 American Chemical Society

https://www.twirpx.org & http://chemistry-chemists.com

Table 2 Limit and range of IFV detection

Peptide dendrimer	Peptide density (pmol/cm^2)	Viral subtype[a]	Solution	R_{ct0} (Ω)	Limit of detection (pfu)	Range of detection (pfu)[b]
2 mer	0.11	Human H1N1	PBS	2180 ± 3	12.5	20–400[29]
2 mer	3.6	Human H1N1	PBS	156 ± 2	3.3	6–400
2 mer	3.6	Human H3N2	PBS	98 ± 4	0.91	6–400
4 mer	0.11	Human H1N1	PBS	1066 ± 98	15	20–400
4 mer	3.6	Human H1N1	PBS	267 ± 6	3.0	6–200
4 mer	3.6	Human H1N1	BSA/PBS	68 ± 6	0.33	3–400
4 mer	3.6	Human H1N1	HSA/PBS	74 ± 2	0.60	3–400
4 mer	3.6	Duck H5N3	PBS	48 ± 1	0.13	3–400
4 mer	3.6	Duck H7N1	PBS	126 ± 5	0.38	3–400
4 mer	3.6	Duck H9N2	PBS	63 ± 1	6.7	3–400

[a] A/Puerto Rico/8/34 (H1N1); A/Aichi/2/68 (H3N2); A/duck/Hong Kong/820/1980 (H5N3); A/duck/Hong Kong/301/1978 (H7N1); A/duck/Hong Kong/448/1978 (H9N2).
[b] Detection was significantly better than with the Lys-terminated BDD electrode (0 pmol/cm^2).
Adapted with permission from [22]. Copyright 2020 American Chemical Society

5 Conclusion

In this chapter, we described the detection of IFV in the range of 3–400 pfu using the combination of a sialic acid-mimic peptide and BDD electrode. This sensitivity is approximately 300-fold higher than that of the RDT kit. We may perform a diagnosis at any onset time using our peptide-terminated electrode where necessary for the administration of anti-influenza drugs. The sugar chain-mimic peptide used to capture the virus may bind to the virus independent of the subtypes; therefore, this electrode will be useful for the emergence of new strains. IFV detection based on this methodology may be applicable to clinical practical in the future.

Acknowledgements The bare BDD materials and guide of electrochemical procedures were provided by Prof. Y. Einaga and Prof. T. Yamamoto (Keio University). Electrochemical measurements were performed by Dr. M. Ujie and Ms. M. Akahori. Avian IFVs were provided by Prof. T. Nakaya and Prof. T. Daidoji (Kyoto Prefectural University of Medicine). We greatly thank all the collaborators.

https://www.twirpx.org & http://chemistry-chemists.com

References

1. Paules C, Subbarao K (2017) Influenza. Lancet 390(10095):697–708
2. Webster RG, Govorkova EA (2014) Continuing challenges in influenza. Ann N Y Acad Sci 1323:115–139
3. Gamblin SJ, Skehel JJ (2010) Influenza hemagglutinin and neuraminidase membrane glycoproteins. J Biol Chem 285(37):28403–28409
4. Lai S, Qin Y, Cowling BJ, Ren X, Wardrop NA, Gilbert M, Tsang TK, Wu P, Feng L, Jiang H, Peng Z, Zheng J, Liao Q, Li S, Horby PW, Farrar JJ, Gao GF, Tatem AJ, Yu H (2016) Global epidemiology of avian influenza A H5N1 virus infection in humans, 1997–2015: a systematic review of individual case data. Lancet Infect Dis 16(7):e108–e118
5. Li Q, Zhou L, Zhou M, Chen Z, Li F, Wu H, Xiang N, Chen E, Tang F, Wang D, Meng L, Hong Z, Tu W, Cao Y, Li L, Ding F, Liu B, Wang M, Xie R, Gao R, Li X, Bai T, Zou S, He J, Hu J, Xu Y, Chai C, Wang S, Gao Y, Jin L, Zhang Y, Luo H, Yu H, He J, Li Q, Wang X, Gao L, Pang X, Liu G, Yan Y, Yuan H, Shu Y, Yang W, Wang Y, Wu F, Uyeki TM, Feng Z (2014) Epidemiology of human infections with avian influenza A(H7N9) virus in China. N Engl J Med 370(6):520–532
6. Yu K, Luo C, Qin G, Xu Z, Li N, Liu H, Shen X, Ma J, Wang Q, Yang C, Zhu W, Jiang H (2009) Why are oseltamivir and zanamivir effective against the newly emerged influenza a virus (A/H1N1)? Cell Res 19(10):1221–1224
7. Salomon R, Webster RG (2009) The influenza virus enigma. Cell 136(3):402–410
8. von Itzstein M (2007) The war against influenza: discovery and development of sialidase inhibitors. Nat Rev Drug Discovery 6(12):967–974
9. Ikematsu H, Hayden FG, Kawaguchi K, Kinoshita M, de Jong MD, Lee N, Takashima S, Noshi T, Tsuchiya K, Uehara T (2020) Baloxavir marboxil for prophylaxis against Influenza in household contacts. N Engl J Med 383(4):309–320
10. Sakai-Tagawa Y, Ozawa M, Tamura D, Le M, Nidom CA, Sugaya N, Kawaoka Y (2010) Sensitivity of influenza rapid diagnostic tests to H5N1 and 2009 pandemic H1N1 viruses. J Clin Microbiol 48(8):2872–2877
11. Hayden FG, Osterhaus AD, Treanor JJ, Fleming DM, Aoki FY, Nicholson KG, Bohnen AM, Hirst HM, Keene O, Wightman K (1997) Efficacy and safety of the neuraminidase inhibitor zanamivir in the treatment of influenza virus infections. GG167 Influenza Study Group. N Engl J Med 337(13):874–880
12. Ruest A, Michaud S, Deslandes S, Frost EH (2003) Comparison of the Directigen flu A+B test, the QuickVue influenza test, and clinical case definition to viral culture and reverse transcription-PCR for rapid diagnosis of influenza virus infection. J Clin Microbiol 41(8):3487–3493
13. Smith GP, Petrenko VA (1997) Phage display. Chem Rev 97(2):391–410
14. Matsubara T, Onishi A, Saito T, Shimada A, Inoue H, Taki T, Nagata K, Okahata Y, Sato T (2010) Sialic acid-mimic peptides as hemagglutinin inhibitors for anti-influenza therapy. J Med Chem 53(11):4441–4449
15. Hatano K, Matsubara T, Muramatsu Y, Ezure M, Koyama T, Matsuoka K, Kuriyama R, Kori H, Sato T (2014) Synthesis and influenza virus inhibitory activities of carbosilane dendrimers peripherally functionalized with hemagglutinin-binding peptide. J Med Chem 57(20):8332–8339
16. Matsubara T, Onishi A, Yamaguchi D, Sato T (2016) Heptapeptide ligands against receptor-binding sites of influenza hemagglutinin toward anti-influenza therapy. Bioorg Med Chem 24(5):1106–1114
17. Luong JH, Male KB, Glennon JD (2009) Boron-doped diamond electrode: synthesis, characterization, functionalization and analytical applications. Analyst 134(10):1965–1979
18. Einaga Y (2010) Diamond electrodes for electrochemical analysis. J Appl Electrochem 40(10):1807–1816

https://www.twirpx.org & http://chemistry-chemists.com

19. Leroux YR, Fei H, Noel JM, Roux C, Hapiot P (2010) Efficient covalent modification of a carbon surface: use of a silyl protecting group to form an active monolayer. J Am Chem Soc 132(40):14039–14041
20. Natsui K, Yamamoto T, Akahori M, Einaga Y (2015) Photochromism-induced amplification of critical current density in superconducting boron-doped diamond with an azobenzene molecular layer. ACS Appl Mater Interfaces 7(1):887–894
21. Matsubara T, Ujie M, Yamamoto T, Akahori M, Einaga Y, Sato T (2016) Highly sensitive detection of influenza virus by boron-doped diamond electrode terminated with sialic acid-mimic peptide. Proc Natl Acad Sci USA 113(32):8981–8984
22. Matsubara T, Ujie M, Yamamoto T, Einaga Y, Daidoji T, Nakaya T, Sato T (2020) Avian influenza virus detection by optimized peptide termination on a boron-doped diamond electrode. ACS Sens 5(2):431–439
23. Kolb HC, Finn MG, Sharpless KB (2001) Click chemistry: diverse chemical function from a few good reactions. Angew Chem Int Ed 40(11):2004–2021
24. Yamamoto T, Akahori M, Natsui K, Saitoh T, Einaga Y (2018) Controlled decoration of boron-doped diamond electrodes by electrochemical click reaction (e–CLICK). Carbon 130:350–354
25. Tam JP (1988) Synthetic peptide vaccine design: synthesis and properties of a high-density multiple antigenic peptide system. Proc Natl Acad Sci USA 85(15):5409–5413
26. Kira M, Matsubara T, Shinohara H, Sisido M (1997) Synthesis and redox property of polypeptides containing L-ferrocenylalanine. Chem Lett 1:89–90

https://www.twirpx.org & http://chemistry-chemists.com